Adsorption and Thin Film Growth of Oligo-phenylenes on Gold Surfaces

PhD Thesis

by
Dipl.-Ing. Stefan Müllegger

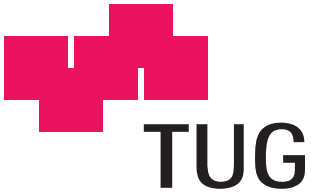

carried out at the
Institute of Solid State Physics
Graz University of Technology, Austria

under the supervision of
Ao. Univ.-Prof. Dipl.-Ing. Dr. techn. Adolf Winkler

for obtaining the academic degree
"Doktor der Technischen Wissenschaften"

Graz, October 2005

for my family

Acknowledgement

Obtaining a PhD is more than just writing a book. For me it has been exciting years of scientific effort and cooperational work with many interesting people. Of course, some of them have been more helpful than others, but each of them has left behind a sustainable mark not only from a scientific point of view but has also contributed his or hers very personal character. I have eminently enjoyed working in such a pleasant environment!

First and foremost I am deeply grateful for the prudent support of my doctoral advisor, A. Winkler. It was my great pleasure to work with such an able and precise scientist and amicable colleague. For their scientific support I also want to thank G. Hlawacek, C. Teichert, S. Holzleitner, R. Resel, T. Haber, I. Salzmann, M. Oehzelt, A. Stupnik, M. Leisch, C. Wöll, K. Hänel, A. Birkner, P. Pölt, S. Mitsche and T. Strunskus. I also thank my colleagues of the Surface Science Group, M. Kratzer, G. Pauer, R. Schennach and G. Krenn, as well as all the members of the Institute of Solid State Physics of the Graz University of Technology and all the members of the Project Cluster "Highly Ordered Organic Epilayers". I thank the Austrian Science Fund (FWF), the Austrian Research Community (ÖWG) and the Graz University of Technology (TUG) for the financial support of this work.

And, most important, I am deeply grateful to my family and my girlfriend Waltraud for their love and emotional support.

Abstract

The present work investigates fundamental aspects concerning the adsorption and thin film growth of the organic semiconducting materials p-quaterphenyl (4P) and p-hexaphenyl (6P) on different single- and polycrystalline gold surfaces. The organic films have been grown by physical vapour deposition under ultra-high vacuum conditions. A variety of complementary surface sensitive analytical methods have been applied, such as thermal desorption spectroscopy (TDS), low energy electron diffraction (LEED), x-ray diffraction (XRD), Auger electron spectroscopy (AES), x-ray photo-electron spectroscopy (XPS), atomic force microscopy (AFM), scanning tunneling microscopy (STM) and near-edge x-ray absorption fine structure spectroscopy (NEXAFS).

One focus of this work lies in the determination of the organic thin film structure relative to the gold substrate over a wide thickness range spanning from ultra-thin films in the submonolayer regime (< 0.1 nm) to the bulk phase (> 100 nm). In particular, it is demonstrated that 4P and 6P forms highly ordered crystalline films that grow quasi-epitaxially on a single crystalline Au(111) surface at adsorption temperatures between 270 K and 420 K. A Stranski-Krastanov type film growth is observed, where a highly regular monomolecular wetting layer serves as a structural pre-stage for the bulk phase. The oligo-phenyl monolayer (ML) on Au(111) exhibits a characteristic edge-face packing structure of flat and side-tilted molecules. A defined azimuthal alignment of the oligo-phenyl molecules parallel to the Au$\langle 1\bar{1}0\rangle$ and Au$\langle 11\bar{2}\rangle$ directions of the gold substrate exists for both the bulk crystals and the monolayer. Structural models are proposed concerning the molecular packing of the semilayer (0.5 ML) and the saturated monolayer, respectively. At adsorption temperatures smaller than about 270 K, a disordered growth predominates, in particular, for the wetting layer. The structural investigations are complemented by experiments concerning the energetics and kinetics of the adsorption and desorption of the organic molecules on gold surfaces. In particular, the monolayer and multilayer desorption energies of 4P and 6P together with the pre-exponential (frequency) factors are determined based on a sophisticated Polanyi-Wigner approach.

It is demonstrated that upon heat treatment (roughly above 600 K) a significant fraction of the oligo-phenyl monolayer is dehydrogenated and cannot be desorbed intact from the gold surface. In a multi-step dehydrogenation process the oligo-phenyl molecules adsorbed on the surface partially loose their hydrogen atoms, forming new supermolecular polycyclic aromatic intermediates, and finally form a graphitic-like carbon layer on the gold surface upon a complete dehydrogenation at a further increase of the temperature.

Several alternative strategies are investigated that allow to control the crystal orientation and film morphology of 4P and 6P thin films on different gold substrates. This includes either a variation of the substrate surface geometry (stepped surfaces like a single-crystalline vicinal Au(433) or a poly-crystalline Au surface), or the substrate surface chemistry (partial carbon pre-coverage) or the substrate temperature. It is demonstrated that a tailoring of the organic thin films can be realized, which means the controlled growth of highly crystalline thin films exhibiting a specific crystal orientation. Several different crystal orientations comprising either lying or standing upright molecules are demonstrated. Simultaneous to the transition from one crystal orientation to another proceeds a change of the film morphology and this way both an island-like as well as a layer-by-layer growth of the organic film can be realized. This is important for device applications.

Kurzfassung

Die vorliegende Arbeit untersucht fundamentale Aspekte hinsichtlich der Adsorption und des Dünnfilmwachstums der halbleitenden organischen Materialien p-Quaterphenyl (4P) und p-Hexaphenyl (6P) auf verschiedenen ein- und polykristallinen Goldoberflächen. Die organischen Filme wurden mittels Gasphasenabscheidung unter Ultrahochvakuumbedingungen aufgedampft. Eine Vielzahl komplementärer oberflächensensitiver Analyseverfahren wurde eingesetzt, wie zum Beispiel Thermische Desorptionsspektroskopie (TDS), Beugung niederenergetischer Elektronen (LEED), Röntgenbeugung (XRD), Augerelektronenspektroskopie (AES), Röntgen-Photoelektronenspektroskopie (XPS), Atomkraftmikroskopie (AFM), Raster-Tunnelmikroskopie (STM) und Röntgenabsorptionsspektroskopie (NEXAFS).

Eine wichtiger Bestandteil dieser Arbeit besteht in der Strukturbestimmung der organischen Dünnschichten relativ zum Goldsubstrat über einen weiten Dickenbereich, der sich von ultradünnen Schichten (< 0.1 nm) bis hin zur Kristallphase (> 100 nm) erstreckt. Insbesondere wird gezeigt, daß 4P und 6P hochgeordnete kristalline Filme ausbildet, welche bei Temperaturen zwischen 270 K und 420 K quasiepitaktisch auf einer Au(111) Einkristalloberfläche aufwachsen. Ein Stranski-Krastanov typisches Filmwachstum kann beobachtet werden, wobei ein hochgeordneter monomolekularer Wettinglayer (benetzende Monolage) als strukturelle Vorstufe für die Kristallphase fungiert. Die Oligophenylmonolage (ML) auf Au(111) weist eine sogenannte "edge-face" Struktur von flach liegenden und seitlich gedrehten Molekülen auf. Eine bestimmte azimuthale Ausrichtung der Oligophenylmoleküle parallel zu den Au$\langle 1\bar{1}0\rangle$ und Au$\langle 11\bar{2}\rangle$ Richtungen des Goldsubstrates existiert sowohl in der Bulkphase als auch in der Monolage. Betreffend die Semilage (0.5 ML) und die gesättigte Monolage werden Strukturmodelle für die molekulare Anordnung vorgeschlagen. Für Adsorptionstemperaturen, die kleiner als etwa 270 K sind, dominiert ein ungordnetes Wachstum, insbesondere für den Wettinglayer. Die Strukturuntersuchungen werden ergänzt durch Experimente betreffend die Energetik und Kinetik der Adsorption und Desorption der organischen Moleküle auf Goldoberflächen. Insbesonders werden die Desorptionsenergien sowie die Präexponetialfaktoren (Frequenzfaktoren) von 4P und 6P für die Monolage und die Multilage, basierend auf einem verfeinerten Polanyi-Wigner Ansatz, bestimmt.

Es wird gezeigt, daß bei einer Wärmebehandlung (über etwa 600 K) ein signifikanter Bruchteil der Oligophenylmonolage dehydrogeniert und nicht mehr intakt von der Goldoberfläche desorbieren kann. In einem mehrstufigen Dehydrogenationsprozess ver-

lieren die auf der Oberfläche adsorbierten Oligophenylmoleküle stufenweise ihre Wasserstoffatome, um neue supermolekulare polyzyklische aromatische Zwischenprodukte, und schlußendlich unter einer vollständigen Dehydrogenation nach erfolgter weiterer Temperaturerhöhung eine graphitähnliche Kohlenstoffschicht auf der Goldoberfläche zu bilden.

Mehrere alternative Strategien werden untersucht, welche es erlauben, die Kristallorientierung und die Filmmorphologie von 4P und 6P auf verschiedenen Goldoberflächen zu kontrollieren. Dies beinhaltet entweder eine Variation der Oberflächengeometrie des Substrates (gestufte Oberflächen wie etwa eine einkristalline vizinale Au(433) oder eine polykristalline Goldoberfläche) oder der Oberflächenchemie (teilweise Kohlenstoffbedeckung) oder der Substrattemperatur. Es wird gezeigt, daß ein sogenanntes "Tailoring" der organischen Filme verwirklicht werden kann, welches ein kontrolliertes und gezieltes Wachstum von hochkristallinen Dünnschichten mit einer spezifische Kristallorientierung bezeichnet. Mehrere verschiedene Kristallorientierungen werden nachgewiesen, welche entweder liegende oder aufrecht stehende Moleküle beinhalten. Gleichzeitig mit dem Übergang von einer Kristallorientierung in eine andere findet ein Wechsel der Filmmorphologie statt, und auf diese Weise kann sowohl ein inselartiges als auch ein schichtartiges Wachstum der organischen Filme verwirklicht werden. Dies ist in der Herstellung von Bauteilen von großer Bedeutung.

Contents

List of Figures

List of Tables

Symbols and Abbreviations

4P, 6P	para-quaterphenyl, para-hexaphenyl
α	multilayer desorption peak
AES	Auger electron spectroscopy
AFM	atomic-force microscopy
amu	atomic mass unit
β	monolayer desorption peak
CHA	concentric hemispheric analyzer
EBS	electron back scattering
E_{des}	energy of desorption
fcc	face-centered cubic
FWHM	full width at half maximum
HWE	hot wall epitaxy
LEED	low energy electron diffraction
MCP	micro-channelplate
ML	monolayer
NEXAFS	near edge X-ray absorption fine structure
nP	oligo-phenylene(s)
OM	optical microscopy
OMBD, OMBE	organic molecular beam deposition or -epitaxy
PVD	physical vapour deposition
QMS	quadrupole mass spectrometer
RGA	residual gas analysis
RT	room temperature
SC	semiconductor
SEM	scanning electron microscopy
STM	scanning tunneling microscopy
T	temperature
TDS	thermal desorption spectroscopy
Θ	coverage
UHV	ultra-high vacuum
XPS	X-ray photoelectron spectroscopy
XRD	X-ray diffraction

Introduction

Recently, there has been growing activity, both in academic and in industrial research, to develop organic-based thin film electronic devices. One of the most prominent developments are organic thin film transistors [1–3]. These are supposed to satisfy a growing demand for inexpensive low-level electronics, which can be used for intelligent electronic labels (so-called "smart-tags") or smart cards. Also organic light-emitting devices have been developed [4, 5] and in some cases they have already replaced conventional inorganic products like light-emitting diodes or liquid crystal displays. But organic semiconductors are also suitable for photo-detector, solar cell or sensor applications. The term "organic" indicates the hydrocarbon nature of the used molecules. The starting point for the research in this field was set in the year 1976. Back then, it was discovered that doping hydrocarbon polymers, and in particular polyacetylene, can change their behaviour from insulating to metallic[1]. Since then the number of different conducting organic materials has been enormously increased and they have also gained technological relevance. Conducting polymers have been used for electromagnetic shielding, antistatic coatings or windows with changeable optical properties. Even more attractive for applications, however, are certain undoped polymers which exhibit semiconducting and sometimes electroluminescent properties. This, of course, has opened a completely new field of potential applications based on organic semiconductors.

It was soon discovered that also shorter aromatic molecules, the so-called oligomers, exhibit properties similar to the semiconducting polymers. From a chemical point of view the oligomers consist of less than about 50 monomeric units. Thus, they are frequently denoted as "small molecules", emphasizing the smaller Van-der-Waals dimensions of a few nm and the smaller molecular weight of less than about 1000 amu, compared to polymers. In many cases oligomer materials are even more suitable for application than polymers. A big advantage of oligomers over polymers is their ability to form well-defined and highly crystalline thin films. This enables to control the intrinsic material properties and the thin film growth, e.g. on single crystalline substrates. The fabrication of oligomer thin films is most frequently performed by physical vapour deposition (PVD), organic molecular beam deposition (OMBD) [6] or hot-wall epitaxy (HWE) [7]. All of these techniques make use of the fact that oligomers are readily evaporated under vacuum conditions.

The ability to grow well-defined organic thin films is of utmost importance for many

[1]Nobel chemistry laureates 2000: Alan J. Heeger, Alan G. MacDiarmid and Hideki Shirakawa "... for the discovery and development of conductive polymers".

applications since most of the organic-based devices exhibit a so-called "sandwich structure". This concept combines multiple thin layers of different compounds, both organic and inorganic. The thickness of the layers usually ranges between 1 nm and 1000 nm. Various heterogeneous interfaces exist in such devices, either organic-organic, organic-inorganic or inorganic-inorganic. The interfaces are crucial for the performance of the devices (charge injection) [8, 9] and, in particular, the interface between the organic compound and the contact electrode is significant. In many cases the interface properties are determined by intermolecular interactions between the organic molecules and the substrate, which is often an inorganic crystalline material. Similarly important are, of course, the intrinsic material properties of the organic compound itself as well as the morphology of the organic thin film [10].

The basis for the development and improvement of applications has always been a profound understanding of the fundamental physics. An important side-effect of the research on organic semiconductors has been the strong interlink between different scientific disciplines. This inter-disciplinarity has been reinforced by a steadily increasing technological relevance of organic semiconductors [11]. The most prominent sciences involved in the interdisciplinary research on organic semiconductors are:

- solid state physics
- organic chemistry
- nanotechnology
- surface science

From what has been said so far, two important factors can be named, which help to confine the scope of this PhD thesis. Firstly, the importance of heterogeneous adsorbate/substrate interfaces to the properties of organic thin films. This aspect strongly involves surface science. And secondly, the possibility of oligomer materials to form highly ordered and structurally well-defined thin films in a controlled manner, which is important for both fundamental research and application.

Although a lot of work has already been done concerning the growth of crystalline organic thin films on solid substrates (compare Section 1.3.1) there is still plenty of open questions. For instance, there is only little knowledge on the mechanisms governing the preferred growth of organic crystallites or the conditions for epitaxial growth on inorganic substrates. The interstitial coverage regime spanning from the first monolayer up to the actual bulk structure is not well understood, either. This regime is important as it covers the transition from the 2-dimensional monolayer structure to the 3-dimensional bulk structure of the organic film. Equally obscure is still the situation when organic thin films have to be electrically contacted. This is most often done with the help of metallic electrodes, which often implies large structural mismatches, electric dipole layers and inter-diffusion at the interfaces.

The present work describes fundamental experimental investigations on oligo-para-phenylene (nP) thin films grown on crystalline gold surfaces. The nPs are oligomer model systems with a certain relevance for (opto)electronic applications. In particular, p-quaterphenyl (4P) and p-hexaphenyl (6P) have been grown on different crystalline gold surfaces like single crystalline Au(111) and Au(433) or poly-crystalline Au. The formation of highly ordered organic thin films has been investigated in detail. A strong emphasize was put on the surface science aspect. Thus, a majority of surface-sensitive techniques has been applied together with ultra-high vacuum equipment to ensure well-defined experimental conditions. This has enabled a detailed study of the heterogeneous interface between the organic adlayer and the inorganic substrate. In particular, the influences of substrate properties like geometric structure or chemistry on the formation of the organic adlayer have been investigated. The presented results have been published in international scientific journals. The corresponding references are given in the reference list [12–21].

Overview

Chapter 1 gives a short summary of some fundamental aspects concerning this work, followed by Chapter 2 and 3, which provide an overview of the used analytical methods and experimental setup. In order to find a reasonable structure for the presentation of all the experimental findings that have been gained in this work, the first experimental chapter (Chapter 4) summarizes the data of 4P and 6P grown on the Au(111) surface. This system shall act as a "reference" to which later experimental results can be compared for a better understanding. Chapter 5 treats the influences of geometrical aspects of the substrate surface on the formation of the oligo-phenylene thin films. Besides stepped vicinal surfaces also poly-crystalline surfaces have been investigated. Chapter 6 reports on the chemical decomposition of nP molecules adsorbed on Au surfaces upon thermal treatment. These findings have lead to the development of tailoring methods for the aimed growth of specific nP film structures applying sub-monolayer carbon coverages. Those are described in Chapter 7, which reports on the possibilities of manipulating the organic films by changing the substrate chemistry, in particular by applying defined carbon pre-coverages to the gold substrates prior to the thin film deposition. Finally, Chapter 8 describes the possibilities of changing the nP film structure and morphology by growing the films at different substrate temperatures.

Part I

Prerequisites

Chapter 1

Fundamentals

This chapter gives a brief introduction to conjugated organic materials and in particular to the oligo-phenylenes. Their specific material properties are discussed together with some aspects concerning the structure and morphology of organic thin films grown on solid surfaces. Additionally, the properties of the single-crystalline Au(111) and Au(433) surfaces are described.

1.1 Conjugated organic materials

Concerning aromatic hydrocarbons the term "conjugation" denotes the molecular property of having alternating carbon single- and double bonds, which causes $sp^2 + p_z$ hybridization [22, 23]. The carbon sp^2 orbitals are exclusively involved in building up the backbone of the molecule, which determines the geometric structure and mechanical properties. The carbon p_z electrons, however, are delocalized across the conjugated area of the molecule to form extended π orbitals. Thus, the corresponding electrons are often denoted as π electrons. A prototypical example of a conjugated organic molecule is benzene.

In many cases conjugated organic molecules are semiconducting, which makes them attractive for (opto-)electronic applications. For these materials the electronic band gap between the HOMO and the LUMO [1] level is in the order of only a few eV, leading to low-energy excitations and semiconducting behaviour [24]. The electronic and optical properties can be changed rather easily, compared to inorganic semiconductors (SCs), by chemically "adjusting" the conjugated part of the molecules. Optionally, so-called functional groups can be attached to the conjugated molecular backbone, which is even a more powerful tool of tuning the opto-electronic properties. The thin film structure and morphology, however, is in some cases rather insensitive to such chemical modifications. Alternatively, the use of functional groups enables the growth of nano-structured thin films via self-assembling [25]. This is based on a well-defined relation between the orientation of the molecules and the substrate surface. This property is also very attractive for ap-

[1] The terms HOMO and LUMO denote the "highest occupied molecular orbital" and the "lowest unoccupied molecular orbital", respectively.

Table 1.1: Comparison of undoped organic and inorganic semiconductors.

	Inorganic SC	Organic SC	Ref.
Material	atomic crystal	molecular crystal	
Bond type	covalent	V.d.Waals, electrostatic (inter-) covalent (intramolecular)	
Crystal structure	diamond; cubic	monoclinic	
Charge transport	band-type	band-like (low T) polaron hopping (RT)	
Electron bands	strong dispersion	flat, narrow (10 - 100 meV)	[27]
Charge carrier mobility ($\frac{cm^2}{Vs}$)	10^2 - 10^4	10^{-6} - 15	[22, 28, 29]
Exciton binding energy (eV)	≤ 0.025	0.1 - 1	[29, 30]
Dielectric constant	11	3 - 4	[29]
Surface energy (J/m^2)	1	10^{-3}	

plications requiring highly ordered organic thin films. The high flexibility in varying the materials properties is one big advantage of conjugated organic materials over conventional inorganic SCs in terms of application.

In contrast to conventional inorganic SCs like silicon or germanium, which are atomic crystals with covalent bonds in all three spacial dimensions, the organic SCs are **molecular crystals**. In this case, the crystal building units are large aromatic molecules that are bonded via electrostatic and/or Van der Waals forces between each other [22]. Due to this fundamental difference several material properties, which are important for device applications, differ significantly from those of conventional SCs. Some of the most important differences concern the mechanisms of charge carrier transport [26]. If an electric charge (e.g. an electron) is added to a molecule, a local relaxation of the molecular backbone occurs in the vicinity of the charge carrier [24]. This electron-phonon coupling results in a self-localization of the added charge carrier. This state is usually denoted as polaron. In order to point out the most important differences of the material properties between organic and inorganic SCs, these are listed in Table 1.1.

The organic SCs can be classified according to the "length" of the molecules (number of monomeric units) into polymers and **oligomers**, so-called "small molecules", as described in the introduction. Both have their pros and cons in terms of thin film fabrication and (opto)electronic applications. However, the particular interest in oligomer materials is that they can be processed into highly crystalline thin films by vapour deposition. A beneficial side-effect is that the material is purified during the vapour deposition. A comparable high degree of chemical purity is difficult to achieve with solution-processed polymer materials. In addition, the high crystallinity achievable with oligomer materials is very attractive for both fundamental and applied research.

To name but a few, some of the most thoroughly investigated purely hydrocarbon conjugated oligomers are listed. Linear molecules: the oligo-phenylenes (biphenyl, terphenyl, quaterphenyl, hexaphenyl) and the oligo-acenes (naphtalene, anthracene, tetracene, pentacene). Polycyclic plate-like compounds: perylene, coronene and rubrene. Figure 1.1 shows the chemical structure of some prominent conjugated aromatic oligomers. In addi-

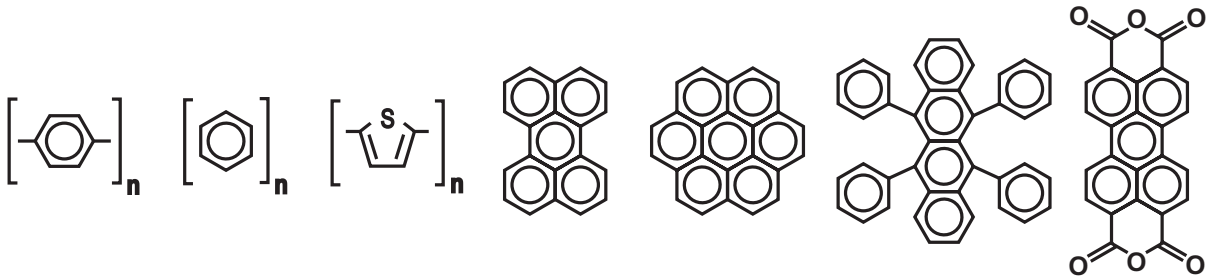

Figure 1.1: The chemical structure of some prominent conjugated aromatic oligomers. Left to right: oligo-phenylenes, -acenes ($n = 2 - 5$: naphthalene, anthracene, tetracene, pentacene), -thiophenes, perylene, coronene, rubrene, PTCDA.

tion to the purely hydrocarbon molecules there exists a variety of functionalized molecules. These molecules carry so-called functional side groups that comprise for instance oxygen, like the perylene-tetracarboxylicacid-dianhydride (PTCDA) molecule, or sulfur, like the oligo-thiophenes. The method of functionalization has triggered a whole new area of research, since it allows to chemically add specific functionalities to each molecule. These can be for instance electron transport or optical properties. In the case of self-assembled monolayers (SAMs) the molecules posses a functional anchor group providing strong binding to the substrate. Some of the semiconducting organic materials (either functionalized or not) have already found their way to industrial applications. A comprehensive overview can be found on `http://www.orgworld.de/`.

1.2 Oligo-phenylenes

The oligo-phenylenes (nPs) are good model systems of linear conjugated organic molecules. Several species with different molecular length are commercially available. They are named according to the number of phenyl rings per molecule, i.e. biphenyl (2P), terphenyl (3P), quaterphenyl (4P), quinquephenyl (5P), hexaphenyl (6P) and septiphenyl (7P). The limiting case of theoretically infinite phenyl rings, the phenylene-based polymer, is poly-paraphenylene (PPP). Different from PPP, the phenylene oligomers can be evaporated under UHV conditions for thin film preparation. Under ambient conditions they are chemically stable and highly emissive in the blue/UV-vis spectral region (photoemission, electroluminescence). The π-conjugation extends along the whole molecular backbone. The nPs are semiconducting, exhibiting an electronic band gap which scales inversely with the number of phenyl rings per molecule [31]. Band gap values between 2.4 eV for PPP and 5.1 eV for 2P have been observed [32, 33]. The nPs are attractive candidates for (prototypical) applications as well as for fundamental research. This is due to the possibility of forming highly ordered crystallites, the high degree of anisotropy in the (opto-)electronic properties [34–36], the high electro- and photoluminescent yield, the high degree of polarization of the electroluminescent light [37], the wave-guiding properties [38, 39] and last but not least the lasing properties [40].

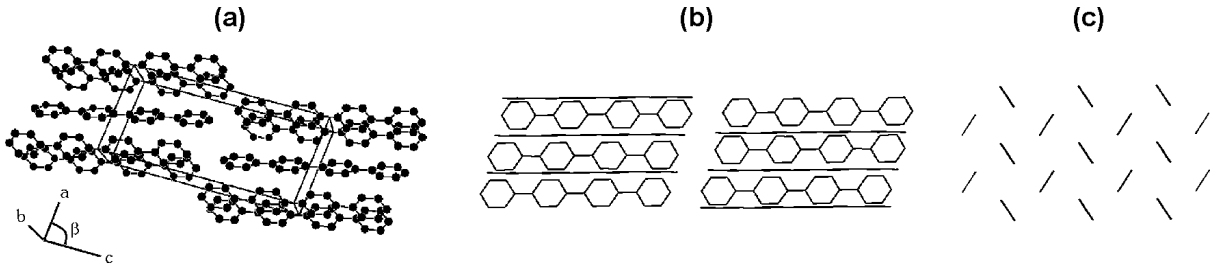

Figure 1.2: (a) The crystal structure of para-Quaterphenyl (4P) at room temperature. The hydrogen atoms are not shown. (b) Projection along the a axis exposing herringbone packed 4P layers. (c) Projection along the long molecular axes.

Molecular mechanics calculations predict non-planar conformations for isolated nP molecules, implying that the conjugation between phenyl rings is insufficient to overcome the repulsion between the ortho-hydrogens [37, 41]. Accordingly, the nPs are non-planar molecules in the gas phase. The aromatic rings are twisted with respect to each other and typical inter-ring twist angles are between 30° and 40°. Upon condensation in the solid state (bulk structure), however, the nP molecules adopt a more planar conformation, i.e. the interring tilt angles are reduced [42]. The benzene rings are, on the time average, coplanar but can still undergo librational motion [34, 43]. Still, there is an ongoing debate about whether these librational degrees of freedom disappear upon adsorption on a solid surface, or not. Recent sub-molecular resolution STM investigations of 6P on Ni(110)(2 × 1)-O revealed that single 6P molecules predominantly adopt a planar conformation upon adsorption. However, a small fraction of adsorbed 6P molecules was found with a twisted conformation, too [44]. For the system 6P/Ag(111) an interring twist angle of 11.4° has been observed for a single 6P molecule adsorbed on a Ag(111) surface. Obviously, the adsorption on a metal surface can force the molecule into a more coplanar conformation with an increased π-electron overlap.

The nP bulk crystal structure at room temperature is monoclinic [43] and well-known as **herringbone structure**, which is characteristic not only of the nPs but also of various other conjugated aromatic molecules. The characteristic features of the nP herringbone bulk structure are demonstrated in Figure 1.2 by means of the 4P crystal structure. It is representative for all nPs. The molecules are oriented roughly parallel[2] to the long side of the unit cell c. They are packed side-by-side to form stacked layers of neighbouring molecules. The layers can be best seen by projecting the crystal structure along the a axis, as illustrated in Figure 1.2 (b). The monoclinic unit cell contains two molecules that are twisted with respect to each other. This twisted orientation within each stacked layer is shown in 1.2 (c). For the different nPs, all structural parameters are very similar, except for the long side c of the unit cell, which is proportional to the Van der Waals length of the molecules. For the longer nPs like 6P an increased packing density has been

[2]The setting-angle between the long molecular axis and the long cell vector c is 17° for 4P and 19° for 6P, respectively [43].

Table 1.2: Fundamental properties of oligo-phenylenes.

	4P	6P	Ref.
Stoichometric formula	$C_{24}H_{18}$	$C_{36}H_{26}$	
CAS Registry number	135-70-6	4499-83-6	
Formula mass (amu)	306.4	458.59	[46]
Density (g/cm^3)	1.25	1.288	[43, 47]
Melting point (K)	587 - 593	702 - 748	[43, 46]
Sublimation enthalpy (kJ/mol)	156	211†	[46]
Van der Waals dimensions (nm^3)	2.04×0.35×0.67	2.85×0.35×0.67	
Crystallographic phase at 300 K:	monoclinic	monoclinic‡	[43, 47]
Space group	P2$_1$/a, Z=2	P2$_1$/c, Z=2	
Lattice vectors a, b, c (nm)	0.81, 0.56, 1.79	0.81, 0.56, 2.62	
Monoclinic angle β (°)	95.8	98.2	
Crystallographic phase at 110 K:	monoclinic	monoclinic	[43, 48]
Space group	P-1, Z=4		
Lattice vectors a, b, c (nm)	1.60, 1.12, 1.77	1.60, 1.12, 2.63	
Monoclinic angle β (°)	95.6	99.8	

† According to the measurements presented in this work.
‡ This is the so-called β-phase of 6P.

observed compared to the short oligomers [34]. This demonstrates the effect of strengthened intermolecular bonds caused by an increased number of phenyl rings per molecule.

For many organic molecules, particularly hydrocarbons, dispersion energy (Van der Waals) is the major component of the attractive intermolecular bonding. The herringbone structure found for the nPs, however, cannot be explained by dispersion effects alone. Additionally, the existence of rather small, yet substantial electrostatic intermolecular interactions has been shown to account for the herringbone structure [45]. Viewing along the long molecular axis, the molecules can be considered as electrostatic quadrupoles, carrying a negative differential charge on the ring carbons (π orbitals), and a positive differential charge of about $+\delta \approx 0.15$ on the hydrogen atoms, that are arranged along the edge of the molecule. The herringbone structure is the energetically most favourable structure, where differential charge densities of opposite sign lie next to each other.

The crystallographic data of 4P and 6P at room temperature are listed in Table 1.2. In addition to the most frequently observed monoclinic β-phase, a second room temperature phase of 6P has been identified. This orthorhombic structure is called γ-phase and has been observed in 6P thin films grown on glass substrates under certain evaporation conditions [49]. The γ-phase exhibits an orthorhombic unit cell ($a = 0.55$ nm, $b = 0.78$ nm and $c = 5.5$ nm) that contains twice the number of 6P molecules compared to the monoclinic β-phase. At low temperatures the nPs, and in particular 4P and 6P, undergo a reversible phase transition, where they adopt a structure different from the β-phase. The crystallographic data of the low temperature phases of 4P and 6P at 110 K are also listed in Table 1.2. In the low temperature structures the unit cell parameters a and b are

approximately doubled compared to the room temperature phase, while the long side c remains nearly unchanged.

The herringbone structure brings about a variety of different cleavage planes for the nP crystals. These are crystal planes of the bulk structure, which do not cut through single molecules, i.e. the material cleaves most easily along such planes. In the case of 4P the cleavage planes for the room temperature bulk structure are: (001), (211), (311), (201). Similar to that, the 6P cleavage planes are (001), (20$\bar{3}$), (11$\bar{1}$), (11$\bar{2}$), (21$\bar{3}$). Figure 1.3 shows 3D models of the molecular packing along the cleavage planes for 4P and 6P, respectively.

1.3 Growth of organic molecules on solid surfaces

Considering structural and morphological aspects of crystalline organic thin films grown on surfaces requires clear definitions of the used terms. Firstly, it is important to distinguish between the **nanoscopic structure** and the microscopic/mesoscopic structure of an organic film. The nanoscopic structure denotes the molecular packing, i.e. the crystallographic structure. The microscopic/mesoscopic structure denotes the film **morphology**, i.e. the size, shape and orientation of the organic crystallites. Additionally, the term **"texture"** describes the existence of a strict alignment of the crystallites within a (poly)crystalline film along some preferential direction(s) relative to the substrate. In contrast to that, a **fiber-texture** denotes the complete lack of a preferential azimuthal orientation.

According to the morphology of the adsorbate film, three common **growth modes** can be distinguished [50]: *Volmer-Weber* growth (islands), *Stranski-Krastanov* growth (islands grow on top of a monomolecular wetting layer) and *Frank - van der Merwe* growth (layer-by-layer).

The **coverage** Θ of an adsorbate is usually given in terms of the absolute number of adsorbate species per unit area of the surface, e.g. molecules/cm^2. Alternatively, Θ can be defined as the ratio $\frac{N_{ads}}{N_0}$ of the total number of adsorbate species, N_{ads}, and the total number of surface atoms of the substrate, N_0, per unit area [51]. However, in the case of adsorbate species that are much larger than the interatomic distances of the substrate surface, e.g. for organic molecules, a different definition of the coverage is useful: Instead of N_0, the maximum number of adsorbate species N_{sat} within a saturated monomolecular layer is used. Accordingly, the coverage is given in monolayer equivalents by $\Theta = \frac{N_{ads}}{N_{sat}}$. This notation is called **physical monolayer**.

In many cases of thin film growth it is reasonable to discern different coverage regimes according to the nominal thickness of the adsorbate film. The later can be specified in terms of monolayer equivalents. Accordingly, three different coverage regimes can be discerned, i.e. the sub-monolayer regime ($\Theta < 1$), monolayer regime ($\Theta = 1$) and multilayer regime ($\Theta > 1$). In general, these coverage regimes are dominated by various types of atomic or molecular interactions, which can be classified into two major groups:

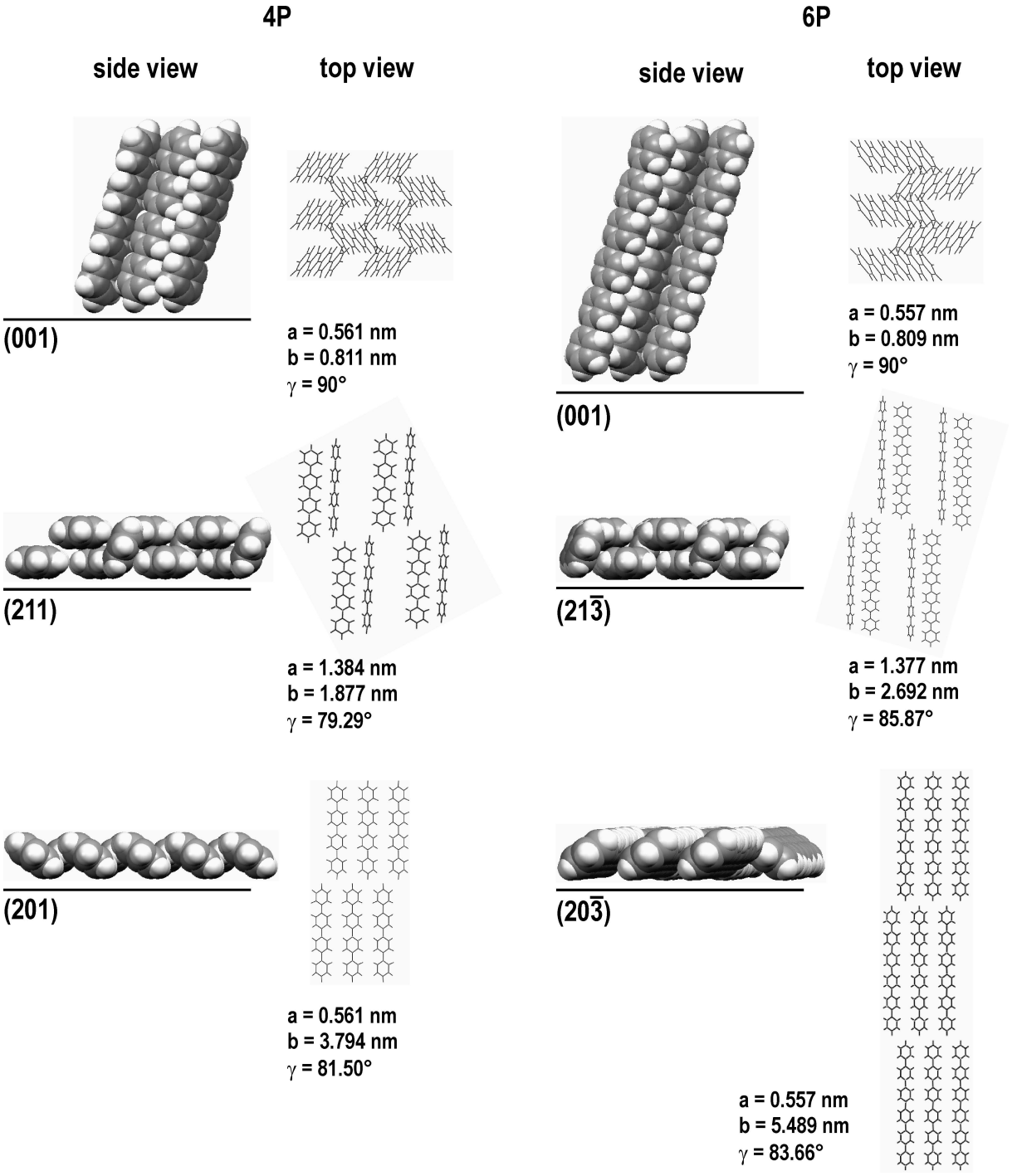

Figure 1.3: Real space representation of some important cleavage planes of the 4P and 6P bulk crystal structures.

(1) Adsorbate-substrate interactions Possible interactions of this type are charge transfer, covalent chemical bonding, electrostatic multi-pole interactions and Van der Waals interactions (physisorption). In many cases these interactions influence only the molecules within the first organic monolayer, whereas the second and subsequent layers are unaffected.

(2) Intermolecular interactions In the case of molecular crystals, these interactions are of Van der Waals type and/or electrostatic multi-pole interactions. They are present throughout the organic bulk material.

It has been found that the relative strength of these two types of interaction is a key parameter which influences the molecular packing and therefore the structure of the first adsorbed monolayer [52]. The packing within the first monolayer, in turn, strongly influences the structure of the subsequent layers. Accordingly, the structure of the organic film may vary to a great extent, depending on the coverage. Depending on which material combination is chosen for the substrate and the organic film, the adsorbate-substrate interaction energy, E_{A-S}, may differ significantly from the intermolecular interaction energy, E_M. The relative strength of the two complementary factors determines the structure of the organic film already during the initial stage of film growth (sub-monolayer regime). In particular, it determines wether a continuous first monolayer is established. This interfacing first monolayer, which is often denoted as **"wetting layer"** can have a significant influence on the structure of the second, third and subsequent layers. In some cases the crystal structure and morphology of a several nm thick organic film is completely determined by the structural properties of the first layer. A different organic/substrate system, however, may result in a complete lack of a wetting layer, in particular, if $E_M \gg E_{A-S}$.

In the case of a crystalline substrate, additional features have to be considered. The organic molecules may align along preferential directions relative to the substrate surface. Such an orientational anisotropy may be exploited for tailoring the organic film. In case that the molecule-substrate interaction is sufficiently strong, a structural matching between the substrate surface and the organic wetting layer occurs. Either the organic layer can adopt a regular structure similar to the substrate surface or the later is reconstructed by the presence of an organic adlayer. In particular, this has been shown for the so-called "lander molecule" [53].

In some cases large organic molecules form highly regular structures on single-crystalline substrates [52, 55]. In analogy to heterogeneous inorganic systems, the term "epitaxy" is frequently used to denote the existence of a defined relationship between the two-dimensional regular structures of the adsorbate film and the substrate surface[3]. Several modes of epitaxy can be distinguished [54, 56]: **Commensurism** denotes a situation, where each overlayer lattice point resides on a symmetry equivalent substrate lattice site.

[3]Epitaxy is generally used to describe lattice registry between two opposing lattice planes. In conjunction with organic films the term quasi-epitaxy is often used in order to emphasize that one condition necessary for "true" epitaxy is actually not fulfilled: The size of the surface unit cells of the organic adsorbate film and the substrate surface differ significantly.

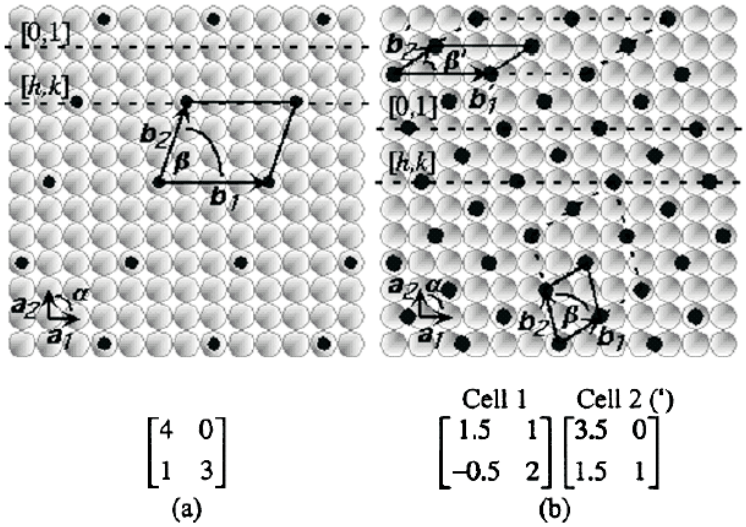

Figure 1.4: Different modes of epitaxy, as depicted in [54]. (a) Commensurism, (b) Coincidence I, point-on-line.

Accordingly, the transformation matrix[4] has only integer values, as shown in Figure 1.4(a). **Coincidence** denotes a situation, where the coefficients of the transformation matrix are integer and/or rational numbers. In particular, the term **point-on line coincidence** is used in case that one column of the matrix comprises only integer coefficients, as presented in Figure 1.4(b). In this case, all the overlayer lattice points are aligned along primitive lattice lines, $< 01 >$, of the substrate lattice. As a guide to the eye, some $< 01 >$ lattice lines are indicated by horizontal dotted lines in (b). Additionally, in the case of a hexagonal substrate surface, point-on-line coincidence is also present if both row sums yield integer numbers. **Incommensurism** implies at least one matrix coefficient to be irrational.

Concerning the type of interaction dominating the organic-substrate interface a phenomenological classification has been proposed [52, 55]. It is based on a large variety of experimental data from different systems that can be found in the literature. Accordingly, the following classification can be made, which is based on the reactivity of the substrate surface. It is implied that the organic molecules do not carry highly reactive functional groups. Otherwise, this would, of course, change the classification insofar, as the high reactivity of the functional groups would be the determining factor.

Strongly interacting surfaces like element semiconductors, transition metals *sp* metals or *d* metals with partially filled *d* bands. Adsorbed organic molecules either dissociate upon adsorption or are immediately bound in various orientations at those surface sites, where they impinge on the surface. No lateral order is usually found in such films and multilayers grow disordered.

[4]The matrix notation of regular two-dimensional surface structures is described in Appendix C.

Poorly interacting surfaces like noble metals (e.g. Ag, Au). In this case weak chemisorption occurs. These metals tend to bind organic molecules rather strongly (deep potential wells perpendicular to surface). However, the molecules can easily diffuse on the surface (low lateral potential wells). The molecules retain intact and can diffuse over large distances to form huge, ordered islands. The adsorbate superstructures, however, are determined by the substrate surface. A Stranski-Krastanov growth is frequently observed for such systems, reflecting the dominant influence of the substrate surface for the organic monolayer and the following dominant influence of the organic bulk.

Inert surfaces like graphite or many insulators (e.g. SiO_2, NaCl, KCl). Molecular self-organization is observed, which is more or less independent of the substrate. The molecules take the substrate as a smooth, two-dimensional basis for the formation of monolayers, which are essentially determined by the intermolecular forces. Hence, long-range order is often observed, but this is hardly influenced by the symmetry of the substrate. Because the interactions are in general weak, highly crystalline structures can be formed without the necessity of lattice matching. Multilayers grow polycrystalline, where the homogeneity of the layer and the size and orientation of the crystallites are essentially determined by the properties of the organic crystallites (self-arrangement due to intermolecular forces and molecular shape). Frequently, a layer-by layer growth is observed, as well as a "standing" orientation of the molecules relative to the substrate [37].

1.3.1 Overview of reported nP thin film structures

Various organic thin film systems grown on inorganic substrates have already been investigated and reported in the literature. Comprehensive reviews can be found in [9, 11, 52, 53, 55]. Here, a short review is given, concerning some recent publications on the growth of oligo-phenylene thin films on different inorganic surfaces. The corresponding films have been vapour deposited under vacuum conditions.

- 4P/NaCl(001) [57, 58]: 4P molecules accumulate around surface defects; bulk: at RT standing molecules; bulk structure confirmed; similar on NaF, LiF; ML(300 K): standing, LEED spots;
- 4P/KCl(001) [37, 58]: bulk at RT standing (layer growth);
- 4P/mica(001) [58]: bulk: at RT standing (001); ML: at RT lying $(1\bar{1}1)$;
- 6P/KCl(001) [37, 58, 59]: bulk: at RT rod-like crystallites, lying 6P$(11\bar{1})$; at 150°C planar crystallites with standing (001); at 250°C coexistence of lying (rod-like) and standing (terraces); ML(335 K): standing, LEED spots;
- 6P/NaCl(001) [36]: bulk: at RT needles, lying molecules; at 150°C columnar grains (terraces) standing (001);

- 6P/glass [60]: bulk: at 470 K standing (001)
- 6P/mica [61–63]: bulk: dipole-assisted growth induces a strong preferential alignment of the molecules; at 350 K needles, lying $(1\bar{1}\bar{1})$, Plank: coexistence of $(11\bar{1})$, $(11\bar{2})$, $(20\bar{3})$ and $(21\bar{3})$; ML: at RT lying;
- 6P/Al(111) [64, 65]: bulk: at RT $(21\bar{3})$; at 423 K coexistence of (001) and $(21\bar{3})$; ML: at RT lying, aligned parallel to $\langle 1\bar{1}0\rangle$;
- 6P/Ni(110)(2x1)O [44]: planar adsorption;
- 6P/Au(111) [66]: ML at 457 K flat lying molecules; bulk 2D cell compressed with respect to ML;

Summarizing those features that are most frequently observed in organic thin film systems similar to those cited above, yields a listing of several experimental findings. It is supplemental to the features described before and can be regarded as some kind of general guideline for organic thin film growth on solid substrates:

1. **Polymorphism**: Denotes the coexistence of different bulk crystal structures on the same sample.
2. **Polycrystallinity**: It denotes the coexistence of different crystal orientations on the same sample.
3. Azimuthal alignment of the organic crystallites relative to the substrate. On a molecular scale this can be explained by a strict azimuthal alignment of the molecules to some preferential direction of the substrate surface.
4. In the case of elongated molecules, needle-like crystallites indicate flat lying molecules, whereas upright standing molecules preferentially grow plane terrace-like crystallites.
5. The film morphology strongly depends on the substrate temperature and deposition rate during the film growth.
6. The long molecular axis of nPs is oriented close to perpendicular to the direction of the needle growth. This is due to an enhanced intermolecular binding on the long sides of the molecules.
7. Epitaxial growth can be achieved for organic thin films under certain growth conditions.
8. Vapour deposition enables to grow highly crystalline thin films.
9. The packing order of the molecules within the first monolayers is decisive for the subsequent growth of crystalline thin films.
10. The formation of the first monolayers is determined by a delicate interplay between the adsorbate-substrate interactions and intermolecular interactions.

1.4 The Gold (111) surface

The gold bulk crystal structure is face-centered-cubic (fcc) with a lattice constant of $a_0 = 0.4078$ nm. The idealized Au(111) surface has a 6-fold symmetry (hexagonal). However, considering the first and second topmost atomic layers, the symmetry of the surface structure reduces to a 3-fold rotational symmetry (2D space group: p3m1). The inter-atomic distance of the ideal Au(111) surface is $a_{111} = a_0/\sqrt{2} = 0.288$ nm and the corresponding inter-row distance is $d_{111} = a_{111} \cdot \sqrt{3}/2 = 0.249$ nm, as illustrated in Figure 1.5(a). The mean number of surface atoms is $1.39 \cdot 10^{15}$ atoms/cm^2.

Different from all other fcc metals, however, gold exhibits a reconstruction of the real (111) surface at room temperature [67]. The driving force behind this reconstruction is the relief of surface stress. The topmost atomic layer is compressed by about 4.5% along the $\langle 1\bar{1}0 \rangle$ direction relative to the second layer, while in the perpendicular $\langle 11\bar{2} \rangle$ direction the relative interatomic distances remain unchanged. Accordingly, the topmost monoatomic layer exhibits along the $\langle 1\bar{1}0 \rangle$ direction atomic rows where 23 atoms align on the same length as 22 atoms in the underlying layer. On the atomic scale, this surface reconstruction can be fully explained by a rectangular $(22 \times \sqrt{3})$ surface unit cell, as shown in the lower part of Figure 1.5(b). The black rectangle indicates the surface unit cell of the superstructure. As can be seen, the 46 atom basis is rather complex because the $\langle 1\bar{1}0 \rangle$ atomic rows are periodically deformated (translated) in the perpendicular $\langle 11\bar{2} \rangle$ direction. This periodicity is equal to the length of the rectangular surface unit cell (6.3 nm) [67]. In addition to that in-plane deformation, the surface reconstruction also exhibits an out-of-plane corrugation in the z-direction normal to the surface plane, with a maximum value of about 0.02 nm [67]. This is shown in the upper part of Figure 1.5(b). The corrugation is clearly visible in STM in terms of different grey values, as shown in Figure 1.5(c). The pair of bright "lines" is often denoted as the so-called "discommensuration lines". They separate surface regions with alternating local fcc and hcp stacking between the topmost and second layer, respectively. The distance between neighbouring pairs is 6.3 nm, while individual lines within a pair are separated by 2.8 nm [68].

The surface reconstruction that has been described so far constitutes one single structural domain, which is usually denoted as "stripe domain". It has a local, two-fold symmetry. A single stripe domain itself is characterized by pairs of parallel discommensuration lines (or corrugation lines) running along the $\langle 11\bar{2} \rangle$ direction.

Due to the three-fold symmetry of the fcc (111) surface three different stripe-domains can principally exist that are rotated by 120° against each other [68]. The stripe domains form their own superstructure with equally spaced, parallel domain boundaries. The domain width can vary between about 12 to 20 nm [70] and two neighbouring domains are always rotated by 120° relative to each other. STM experiments have shown that on a single mono-atomic terrace of the Au(111) surface only two different 120°-rotational domains occur, while the third one never appears. This produces a zig-zag like surface pattern [71] as shown in Figure 1.5(c), which is well-known in the literature as herringbone reconstruction or "Chevron" structure [72]. The absence of the third rotational stripe domain has been explained by surface stress arguments, such that two rotational domains are sufficient

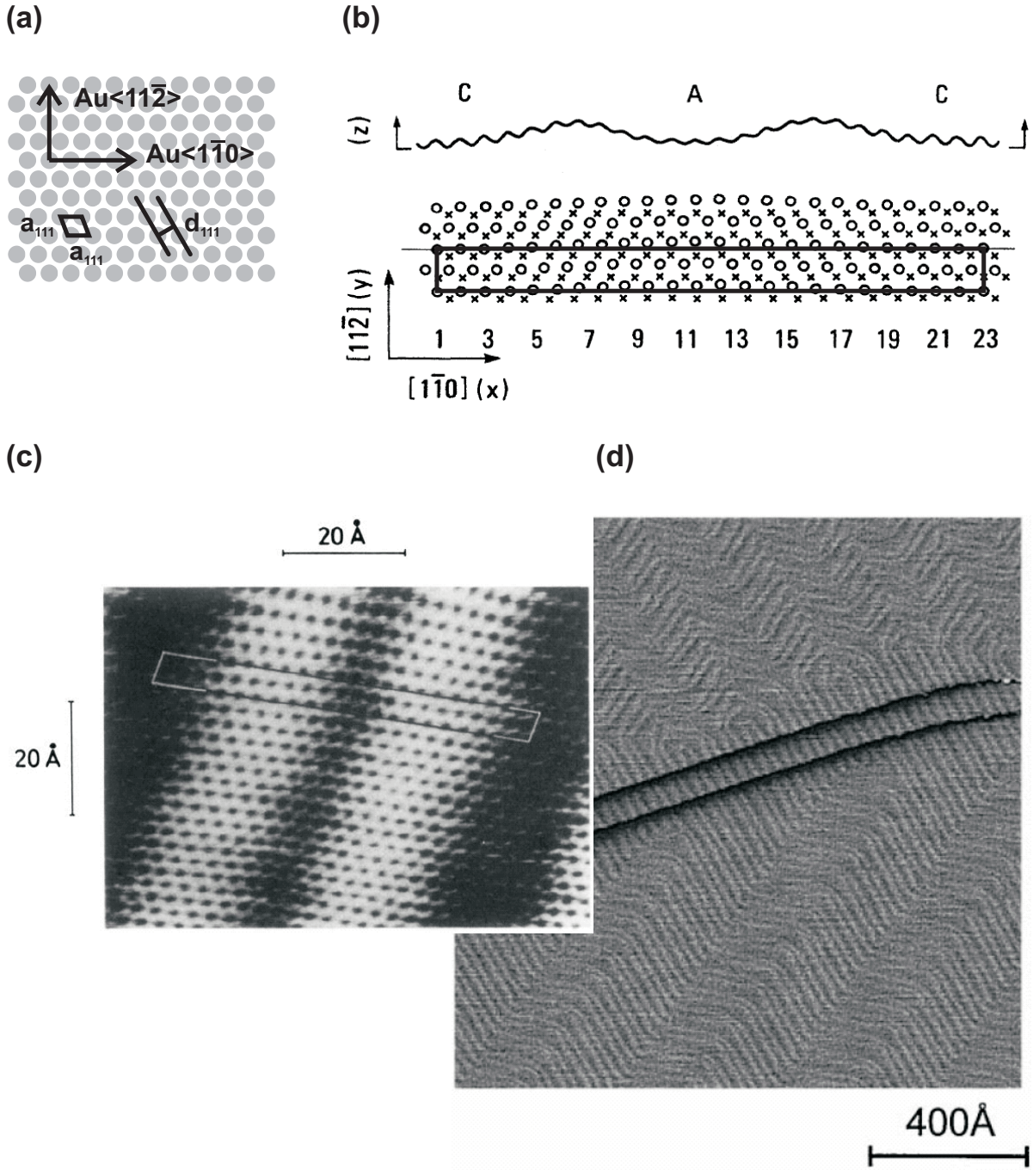

Figure 1.5: (a) Illustration of the ideal fcc(111) surface. The parameters are described in the text. (b) Au(111) surface reconstruction schematics of the atom positions of the reconstructed $(22 \times \sqrt{3})$ surface unit cell [67]. (c) Atomic resolution STM image of the reconstructed Au(111) surface stretching over a pair of corrugation lines [68]. The unit cell is indicated by the parallelogram and appears not rectangular in the image due to the un-corrected image drift. (d) High resolution STM image of the "Chevron" stripe domains on the reconstructed Au(111) surface [69].

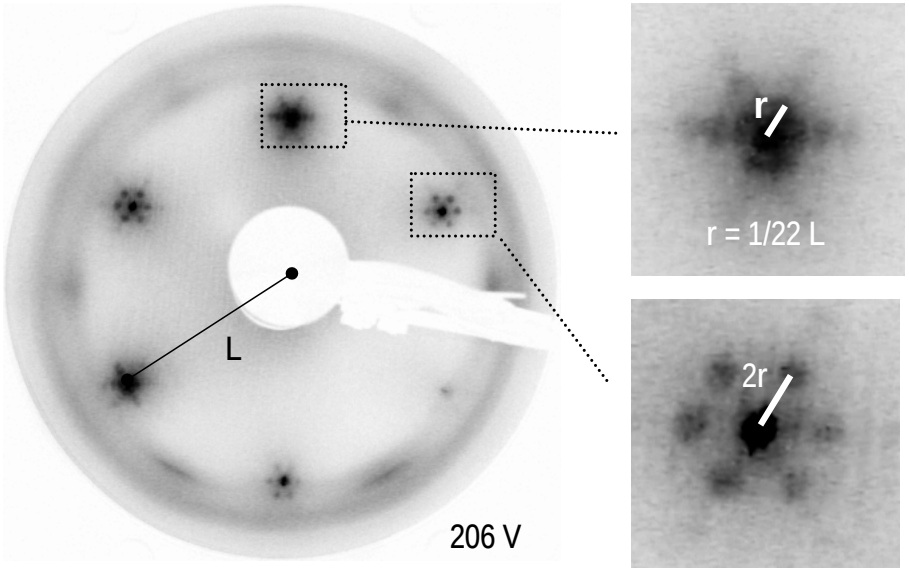

Figure 1.6: LEED image of the clean reconstructed Au(111) surface.

for a surface stress relief in two dimensions [71, 73].

In Figure 1.6 is illustrated that the surface reconstruction of Au(111) produces additional LEED reflections that can be experimentally observed. This has been previously reported by Van Hove et al. [74]. Each of the principal reflections is surrounded by a six-fold symmetric pattern of additional spots. The separation of these spots, r, is 1/23 of the radial distance L of the 01 reflection.

1.5 Gold (111) vicinal surfaces

A comprehensive review on stepped surfaces can be found in [78] and in particular on Au vicinal surfaces in [79]. The vicinal Au(433) surface has been investigated in the present work. The idealized Au(433) surface is inclined by 8.05° with respect to the (111) surface and exhibits (111) terraces that are equally spaced by about 1.68 nm. The monoatomic steps run along the Au$\langle 1\bar{1}0\rangle$ direction, i.e. the steps consist of {100} micro-facets. However, the real Au(433) surface is thermodynamically not stable and reconstructs upon heating above 430 K into a step-bunched surface [75]. Although the step direction does not change during this reconstruction, the terrace width does. The step-bunching becomes manifest in terms of an alternation of one broad 4 nm wide (111) terrace followed by five 1.4 nm wide terraces. This produces a super-periodicity of about 11 nm, as shown in Figure 1.7(a). The single (111) terraces show no $22 \times \sqrt{3}$ reconstruction compared to the plain Au(111) surface [79]. This can be observed in STM, as shown in Figure 1.7(c)-(d).

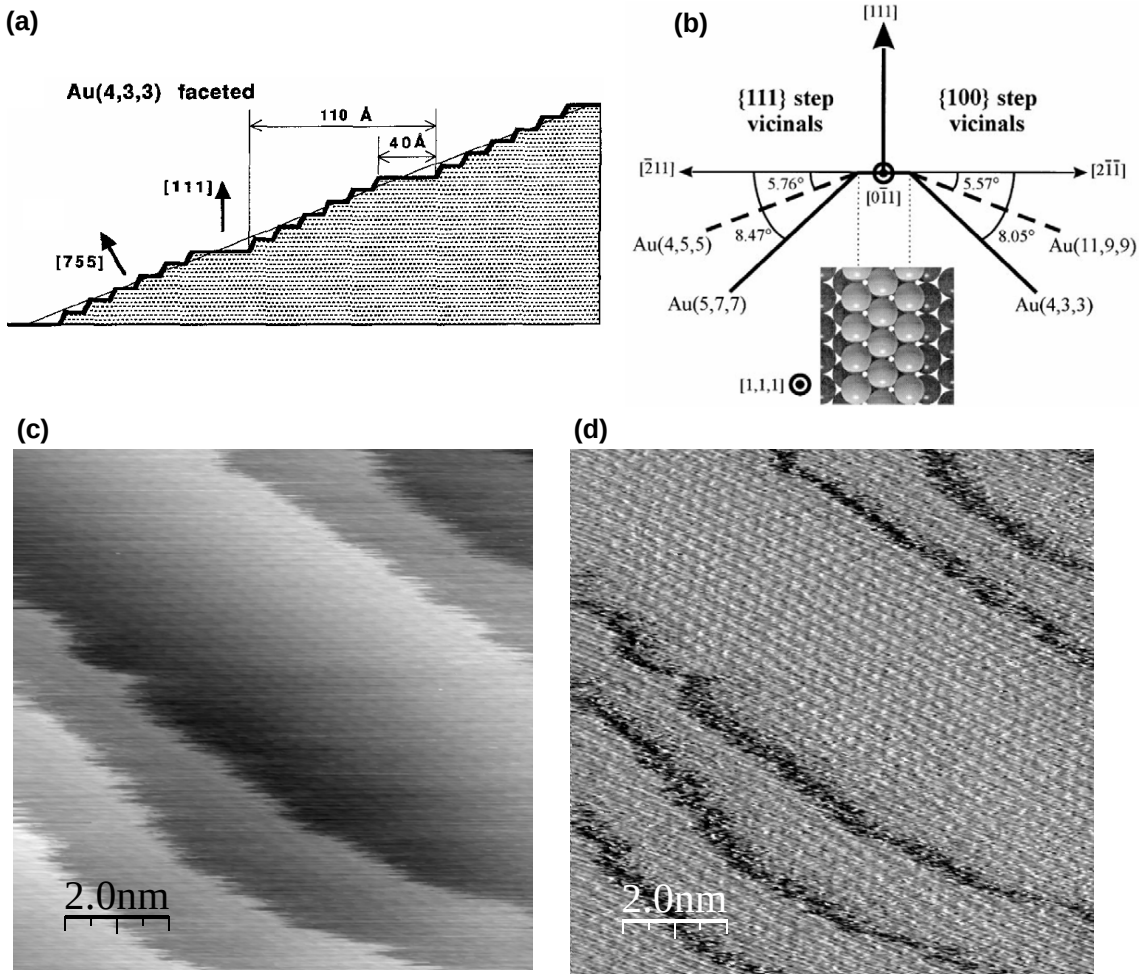

Figure 1.7: (a) Schematics of the Au(433) surface (step bunching) [75]. (b) Schematic side view showing the misorientation of different Au vicinal surfaces with respect to [111] in the [0$\bar{1}$1] zone axis. The inset is a top view showing the different step structures [76]. (c) Atomic resolution STM image of the reconstructed Au(433) surface at room temperature and (d) its derivative [77].

Chapter 2

Analytical methods

The fact that various different aspects of the samples are investigated in this work brings about the application of a large number of complementary analytical techniques. Most of them are specifically sensitive to the surface, while others probe the bulk properties. The following sections provide a compact overview of the used techniques.

2.1 Thermal desorption spectroscopy of large organic molecules

The thermal desorption spectroscopy technique is routinely used for investigating the energetics and kinetics of mono-atomic or low-weight molecular gases adsorbed on solid surfaces since several decades. The sample, i.e. the substrate plus adsorbate, is placed inside a vacuum system and heated in a well-defined way. Simultaneously, the **desorption rate** of the adsorbate species, R_{des}, is measured versus the sample temperature, yielding the so-called TD spectrum. Usually, R_{des} is given in molecules/(cm^2 s):

$$R_{des} = -\frac{dN}{dt} \cdot \frac{1}{A} = -\frac{d\Theta}{dt} \tag{2.1}$$

N is the absolute number of adsorbate species on the surface (surface density), A is the sample surface area and Θ is the coverage (molecules/cm^2). For the different definitions of Θ refer to page 34.

In order to determine R_{des}, one considers a vacuum system at equilibrium, into which gas is being leaked upon thermal desorption. It is assumed that no re-adsorption of the desorbing species occurs during the desorption process. According to Redhead [80], the desorption rate depends on the pressure increase above the background, p^*, that is caused by the desorption, according to

$$R_{des} = \frac{1}{AkT} \cdot (p^* S + V\frac{dp^*}{dt}) \tag{2.2}$$

k the Boltzmann constant, T the temperature, S is the effective pumping speed (l/s) and V the volume of the recipient. For a sufficiently high pumping speed ($S \gg$) the last term in Equation 2.2 can be neglected and R_{des} becomes directly proportional to p^*, a quantity which is easy to measure experimentally.

One of the most commonly used theoretical approaches for describing the thermal desorption rate is the **Polanyi-Wigner** formalism [81]. Here, the desorption process is described as a desorption reaction within the framework of reaction kinetics, as $R_{des} = k_n(E, \Theta) \cdot \Theta^n$, where k is a coverage- and energy-dependent speed constant and n denotes the reaction order. The speed constant can be written as the product of a so-called pre-exponential factor, ν, and an arrhenius factor, yielding the Polanyi-Wigner equation

$$R_{des} = \nu(\Theta) \cdot \Theta^n \cdot e^{-\frac{E_{des}(\Theta)}{kT}} \tag{2.3}$$

Θ is the adsorbate coverage (in molecules/cm^2) and E_{des} the activation energy for desorption (desorption energy). In this context, the parameters ν, n and E_{des} are frequently called the **kinetic parameters**. If the interaction between neighboring adsorbate molecules can be neglected, the kinetic parameters become independent of the coverage. In this case, an analysis of the TD data according to the Polanyi-Wigner formalism is straightforward [80, 82].

In the case of a first-order desorption (n=1), the product $\nu \cdot \Theta$ is around 10^{28} molecules per cm^{2}s. Because usual coverages are about 10^{15} atoms/cm^2, the pre-exponential factor is assumed to be 10^{13} s^{-1}, which is a proper approximation for many mono-atomic or low weight molecular adsorbates [51].

The analysis of the TD spectra is not straightforward if **lateral interactions** between the adsorbate species are present. A good example for such a situation is the monolayer desorption of oligo-phenylenes (nP) from a Au(111) surface (see Chapter 4). The lateral interactions between the adsorbate species cause the kinetic parameters, and in particular E_{des}, to become coverage-dependent. The Elovich approach accounts for this problem by introducing a coverage-dependent interaction energy term to the Polanyi formula [81]. Now, the effective desorption energy is coverage dependent as

$$E_{des}(\Theta) = E_{des} \pm \omega\Theta \tag{2.4}$$

The interaction energy ω between the adsorbate species can either be positive or negative, corresponding to **repulsive** interaction ($-\omega$) or **attractive** interaction ($+\omega$), respectively. Hence, attractive interactions between the adsorbate molecules will increase the absolute value of the heat of adsorption with increasing coverage. Similarly, repulsive interactions will decrease the heat of adsorption. Accordingly, attractive(repulsive) interactions shift the TD peaks to higher(lower) temperatures [83]. An analysis of the **Elovich** equation

$$\frac{R_{des}}{N_0} = \nu(\Theta) \cdot \Theta^n \cdot e^{-\frac{(E_{des} \pm\ \omega \cdot \Theta)}{kT}} \tag{2.5}$$

is no more straightforward, because the kinetic parameters are coverage-dependent. In such a case also the so-called **compensation effect** has to be considered. It is encountered, for

instance, when experimental TD data are numerically fitted with the Polanyi equation in order to derive the kinetic parameters. It turns out, that E_{des} and ν cannot be calculated independently, because for any arbitrarily chosen value of ν can be found a proper value of E_{des}, which fulfills the numerical fitting procedure. The compensation effect denotes the linear dependency of the logarithmic pre-exponential factor on the desorption energy [83, 84]: $\ln \nu \propto E_{des}$. Therefore, a determination of the kinetic parameters becomes ambiguous.

Large organic molecules have been frequently observed to exhibit very large pre-exponential factors of up to $10^{19} - 10^{30}$ [85, 86]. This can be explained in terms of Eyring's **transition state theory** [51, 81]. This approach takes into account the intramolecular degrees of freedom, like vibrations. According to the transition state theory, the pre-exponential factor of Equation 2.3 can be expressed in terms of the molecular partition functions, $z^{\ddagger}$ and z_{ads} of the transition state and the adsorbed state, respectively.

$$\nu = \frac{kT}{h} \cdot \frac{z^{\ddagger}}{z_{ads}} \tag{2.6}$$

The first factor, kT/h, is approximately 10^{13}, while the second factor can vary to a great extent, depending on the degrees of freedom involved. If the adsorbed molecule gains degrees of freedom upon approaching the transition state, then the second factor becomes > 1. In particular, this is believed to explain the large pre-exponential factors in the case of large organic molecules. The partition function of the transition state of desorption is much higher than that of the adsorbed species [85].

Leading edge method

This is a convenient approximation method [1] for evaluating the kinetic parameters. It is based on the assumption that at the beginning of desorption [2], when the desorption rate is still very small, the change of the adsorbate coverage is sufficiently small to be neglected. Thus, the coverage-dependency in equation 2.3 can be omitted. A simple Arrhenius plot of the logarithm of the desorption rate versus the reciprocal temperature (ln(R) vs. $\frac{1}{T}$) yields the kinetic parameters: E_{des} as the slope of a fitted straight line and ν as the ordinate axis intercept.

2.2 X-ray photoelectron spectroscopy

Complementary to Auger spectroscopy, this is a standard technique for monitoring the chemical composition of the sample surface. Detailed descriptions of this method can be found in the literature [87–89]. The fundamental process of generating photoelectrons is illustrated in Figure 2.1. The kinetic energy of photoelectrons generated by irradiating photons of energy $h\nu$ is characteristic of the element:

$$E_{kin} = h\nu - E_{bind} - \Phi_{spec} \tag{2.7}$$

[1] In case of a zero-order desorption this method gives the exact values of the kinetic parameters.
[2] Along the leading edge of the desorption peak

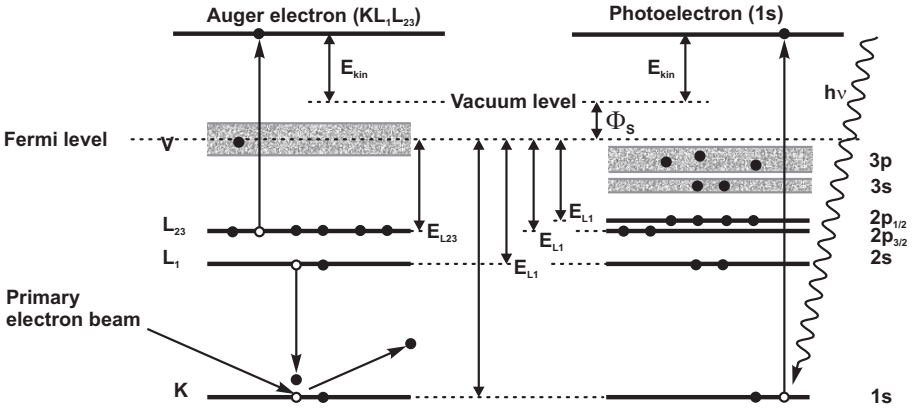

Figure 2.1: Schematic diagram of the process of Auger electron (left) and photoelectron (right) generation.

E_{bind} is the binding energy of the photoelectron state and Φ_{spec} is the spectrometer work function. For a detailed description of a quantitative analysis using XPS please refer to Appendix E.

2.3 Auger electron spectroscopy

Together with the complementary XPS technique, the Auger electron spectroscopy (AES) method is a standard surface analytical tool for investigating the chemical composition of solid surfaces under UHV conditions. It is based on the well-known Auger effect of generating secondary electrons, which carry an element-specific kinetic energy, upon ionization of an inner atomic shell (cf. Figure 2.1). For details on this technique the reader is referred to the literature [87–91]. An Auger transition is characterized primarily by the location of the initial hole and the location of the final two holes. The kinetic energy of Auger electrons, emitted upon an Auger process involving the primarily ionized electron level E_1 and the higher levels E_2 and E_3, is approximately given by the binding energies of the involved electronic states, i.e. E_1, E_2 and E_3.

$$E_{kin} = E_1 - E_2 - E_3 - \Phi_{spec} \tag{2.8}$$

Φ_{spec} is the spectrometer work function [3]. For a detailed description of a quantitative analysis using Auger spectroscopy please refer to Appendix F.

[3] A more accurate treatment requires to consider also the interaction energy between the holes generated at certain energy levels as well as the intra- and extra-atomic relaxation energies [87, 89].

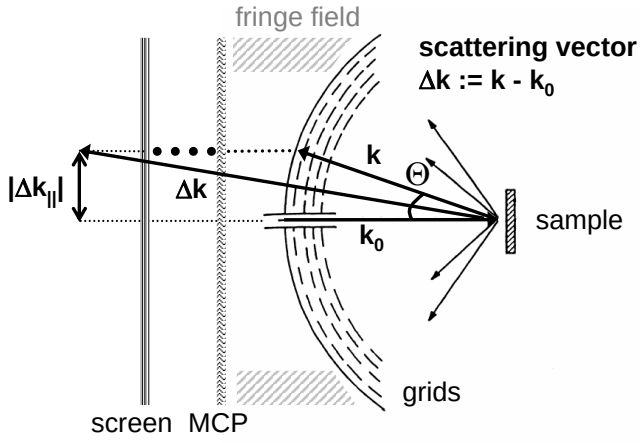

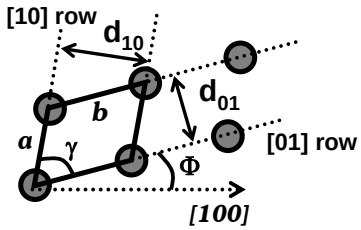

Figure 2.3: Geometric parameters of a two-dimensional lattice in real space.

Figure 2.2: Schematics of the MCP-LEED technique.

2.4 Micro-channelplate enhanced low energy electron diffraction

In some cases large organic molecules can form highly ordered structures on crystalline substrates. If the thickness of an organic film is as small as a single monomolecular layer, its structure is influenced by the specific properties of the interface between the substrate and the organic molecules. The low energy electron diffraction (LEED) method is well suited for probing the structures of such regular organic monolayers on surfaces. Its pronounced surface sensitivity stems from the small inelastic mean free path of low energy electrons in solids (< 1 nm) [87, p. 186]. For an introduction to the LEED method the reader is refered to the literature [89–92]. A comprehensive introduction to LEED analysis of stepped surfaces can be found in [93, 94].

When analyzing an organic adlayer with a conventional LEED apparatus the measurements are severly restricted by the electron beam damage caused within the organic film. Molecules with weak intra-molecular bonding or species which are weakly bonded to the surface can dissociate or desorb under the electron beam. This problem is overcome by applying very low primary electron beam currents (nA) in conjunction with a microchannel plate (MCP) for signal amplification. A schematic of the MCP-LEED technique is shown in Figure 2.2. After passing the analyzer grids, the elastically scattered electrons (wave vector $\vec{k}$) are co-axially deflected towards the MCP by a supplemental electron optics - the fringe field corrector. The electic field between the grids and the MCP has to be very homogeneous and radially symmetric around the axis defined by the primary beam. At the MCP the impinging electrons generate an amplified cloud of secondary electrons, which are accelerated towards the fluorescent screen where a visible spot is produced similar to a conventional LEED apparatus. Although the MCP-LEED is able to detect low peak intensities, the maximum detectable diffraction angle is restriced to about 35-40°, which is considerably smaller compared to a conventional LEED apparatus (about 55°).

The LEED patterns recorded within this work have been analyzed according to a kinematic approximation. Such is based on the assumption, that only single scattering processes of the primary electrons with the periodic surface structure have to be considered [90]. Although fairly simple, the kinematic approximation yields the correct positions of the diffraction spots.[4] A common approach of kinematic LEED analysis is similar to the well-known 3-dimensional Bragg equation. In case of normal incidence it reads

$$d_{hk} \cdot sin(\Theta) = \lambda \tag{2.9}$$

where d_{hk} is the inter-row distance of real space scattering rows (hk)[5] as shown in Figure 2.3 and also in Appendix C, Θ is the diffraction angle or scattering angle and λ is the electron wavelength. The latter can easily be expressed in terms of the electron beam voltage, U, by an approximative numerical equation:

$$\lambda[\mathring{A}] \approx \sqrt{\frac{150.4}{U[V]}} \tag{2.10}$$

The combination of these two equations forms the basis of kinematic LEED analysis. Additionally, some geometrical parameters specific of the LEED instrument have to be considered, as shown in Appendix D, where a detailed description of the practical LEED pattern analysis performed in this work, is given.

2.5 X-ray diffraction

This technique is well-suited for determining the (crystal) structure of the crystallites in organic thin films. A major limitation is the minimum film thickness required, which stems from the detection limit of scattering intensities. The organic films investigated in this work with XRD have been thicker than about 10-20 nm in order to produce proper diffraction patterns. Thus, the structural information gained by XRD corresponds to the bulk of the material - complementary to the surface-sensitive LEED technique. A comprehensive introduction to XRD can be found in the literature [95, 96]. For constructive interference (diffraction), two conditions have to be fulfilled: Firstly, the well-known Bragg law

$$2 \cdot d_{hkl} \cdot sin(\Theta) = \lambda \tag{2.11}$$

where d_{hkl} is the inter-planar spacing of crystal net planes (hkl), Θ the diffraction angle and λ the wave length of the X-rays. And secondly, the normal vector of the reflecting net plane $\vec{n}$ has to be parallel to the scattering vector $\Delta\vec{k}$:

$$\vec{n} \parallel \Delta\vec{k} \tag{2.12}$$

[4] A dynamical treatment of the LEED patterns, giving information on the molecular packing within the unit cell, was not performed. The complexity of such an analysis in case of organic materials would have exceeded the scope of this work.

[5] An equivalent notation replaces the 2D Miller indices h and k by the so-called "order of diffraction" n.

It follows from geometric considerations that if the scattering conditions are fulfilled for a certain incident angle Θ, then the Bragg reflection is observed at an angle of 2Θ with respect to the incident wave vector.

For the structure determinations presented in this work three different XRD techniques have been used :

Specular scan ($\Theta/2\Theta$)

Given is a polycrystalline sample, where the crystal orientations are statistically distributed. At a fixed incident angle Θ, monochromatic X-rays are diffracted only by certain crystal planes, whose orientations fulfill the scattering conditions given by the Equations 2.11 and 2.12. For the specular scan method a symmetric measuring geometry is used, i.e. the incident angle and the detection angle are the same with respect to the macroscopic sample surface (reference plane), i.e. the scattering vector $\Delta\vec{k}$ is always perpendicular to the reference plane. This can be achieved by rotating the detector with the double angular speed as the specimen. This setup guarantees that only those net planes can be detected that are oriented parallel to the reference plane. Varying the Θ angle then yields sharp Bragg reflections at well-defined angles of 2Θ, whenever a certain set of net planes, which fulfills the above conditions, lies parallel to the reference plane (powder pattern).

The analysis of the measured $\Theta - 2\Theta$ spectra is done by a comparison with calculated spectra that are based on the already well-established crystal structure of the investigated compound.

Pole-figures

Polycrystalline samples exhibit a certain distribution of the crystallite orientations. The XRD pole-figure technique is used for determining the azimuthal orientation distribution of the crystallites relative to the substrate surface, which is often denoted as texture [96]. The angle Θ is fixed at a value of a strong Bragg reflection corresponding to a certain set of net planes. This value has been gained from a specular scan in advance. Thus, the first condition for constructive interference, equation 2.11, is fulfilled. However, the second condition is in general not fulfilled, due to the orientation distribution of the crystallites. Thus, the sample is rotated (by the angle ϕ) and tilted (by the angle ψ) according to Figure 2.4. Constructive interference (diffraction peak, enhanced pole density) appears at certain ϕ/ψ-values, where the normal vector of a certain crystallite is parallel to the scattering vector. From these ϕ/ψ-values the orientation of the crystallite(s) can be reconstructed.

Rocking curves

Rocking curve measurements yield information about the "crystal quality" of the crystallites in a sample. Both X-ray source and detector are fixed, while the sample is tilted ("rocked") around. The characteristic quantity measured by this technique is the full width

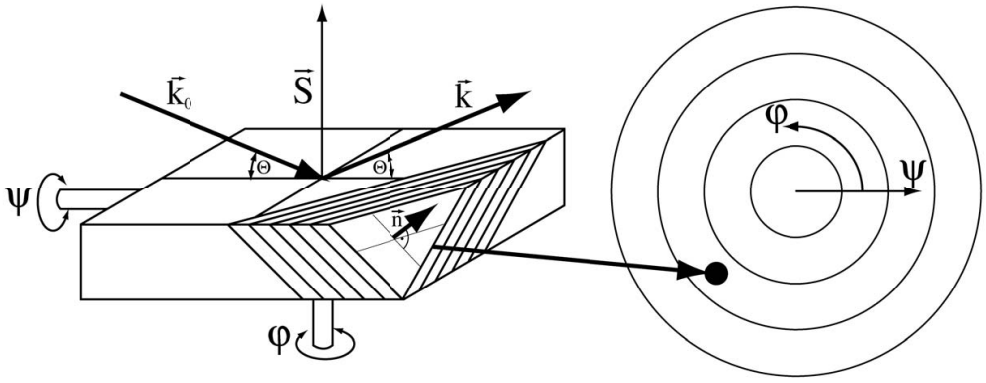

Figure 2.4: Schematics of the XRD pole-figure technique. $\vec{k_0}$ and $\vec{k}$ are the wave vectors of the incident and scattered wave, $\vec{S}$ the scattering vector, Θ the scattering angle, $\vec{n}$ the normal vector of a set of net planes and ϕ and ψ the rotation and tilt angles, respectively.

at half maximum (FWHM) of the diffraction peaks [96]. The narrower the peaks are, the better is the crystallinity of the sample, i.e. the fewer lattice mismatches etc. occur.

2.6 Scanning tunneling microscopy

In this technique the probe is a sharp metal tip, which is laterally scanned across a conducting sample surface at a distance small enough to enable a tunneling current (a few nA) to flow from the tip to the sample or vice versa, if a small voltage is applied between those two [89, 97]. The local tunneling current is strongly dependent on the electronic structure of the surface and thus enables a topographic imaging of the surface at atomic resolution. Figure 2.5 illustrates the measuring principle. Although this technique is not applicable to organic films thicker than a few monolayers due to charging effects, it is possible to image single organic molecules adsorbed on a crystalline metal surface (e.g. 6P on Ni [44]).

2.7 Atomic-force microscopy

Complementary to STM the atomic-force microscope (AFM) is not limited to electrically conducting samples. Thus, it is well-suited for the investigation of the morphology of oligo-phenylene thin films grown on solid substrates. The AFM enables investigations over a very large lateral range spanning from several 100 μm down to a few nm. The measuring principle of AFM is rather simple [89, 98]: a very thin and sharp tip (mounted to a small cantilever) is moved linearly across the sample surface at a distance low enough for attractive and/or repulsive forces to act between the atoms of tip and those of the sample surface. The cantilever shown in Figure 2.6 is slightly bent according to the surface corrugation of the sample. This z-signal (local altitude of the surface corrugation) is recorded versus the xy coordinates of the lateral tip position. In this way the three-

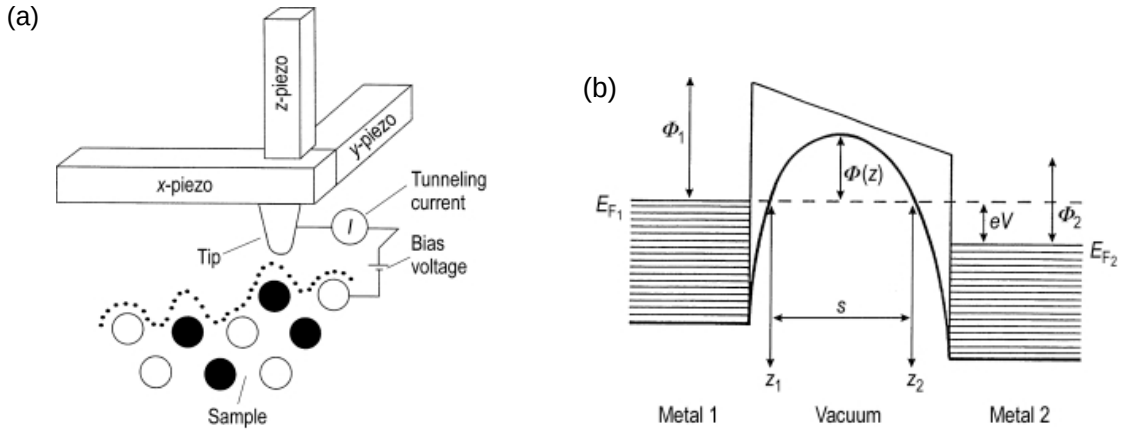

Figure 2.5: (a) Schematics of the scanning tunnelling microscopy (STM) technique. (b) Potential energy diagram for the tunneling situation. Φ is the work function and V denotes the voltage applied between the tip and the sample surface.

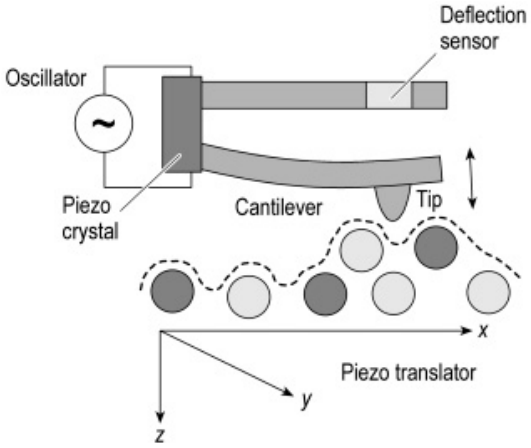

Figure 2.6: The principle of atomic-force microscopy (AFM).

dimensional topography of the sample surface can be reproduced. Although in principle atomic resolution is possible, all AFM measurements presented in this work were made with lower resolution. However, this has been sufficiently good for the given samples and measurement conditions (The AFM experiments have been done under ambient air conditions).

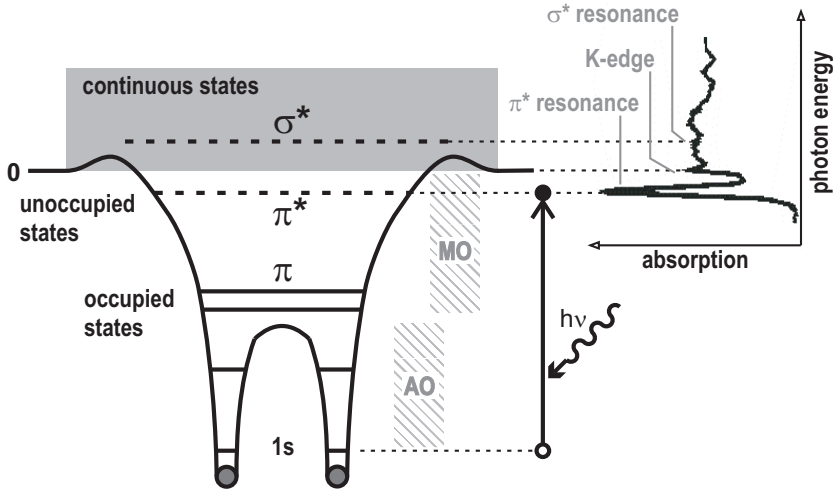

Figure 2.7: Schematics of the fundamental x-ray absorption induced $1s \rightarrow \pi^*$ transition investigated with the NEXAFS technique [100]. The vertical arrow indicates the π^* transition. AO and MO are atomic and molecular orbitals.

2.8 Near edge X-ray absorption fine structure

The NEXAFS (or XANES X-ray absorption near edge structure) method probes the absorption of highly monochromatic X-ray radiation in an energy range close to a characteristic absorption edge until about 50 eV above the edge [99]. In the case of organic molecules the most important energy regimes investigated are the C 1s (285 eV), N 1s (401 eV) and O 1s (531 eV) edge, respectively. The well-known absorption edges of the X-ray absorption coefficient correspond to the threshold of a core electron excitation via X-ray absorption. The need for a tunable, yet highly monochromatic X-ray radiation predestines synchrotron sources. Different signals can be used for detection that are proportional to the absorption coefficient, i.e. Auger electrons, secondary electrons and fluorescent photons generated during the decay of the excited state(s) or photoelectrons. However, the latter are generated only for energies above the absorption edge and thus not suitable for detecting the π^* resonances (see below). The escape depth of the secondary electrons is about 2 nm [99].

For planar aromatic molecules the most prominent resonance in NEXAFS spectra is related to the transition of a carbon $1s$ core electron into an unfilled molecular orbital with π symmetry. The π^*-resonance appears typically about 5 eV before the characteristic K-edge, as illustrated in Figure 2.7. Additionally, on the high energy side of the K-edge σ^* resonances can be observed. Depending on the hybridisation states of the molecular orbitals the σ and π bonds can be oriented in different ways with respect to the molecular backbone. This is illustrated in Figure2.8 for four important groups of molecules.

For many aromatic molecules and, in particular, for the oligo-phenylenes the transition dipole $\vec{T}$ for the π^* transition is oriented perpendicular to the aromatic plane [102]. Hence, for an oriented molecule dipole-selection rules will cause a strong polarization dependence of the π^*-resonance. This is the so-called **linear dichroism**. In case of planar adsorption

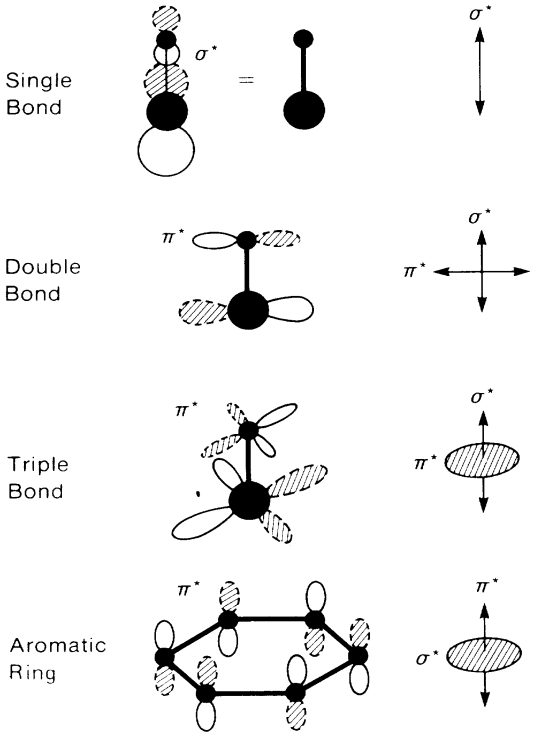

Figure 2.8: Schematic illustration of the orientation of molecular π^* and σ^* orbitals for four different types of hybridisation found in organic compounds [101].

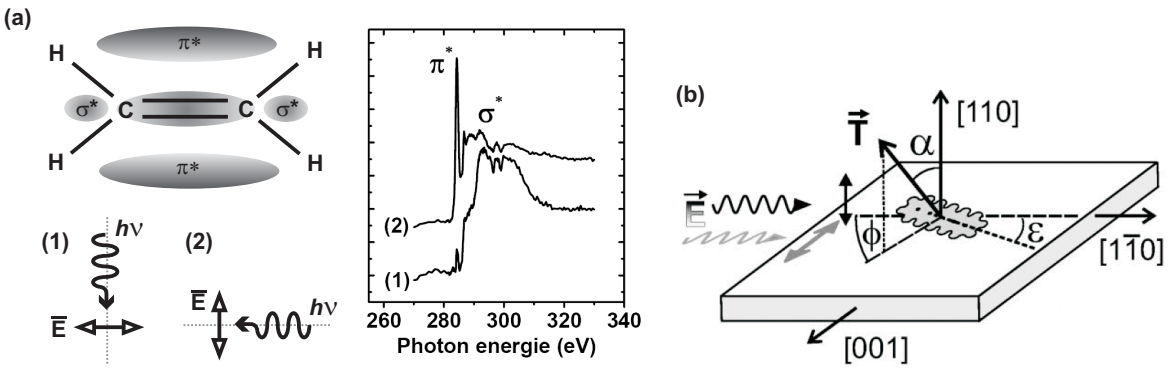

Figure 2.9: (a) Illustration of the different X-ray absorption behaviour upon (1) normal and (2) grazing incidence leading to either σ^* or π^* resonances. $\bar{E}$ denotes the electric field vector. (b) Schematics of the NEXAFS geometry [100]. The transition dipole $\vec{T}$ is indicated together with the orientation angles ϕ, ϵ and α.

on a solid surface the π^*-transition is very intense for p-polarized light (grazing incidence) and zero for s-polarized light (normal incidence, 90°), see Figure 2.9. Given the electric field vector $\vec{E}$, the absorbed intensity depends on the orientation of the $1s \rightarrow \pi^*$ transition dipole momentum $\vec{T}$ according to the relation

$$I_{absorbed} \propto |\vec{E} \times \vec{T}|^2 \tag{2.13}$$

Usually, the NEXAFS spectra are recorded for three different incident angles of the linearly polarized X-ray radiation. This enables the determination of the orientation of the transition dipole $\vec{T}$ relative to the substrate surface plane. A detailed description of the evaluation procedure for NEXAFS spectra can be found in [101]. In many cases, the molecular orientation can be immediately concluded from the orientation of $\vec{T}$. If, however, the molecular conformation is significantly changed upon adsorption on the surface, also the relative orientation of $\vec{T}$ with respect to the molecular backbone can be changed and an determination of the molecular orientation is no more straight forward [103].

2.9 Scanning electron microscopy

In this work SEM has been used complementary to AFM for the investigation of the microscopic thin film morphology ex-situ at room temperature. For details on SEM the reader is referred to the literature. A comprehensive introduction can be found in [104].

Electron backscatter diffraction

In addition to recording standard SEM images also an electron backscattering (EBS) detection system has been used, which allows the determination of the crystal orientations of individual crystallites relative to the macroscopic surface plane of a polycrystalline sample. The whole analytical method is called "space mapping" [105], with the space map being a colour-coded representation of the crystalline orientations. It is based on the strong dependency of electron backscattering images (Kikuchi patterns) on the orientation of a crystalline substrate. A space map provides the full crystallographic information of the sample surface (Eulerian angles). The probing depth ranges typically between 10 and 100 nm.

Chapter 3

Instrumentation

This chapter describes the specific experimental setup, the used instrumentation and the fabrication techniques that have been applied for the sample preparation.

As far as the analytical techniques are concerned that have been used in this work, three types of measurements can be distinguished according to the environmental conditions under which they have been performed. 1) Experiments under ambient conditions: atomic-force microscopy (AFM), X-ray diffraction (XRD) and optical microscopy (OM), 2) Experiments under HV conditions: electron backscatter diffraction (EBS) and scanning electron microscopy (SEM) and 3) Experiments under UHV conditions: Auger electron spectroscopy (AES), low energy electron diffraction (LEED), near-edge X-ray absorption fine structure (NEXAFS), scanning tunneling microscopy (STM), thermal desorption spectroscopy (TDS), X-ray photoelectron spectroscopy (XPS) and in-situ optical microscopy (in-situ OM). The first and second group of experiments as well as the NEXAFS and STM measurements have been predominantly carried out in co-operation with one of our partner groups (Graz, Leoben, Berlin, Bochum), whereas all other UHV experiments have been performed in our home laboratory.

3.1 The UHV setup

The AES, TDS, XPS, in-situ OM and LEED experiments have been carried out under UHV conditions at a base pressure of about 10^{-10} mbar. A schematic side view of the UHV chamber is depicted in Figure 3.1 including the details of the pumping system. The **sample** is placed on a sample holder situated in the center of the chamber and can be rotated around 360° within the measuring plane (see below). Common of all the different substrates used in this work, the samples were clamped into two Cu electrodes on the sample holder with the help of a 0.2 mm tantalum wire. In the case of the Au(poly) samples, the latter has been spot welded to the back side of the sample. The cylindrical single crystals used in this work exhibited a circular groove running around their side walls, where the Ta wire could be wound around for mounting purposes. Both types of sample mounting allowed an Ohmic heating of the samples up to about 1000 K. Additionally, the

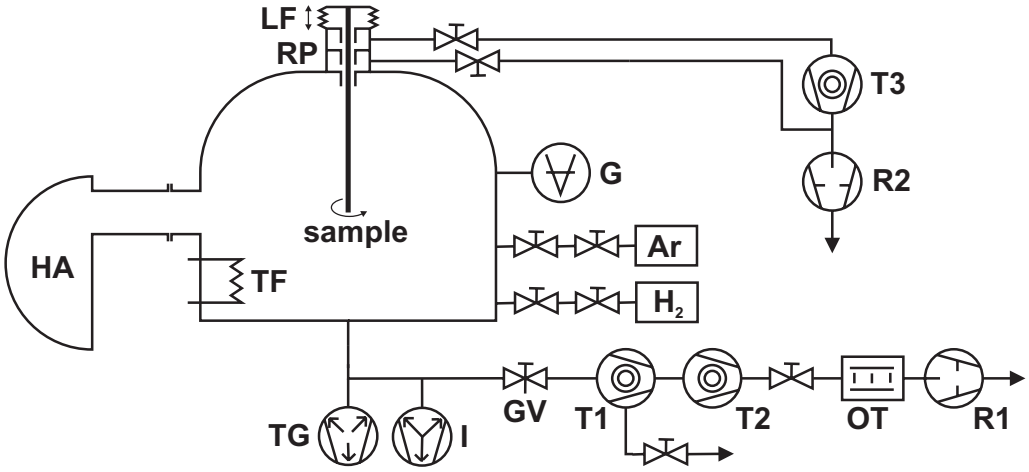

Figure 3.1: Schematic side view of the UHV chamber. Abbreviations: G ionization gauge, GV gate valve, HA hemispherical analyzer, I ionization getter pump, LF linear motion feedthrough, OT oil trap, R rotary vane pump, RP rotational platform, T turbo-molecular pump, TF tungsten filament, TG titanium getter pump.

samples could be cooled down to about 93 K via a liquid nitrogen cold finger attached to the sample holder. The temperature was measured with a NiCr-Ni thermocouple spot-welded to the back side of the Au samples. A computer-controlled heating stage enabled to maintain both a constant sample temperature as well as a linear heating of the sample.

The analytical equipment of the UHV chamber is placed annular around the sample within the measuring plane. The sample can be positioned in front of each instrument with the help of the rotational feedthrough. A combined **XPS/AES system** (Leybold Inc.) featuring a concentric hemispheric analyzer (CHA) was used. There are two retarding modes in which the CHA can be used [87]. The constant $\frac{\Delta E}{E}$ mode features a constant relative energy resolution together with an analyzer transmission $T(E)$, which is directly proportional to the kinetic energy E at the peak position, i.e. $T(E) \propto E$. Complementary, the constant ΔE mode features a constant absolute resolution and the transmission is inversely dependent on the energy: $I(E) \propto \frac{1}{E}$. The **X-ray source** can be switched between Mg K_α (1253.6 eV) and Al K_α (1486.6 eV) radiation. The source voltage was set to 10.5 kV and the emission current was 30 mA. No additional monochromator was used. The energy resolution for XPS was about 1.5 eV. The **electron gun** for AES was operated with an emission current between 0.007 - 0.07 mA and the beam voltage was between 1.5 and 2.0 kV.

The LEED experiments were performed with a 3-grid micro-channelplate-enhanced series 855 **MCP-LEED instrument** (Omicron Inc.). Details on the LEED optics are described in Appendix D. The electron gun features a thoriated tungsten (WTh) filament, providing a FWHM of 0.7 eV. The transfer width is greater than 25 nm at 100 eV. A computer-aided digital image acquisition was used. For the TD experiments a QMS 400 in-

line quadrupole mass spectrometer (Pfeiffer Inc.) equipped with a magnetic field enhanced cross-beam ion source was used. The detectable mass range was 1 - 512 amu. Some of the early TD experiments of 4P and supplemental residual gas analysis (RGA) were performed with a Prisma 200 quadrupole mass spectrometer (Pfeiffer Inc.), featuring a smaller detectable mass range from 1 to 200 amu. The TD experiments were done at a linear heating rate of 1 K/s.

3.2 In-situ UHV optical microscopy

In order to investigate the organic thin film morphology in-situ during film growth a special mounting system has been developed for attaching a Leica MZ 12.5 stereo-microscope to the UHV chamber. Alternative to the LEED instrument a home-built UHV flange with a quartz glass window could be attached to this position. This specially designed flange enables in-situ OM investigations from the outside of the UHV chamber. The working distance of the microscope was about 5 cm. It was equipped with an apo-chromatic objective lens system and a co-axial sample illumination (halogen lamp, Philips Inc.). A lateral resolution of about 1 μm has been achieved. The microscope was attached to the vacuum chamber with the help of a home-built mounting system. Figure 3.2 shows a photograph of this "lafette". It allows a free translation and rotation of the microscope in three spatial dimensions in order to adjust the optical axis of the microscope perpendicular to the sample surface. This condition was found to be necessary for a proper imaging in conjunction with the co-axial sample illumination: During the course of building up the microscope setup, it was found that a proper orientation of the microscope relative to the sample surface is an important pre-requisite for optical imaging. Small angular deviations in the order of a few degrees result already in a total loss of image contrast from the organic crystallites.

3.3 Gold substrates

Various different gold substrates have been used in this work. On the one hand, a Au(111) and a Au(433) single crystal have been applied. Both were purchased from MaTecK Inc. The single crystals were of cylindrical shape with 10 mm in diameter and a thickness of 2 mm. The side of the cylinder exhibited a 0.2 mm wide groove running annular around the whole crystal cylinder. This groove was used for the mounting of the crystal with the help of a Ta wire wound around the crystal within the groove. Alternatively to the single crystallites, a 99.99% high purity poly-crystalline gold foil purchased from Ögussa Inc. (10 mm x 10 mm x 0.1 mm) was used, which was spot-welded onto two 0.2 mm Ta-wires.

The cleaning of the Au samples under UHV conditions was in principle rather easy. Short sputtering with Ar^+ ions (1 kV) for about 10 to 30 min at an Ar pressure of $5 \cdot 10^{-5}$ mbar and consecutive annealing at 900 to 925 K is sufficient to obtain an atomically clean Au surface, as verified by Auger electron spectroscopy. In the case of

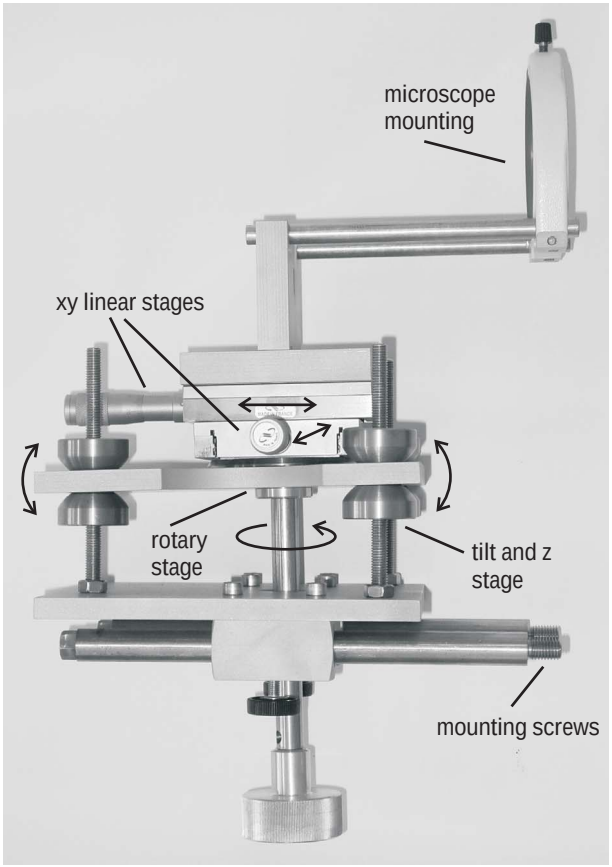

Figure 3.2: Photograph of the home-built mounting system of the stereo microscope used for in-situ optical microscopy.

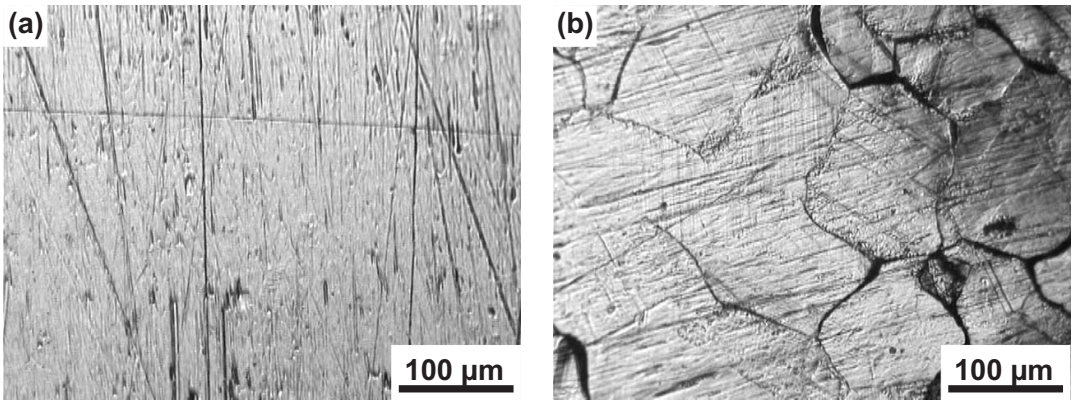

Figure 3.3: Optical micrograph of the poly-crystalline Au surface (a) before and (b) after a proper sputtering/annealing treatment. The crystalline grains and grain boundaries are clearly visible in (b).

the Au(poly) sample a proper treatment of several consecutive cycles of sputtering and annealing was applied after transferring it to the UHV chamber. This treatment yields a microcrystalline surface consisting of a large variety of single-crystalline Au grains. Figure 3.3 (b) shows an optical micrograph of the poly-crystalline Au surface after the proper sputtering/annealing. The image was recorded with a co-axial sample illumination. The image contrast in this case is very sensitive to the sample orientation (see above). Thus, the OM image indicates that the terminating surface plane of each Au grain is nearly parallel to the macroscopic sample surface plane. The size of the individual Au grains ranges from 50 to 200 μm. EBSD measurements have proven the high crystallinity of the Au grains (cf. Chapter 5). The mean density of surface atoms of the Au(poly) can be approximated by assuming that the three lowest index Au facets, i.e. the (100), (110) and (111), are equally distributed on the Au(poly) surface. Averaging the corresponding surface densities for these three facets yields a surface density of 1.2×10^{15} atoms/cm^2 for Au(poly).

3.4 Carbon pre-covered gold substrates

Besides atomically clean Au surfaces also carbon covered Au surfaces have been used in this work. After the cleaning procedure the Au surface was intentionally covered by a certain amount of carbon. The preparation of well-defined carbon pre-coverages was done by either one of two methods: 1) thermal dissociation or 2) X-ray induced dissociation of nP molecules, which have been pre-deposited on the clean Au surface. Thermal dissociation takes place upon heating of an nP thin film above a certain temperature, which depends on the type of nP molecule used. Details are described in Chapter 6. In the case of 4P and 6P the films were heated to 873 K or 1023 K, respectively. The total amount of dissociated nP during one heating cycle depends on the film thickness, the substrate surface and, of course, on the type of nP molecules. The maximum carbon coverages that can be prepared this way are limited by the dissociation process (see Chapter 6). It can be reached by applying several consecutive adsorption/desorption cycles without interstitial cleaning of the surface. The second method for preparing carbon coverages utilizes X-ray induced dissociation of nP molecules. The deposited nP films were exposed to the MgK_α radiation of the XPS instrument for a certain period of time, which determines the final carbon coverage. After the X-ray treatment the residual intact molecules were thermally desorbed. This method enables the preparation of carbon coverages that are larger than the above described saturation coverage that is reachable by thermal dissociation. However, it is not well suited for preparing very small carbon coverages.

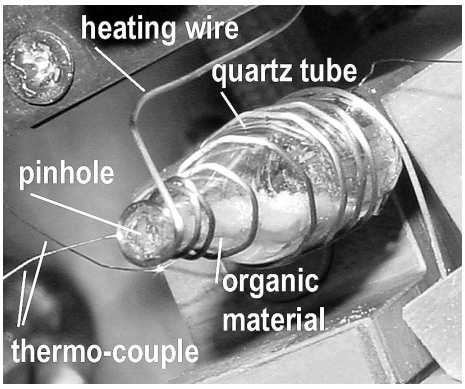

Figure 3.4: Photograph of the home-built Knudsen cell (pinhole diameter 1 mm).

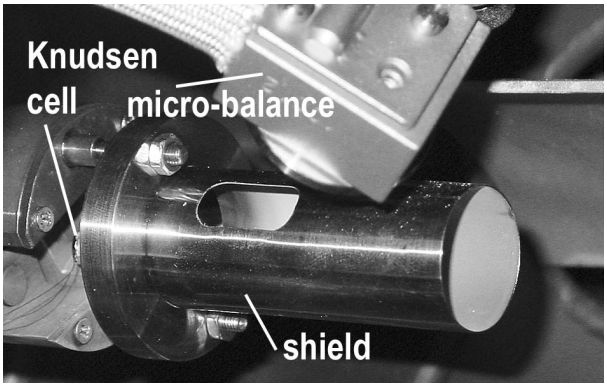

Figure 3.5: Photograph of the evaporation source.

3.5 Preparing the organic thin films

The organic material used in this work was purchased from Sigma Aldrich Inc. (4P) and Tokyo Kasei Inc. (6P) respectively. The organic thin films have been fabricated by organic molecular beam deposition (OMBD) within the UHV chamber described above. A comprehensive review on the OMBD technique was given by Forrest [6]. In the present work the organic material was evaporated from a home-built Knudsen cell. A photograph of the cell is shown in Figure 3.4. The design of this evaporation source is based on a 5 mm diameter quartz glass tube exhibiting a 1 mm pinhole on one end, while the other end is sealed. Further details are described in [106]. The organic material inside the quartz tube is heated with the help of a 0.2 mm tantalum wire wound around the outside of the tube, which can be Ohmically heated. The evaporated material effuses through the pinhole of the Knudsen cell towards the sample. The latter is located about 5 cm away from the cell. A cylindrical shield is used to shape the molecular flow only in the direction towards the sample and prevent an excessive evaporation of the material into the vacuum recipient. A mechanical shutter enables to control the deposition process. The support for the Knudsen cell was water cooled, in particular during the baking of the UHV system, to avoid uncontrolled evaporation of the organic material. A quartz microbalance (Inficon Inc.) is permanently positioned about 30° off the axis of the Knudsen source. The microbalance allows an in-situ control of the evaporation rate. For the calibration of the impingement rate on the sample, the latter was temporarily replaced by a second quartz microbalance, as described in [106]. This enabled a quantification of the deposition rate, i.e. the reading of the frequency change in Hz on the microbalance monitor could be related to an absolute mass thickness Δm in g/cm^2 of the deposited material. The latter is given by

$$\Delta m = -\frac{1}{S} \cdot \frac{\Delta f}{f^2} \tag{3.1}$$

Table 3.1: Values of mass thickness Δm and mean film thickness d equivalent to a frequency change of the quartz microbalance of $\Delta f = 1Hz$ upon deposition of an nP film.

	Δm (molecules/cm^2)	d (nm)
4P	$2.56 \cdot 10^{13}$	0.099
6P	$1.62 \cdot 10^{13}$	0.096

where S is the integral mass sensitivity and f (Δf) is the frequency (frequency change) of the quartz microbalance. The used quartz crystal had a frequency of $f = 5.98 \cdot 10^6 Hz$. The value of the integral mass sensitivity S can be calculated from fundamental material properties. The value given by the manufacturer of the quartz microbalance is [107]

$$S = \frac{2}{\sqrt{G \cdot \rho}} = 2.273 \cdot 10^{-6} \frac{cm^2 \cdot s}{g} \tag{3.2}$$

where G is the shear modulus and ρ is the density of quartz. Using S together with the molecular mass of a single nP molecule certain mass thickness values ($molecules/cm^2$) have been obtained that are equivalent to a frequency change of $\Delta f = 1Hz$. Based on the density values of 4P and 6P, one can additionally calculate the equivalent mean film thickness. The corresponding values are summarized in Table 3.1.

The deposition rate of the home-build evaporation source exhibits roughly an exponential dependence of the source temperature. However, it has turned out that after several hours of operation the evaporation rate at a given temperature significantly decreases compared to the initial rate that was measured right after the source had been cleaned and re-filled. Consequently, the cell has to be heated up to higher temperatures in order to achieve the same rate. This behaviour might be explained by a successive narrowing of the nozzle diameter (pinhole), which is caused by a crystallisation/agglomeration of nP material on the inside of the cell walls near the nozzle shown in Figure 3.4. The experimentally determined temperature dependence of the 4P and 6P evaporation rate is shown in Figure 3.6. The data points have been collected over a time period of several weeks. The change of the rate is indicated by an arrow.

3.6 Ex-situ measurements

After removing the properly prepared samples from the UHV system they have been transferred to several different instruments in order to perform complementary measurements. The sample transfer has been done under ambient conditions.

Scanning electron microscopy (SEM) was performed using two different instruments. The first one, a Gemini DSM 982 (Zeiss Inc.) was located at the FELMI (TU Graz). Besides of a standard secondary electron detector, it was equipped with an electron backscattering (EBS) detection system for recording space maps. The second instrument, a JSPM-4500S (JEOL Inc.) scanning probe microscope, was located at the "Institut für Physikalische Chemie, Ruhr Universität Bochum" (Germany). This instrument allowed to perform

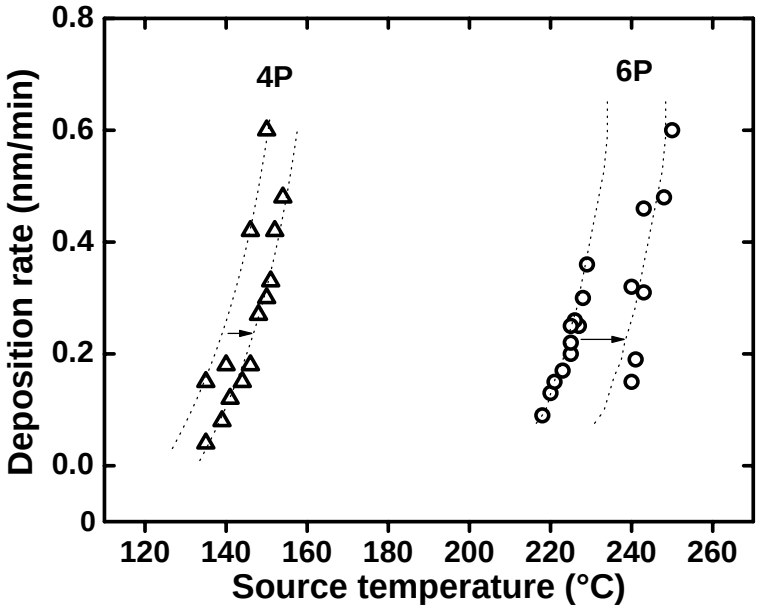

Figure 3.6: Temperature dependent deposition rate of the nP evaporation source. The arrow and the dotted lines indicate the time dependent variation of the rate.

combined STM and SEM measurement at the same probing position on the sample.

X-ray diffraction (XRD) measurements were performed with two different instruments. An X'PERT texture goniometer (Philips Inc.) equipped with an ATC3 cradle (sample holder for rotating and tilting the sample) using CrK_α radiation and a flat secondary graphite monochromator for the pole figure measurements. The pole figures were measured in $\phi-$ and ψ-steps of 1° and 3°, respectively. A $D501$ diffractometer (Siemens Inc.) in Bragg-Brentano geometry using CuK_α radiation and a secondary graphite monochromator was used for the specular $\Theta/2\Theta$ scans. All XRD measurements were done under ambient conditions.

Atomic-force microscopy (AFM) was performed with a Nanoscope Multimode IIIa scanning probe microscope (Digital Instruments Inc., Santa Barbara, CA) equipped with an AS-130(J) scanner. This instrument was located at the Institute of Physics, University of Leoben, Austria. The measurements were performed in tapping mode under ambient conditions. Both conventional Si tips as well as high density carbon (HDC) tips, consisting of a carbon whisker attached to a conventional Si cantilever, were applied. The higher aspect ration of the sharpened tips allows to image crystallites with steep side walls.

The near-edge X-ray absorption fine structure (NEXAFS) experiments in this work have been performed at the BESSY II synchrotron in Berlin (Germany) at the beamline HE-SGM.

Scanning tunneling microscopy (STM) has been performed on two different machines. The first one was a JSPM-4500S (JEOL Inc.) scanning probe microscope located at the "Institut für Physikalische Chemie, Ruhr Universität Bochum" (Germany). The STM

images have been recorded with tungsten tips in constant current mode under UHV conditions at room temperature. The second STM instrument was an STM-1 (OMICRON Inc.) located at the Institute of Solid State Physics of the Graz University of Technology (Austria). The instrument has been operated with electro-polished tungsten tips at room temperature under UHV conditions.

Part II

Experimental results

Chapter 4

Oligo-phenylenes on Gold(111)

The chapter is a compilation of some fundamental aspects concerning the adsorption and desorption kinetics, the structure, growth and morphology of 4P and 6P on the atomically clean Au(111) surface. It is intended to serve as a "reference" of comparison for later chapters.

4.1 Monolayer thermal desorption

As far as the initial stages of nP growth on Au(111) is concerned, a fundamental question arises according to the existence of a mono-molecular **wetting layer**. Addressing this question, the existence of a wetting layer has been demonstrated in TDS experiments for both 4P and 6P over a temperature range from 93 K to room temperature. For both 4P and 6P no significant differences have been observed in the TD spectra for films grown at 93 K or 300 K. Two representative TD series covering the monolayer regime of 4P grown at 93 K and 6P grown at 300 K are shown in Figure 4.1 and 4.2, respectively. The films have been grown on atomically clean Au(111). Although some significant differences exist between the presented TD spectra of 4P and 6P, also some important qualitative similarities can be observed, in particular, in the low coverage regime [14, 20]. Those similarities will be discussed at first.

Starting from coverages below 0.1 nm a first TD peak appears at considerably high temperatures between 500 K and 700 K. This peak is labelled β_1. With increasing film coverage it strongly shifts towards lower temperatures until saturation takes place. The peak maximum of the saturated β_1 peak appears at about 520 K for 4P and 630 K for 6P, respectively. If the coverage is further increased beyond the saturation of β_1, a second peak arises at the low temperature side which is labelled β_2. It shows the same direction of temperature shift with increasing film coverage compared to β_1 and also exhibits a saturation behaviour. For both 4P and 6P the peak maximum of the saturated β_2 peak lies about 120 K lower compared to β_1.

Applying the Polanyi-Wigner formalism described in Section 2.1, one can try to assign the β_1 and β_2 peaks to kinetic desorption processes with an integer order of desorption n.

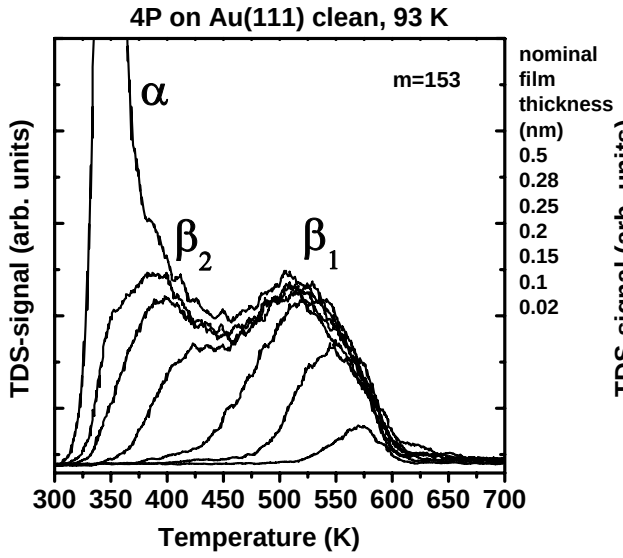

Figure 4.1: Monolayer TD regime of 4P grown on Au(111) at 93 K.

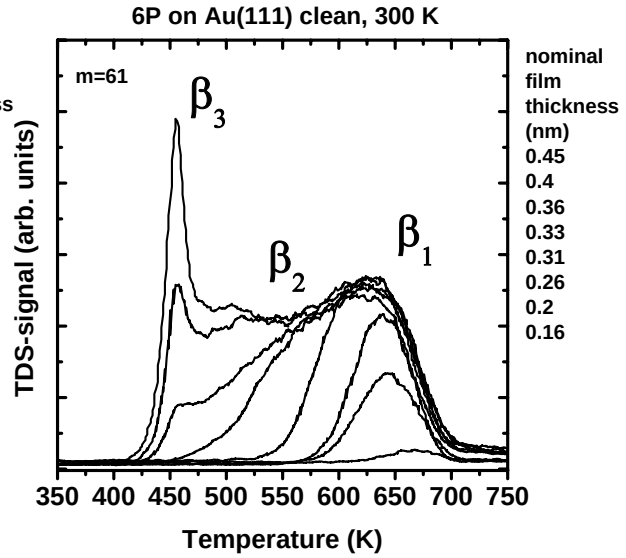

Figure 4.2: Monolayer TD regime of 6P grown on Au(111) at 300 K.

This is based on three experimental facts: 1) Within the desired temperature regime no desorbing hydrocarbon dissociation products have been observed, i.e. the nP molecules desorb as intact single molecules from the Au surface. This rules out n to be greater than one. 2) The characteristic broad peak shape rules out n to be zero. 3) Finally, the coverage dependent peak shift towards lower temperatures suggests a **first order** desorption with **repulsive** intermolecular **interactions** [81]. The latter is responsible for the observed negative temperature shift of β_1 and β_2 with increasing coverage, since a normal first order desorption exhibits a fixed peak maximum temperature.

The **saturation** of the full double peak $\beta_1 + \beta_2$ appears at a coverage Θ_{sat}, which has been quantitatively determined. A quantification with the quartz micro-balance has yielded $\Theta_{sat} = 6.6 \cdot 10^{13}$molecules/cm^2 for 4P and $5.9 \cdot 10^{13}$molecules/cm^2 for 6P, respectively. Alternatively expressed in terms of the mean film thickness this equals 0.27 nm for 4P and 0.35 nm for 6P.[1] These values are similar to the Van der Waals "thickness" of the oligo-phenylene molecules as depicted in Table 1.2. Independently, those saturation coverages have also been determined with LEED, as will be shown later (cf. Table 4.2). Together with the above finding that both β_1 and β_2 exhibit a saturation behaviour, this is a clear indication that the peaks β_1 and β_2 belong to the **first monolayer**. Furthermore,

[1]The measured values of the quartz micro-balance, given in $\mu g/cm^2$, can be easily converted into molecules/cm^2 with the help of the molecular weights of 4P an 6P, respectively. Consequently, the values for the "mean nominal film thicknesses", given in nm, can be calculated with the help of the nP bulk densities. However, these values do not necessarily represent the actual layer thicknesses, because the packing structures of the nP layers can differ significantly from the bulk structures. Instead, the nominal film thickness of an nP layer denotes the thickness of an equivalent bulk structure nP film (1 cm^2) that contains the same number of molecules/cm^2.

it can be concluded that the nP molecules within the first layer adopt a **flat lying conformation** upon the adsorption on the Au(111) surface. This means that the long molecular axes are oriented roughly parallel to the (111) plane. Alternatively, the existence of two distinct TD peaks in the monolayer regime might also be interpreted in terms of a 1st nP layer corresponding to β_1 and a second layer β_2. However, the quantification of the saturation coverages together with the structural model derived from LEED experiments (see Section 4.2) favour a different interpretation: The peak β_1 belongs to the first half monolayer or **semilayer** and β_2 to the second one, accordingly. The observed large temperature difference of about 120 K between the peak positions of β_1 and β_2 indicates a fairly stronger bonding of the molecules in the first semilayer β_1 compared to the second one. This can be interpreted in terms of a different molecular adsorption geometry relative to the Au surface of the molecules within the first and second semi-layer, as described below in terms of an edge-face packing.

Whereas in the case of 4P such an interpretation agrees well with the TD data, where both peaks are roughly of the same size, the TD spectra of 6P request a further interpretation. Both peaks β_1 and β_2 are fairly broad and overlap strongly, which makes it difficult to evaluate the integral peak areas of both peaks separately. An approximative peak integration yields the ratio of the peak areas $\beta_1 : \beta_2$. Clearly, this ratio is different for 4P (1:1) and 6P (1.5:1), and, most important, the β_1 peak is significantly larger in the case of 6P. A possible explanation for this experimental finding is as follows: Still, the β_1 and β_2 are attributed predominantly to the flat and edge-on adsorbed molecules, as described above. However, the different peak area ratios may indicate that the **kinetic processes** during thermal desorption from the monolayer are significantly different for 4P and 6P, because they are influenced by intermolecular and adsorbate-substrate interactions. The latter are differently strong for 4P and 6P, which can also be observed as the determining factor for the different fractional dehydrogenation of 4P and 6P described in Chapter 6.

The calculated values for the nominal film thickness of the saturated monolayer differ by about 30% between 4P and 6P. Taking into account that the bulk densities of 4P and 6P, which are used for the calculation of the nominal thickness values, are nearly identical (difference <3%), this would suggest that the 6P monolayer is significantly more compressed compared to the 4P monolayer. However, the LEED results do not corroborate this trend, as described in Section 4.2. This discrepancy can be explained by considering the difficulties encountered in TDS to accurately determine the absolute saturation coverages due to the strong overlap of the peaks. In particular, for 6P also the second layer starts to grow simultaneously to the first monolayer (see below), which increases the difficulties of determining the saturation coverages exactly. Therefore, the above conclusion from the TD data, i.e. that the packing density in the 6P monolayer would be significantly larger compared to the 4P monolayer, has to the discarded.

Another difference between 4P and 6P concerns the positions of the peak maxima of β_1 and β_2. It has been quite difficult to accurately determine those positions because of the broad shape and the strong overlap of the TD peaks. Thus, an estimated error of about ±5-10 K has to be considered. In the case of 4P the peak maxima at saturation have been observed around 400 K and 520 K, respectively, and in the case of 6P, they lie at

significantly higher temperatures, namely at 520 K and 640 K. Within the margin of error, the temperature difference between the saturated β_1 and β_2 peaks of roughly 120 K is the same for both 4P and 6P. This suggests that for both 4P and 6P **similar desorption processes** underlie and, in particular, that the **first and second semilayers** are similarly composed. The constant shift towards higher temperatures of the 6P monolayer desorption peaks compared to 4P can be obviously explained by the stronger bonding of the 6P molecules to the Au(111) surface, i.e. stronger adsorbate-substrate interactions, which is due to an increased number of phenyl rings per molecule.

In some cases it is difficult to decide from the experimental TD data, if the β_2 peak also shows the same negative peak shift like β_1. Although a peak shift is clearly observed in the case of 4P for both β_1 and β_2, the situation is not as clear for 6P. According to the first semilayer, β_1, we have observed indications for **repulsive** intermolecular interactions for both 4P and 6P. Considering a flat adsorption configuration[2] of the phenylene molecules on Au(111) the following interpretation is reasonable: The hydrogen atoms of the nP molecules are expected to cause electrostatic repulsion between molecules that are adsorbed next to each other. An experimental indication for the repulsive behavior has been observed, for example, in the case of a 0.5 ML 4P film grown on Au(111), where a significantly enlarged surface unit cell exists compared to the saturated 4P monolayer structure (cf. Section 4.3). This experimental finding corroborates the intermolecular repulsion between neighboring flat lying nP molecules.

For both 4P and 6P the initial monolayer growth starts with the build-up of the first semilayer (β_1) and right after its saturation the second semilayer starts to grow. The growth of the two semilayers is strictly separated. The further growth of thicker films, however, is significantly different for 4P compared to 6P. In case of 4P, the 2nd and consecutive layers (multilayer) start to grow not before the first monolayer has saturated. This is clearly shown in Figure 4.1. The multilayer peak is labelled peak α. Different from that, in the case of 6P the existence of an additional distinct peak has been observed that clearly separates from the multilayer peak. The new peak is labelled β_3 and can be seen in Figure 4.3. Here, the ordinate has been up-scaled by a factor of 10 compared to Figure 4.2, whereby β_1 and β_2 appear very small. The distinct peak β_3 emerges around 455 K after the saturation of the first monolayer and shifts with higher coverage to higher temperatures. This positive peak shift indicates attractive intermolecular interactions and clearly discerns the β_3 peak from the two 1st layer peaks β_1 and β_2 that exhibit a negative shift. The narrow peak shape of β_3 is similar to that of the multilayer peak α. However, a saturation of β_3 is observed at a nominal film thickness of 0.8 nm. These findings suggest that the β_3 peak stems from the desorption of the **second monomolecular layer**. This is remarkable insofar, as 4P exhibits no distinct 2nd layer peak in TDS. The thickness of the second layer is about 0.4 nm, similar to that of the first layer, and the peak maximum of the saturated β_3 lies around 463 K. This is only about 25 K above the beginning multilayer

[2]This means that the molecule is considered to adopt a more or less planar configuration, where the long molecular axis as well as the aromatic plane of the molecule are oriented almost parallel to the substrate surface plane.

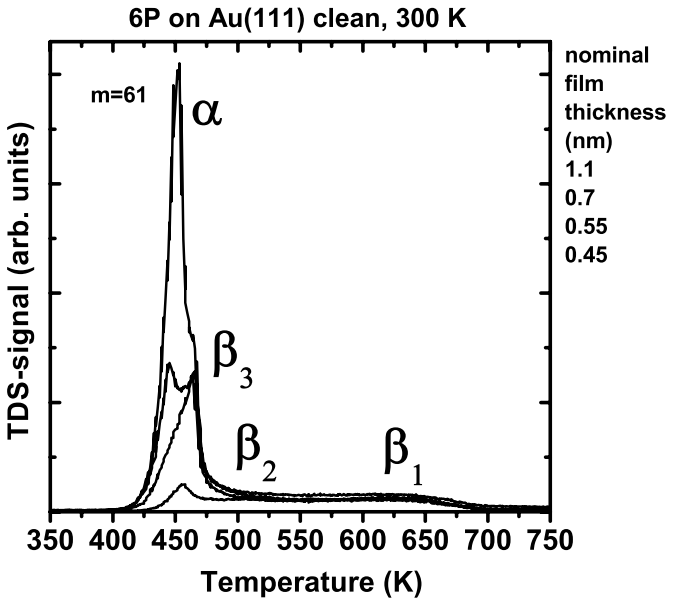

Figure 4.3: Series of thermal desorption spectra of 6P grown on Au(111) at room temperature. The film thicknesses have been chosen to cover the regime of the 2nd layer.

peak. The growth of the second layer starts already before the first layer has saturated, as shown in Figure 4.2. This is in good agreement with the Stranski-Krastanov growth mode observed for both 4P and 6P multilayer films on Au(111).

As will be shown later on, the molecular packing of the second 6P layer is similar to that of the first monolayer (edge-face packing structure). However, the second layer exhibits in TDS only one single peak, compared to two peaks found for the first monolayer. This behaviour is already similar to the multilayer. Obviously, the second 6P layer is still interacting with the Au surface to a certain amount, which leads to a slightly stronger bonding compared to the multilayer. Interestingly, however, the different orientations of flat and side-tilted molecules, with respect to the Au(111) plane, seem to have no effect on their desorption energy, any more. A similar behaviour, i.e. a distinct second layer desorption, has been reported also in the literature for various systems like PTCDA (perylene-tetracarboxylicacid-dianhydride) on Ag(111) [108], EC4T (end-capped quaterthiophene) on Ag(111) [109], alkanes on graphite [85] and bithiophene on Cu(110)-(2x1)-O [110].

4.1.1 Reproducibility of TD Data

Due to slight variations in the cleaning procedure of the substrate surface during several months of experimental work, e.g. local changes of the sputter rate, the experimentator usually has to overcome systematic uncertainties in reproducing the substrate surface properties. Hence, surface parameters like defect concentration or step density can vary to

some extent during the long time period of experimental work. It should be mentioned at this point, that the reproducibility of the TD spectra recorded for 4P and 6P was in some cases slightly moderate due to the reasons mentioned above.

In particular, the relative heights of the monolayer desorption peaks were from time to time affected by such influences. In some cases not shown here, the β_1 peak, for example, appeared larger in the spectrum, while in turn the β_2 peak was lowered. However, the maximum observed deviations of the peak heights in the spectra shown in the figures can be estimated to roughly smaller than 30%. On the other hand, the peak positions (temperature) exhibited an excellent reproducibility.

4.1.2 Monolayer desorption energy

A direct analysis of the monolayer desorption spectra and a determination of the kinetic parameters is rather complicated for the oligo-phenyl monolayer desorption regime, as described in Section 2.1. To overcome these difficulties, an approximative approach is discussed in the following, which yields, at least, approximative values for the desorption energies of the nP monolayer desorption peaks β_1 and β_2.

According to Redhead [80], for a first-order desorption the desorption energy E_{des} (in cal/mol) can be approximated with the help of the peak maximum temperature T_p (in K) of the corresponding desorption peak by the numerical equation

$$E_{des}\ [cal/mol] = (ln(\frac{\nu_1 T_p}{\beta}) - 3.64)RT_p \tag{4.1}$$

where ν_1 (in 1/s) denotes the frequency factor or rate constant of the first order desorption, β is the heating rate, which was set to 1 K/s in the present experiments, and R is the molar gas constant ($R \approx 2$ cal/(mol K)). Tn general, the frequency factor of first-order desorption, ν_1, is coverage dependent. For the present approximation this can be neglected and ν_1 is approximated by the coverage-independent frequency factor of zero-order desorption, ν_0. The latter has been independently determined from the 4P and 6P multilayer desorption data, as described in Section 4.5.1. The values following values have been obtained:

$$\begin{aligned} 4P: \quad \nu_0 &= 1.6 \cdot 10^{21}\ s^{-1} =: \nu_1 \\ 6P: \quad \nu_0 &= 5.6 \cdot 10^{25}\ s^{-1} =: \nu_1 \end{aligned}$$

In a next step, the peak maximum temperature T_p for both first order monolayer desorption peaks β_1 and β_2 has been determined from the experimental TD data for the limiting case of very small coverages ($\Theta \to 0$). Based on the corresponding TD series of the 4P and 6P monolayer regime presented in Figure 4.2, an approximation has been made for the peak maxima of the two monolayer desorption peaks. This is demonstrated in Figure 4.4, where the monolayer desorption peak maxima temperatures for $\Theta \to 0$, which are indicated by circles, are approximately determined with the help of extrapolating the peak maxima positions of higher coverages indicated by dashed lines. This graphic analysis yields for 4P the values of $T_p = 580$ K for β_1 and $T_p = 460$ K for β_2, and in the case of 6P the

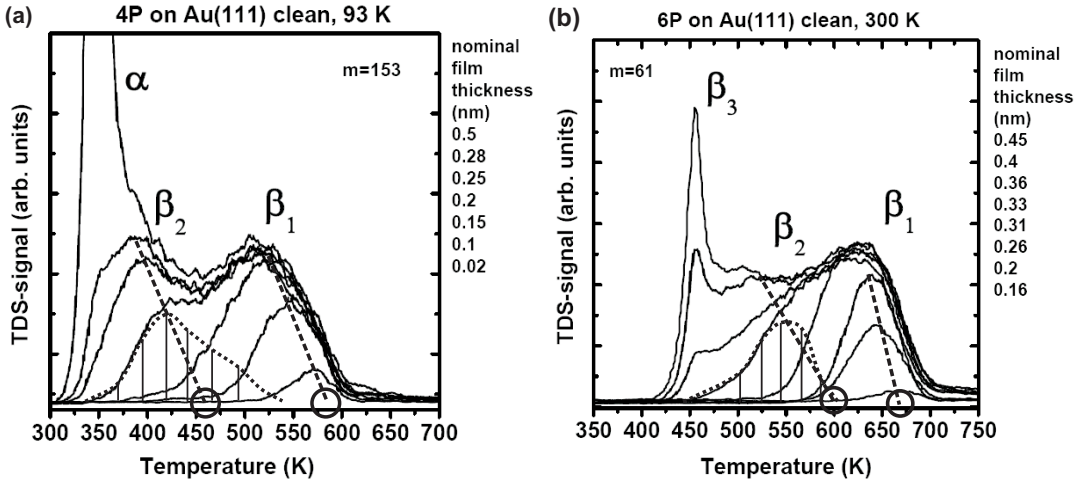

Figure 4.4: Approximative graphic determination of the monolayer desorption peak maxima for (a) 4P and (b) 6P on Au(111). A difference spectrum (dotted line) between the saturated β_1 spectrum and the first following curve helps to determine graphically the peak temperature of the β_2 curve for the limiting case of very small coverage. This is indicated by the circle.

values are $T_p = 670$ K for β_1 and $T_p = 600$ K for β_2, respectively. Inserting these data into equation 4.1 yields for both monolayer peaks β_1 and β_2 the numerical relations:

$$4P: \quad E_{des}\ [cal/mol] \approx 103 \cdot T_p\ [K] \tag{4.2}$$

$$6P: \quad E_{des}\ [cal/mol] \approx 124 \cdot T_p\ [K] \tag{4.3}$$

Those differ significantly from the well-known relation $E_{des}\ [cal/mol] \approx 60 \cdot T_p\ [K]$, which can be derived from Equation 4.1 in the case of $\nu \approx 10^{13}$. The latter holds true only in the case of small adsorbate species. According to the Equations 4.2 the desorption energies E_{des} of the 4P and 6P molecules desorbing from the first and second semilayers β_1 and β_2 from the Au(111) surface for the limiting case of very small coverages, $\Theta \ll$, can be determined. The values for 4P read:

$$\begin{aligned} E_{des}(\beta_1) &= 59.7\ kcal/mol = 2.6\ eV/molecule \\ E_{des}(\beta_2) &= 47.4\ kcal/mol = 2.1\ eV/molecule \end{aligned}$$

and for 6P:

$$\begin{aligned} E_{des}(\beta_1) &= 83.1\ kcal/mol = 3.6\ eV/molecule \\ E_{des}(\beta_2) &= 74.4\ kcal/mol = 3.2\ eV/molecule \end{aligned}$$

Those values are in good agreement with the experimental TD data insofar, as they help to explain the experimentally observed different temperature regimes of the nP multilayer and monolayer desorption peaks. In particular, for the desorption from the first (β_1) and second (β_1) semilayer an energy difference of about 0.4-0.5 eV can be observed, which is roughly independent of the length of nP molecule.

At first glance, the rather high activation barriers per single nP molecule for the monolayer desorption indicates a considerably strong **adsorbate-substrate interaction** of the nP molecules with the Au(111) surface. For a first approximation it can be assumed that only the C atoms in the nP molecules are involved in the adsorbate-substrate interactions via their extended π orbitals. Considering the total number n of C atoms per single 4P ($n = 24$) and 6P ($n = 36$) molecule, yields for both 4P and 6P almost the same values for the interaction energies per C atom (see below). This fact strongly corroborates the validity of the used analysis method. Moreover, it indicates that the nP molecules interact via similar processes with the substrate surface independent of the molecular length. A summation of the contributions of each C atom in the nP molecule yields the molecular interaction energy and the above results suggest a linear dependency of the molecular desorption energy from the chain length.

For the first nP semilayer β_1 on Au(111) a value of about 110 meV per C atom is obtained and for the second semilayer β_2 about 90 meV per C atom. These values can be attributed to flat (face-on) and side-tilted (edge-on) oriented nP molecules in terms of the different adsorption geometries of the molecules from β_1 and β_2 as described in Section 4.2. Both values are typical for **physisorbed** states. A comparison of the desorption energies of 4P and 6P as determined in this work with reported literature values additionally corroborated the above values. For instance, the desorption energy of benzene adsorbed on Au(111) is 603 meV/molecule or 57.9 kJ/mol similar to that of n-hexane on Au(111) of 544 meV/molecule or 52.2 kJ/mol [111]. Assuming a linear dependency on the chain length, the interaction energies per C atom (or per monomeric unit) can be calculated yielding values around 100 meV per C atom similar to 4P and 6P. This holds true for a variety of hydrocarbons physisorbed on different metal surfaces.

According to the Elovich formalism described on page 46 it is possible to consider **intermolecular interactions** between neighbouring adsorbed nP molecules in the monolayer coverage regime by introducing the coverage dependent desorption energy

$$E_{des}(\Theta) = E_0 \pm \omega \cdot \Theta \tag{4.4}$$

where E_0 is the desorption energy for the limiting case of very small coverages ($\Theta \rightarrow 0$), Θ is the coverage and ω the interaction energy. In the case of nP molecules adsorbed on Au(111) **repulsive** interactions should be expected, leading to a peak shift of the monolayer desorption peak towards lower temperatures with increasing coverage. This is in good agreement to the experimental TD spectra shown in Figure 4.4. In a next step, it is possible to derive the peak maximum positions of the monolayer peaks β_1 and β_2 for different coverages from the experimental TD spectra and calculate the corresponding desorption energies with the help of equation 4.2. In agreement with the previous interpretation, a decrease of the desorption energy with increasing coverage can be observed. In particular, this coverage dependance of the desorption energy is shown in Figure 4.5 for the β_1 peak of 4P and 6P, respectively. Please note, that in this case the coverage has to be related to the saturation coverage of the single β_1 peak, which is done by introducing the relative coverage Θ_{rel}. It can be clearly seen, that the expected linear dependency of the desorption

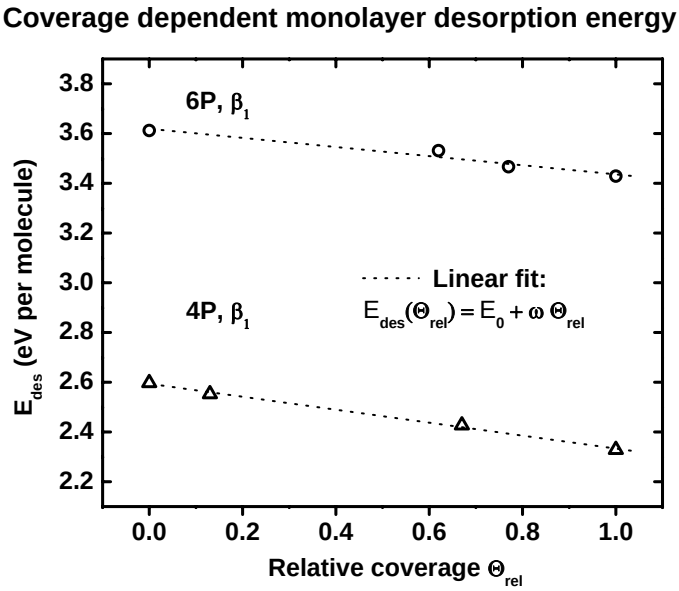

Figure 4.5: Determination of the repulsive intermolecular interaction energy, ω, for the 4P and 6P high temperature monolayer desorption peak β_1.

energy on the coverage is well reproduced. In particular, linear fits have been applied to the data as indicated by the dotted straight lines in Figure 4.5. The fitting procedure has yielded the values of the interaction energies of $\omega = -0.18 \pm 0.03$ eV/molecule for 4P and $\omega = -0.26 \pm 0.01$ eV/molecule for 6P, respectively. The negative sign indicates the repulsive nature of the interaction. Although the errors from the fitting procedure appear rather small, an estimated reading error of about ± 10 K has to be considered additionally during the previous determination of the peak temperatures. Nevertheless, the above values are supposed to give a good estimate of the repulsive intermolecular interaction energies between neighbouring adsorbed 4P and 6P molecules in the first semilayer (β_1).

4.2 Monolayer structure

Another fundamental question concerns the structure of the nP monolayer on Au(111). Based on experimental data gained from LEED and XRD experiments, a clear answer can be given: Highly **regular structures** have been observed for the 4P and 6P monolayers grown on Au(111). The high degree of ordering, however, is only established above a characteristic **threshold temperature** $T_{ordered}$. This has been verified by temperature-dependent LEED experiments. The monolayers have been initially deposited at a substrate temperature of 93 K, where no regular LEED pattern has been observed, neither for 4P nor for 6P on atomically clean Au(111). Hence, the nP monolayer on Au(111) is disordered at such low temperatures (compare to nP grown on C-covered Au surfaces discussed in Section 7.2). A value of $T_{ordered} = 270 \pm 10$ K has been determined independently for both

4P and 6P by monitoring the evolution of the monolayer LEED signal upon a controlled annealing of the film. In the case of 4P, a rather sharp transition can be observed from disordered to ordered growth around 270 K. Different from that, in the case of 6P the ordering process starts already at a lower temperature and proceeds over a temperature regime of about 70 K, until at 270 K a high degree of order is observed in LEED.

The structure of the ordered nP monolayer grown on Au(111) has been found independent of the substrate temperature in a wide range, i.e. from the beginning of an ordered growth around 270 K up to the onset of thermal desorption, as monitored with LEED. A similar behaviour has been reported for PTCDA/Au(111) [112]. It has been carefully checked that within the desired temperature regime no structural transition occurs, which would cause misinterpretation. Although at room temperature both 4P and 6P already form regular monolayers, the samples used for the analytical LEED experiments presented in this work have been grown at elevated temperatures. In particular, the 4P monolayers have been prepared between 300 K and 360 K. In the case of 6P, the higher desorption temperature allows a wider temperature range for annealing the films. Accordingly, the 6P monolayers were grown between 300 K and 430 K. **Annealing** or growth at elevated temperatures are known to produce in some cases, like 6P, a better crystallinity of the organic films [6, 55, 108], which is beneficial for a LEED analysis. All LEED measurements have been performed at 93 K.

For each of the individually prepared nP monolayer samples on Au(111) a series of several ten LEED images has been recorded. For the sake of simplicity only some representative LEED images of the 4P and 6P monolayer grown on Au(111) are shown in Figure 4.6. An analysis of the LEED data according to the procedures described in Appendix D has yielded the dimensions of the two-dimensional real space **surface unit cells** of the regular 4P and 6P monolayer on Au(111), respectively. The corresponding parameter values are listed in Table 4.1. In the case of 6P, the values of a and b agree well with previous data reported by France et al. that have been gained from STM investigations [66]. However, the unit cell angle derived in the present work with LEED ($\gamma = 73°$) is significantly smaller compared to that from the reported STM data ($\alpha = 91°$). This difference is most probably due to the fact that LEED is an integrating method, whereas with STM the structure is probed only locally. Therefore, local variations of the packing structure, as observed in STM are averaged out in LEED. Unfortunately, in the case of 4P no literature values have been reported, yet, to the best of our knowledge.

In order to check the consistency of the structural data derived from the experiment, a simulation of the LEED patterns has been performed. The simulation was based on the experimentally obtained data. Further details on the simulation procedure are described in Appendix D. A comparison of the simulated LEED patterns with the experimental data is shown in Figure 4.7, where a good agreement between the experiment and simulation is clearly visible. In some cases single reflections hk found in the simulation could not be reproduced by the experiment. This fact is attributed to the existence of strong intensity variations and/or extinction of certain LEED reflections, that is caused by the structure factor for electron diffraction of the surface unit cell of the regular organic overlayer (cf. Section 4.6.1).

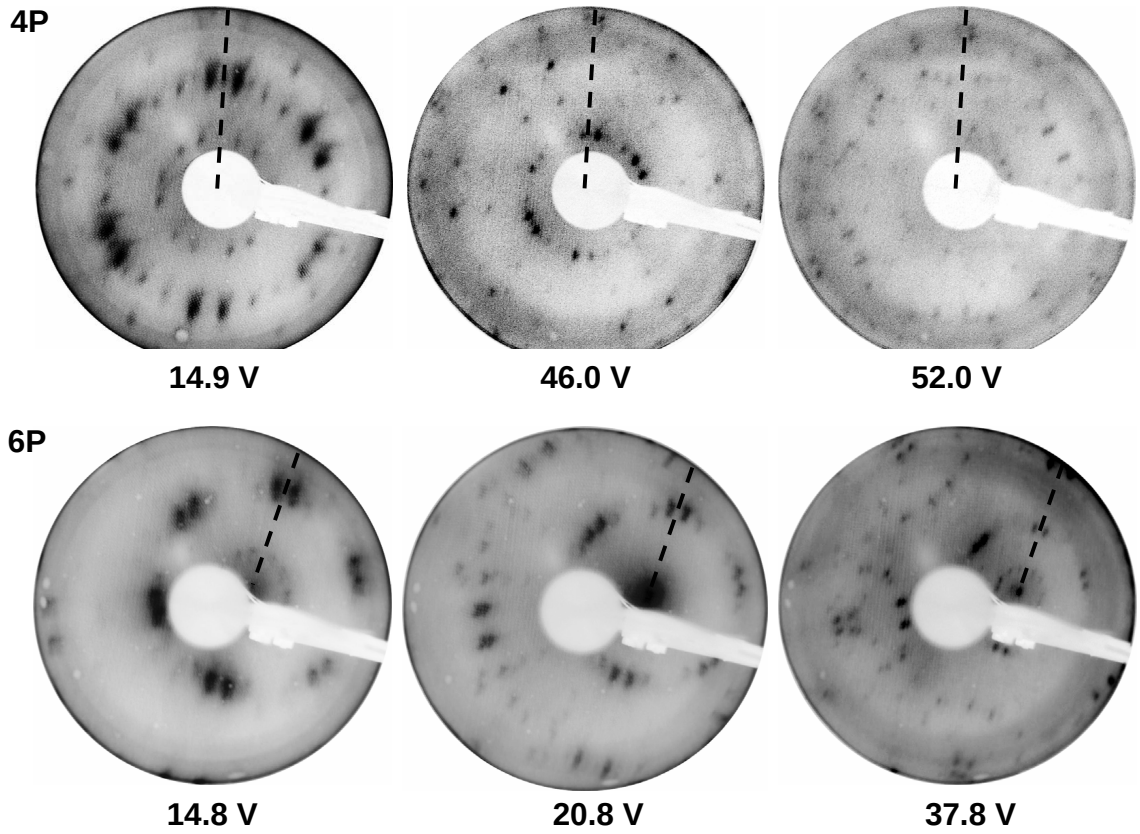

Figure 4.6: Representative LEED images of the regular monolayer of 4P (top) and 6P (bottom) grown on Au(111) at 360 K and 430 K, respectively. The images were recorded at normal incidence (4P) and angular incidence (6P), respectively. The corresponding beam voltages are indicated together with the Au$\langle 11\bar{2} \rangle$ direction (dashed line).

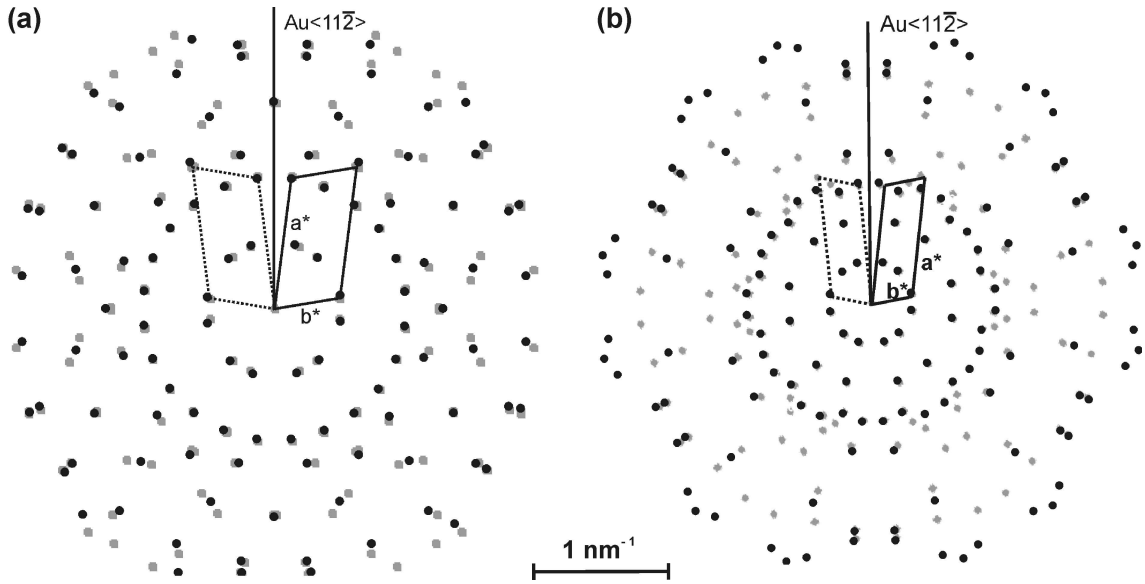

Figure 4.7: Comparison of the experimental LEED data (black) with simulation (grey) for a common beam voltage of 20 V. (a) 4P monolayer and (b) 6P monolayer on Au(111). The reciprocal unit cell is indicated (solid) together with a mirror equivalent unit cell (dotted). The mirror operation is performed along the Au$\langle 11\bar{2} \rangle$ direction (vertical line), according to the crystallographic symmetry of the substrate surface.

Table 4.1: Geometric parameters of the regular monolayer surface unit cell of oligo-phenylene monolayer grown on Au(111) at 300 K (type A domain).

	a (nm)	b (nm)	γ (°)	ϕ (°)	matrix
4P	1.1	2.2	74	37.5	$\begin{pmatrix} 4.5 & 2.75 \\ 1 & 8 \end{pmatrix}$
6P	1.2	3.3	73	40.9	$\begin{pmatrix} 4.5 & 3 \\ 1 & 12 \end{pmatrix}$

The short side of the monolayer surface unit cell, a, is almost identical for the 4P and 6P structure, whereas the long side, b, differs significantly. The corresponding values of b, which are similar to the Van der Waals lengths of the nPs, suggest that the molecules are aligned roughly parallel to the b side. Interestingly, also the unit cell angles γ are nearly identical for both 4P and 6P monolayer structures. Table 4.1 also provides the matrix notations of the regular monolayer structures. According to the formalism presented in Section 1.3 one finds the same type of epitaxy for both 4P and 6P, i.e. **coincident** overlayers, because of exclusively rational coefficients in the transformation matrix. A comparison of the two surface unit cells is depicted in Figure 4.8.

An interesting observation has been made during the LEED experiments concerning the 6P monolayer annealed at different temperatures between 300 K and 430 K. At a first glance, it seemed as if completely different LEED patterns would exist for monolayer films prepared independently under "identical" conditions. A thorough analysis, however, revealed that the spot positions are identical in all monolayer images. However, some reflections exhibit pronounced **intensity variations**. To illustrate this, Figure 4.9 shows two LEED images of a 6P monolayer on Au(111) recorded at 20 V. The two images correspond to two independently prepared 6P monolayer films that have been prepared under identical conditions at 300 K. Similar intensity variations can be found when comparing monolayer films grown at different temperatures. However, the type of pattern, which is observed, is not reproducible in all cases. Therefore it seems most plausible that slight variations in the molecular packing structure of the nP monolayer on Au(111) can occur that change the structure factor and, hence, the spot intensities in the LEED pattern. A possible reason for this could be local variations of the substrate surface defect concentration. Alternatively, the 6P molecules in the monolayer may still have got some rotational or azimuthal tilting degree of freedom within the unit cell packing structure, which leads to a kind of polymorphism of coexisting monolayer domains with slightly different surface unit cell parameters. It has been carefully checked, that the the LEED geometry (sample position, incident angle) is not responsible for the observed intensity variations of the LEED reflections.

A next step in the analysis of the nP monolayer concerns the development of a **structural model** of the molecular packing within the monolayer. Although the presented LEED data provide no information on the molecular arrangement within the surface unit cell, one can utilize additional information from XRD measurements. Those have been performed on several nm thick nP films and are described in full detail in Section 4.5.

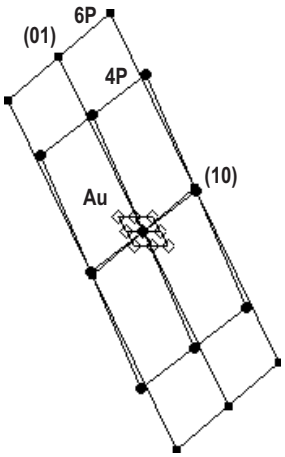

Figure 4.8: Two-dimensional surface unit cells of the 4P and 6P monolayer on Au(111).

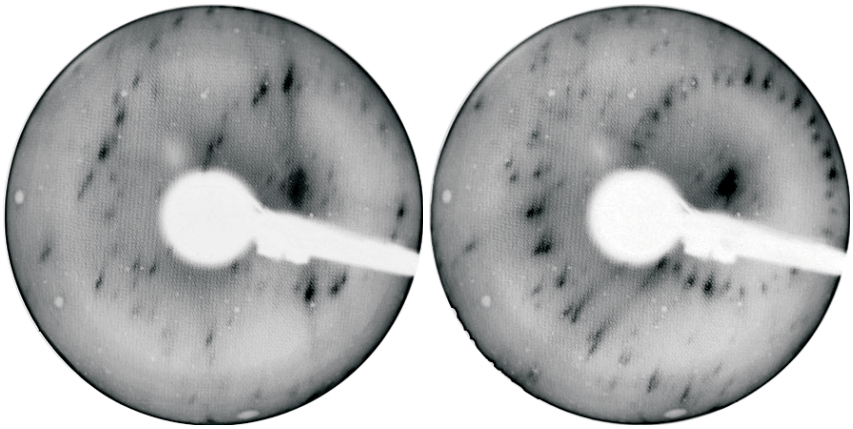

Figure 4.9: Variation of the 20 V LEED patterns of the 6P monolayer on Au(111) for two independently prepared samples at 300 K.

One important XRD result, however, is also relevant for the monolayer analysis: The nP molecules in the bulk phase exhibit a strong anisotropy in their azimuthal orientation with respect to the substrate surface. In particular, they are **aligned** with their long axes roughly parallel to the Au$\langle 1\bar{1}0\rangle$ or Au$\langle 11\bar{2}\rangle$ directions, respectively. Surprisingly, a significant difference in the molecular alignment has been observed between the 4P and 6P monolayer: Whereas the 4P molecules can align along both of the two directions, independent of the substrate temperature, in the case of 6P a temperature dependence of the alignment has been found. Around 300 K only the interazimuthal Au$\langle 11\bar{2}\rangle$ alignment has been observed, exclusively, whereas at 330 K both alignments exist.

A possible explanation for this interesting difference in the azimuthal alignment between 4P and 6P molecules can be given by considering the $(22\times\sqrt{3})$ surface reconstruction of the Au(111) surface. As shown in Figure 1.5(c) the reconstructed Au(111) surface exhibits a periodic corrugation in the z-direction normal to the surface plane. The discommensuration lines run parallel to the Au$\langle 11\bar{2}\rangle$ direction and separate parallel regions of maximum and minimum surface corrugation, i.e. a "groove-like" surface structure. Two different groove widths are observed that are roughly 1 nm and 2 nm wide - the grooves are the dark areas ("stripes") in Figure 1.5(c). Whereas the 4P molecules are short enough (about 2 nm) to align both parallel and normal to the Au$\langle 11\bar{2}\rangle$ direction within the grooves, this is not the case for 6P (V.d.W. length of about 2.9 nm). The 6P molecules simply seem to be too long to align perpendicular to the grooves below a certain threshold temperature. Instead, the the alignment parallel to the Au$\langle 11\bar{2}\rangle$ direction, i.e. parallel to the grooves, is preferred due to energetic reasons. Above a certain threshold temperature around 330 K the activation barrier for the second orientation can be surpassed.

The XRD results from both 4P and 6P clearly demonstrate that the bulk structure exhibits structural properties that are related to the substrate surface. Such a pronounced

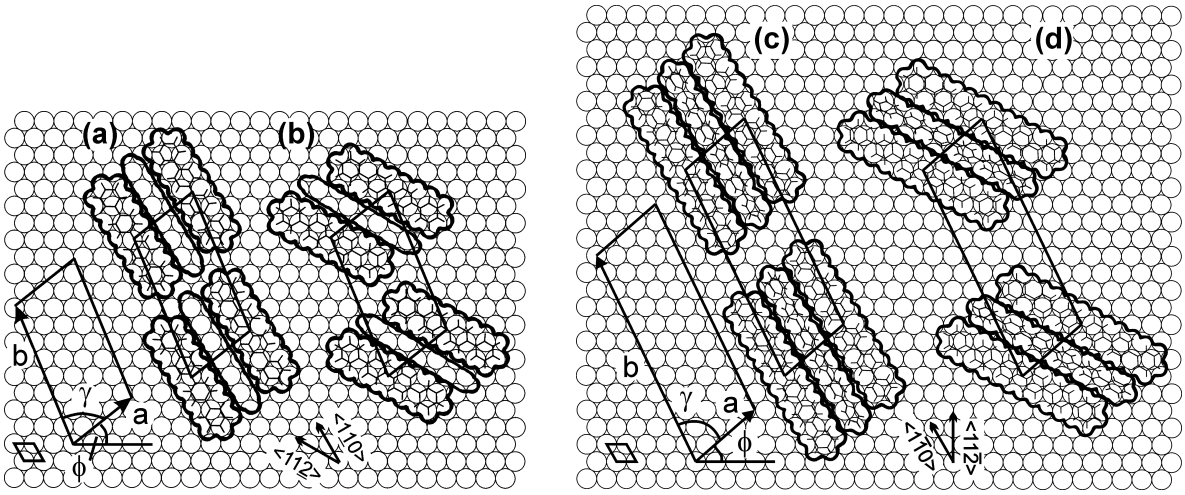

Figure 4.10: Proposed real space Van der Waals models of the 4P (left) and 6P (right) monolayer structure on Au(111). (a) + (c) The molecules are aligned along the Au$\langle 1\bar{1}0\rangle$ direction and (b) + (d) along the Au$\langle 11\bar{2}\rangle$ direction, respectively. In the case of 6P no azimuthal Au$\langle 1\bar{1}0\rangle$ alignment (c) is observed experimentally.

propagation of a surface specific property, i.e. the molecular alignment, into the bulk structure of the nP film implies that also the molecules in the first monolayer have a similar azimuthal alignment. This fact helps to refine the proposed structure models for the nP monolayer on Au(111). Together with the quantitative data gained from TDS structural models are proposed for the 4P and 6P monolayer on Au(111). Concerning the molecular alignment within the surface unit cell of the nP monolayer, the following properties are characteristic: 1) two nP molecules per unit cell, 2) azimuthal Au$\langle 1\bar{1}0\rangle$ and/or interazimuthal Au$\langle 11\bar{2}\rangle$ alignment of the molecules and 3) an **edge-face packing** of neighboring molecules, i.e. one molecule adopts a nearly flat lying conformation while the second molecule is side-tilted. This is a consequence of the spatial limitations encountered when trying to pack two lying molecules per unit cell. The tilt angle of the aromatic plane with respect to the surface cannot be derived from the data presented so far. Further details are given in Section 4.6.2. The proposed structural models for the 4P and 6P monolayer on Au(111) are shown in Figure 4.10.

The strong tendency of the 4P and 6P molecules in the monolayer to align along high-symmetry directions of the Au surface can be explained by the overlap of the delocalized π-orbitals of the organic molecules with the electron density of the Au surface. The latter reproduces the surface corrugation and therefore may induce an azimuthal anisotropy in the orientation of adsorbed molecules, i.e. a preferential molecular alignment. This is also affirmed by recent STM investigations by France et al. performed on the 6P monolayer grown on Au(111) [66], where the preferential molecular alignment is clearly visible. On the other hand, a strictly azimuthal Au$\langle 1\bar{1}0\rangle$ alignment has been observed, for instance, in the case of UHV-deposited alkanes and in particular for octatriacontane ($C_{38}H_{78}$) grown on Au(111) [113].

Table 4.2: Comparison of the nP saturates monolayer coverages determined with two independent methods.

method	4P		6P	
	10^{13} molecules/cm^2	10^{-8} g/cm^2	10^{13} molecules/cm^2	10^{-8} g/cm^2
TDS	6.6-8	3.4	5.9	4.5
LEED	8.6	4.4	5.3	4.0

Based on the geometric parameters of the regular monolayer structure determined with LEED it is possible to calculate the **saturation coverage** Θ_{sat} of the 4P and 6P monolayer on Au(111), respectively. These values are listed in Table 4.2 together with the values determined independently with TDS. Although a rather good agreement between the results from both methods can be seen, the question arises, if one method reflects the "true" nP monolayer better than the other. From an idealized point of view, the LEED results have to be favoured and therefore it is plausible to conclude that the idealized 4P monolayer structure, as shown in Figure 4.10, is about 10% compressed compared to the 6P monolayer. On the other hand, the TDS results directly reflect all kinds of deviations from the idealized picture. For instance, surface defects on the gold sample can locally cause a different packing structure of the monolayer, which does not appear in LEED if the domains are small or disordered. In particular, for 6P the second layer starts to grow already before the first layer has saturated. This non-ideal Stranski-Krastanov growth complicates an interpretation of the TD data.

4.3 Submonolayer structure

An interesting aspect of the growth of nP on a single crystalline Au(111) surface concerns the molecular arrangement at submonolayer coverages ($\Theta < 1$). For the possible build-up of a regular nP overlayer structure similar influences are decisive like in the case of the saturated monolayer. One factor, which is most important, is the surface mobility of the adsorbed nP molecules. It strongly depends on the substrate temperature (see Chapter 8) as well as on the surface defect concentration and on the presence of co-adsorbates (see Chapter 7). Only if those influences allow a high enough surface mobility of the nP molecules, can they principally arrange in a regular structure, at all. Otherwise, the molecules will arrange in a disordered manner on the substrate surface. The presence of a regular overlayer structure has been investigated in LEED experiments for the submonolayer coverage regime.

In particular, a coverage of 1/2 monolayer has been investigated, which corresponds to 0.5 times the saturation coverage of the full monolayer as determined with TDS. This coverage is also denoted as **semilayer** in the following. At room temperature, for both 4P and 6P a 1/2 monolayer thick film exhibits a distinct LEED pattern, which indicates the existence of a regular overlayer structure. It is important to note that the observed LEED images significantly differ from those found for the saturated monolayers. This indicates

Table 4.3: Geometric parameters of the regular semilayer surface unit cell of 4P and 6P on Au(111) at 300 K.

	a (nm)	b (nm)	γ (°)	ϕ (°)	matrix
4P	1.4	2.4	63	-10.5	$\begin{pmatrix} 4.4 & -0.85 \\ 8.7 & 7.5 \end{pmatrix}$
6P	1.4	3.2	74	-12	$\begin{pmatrix} 4 & -1.16 \\ 11 & 11.5 \end{pmatrix}$

that a different packing structure exists for the 1/2 monolayer compared to the saturated monolayer. Figure 4.11 shows representative LEED images that have been recorded at different beam voltages. As far as the experimental LEED images are concerned, no polymorphism has been observed, i.e. the investigated 1/2 monolayer films of both 4P and 6P exhibited unique LEED patterns. In both cases the patterns could be successfully explained in terms of a single surface unit cell. The corresponding unit cell parameters that have been gained from the pattern analysis are summarized in Table 4.3.

Similar to the saturated monolayer, also the LEED patterns of the 1/2 monolayer exhibit pronounced **intensity variations** of the reflections that depend on the beam voltage. Several reflections seem to be generally suppressed. This can be clearly seen in the derived LEED pattern representations, shown in Figure 4.12. Among the low-index reflections, in the case of 4P the intensities of the $(\bar{1}k)$ and $(1\bar{k})$, with $k > 1$, reflections have been found to lie below the detection limit. Apparently, these reflections are suppressed due to the structure factor of the 4P molecules in the unit cell. Most important, however, all of the experimentally observed spots (black dots) are well explained by the simulated pattern (grey dots). This fact corroborates the validity of the proposed unit cell.

Concerning the **molecular arrangement** within the 1/2 monolayer surface unit cell, unfortunately, no direct information could be gained from the experiments. However, some plausibility considerations can be made: First, from the TD experiments described in Section 2.1 it follows that the nP molecules adopt a **lying** configuration. A **planar** configuration is proposed with the aromatic plane parallel to the Au(111) plane. Secondly, an azimuthal alignment of the nP molecules is proposed that is similar to that found in the corresponding monolayer structure. For 4P the long molecular axes are aligned parallel to the Au$\langle 1\bar{1}0\rangle$ or Au$\langle 11\bar{2}\rangle$ direction, whereas for 6P only the molecules align only parallel to the Au$\langle 11\bar{2}\rangle$ direction, respectively. Thirdly, the characteristic length of the b side, which is about equal to the van der Waals length of the nP molecule, suggests a molecular packing, where the long axes of the nP molecules are aligned roughly parallel to the b side. These considerations allow to propose structure models of the 1/2 monolayer nP on Au(111). The proposed real space representations of the structure models are shown in Figure 4.13.

In the case of 4P the area of the real space surface unit cell is about 2.9 nm^2. Given a basis of one 4P molecule per unit cell, the semilayer film corresponds to a 4P coverage of about $3.33 \cdot 10^{13}$ molecules/cm^2 or 0.13 nm of mean film thickness. This is in good agreement with the TDS experiments, where a saturation coverage of about 0.15 nm was

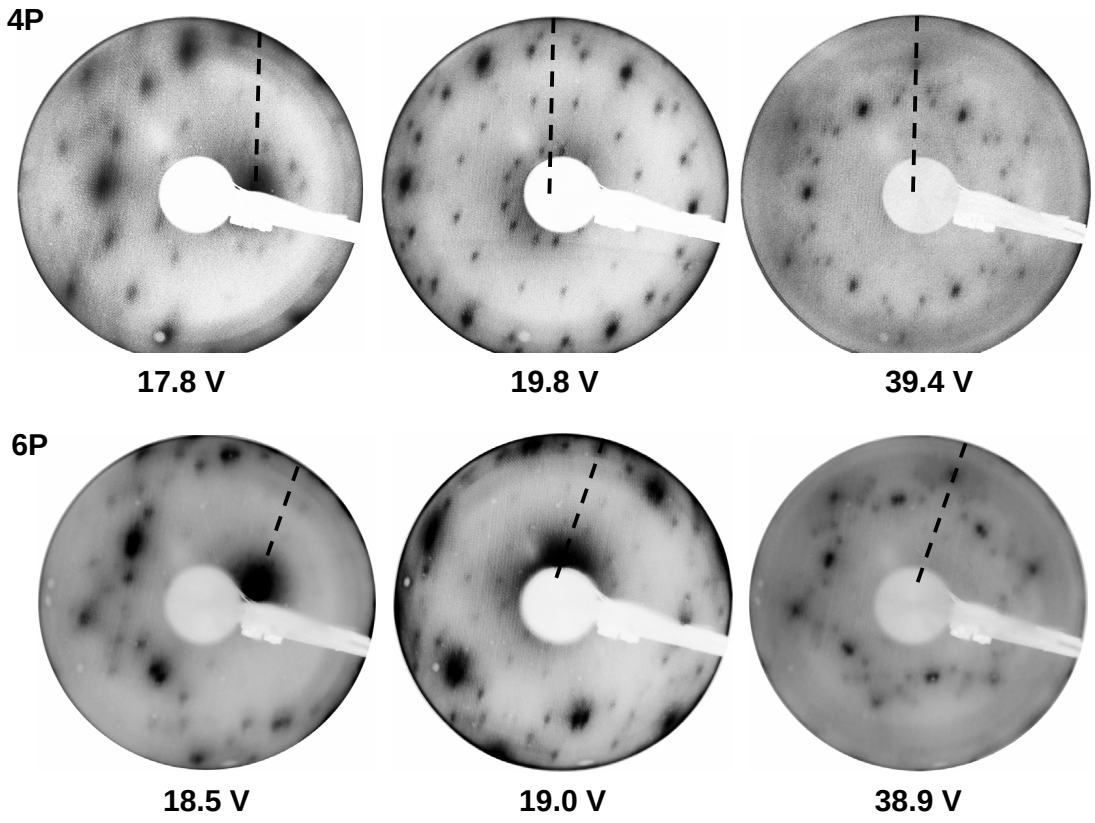

Figure 4.11: LEED images of the regular semilayer of 4P (top) and 6P (bottom) grown on Au(111) at 300 K (annealed at 400 K) and 380 K, respectively. The corresponding beam voltages are indicated together with the Au$\langle 11\bar{2} \rangle$ direction (dashed line).

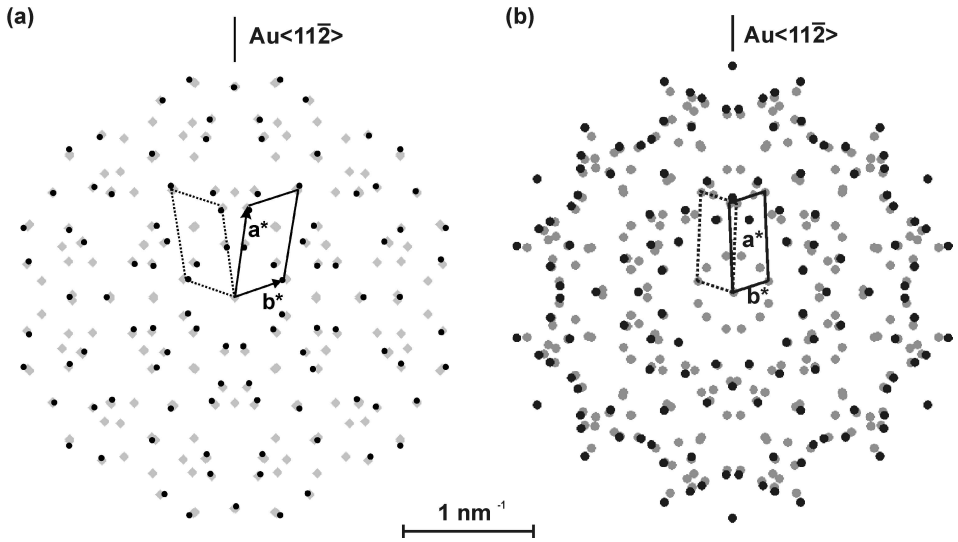

Figure 4.12: Comparison of the experimental LEED data (black dots) with simulation (grey) for the 1/2 monolayer of (a) 4P and (b) 6P on Au(111). The reciprocal unit cell is indicated by a solid parallelogram together with a mirror equivalent unit cell (dotted parallelogram). The mirror operation is performed along the Au$\langle 11\bar{2} \rangle$ direction indicated by the vertical line, according to the crystallographic symmetry of the substrate surface.

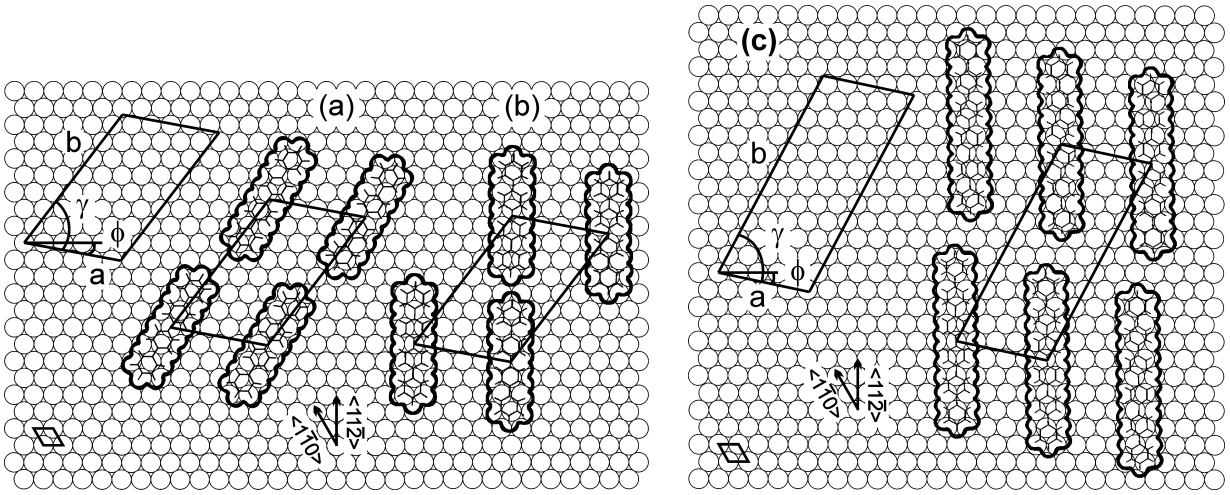

Figure 4.13: Proposed real space Van der Waals models of the (a)-(b) 4P and (c) 6P 1/2 ML on Au(111).

observed for the high-temperature adsorption state, β_1. The 6P unit cell area is 4.3 nm^2 and a value for the coverage of the saturated 1/2 monolayer of $2.33 \cdot 10^{13}$ molecules/cm^2 is obtained which corresponds to a nominal mean film thickness of about 0.14 nm. This is also in good agreement with the TD data.

Compared to the saturated nP monolayer structure, the length of the short cell vector, a, of the semilayer (1/2 ML) structure is increased by about 30% for both 4P and 6P, whereas the length of the long cell vector, b, is hardly changed. Assuming flat lying molecules within the 1/2 ML structure, as indicated by the TDS and XRD data, a molecular packing is obtained with a surprisingly **large intermolecular spacing** in the direction of a as shown in Figure 4.13. This enlargement can be interpreted as a result of **repulsive forces** acting between neighboring molecules over distances up to about 0.6 nm. The repulsive character of the interaction is affirmed by the TDS data. The large distance of about 0.6 nm suggests the existence of long-range interactions different from the intermolecular van der Waals type interactions. Presumably, nP molecules adsorbed on the Au(111) induce localized surface dipole densities due to the interaction with the metallic substrate. This could be caused by local deformations of the nP molecular backbone and in particular by a translation of the hydrogen atoms away from the Au surface [103]. This induces dipoles that cause the long range repulsion between neighboring adsorbate molecules as illustrated in Figure 4.13. Actually, similarly large intermolecular spacings in the submonolayer coverage regime have recently been observed for perylene on Au(110) [114] or Pentacene on Au(111) [115]. Apparently, in the full nP monolayer the presence of the β_2-type adsorbed molecules, i.e. the side-tilted molecules, decreases the long-range repulsion between neighboring β_1-type molecules. This is a consequence of the herringbone-like packing of the nP molecules which is already established in the first saturated monolayer. An optimized herringbone packing is finally reached in the nP bulk phase of thicker films.

It follows from the LEED results (size of the unit cell) together with the TD data (absolute coverage values) that the 1/2 monolayer nP film continuously covers the whole substrate surface, instead of forming closer packed island domains. The intermolecular repulsion between neighboring flat lying nP molecules is obviously strong enough to inhibit a clustering of the adsorbed molecules and a consequent island-like domain formation of the 1/2 monolayer film.

Instead of directly preparing the 1/2 monolayer nP films by depositing the corresponding amount of molecules, also an alternative preparation method has been used. In this case, a thicker nP film (e.g. 3 ML) has been initially prepared, which was then subject to a proper heat treatment. By **annealing** the nP film slightly above the desorption temperature of the low-temperature monolayer peak β_2, only the first semilayer β_1 stays adsorbed on the surface. Samples that have been prepared this way exhibited a very high degree of ordering compared to the conventionally prepared samples. This can be concludes from the superior quality of the observed LEED images, in particular, in very sharp LEED reflections, compared to conventionally prepared films. Beneficially, the annealing does not change the geometric properties of the film structure, i.e. the same LEED patterns are observed.

4.4 The influence of the gold surface reconstruction on the nP monolayer structure

There is an ongoing discussion wether or not the nP monolayer structure is influenced by the reconstruction. Concerning the LEED measurements presented in this work, this question cannot be answered principally. As described in Section 1.4, the $(22 \times \sqrt{3})$ reconstructed Au(111) surface exhibits periodic deviations compared to an ideal fcc (111) surface. In particular, two large scale periodicities dominate the reconstructed gold surface. One is the periodicity of the herringbone stripe domain boundaries that lie parallel to each other. This periodicity lies in the range of 12-20 nm. If the 6P monolayer structure follows this periodic pattern, however, still no extra 6P LEED reflections will be produced compared to an ideal fcc (111) substrate because of the 3-fold rotational symmetry of the stripe domains. The stripe domains are alternatingly rotated by 120° with respect to each other. A second periodicity, which proceeds normal to the $\langle 11\bar{2}\rangle$ direction, is related to the pairs of parallel discommensuration lines of the reconstructed Au(111) surface. It proceeds parallel to the Au$\langle 1\bar{1}0\rangle$ direction and is about 6.3 nm wide, which lies within the same order of magnitude as the Van der Waals dimensions of a flat lying nP molecule. So far, no indications have been observed in the experimental LEED data of nP films grown on Au(111) that can be attributed to the effect of the surface reconstruction on the nP monolayer structure. In particular, neither of the two periodicities have been observed to influence the nP LEED patterns.

On the length scale of atomic distances, there are clear deviations of the reconstructed Au surface compared to an ideal fcc (111) surface (0.02 nm corrugation and 4% in-plane

compression). However, these are approximately two orders of magnitude smaller compared to the dimensions of a flat lying nP molecule. Hence, an influence on the nP packing structure will be presumably too small to affect the LEED pattern.

Different from the LEED data, the XRD measurements presented in this work comprise some information on the effect of the surface reconstruction. In particular, it has been observed for a 30 nm thick 6P film grown on Au(111) at 300 K that the molecules are almost exclusively aligned along the Au$\langle 11\bar{2}\rangle$ direction. The alignment along the Au$\langle 1\bar{1}0\rangle$ direction obviously does not exist in this case, which is a clearly different behaviour compared to the system 4P/Au(111) that exhibits both alignments. This finding can be explained assuming that the herringbone surface reconstruction still exists after the nP film deposition, as described in Section 4.2.

Recent STM investigations performed on a 6P monolayer grown on Au(111) are in good agreement to this, as they suggest that the herringbone reconstruction is still present upon the adsorption of a 6P monolayer [66]. Similar results have been reported for pentacene on Au(111) [115]. For the system PTCDA/Au(111) it has been shown that the $(22 \times \sqrt{3})$ must be considered in order to successfully explain the monolayer structure of PTCDA [116]. For other organic molecules grown on Au(111), one can find complementary results concerning the effect of the Au surface reconstruction on the structure of the organic monolayer. However, in many cases it has been clearly observed that the herringbone reconstruction is still present upon adsorption of an organic monolayer, i.e. for pentacene [115], 1-nitronaphtalene [117]. Recently, it has been demonstrated that the Au(111) surface reconstruction can even be used as a nano-patterned surface template for the selective adsorption of organic molecules [118].

4.5 Bulk

Growing several nm thick nP films on atomically clean Au(111) can result in different film morphologies, depending on the substrate temperature, deposition rate and film thickness. In particular, also the length of the nP molecule has a significant influence on the film morphology. Figure 4.14 presents optical micrographs of different thick 4P and 6P films grown on Au(111) at a temperature between 300 K and 430 K with a deposition rate of 0.4 nm/min. The film morphology is in all cases characterised by the coexistence of a large number of distinct nP crystallites of different size and shape. In the case of 4P predominantly elongated needle-like crystallites are observed similar to the 6P needles found on mica or TiO_2 substrates [7, 119]. Interestingly, the shorter 4P molecules prefer such a needle-like island growth around 300 K (a) rather than the longer 6P molecules that exhibit a more terraces-like growth at room temperature (d). It will be discussed in full detail in Chapter 8 that the tendency of growing preferentially elongated needle-like crystallites strongly depends on the substrate temperature, as can be clearly seen in Figure 4.14(d)-(f) for a 30 nm thick 6P grown on Au(111) at 300 K, 330 K and 430 K, respectively.

Whereas these OM investigations provide only a quick qualitative overview of the film

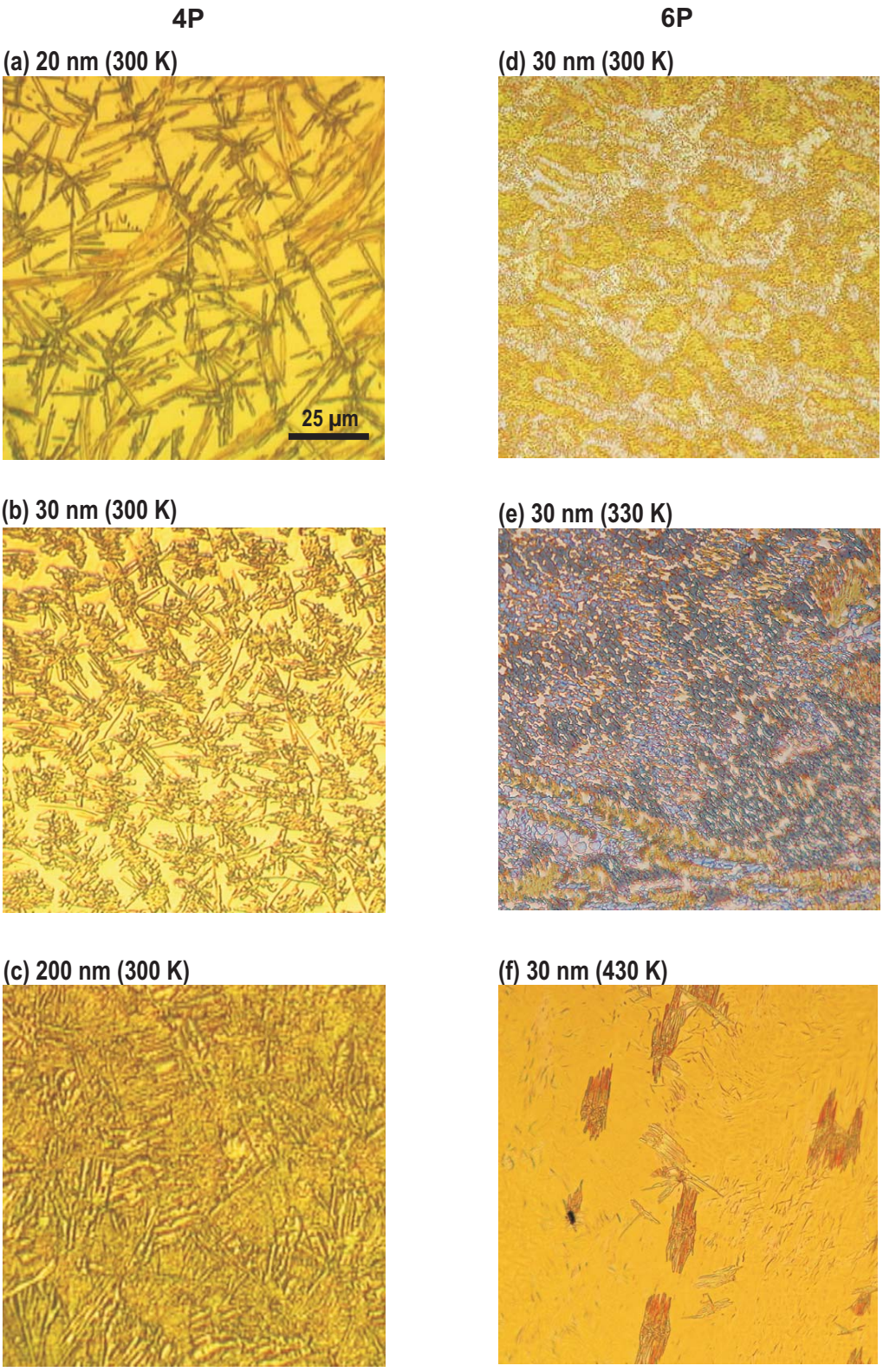

Figure 4.14: Optical micrographs showing the film morphology of different (a)-(c) 4P films and (d)-(f) 6P films grown on Au(111). The deposition rate was between 0.24 and 0.72 nm/min.

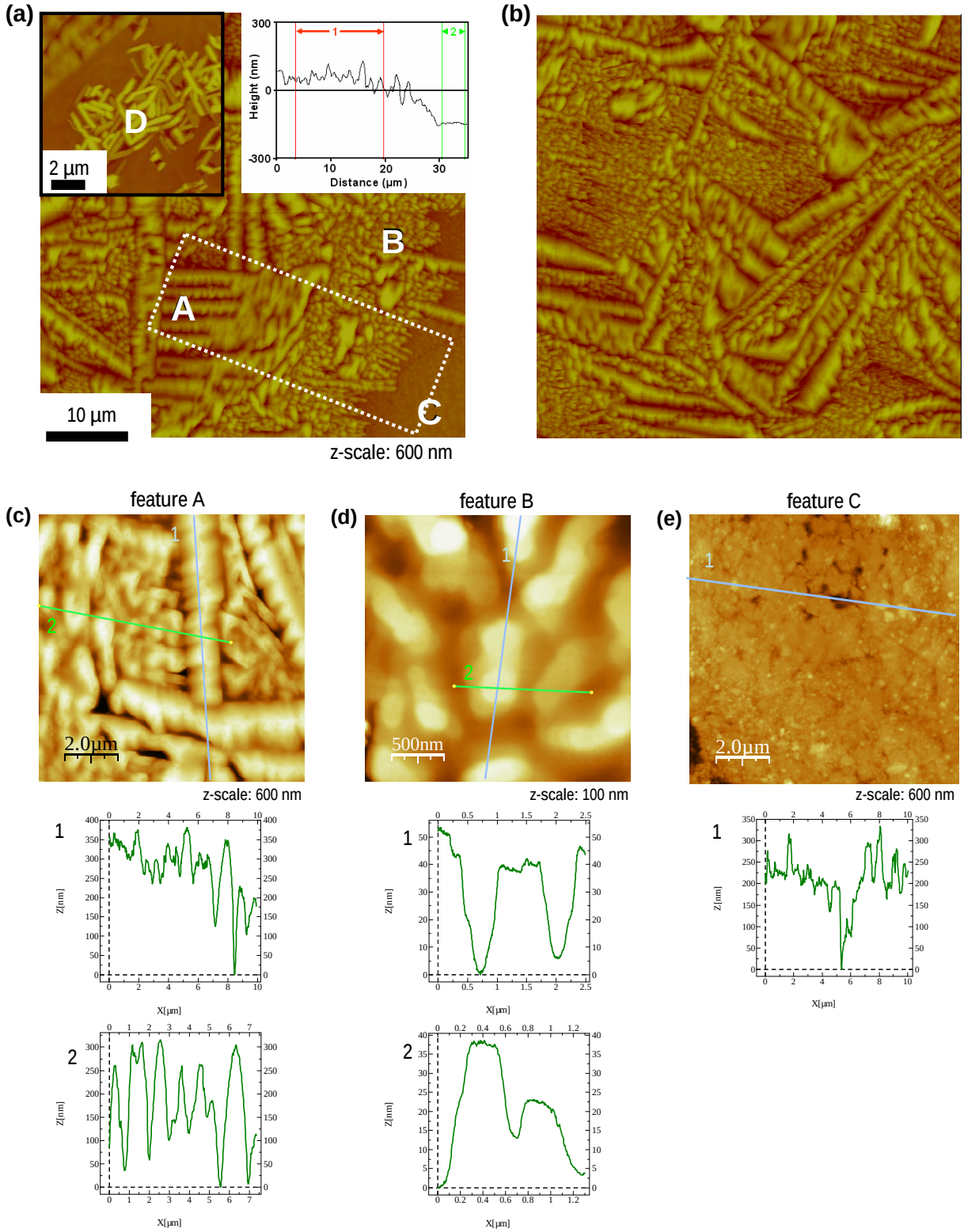

Figure 4.15: (a) and (b) 50×50 μm^2 AFM image of a 200 nm 4P film grown on Au(111) at 300 K. Four morphological features A-D are clearly discerned. The upper left inset shows a 10×10 μm^2 high resolution AFM image (z-scale is1 μm) of an additional morphological feature labelled D. The upper right inset shows an integral step height analysis over the area indicated by the dotted rectangle. (c)-(e) Detail high resolution AFM images of the structural features A-C. Below are shown the corresponding height profile line scans.

morphology, high resolution AFM measurements allow a more detailed view with nanometer resolution in all three dimensions. With AFM the most noticeable morphological properties of nP films on Au(111) that are already visible in OM have been re-affirmed. Additionally, quantitative information on the film morphology has been gained. In the case of a 200 nm 4P film on Au(111) at least four different morphological features have been observed with lateral extensions in the range of about 10 μm which coexist in close vicinity to each other. This is shown in Figure 4.15. The area denoted by A in Figure 4.15(a) consists of parallel **chains of tetragonal islands** with a base edge length of about 1 μm. Their height is between 200 and 250 nm. Within a single chain the islands are all identically oriented and the chain length can be up to several 10 μm. The segmented structure of the 4P chains could not be resolved with OM, where they appear as single elongated needle-like crystallites. At least six different chain directions could be identified relative to the substrate surface. This suggests an orientational influence of the Au(111) surface on the 4P crystal growth, i.e. the adsorbate substrate interactions are sufficiently strong to effect the packing structure of the 4P film.

The observation of a **needle-like morphology**, which has turned out to be actually chains of separate crystallites, can be ascribed to the structural properties of the first monolayer (wetting layer) together with the crystallographic properties of 4P. Since it is well-known that the energy gain for a single aromatic molecule is highest upon arranging in a herringbone packing structure, the characteristic herringbone layers of the 4P crystallites, which are also depicted in Figure 1.2(b), continue to grow preferentially in the direction along the needle axis. Of course, this implies an alignment of the long molecular axes of the 4P molecules roughly perpendicular to the needle axis. Starting the growth of 4P bulk crystallites with the same orientation as that of the molecules in the wetting layer, the herringbone layer grows preferentially in two directions, i.e. along the needle axis and perpendicular to the substrate surface. Most probably, an anisotropic sticking of the 4P molecules to already existing 4P crystallites is responsible for the characteristic needle-like morphology, which is also observed for 6P films.

Area B exhibits significantly smaller, **plate-like crystallites** (diameter <0.5 μm), which are arranged in a disordered manner. The structural features A and B can either abut against each other or they can be separated by regions labelled C that are more or less free of three-dimensional islands. The diameters of these "holes" can be >100 μm and the surface within these areas is significantly flat (rms 15 nm) compared to the features A and B. A fourth structural feature exists, which is presented with higher resolution in the inset of Figure 4.15(a). This area D exhibits a loose group of individual crystallites with a length ranging from 0.8 to 2 mm. The cross-sectional analysis revealed that these islands are almost as high (250 - 550 nm) as wide (300 - 500 nm). In other words, these individual crystallites are rods with a nearly quadratic cross section. Figure 4.15(b) presents an integral step height analysis within the area marked by a dotted rectangle in (a). With this method the height signal is averaged across a line parallel to the short side of the marked area. This integral height is plotted against the lateral distance (long side of the marked area). The difference of the mean height is calculated between the intervals marked by 1 and 2, yielding a step height of about 200 nm between the poorly covered area C

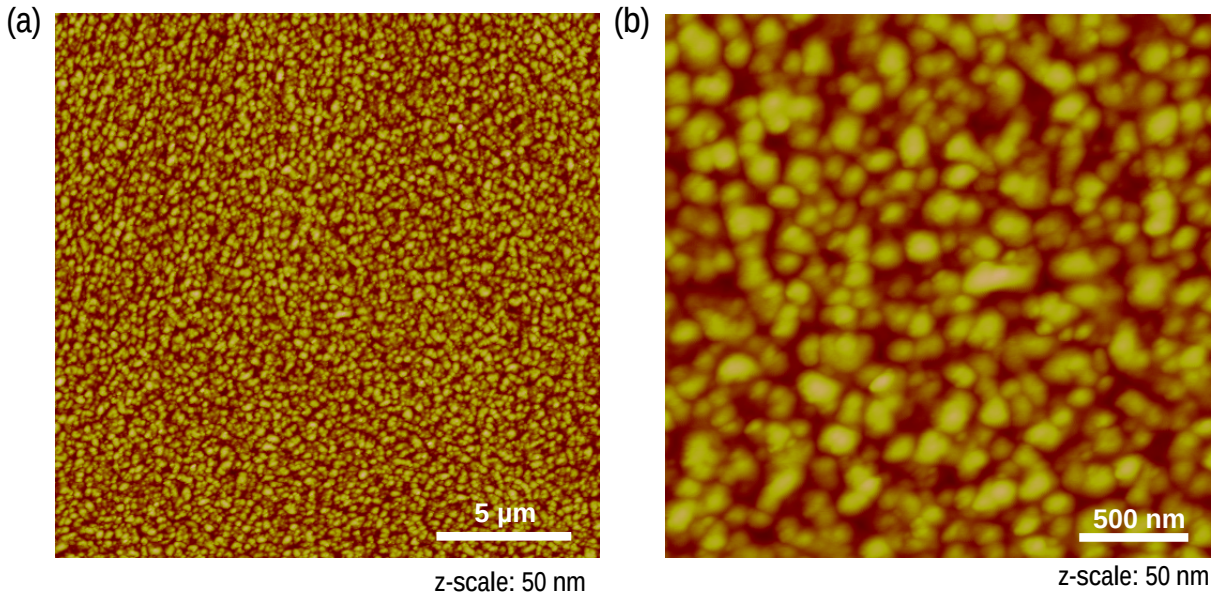

Figure 4.16: Atomic force micrographs with different magnification of a 30 nm 6P film grown on Au(111) at 300 K.

and a fully covered part of the 4P film, which is in good agreement with the nominal film thickness previously measured with the quartz microbalance.

The OM images of different thick 6P films on Au(111) presented in Figure 4.14(d)-(f) have already indicated a different morphology of 6P compared to 4P. This is corroborated by AFM measurements that reveal a fundamentally different morphology for the 6P film at 300 K. Figure 4.16 shows high resolution AFM images of a 30 nm 6P film grown on Au(111) at 300 K. The observed film morphology is best described as island-like/granular. It consists of randomly arranged columnar 6P crystallites with a nearly circular shaped base. The average diameter of the 6P crystallites is about 250 nm, while they appear only about 15-20 nm high. They are considerably smaller than the tetragonal 4P crystallites described before. The considerably small rms roughness of the 6P film of about 6 nm together with the quite uniform size distribution of the 6P crystallites is in good agreement with the fact, that the 6P film appears very homogeneous and layer-like in the OM. Unfortunately, it has not been able to resolve monomolecular terraces (step height) on a single 6P grain. Thus, no information on the molecular orientation (lying or standing molecules) could be derived from AFM. However, the XRD measurements described below clearly indicate a lying orientation of the 6P molecules, i.e. a $(21\bar{3})$ crystal orientation.

Interestingly, both 4P and 6P films comprise lying molecules when grown on Au(111) at 300 K, but the film morphologies are completely different. This finding can be explained by the different **interaction energies** (adsorption/desorption energies) of the 4P and 6P molecules, respectively. Those aspects are discussed later in full detail in Section 4.5.1. At present, it is important only to notice that in the case of 4P the adsorption temperature of

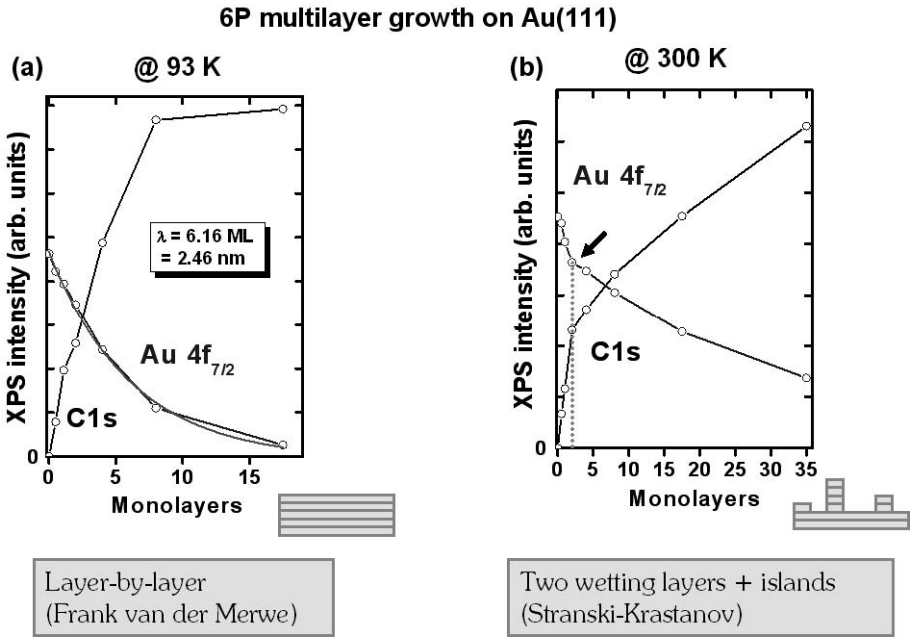

Figure 4.17: Thickness dependence of the substrate Au $4f_{7/2}$ and 6P C 1s signal for 6P films grown on Au(111) at (a) 93 K and (b) 300 K. The arrow marks the kink in the Au $4f_{7/2}$ signal at a coverage of 2 monolayers.

300 K means already growth conditions near the "equilibrium". The multilayer desorption of 4P starts around 310 K as shown in Figure 4.1. In contrast to that, growth near the equilibrium occurs roughly 100 K higher in the case of 6P due to the stronger adsorbate substrate interaction of 6P compared to 4P. As shown in Figure 4.14(e), an increase of the adsorption temperature to 330 K leads also for 6P to a more needle-like film morphology. Further details on the effect of the adsorption temperature on the film morphology are discussed in Chapter 8.

There has been an ongoing discussion whether or not the sample area between the clearly visible three-dimensional nP crystallites, as observed in the AFM images, are still covered by an organic film that is thicker than the monomolecular wetting layer. Most recently, it could be shown by Wöll et al. [120] in combined SEM/STM experiments on 4P films grown on Au(poly) that the sample area between the crystallite islands indeed exhibits a significant 4P coverage that is presumably several ten monolayers thick.

Figure 4.17(a) shows the change of the C 1s and Au $4f_{7/2}$ XPS signal intensities as a function of the mean film thickness of 6P grown on Au(111) for a sample temperature of 93 K. One observes an increase of the C 1s signal and an exponential decrease of the underlying Au $4f_{7/2}$ substrate signal. This is a clear evidence for a continuous layer-like growth mode (**Frank van der Merwe**) of 6P at 93 K. From an exponential fit to the decreasing Au $4f_{7/2}$ signal the mean free path of the Au $4f_{7/2}$ photoelectrons with energy $E_{kin} \approx 1170$ eV) in 6P can be determined to $\lambda = 2.5 \pm 0.3$ nm. This is similar to the

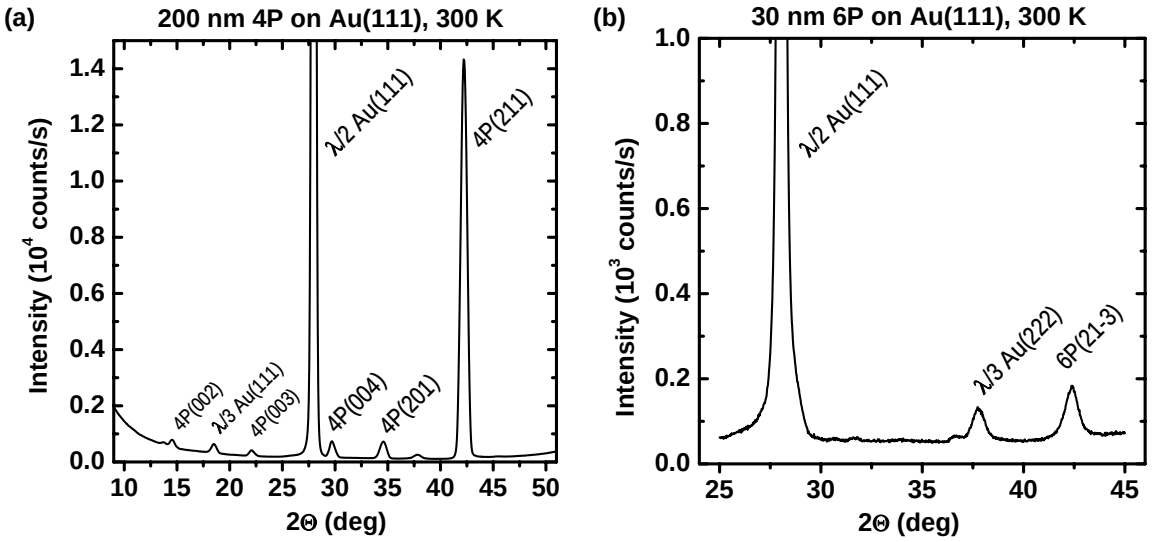

Figure 4.18: XRD specular $\Theta/2\Theta$ scans of (a) a 200 nm 4P film and (b) a 30 nm 6P film grown on Au(111) at 300 K. The scans were recorded for $CrK_{\alpha 1,2}$ radiation.

value of $\lambda = 2.4 \pm 0.3\ nm$ determined in the case of 4P. An important observation in Figure 4.17(a) is, that already at a mean thickness of about 7 nm or roughly 17 ML the Au $4f_{7/2}$ signal of the underlying substrate is completely suppressed.[3]

A quite different type of growth mode is obtained when the same experiment is carried out on a sample hold at 300 K as shown in Figure 4.17(b). After a relatively fast initial decrease at low coverage, caused by the formation of the first and second monolayer, the curve of the Au $4f_{7/2}$ signal exhibits a distinct kink. The further decrease levels off and the signal decreases rather slowly after that point. Even at a mean thickness of about 14 nm (35 monolayers), about 30% of the Au $4f_{7/2}$ signal is still retained. This suggests that the 6P multilayer bulk phase grows in form of rather high, yet narrow islands, exposing large areas of the gold surface that are not covered by 3D islands even at a rather large film thickness. Therefore, at room temperature the growth mode is clearly of the **Stranski Krastanov** type. In the case of 4P similar types of grown mode have been observed.

Unfortunately, it was impossible with AFM to discern the existence of a monomolecular 4P wetting layer in those areas between the 3-dimensional crystallites. Thus, the experimental TDS data remain the only proof of a 4P wetting layer on Au(111). Although the film morphology at room temperature is typically characterized by a large number of distinct nP crystallites of different size and shape, a remarkably **high crystallinity** of the nP crystallites together with a clear epitaxial relationship between the Au(111) surface and the crystallographic orientation of the nP crystallites could be observed. A proof for the high crystallinity of the nP films grown on Au(111) is provided by the XRD $\Theta/2\Theta$ scans presented in Figure 4.18. In the case of 4P (a), a sharp peak is observed at a 2Θ

[3]This fact has been used in combined XPS and TDS experiments to investigate the temperature dependent film morphology, see Chapter 8.

Table 4.4: Distribution of crystal orientations in a 200 nm 4P film grown on Au(111) at room temperature. The reflectivities of the different net planes have been considered in terms of the structure factor $F(hkl)$. The values of F have been calculated with the PowderCell software package using the 4P crystal structure data from [43]. They are given relative to the (211) orientation.

net plane	relative $F(hkl)$	ratio
(211)	1	62%
(311)	0.4	31%
(004)	0.5	5%
(201)	1.4	2%

angle of 42.22°, which is characteristic of the 4P(211) net plane spacing of the well-known crystallographic 4P bulk structure. The theoretical value of the 4P(211) net plane spacing is 3.175 $\AA$, which corresponds to a 2Θ angle of 42.268°. This demonstrates the good agreement between the experimental data and theory. Accordingly, one dominant crystal orientation exists where the 4P crystallites are oriented with the 4P(211) plane parallel to the Au(111) surface plane [96]. The 4P(211) is a cleavage plane that exhibits a molecular packing of flat lying, alternatingly side-tilted, planar 4P molecules. This packing motif is illustrated in Figure 1.3. Besides the dominant (211) orientation three additional crystal orientations have been observed, i.e. the 4P(311), 4P(201) and 4P(001). The (311) orientation does not show up in the presented $\Theta/2\Theta$ scan, because its peak lies beyond the presented angular regime (57.658°). It exhibits a molecular packing very similar to that of (211). The relative proportion between the (211) and (311) orientation was determined on the basis of the observed pole densities in the pole Figure measurements that are discussed below: (211) was found twice as much as (311). Both the (201) and (001) orientations appear as very small peaks in the $\Theta/2\Theta$ scan. Due to the fact that each crystal plane has different reflectivity factors, the peak intensities from the $\Theta/2\Theta$ scans cannot be directly used for a quantification of the different orientations. However, in a first approximation the structure factors $F(hkl)$ of the net planes (hkl) can be used to extract from the peak intensities quantitative information on the distribution of the crystal orientations. The corresponding numbers are listed in Table 4.4. Both (201) and (001) amount only for a few percent of the overall crystal film. They may be attributed to the existence of a small fraction of surface inhomogeneities on the Au(111) crystal surface, like high-index microfacets. This seems plausible insofar, as the Au crystal exhibits a slightly curved macroscopic surface, in particular, near to the circular border area, which is well-known and caused by the preparation procedure (crystal polishing). Both (201) and (001) correspond to a significantly different molecular packing compared to (211), as illustrated in Figure 1.3.

For 6P the $\Theta/2\Theta$ scan presented in Figure 4.18(b) reveals a similar situation compared to 4P. However, only one crystal orientation is observed. A single sharp peak is found in the $\Theta/2\Theta$ scan at 42.37°. The corresponding 6P cleavage plane is the 6P($21\bar{3}$). The packing motif of the 6P($21\bar{3}$) orientation is very similar to that of the 4P(211) plane, as illustrated in Figure 1.3. This is in good agreement with the TD and LEED data of 4P and 6P that

also exhibit similar qualitative features (cf. Section 4.2). Due to the smaller film thickness of the investigated 6P film (30 nm) compared to the 4P film the signal-to-noise ratio of the 6P $\Theta/2\Theta$ scans was poorer. This may account for the lack of additional peaks in the 6P $\Theta/2\Theta$ scan which would indicate that also for 6P a small fraction of the crystallites exhibits a different orientation.

Besides the high degree of order found in both 4P and 6P films and besides the fact that one dominant orientation exists of the nP crystallites relative to the Au(111) plane, another important structural feature has been found. The latter has been observed in **XRD pole figure** measurements performed on both the 4P and 6P films described above. In all pole figures distinct separated areas of enhanced pole density have been observed that are symmetrically arranged annular around the center. This is a clear indication of the existence of a preferential **azimuthal alignment** of the nP crystallites relative to some high symmetry direction(s) of the Au(111) surface. Pole figures have been recorded at different 2Θ angles that correspond to certain *hkl* Bragg reflections of 4P and 6P, respectively. The results are shown for the 200 nm 4P film on Au(111) in Figure 4.19 and for the 30 nm 6P film on Au(111) in Figure 4.20. The indexation process of the pole figures yields the azimuthal alignment of the nP crystallites with respect to certain directions of the Au(111) surface [96]. Together with the crystal orientations determined in the $\Theta/2\Theta$ scans this yields the full **epitaxial relationship**, i.e. the crystallographic information about the net plane (*hkl*) parallel to the substrate surface and its azimuthal alignment.

The distinct azimuthal alignment of the nP crystallites observed in the pole figures clearly indicates a strong tendency of the nP molecules in the bulk phase to align with their long molecular axes parallel to certain preferential directions of the Au(111) surface. In the case of 4P the **molecules** prefer to align with their long molecular axes **parallel to the Au**$\langle 1\bar{1}0\rangle$ **or Au**$\langle 11\bar{2}\rangle$ directions, which are both high-symmetry directions of the fcc(111) surface. Different from that, for 6P films grown at 300 K the molecules align about 3° off the Au$\langle 11\bar{2}\rangle$ direction and, remarkably, no azimuthal $\langle 1\bar{1}0\rangle$ orientation exists. A possible explanation has been given above in Section 4.2. Increasing the adsorption temperature of the 6P films up to 330 K the 6P crystallites grow still in the $(21\bar{3})$ orientation. However, both azimuthal and interazimuthal alignments can be found in such films. Moreover, in this case the molecules are exactly aligned along the Au$\langle 1\bar{1}0\rangle$ and Au$\langle 11\bar{2}\rangle$ direction, i.e. no 3° deviation is observed any more. This finding can be interpreted in terms of a different surface mobility of the 6P molecules at different adsorption temperatures (cf. Chapter 8). A summary of the experimentally observed crystal orientations of 4P and 6P bulk films grown on Au(111) is presented in Table 4.5.

Figure 4.21 shows graphic illustrations of the 4P and 6P bulk crystal orientations on the Au(111) surface. It can be clearly seen that the crystal packing structures that are adopted in the bulk phase are similar for 4P and 6P. The same holds true for a comparison of the nP bulk crystal orientations and the corresponding nP monolayer structures on the Au(111) surface as depicted in Section 4.2. Therefore, it is reasonable to consider the nP monolayer as a structural pre-stage for the bulk structure.

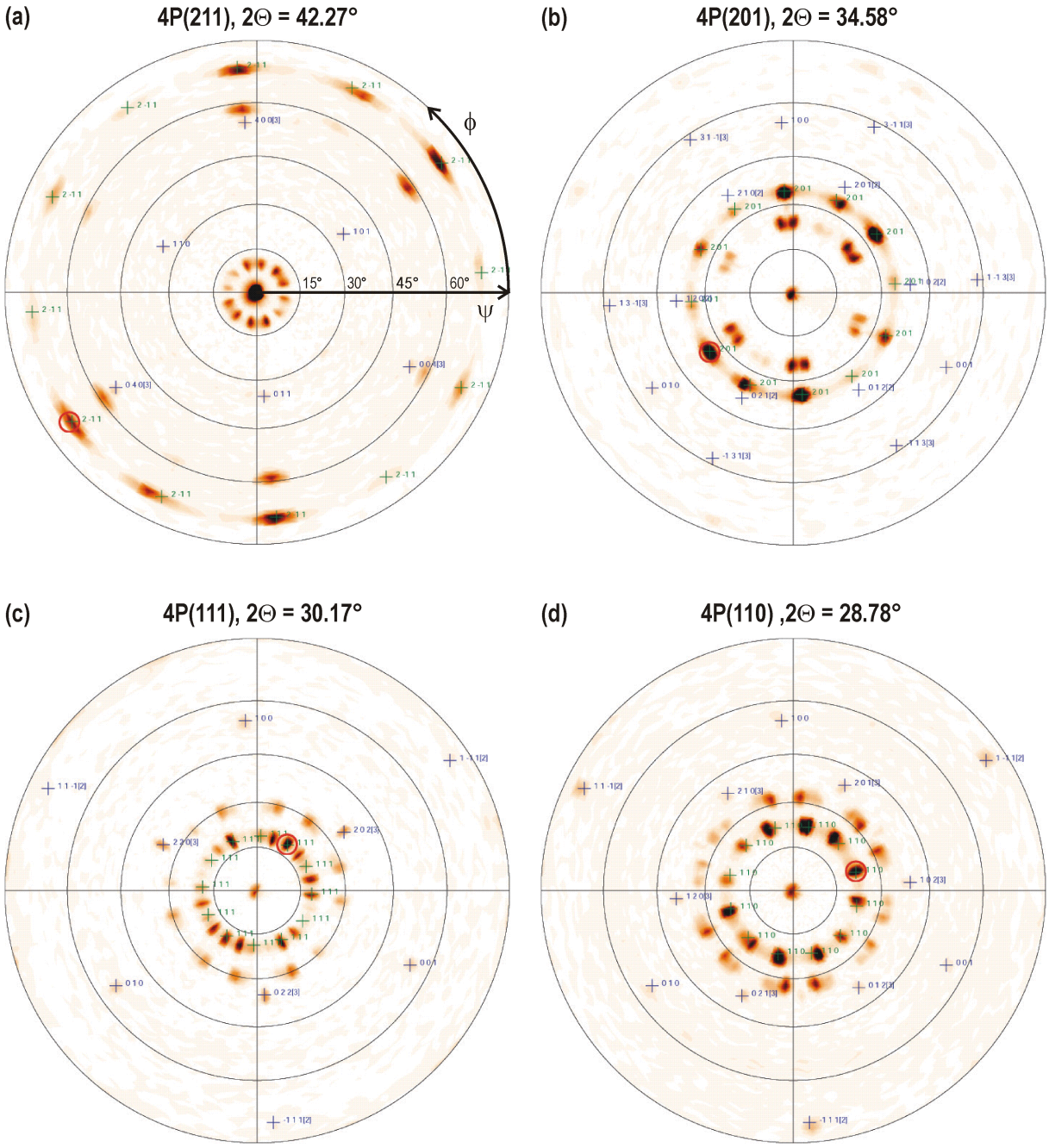

Figure 4.19: Pole figures of 200 nm 4P on Au(111) taken at different 2Θ angles (a)-(d). Pole densities that correspond to the 4P(211) orientation are indexed and labelled in green (blue: Au peaks). The non-labelled poles correspond to a second crystal orientation, i.e. 4P(311). ϕ and ψ denote the rotation angles.

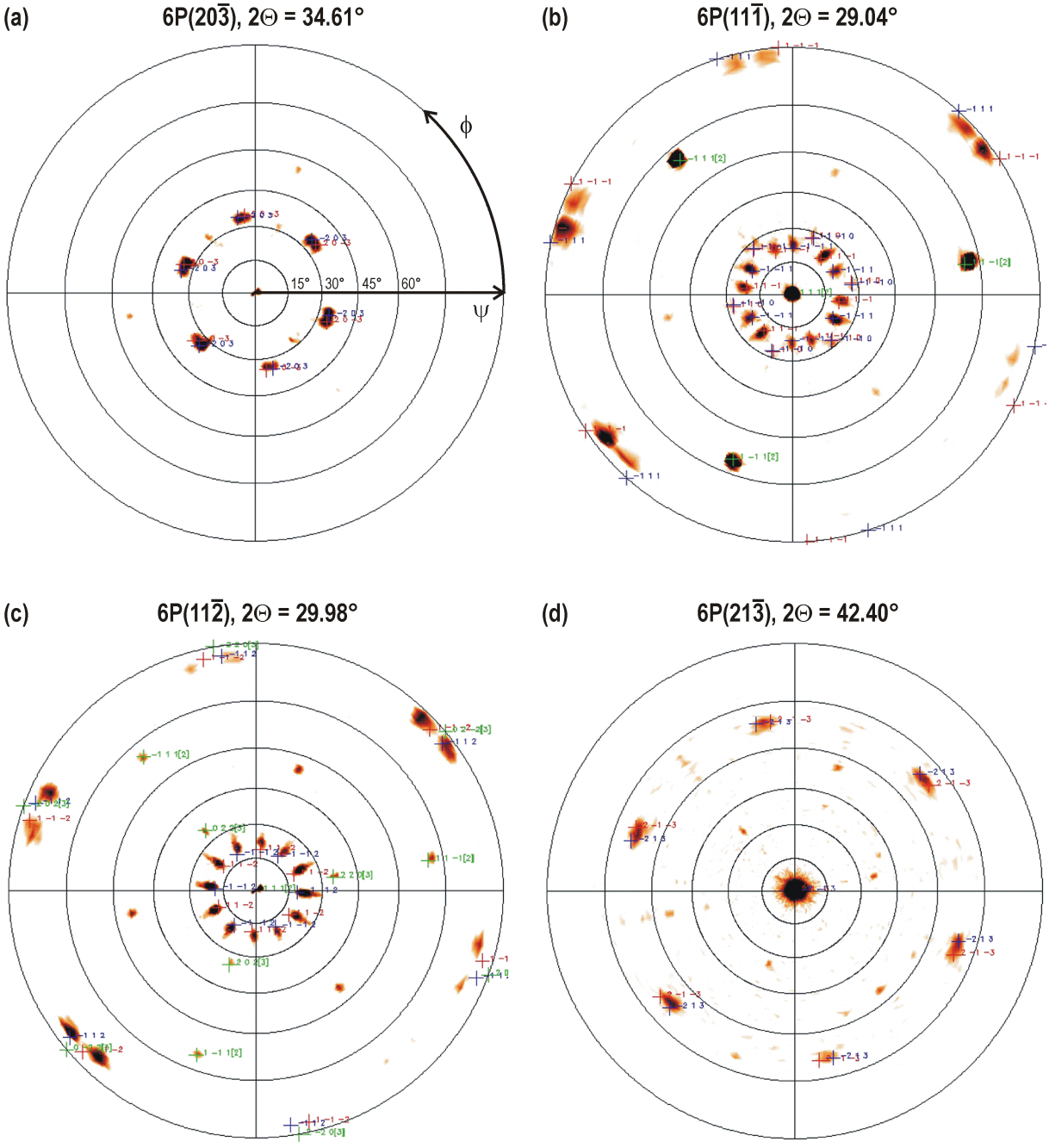

Figure 4.20: Pole figures of 30 nm 6P on Au(111) taken at different 2Θ angles (a)-(d). Pole densities that correspond to the 6P(21$\bar{3}$) and 6P($\bar{2}$1$\bar{3}$) orientation are indexed and labelled in red and blue, respectively. Au peaks are labelled in green. ϕ and ψ denote the rotation angles.

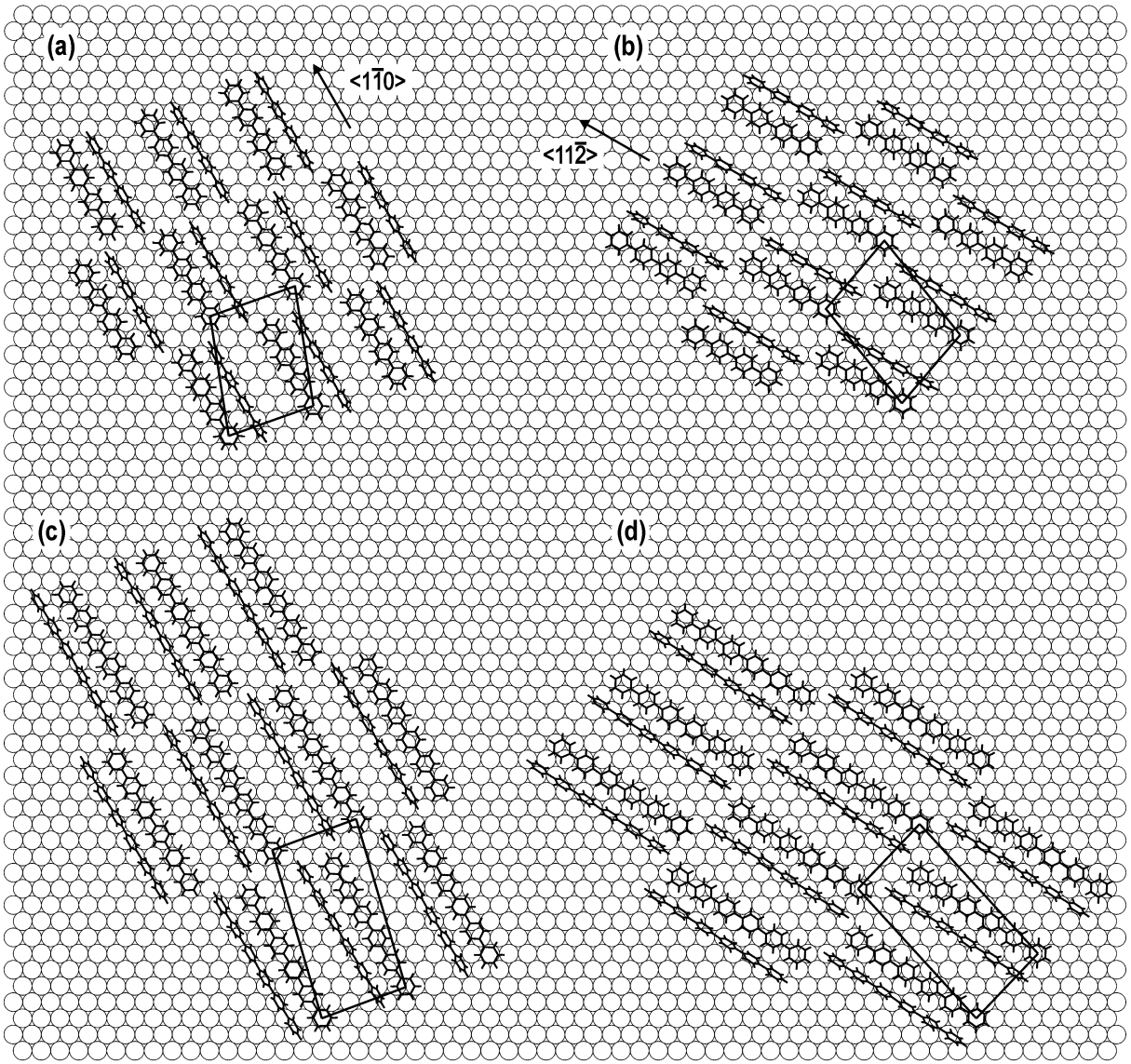

Figure 4.21: Real space representation of the 4P and 6P bulk crystal orientations relative to the Au(111) surface. (a) The 4P(211) orientation with the molecules aligned parallel to the azimuthal or Au$\langle 1\bar{1}0\rangle$ direction. (b) 4P(211) orientation with an alignment parallel to the inter-azimuthal or Au$\langle 11\bar{2}\rangle$ direction. (c) The 6P(21$\bar{3}$) orientation with azimuthal alignment. (d) The 6P(21$\bar{3}$) orientation with a molecular alignment 3° off the inter-azimuthal direction.

Table 4.5: Compilation of the bulk crystal orientations of 4P and 6P on Au(111). The azimuthal orientation denotes the alignment of the long molecular axes of the nP molecules relative to a direction on the Au surface. T_{ads} denotes temperature during film growth.

molecule	T_{ads}	net plane ∥ to Au(111)	azimuthal orientation
4P	300 K	(211), (311)	Au$\langle 1\bar{1}0\rangle$, Au$\langle 11\bar{2}\rangle$
6P	300 K	(21$\bar{3}$)	Au$\langle 11\bar{2}\rangle$ - 3°
6P	330 K	(21$\bar{3}$)	Au$\langle 1\bar{1}0\rangle$, Au$\langle 11\bar{2}\rangle$

Note, that for each of the four crystal orientations (a)-(d) illustrated in Figure 4.21 there exist additional symmetrically equivalent crystal orientations that are not shown in the figure for the sake of clarity. This follows from symmetry considerations as follows: In addition to a net plane (hkl) that characterizes a given crystal orientation also the plane $(\bar{h}\bar{k}\bar{l})$ has to be considered, which doubles the number of possible crystallographic orientations. Moreover, it has been found that, in particular, for the 4P films the number of possible orientations is doubled for a second time, because two symmetrically equivalent alignments existed that have been labelled α and β. The reason for these additional symmetrically equivalent orientations can be best described by a simple thought experiment: The structure of a given orientation, e.g. the 4P(211) starts to grow initially with a single flat lying molecule that is aligned properly on the plain Au(111) surface. A specific crystal orientation is uniquely defined not before a second molecule has condensed next to the first one. The second molecule has, in general, four possibilities to align next to the first molecule. Those can be described as "top left" position, "top right", "bottom left" and "bottom right" with respect to the first molecule. From symmetry considerations it follows further that two of those possibilities correspond to the α and β alignments and the remaining two possibilities correspond to the $\pm(hkl)$ plane orientation, as described above (see also [96]).

The two experimental findings, i.e. 1) the preferential orientation of certain cleavage planes together with 2) the azimuthal alignment of the molecules, are clear indications for the strong influence of the Au(111) substrate surface electronic structure on the crystal growth of nP. Although the Au(111) surface exhibits no pronounced geometric anisotropy, different from a typical one-dimensional structure observed, for instance, on an fcc (110) surface, it indeed has a strong pre-patterning effect on both the nP monolayer AND the multilayer. Such a behaviour is typical for systems where the adsorbate-substrate interactions and the intermolecular interactions are evenly balanced. In this sense, the system nP/Au(111) can be attributed to the second category of the phenomenological categorization that was introduced in Section 1.3.

In analogy to the **LEED experiments** on the monolayer also thicker nP films have been investigated with the same method. In the case of 4P/Au(111), no distinct LEED reflections have been observed that could be attributed to a three-dimensional regular structure of the 4P crystallites in any of the performed experiments. Two coverage regimes could be distinguished: Firstly, films that are thicker than about several 10 nm exhibit no LEED reflections at all. This has been observed, for instance, for a 30 nm 4P film grown

on Au(111). And secondly, several ML thick 4P films exhibit LEED patterns, however, the observed patterns are identical to those of the 4P monolayer on Au(111). For instance, the original monolayer LEED pattern is still visible at coverages up to about 4 ML. A further increase of the film thickness then causes the reflections to become significantly broader and more diffuse and finally to disappear at coverages higher than about 10-30 nm. Keeping in mind the Stranski-Krastanov growth mode of 4P on Au(111), It seem reasonable that between the 3D islands there is still a large area of the sample surface that exposes only the plain 4P wetting layer. Hence, elastic electron scattering at these areas causes the well-known LEED pattern of the monolayer structure. If the film gets thicker, the area between the islands decreases, too, which causes the monolayer pattern to diminish. On the other hand, the absence of a distinct multilayer LEED pattern for thick 4P films is surprising. In the case of several nm thick 6P films, regular LEED patterns have been observed. Figure 8.1 presents some images recorded for a 10.4 nm thick 6P film grown on Au(111) at 380 K. However, in this case a temperature dependence of the LEED images has been found that is described in full detail in Section 8.2. As will be shown there, the adsorption temperature strongly effects the 6P film morphology on Au(111). Only above the threshold temperature for a structural transition from lying to standing upright molecules at high adsorption temperatures a new LEED pattern has been observed, whereas at lower temperatures the observed pattern is similar to that of the monolayer. Hence, it seem plausible to attribute the question, whether or not a distinct nP multilayer LEED pattern is visible, to the nP film morphology. Obviously, the latter can only be observed for very smooth terrace-like multilayer films, as it is the case with upright standing molecules.

4.5.1 Bulk desorption kinetics

Apart from the structural properties discussed so far we have also investigated the **desorption kinetics** of nP bulk films grown on Au(111) with TDS experiments. In particular, up to 7 nm thick films of 4P and 6P have been grown with a deposition rate of about 0.4 nm/min on atomically clean Au(111). The substrate temperature has been varied between 93 K and 300(380) K for 4P(6P), respectively. However, for both 4P and 6P no significant temperature dependence of the multilayer TD data has been observed. Therefore, only two representative TD series are presented in the following, i.e. 4P grown at 93 K and 6P grown at 300 K. The corresponding TD spectra are shown in Figure 4.22. A single sharp desorption peak labelled α is observed for both 4P and 6P, which can be attributed to zero-order desorption from the nP multilayer. According to the increased bonding of 6P compared to 4P, which is caused by the larger number of phenyl rings in 6P, the multilayer desorption of 6P starts at a temperature which is roughly 100 K higher compared to 4P. A similar temperature difference has also been observed for the monolayer desorption peaks of 4P and 6P, as described in Section 4.1. This shows the good agreement of the TD data for different coverage regimes.

From the experimental data shown in Figure 4.22 the **multilayer desorption energy** E_{des} for nP on Au(111) has been extracted with the help of the leading-edge method. The values for 4P and 6P are

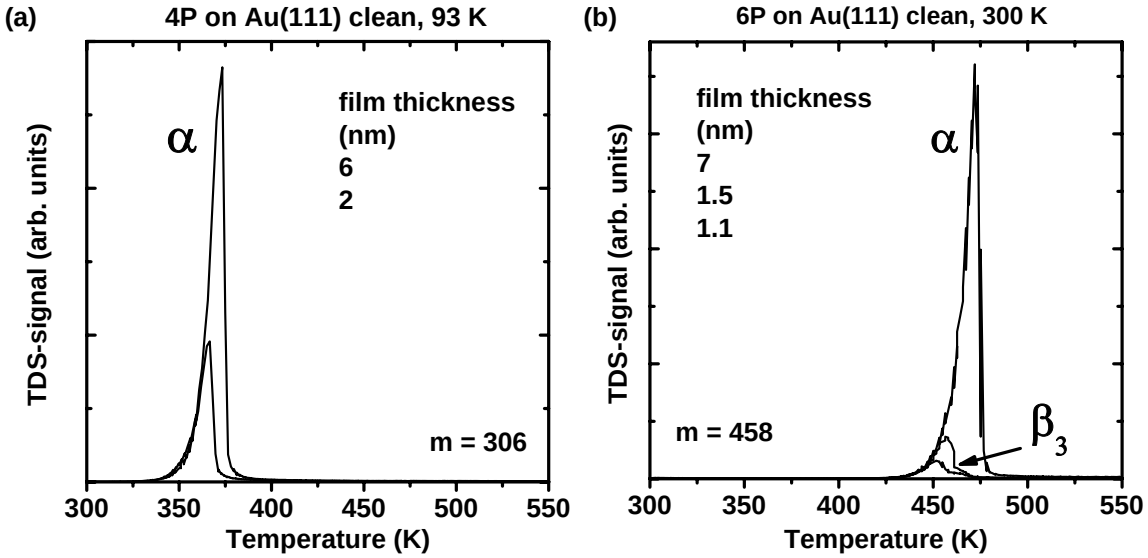

Figure 4.22: Thermal desorption spectroscopy series of the multilayer regime of (a) 4P and (b) 6P grown on Au(111).

$$\text{4P: } E_{des} = 1.52 \text{ eV/molecule (150 kJ/mol)}$$
$$\text{6P: } E_{des} = 2.40 \text{ eV/molecule (223 kJ/mol)}$$

The value of E_{des} for 4P is in rather good agreement to the value for the 4P sublimation enthalpy of 1.62 eV/molecule given in the literature [46]. For 6P, however, to our best knowledge there is only one value of $E_{des} = 1.38$ eV/molecule (136 kJ/mol) published in the literature by France et al. [66], which deviates significantly from our experimental value. A thorough study of the cited publication yields, though, that the analysis of the reported TD data has to be strongly questioned.

For a zero-order desorption the determination of the **pre-exponential factor** ν from equation 2.3 is possible if the TD spectra can be quantified, as described in Appendix B. Then, the ordinate axis intercept of the linear fit in the Arrhenius plot equals the logarithmic of the pre-exponential factor $ln(\nu)$. This is shown in Figure 4.23(a) for a 7 nm thick 6P film and in 4.23(b) for a 6 nm thick 4P film on Au(111). The values for the axis intercept can be derived from Figure 4.23 to 80.8 for 4P and 90.9 for 6P. From the axis intercept the pre-exponential factor ν can be easily calculated and the corresponding values are:

$$\begin{aligned} 4P: \ \nu &= 1.23 \cdot 10^{35} \\ 6P: \ \nu &= 3.00 \cdot 10^{39} \end{aligned}$$

Note, that the dimension of ν is $molecules/(cm^2 s)$. In order to get the so-called frequency factor, ν_0, that has a dimension of $1/s$, one has to consider also the coverage Θ_0 of the nP bulk surface:

$$R_{des} = \nu e^{-\frac{E_{des}}{kT}} = \nu_0 \Theta_0 e^{-\frac{E_{des}}{kT}} \tag{4.5}$$

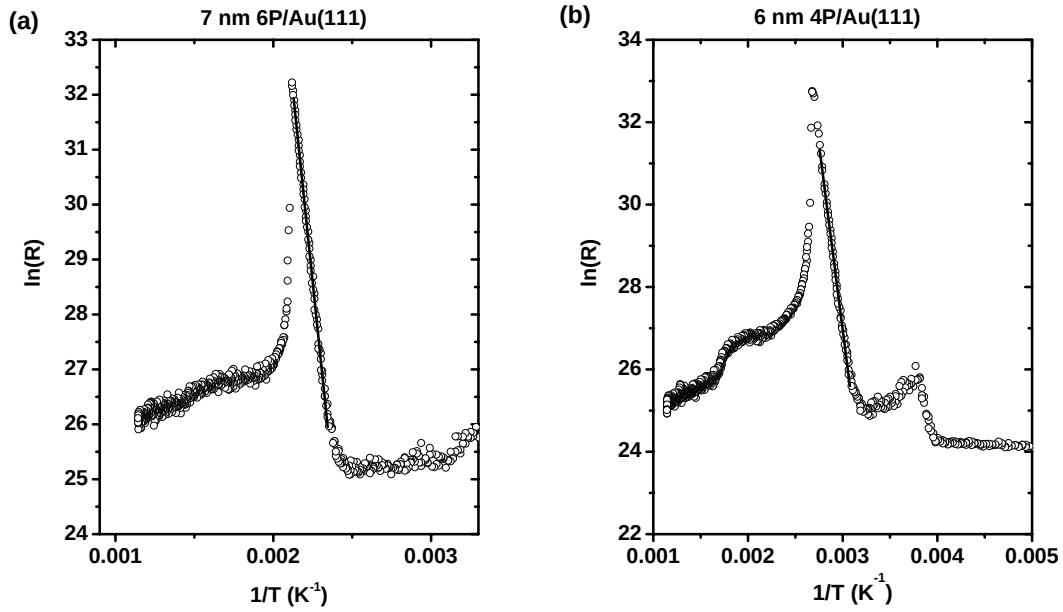

Figure 4.23: Arrhenius plot for (a) 4P and (b) 6P multilayer desorption from Au(111). Linear fits $ln(R) = A + B \cdot T^{-1}$ are indicated by straight lines. The corresponding fit parameters are for (a) $A = 80.8,\ B = -17959$ and for (b) $A = 90.9,\ B = -27717$, respectively.

The absolute value of Θ_0 can be determined from the well-known nP bulk crystal structure. Based on the XRD results for 4P and 6P bulk films on Au(111) it can be presumed that Θ_0 equals the mean surface density of nP molecules within the particular nP crystal plane that lies parallel to the substrate surface. The latter have been determined with XRD to be the 4P(211) and 6P($21\bar{3}$) plane, respectively. The corresponding surface unit cells have an area of 2.6 nm^2 (4P) and 3.7 nm^2 (6P), respectively, and comprise two nP molecules. This yields the values for the coverage Θ_0 of the 4P(211) plane $7.7 \cdot 10^{13}\ molecules/(cm^2 s)$ and for the 6P($21\bar{3}$) plane to $5.4 \cdot 10^{13}\ molecules/(cm^2 s)$. Accordingly, one calculates the values of the frequency factor $\nu_0 = \frac{\nu}{\Theta_0}$ of the zero-order multilayer desorption of 4P and 6P to:

$$4P: \quad \nu_0 = 1.6 \cdot 10^{21}\ s^{-1} \tag{4.6}$$

$$6P: \quad \nu_0 = 5.6 \cdot 10^{25}\ s^{-1} \tag{4.7}$$

This is significantly larger than the frequency factor of 10^{13} commonly assumed for the thermal desorption of small molecules (e.g. H_2, CO, etc.) from surfaces. However, it is in good agreement to recent theoretical and experimental considerations on the frequency factors of large organic molecules adsorbed on surfaces [83, 84, 121], as described in Section 2.1.

4.6 Molecular conformation upon adsorption on metal surfaces

During the last years great effort has been made on understanding the processes that determine the interactions at the organic/metal interface. In particular, it has been shown that the organic molecules can be subject to a change of their molecular conformation that is caused by the interaction with the metal surface upon adsorption. In general, this changes the effective conjugation (π-electron overlap) of the organic molecules that are in direct contact to the metal surface as opposed to those located in the bulk. Consequently, a modified energy level alignment at the interface and, hence, a modified charge injection barrier can be found [42]. Such surface-induced conformational changes of the organic molecules can occur even in the case of rather weak adsorbate-substrate interactions, i.e. in the case of physisorption.

An important question that is still under discussion within the community concerns the interring-tilt angle α between neighbouring benzene rings within the nP molecules adsorbed on solid surfaces, e.g. on Au(111). It is well-known that the nP molecules in the gas phase exhibit an alternating interring twisting (cf. Section 1.2). For instance, 4P in the gas phase at room temperature shows a twist angle of 22.7° between neighbouring inner rings and 17.2° between inner and outer rings, respectively. For the condensed bulk phase, however, it has been reported that the nP molecules adopt a planarized conformation [43]. Recently, it has been proposed, though, that this is true only in the time average, i.e. at room temperature the nP molecules in the bulk still exhibit significant librational motion, resulting in an interring twisting and therefore angles between neighbouring benzene ring planes different from zero. In general, larger interring twist angles lead to smaller conjugation (inter-benzene π-electron overlap) along the 6P molecule and consequently to a shift of energy levels and a larger energy gap.

Recently, it has been shown in high resolution STM measurements that a single 6P molecule adsorbed on a Ag(111) surface still shows an interring twist angle of 11.4° [122]. Obviously, the interaction with the Ag substrate forces the 6P molecule into a more coplanar conformation with increased π-electron overlap compared to the bulk phase. However, still a considerable interring twist angle exits for the adsorbed 6P molecule. This is remarkable also because the interaction between the 6P molecule and the Ag surface can be considered rather weak, i.e. no covalent or chemisorptive bonding has been observed experimentally [42] [4]. For 6P on oxygen passivated Ni(110)(2x1)-O, however, it has been reported that a large fraction of 6P molecules adopts a conformation close to coplanar when adsorbed on the surface. Only in some cases also an interring twisting in the adsorbed molecules could be observed [44].

[4] A chemisorptive bonding implies (significant) differential changes of the electronic orbitals, which can be probed, for instance, with UPS.

4.6.1 LEED simulation and structure factor

The presumption of a coplanar molecular conformation upon adsorption on the Au surface can be tested by performing LEED pattern simulations that consider not only the unit cell geometry, but also the crystallographic basis, i.e. the molecular orientation within the unit cell AND the molecular conformation. A common approach for such simulations is based on the structure factor. The simulations have been performed with the *LEEDSim* software.[5] This way also the intensities of the LEED reflections can be simulated and compared with the experimental data.

The starting point for the test is the experimental finding that certain *hk* reflections are suppressed independent of the beam voltage. This has been already discussed in the previous sections. In particular, the system 0.5 ML 4P/Au(111) has been investigated. Using the experimentally determined unit cell parameters together with a basis of two nP molecules (one aligned flat at (0,0) and one side-tilted at (1/2,0)) several simulations have been performed. Figure 4.24 shows three simulated LEED patterns for different molecular alignments within the surface unit cell. For each case is shown both the structural model and the corresponding LEED pattern below. The azimuthal tilt angle of the 4P molecules has been adjusted either parallel to the Au$\langle 1\bar{1}0\rangle$ or Au$\langle 11\bar{2}\rangle$ direction, respectively. Unfortunately, it has turned out that the intensities of the experimental LEED reflections could not be properly explained by the simulations by any of the three simulated patterns. For a comparison with the experimental LEED data please refer to Figure 4.11. In particular, the experimental finding that certain reflections are constantly suppressed independent of the beam voltage (between about 15 V and 40 V) could not be corroborated by the simulation. Figure 4.25 shows the simulated intensity values of selected low index reflections depending on the azimuthal tilt angle of the 4P molecules. It can be clearly seen that also in this simulation no preferential azimuthal angle of alignment for the 4P molecules can be derived.

The generally poor agreement of the simulated results with the experimental data lead to the conclusion that the structural model used for the simulations has to be modified substantially. Most probably, the structure factor that has been used under the presumption of truly coplanar nP molecules is responsible for the significant disagreement of the above simulations with the experiment. As will be shown in the next section, the idea of truly coplanar adsorbed 4P molecules has to be reconsidered.

[5] Demo version 1.3.6

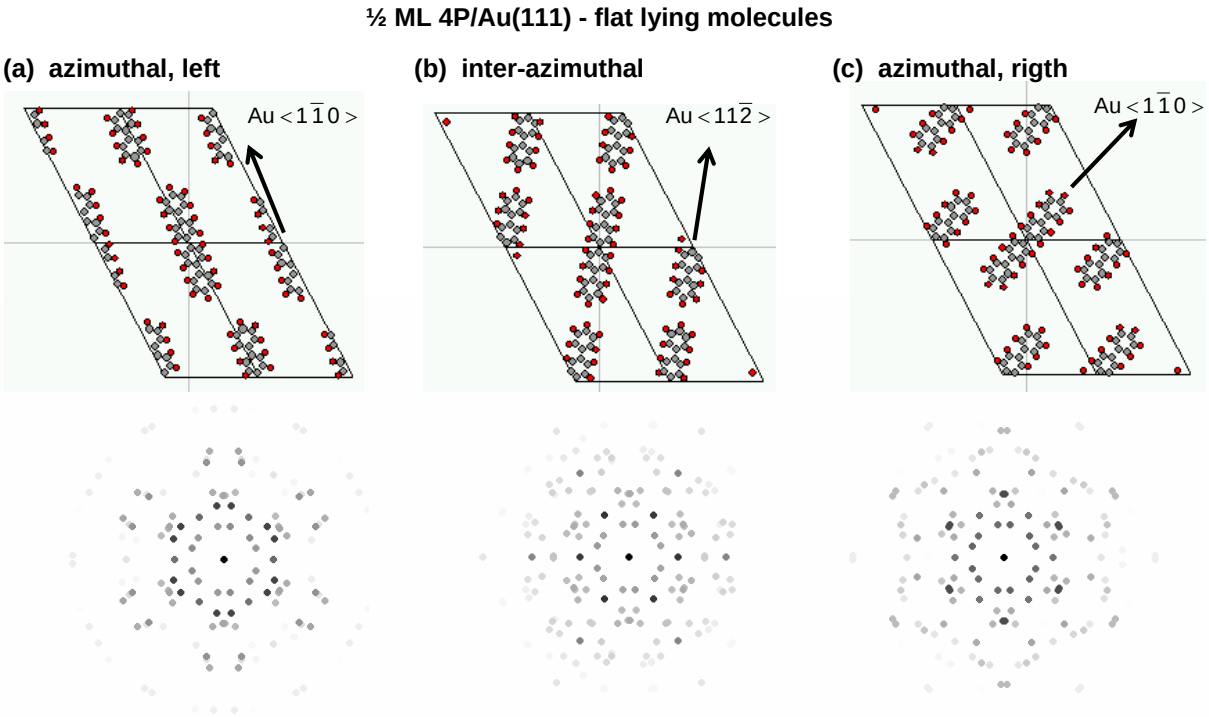

Figure 4.24: Simulated LEED patterns for the 4P semilayer on Au(111) for different azimuthal alignments of the molecules.

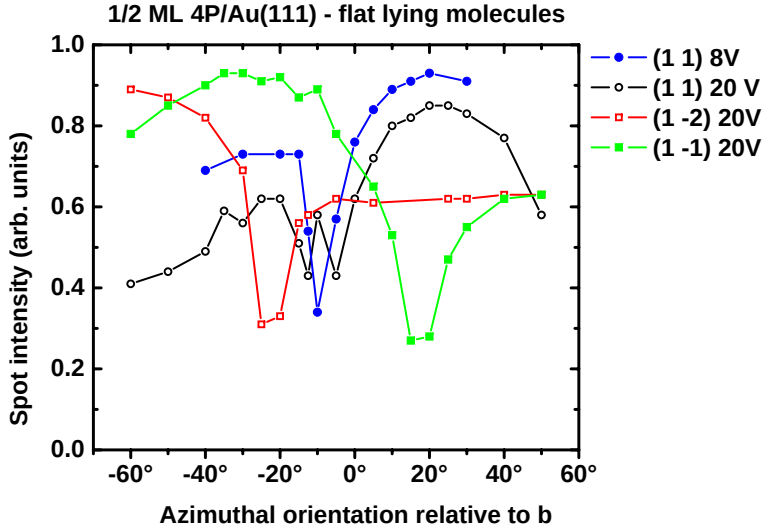

Figure 4.25: Relative intensities of selected LEED reflections of the simulated 4P semilayer LEED pattern for different azimuthal orientations of the molecules.

4.6.2 NEXAFS measurements

Concerning the molecular conformation of the nP molecules within the first and second semilayer on Au(111), NEXAFS measurements have been performed at the BESSY synchrotron facility. Two important questions should be answered: 1) Are the nP molecules adsorbed coplanar, or is there still an interring-twisting present? And 2) can the structural model for the nP semilayer and saturated monolayer that is proposed in Section 4.2 be affirmed (edge-face packing of flat and side-tilted molecules)?.

4P and 6P films have been grown on Au(111) and Au(110) around room temperature. The film thickness ranges between 0.15 nm and 30 nm, respectively. In particular, three characteristic thickness regimes have been investigated: 1/2 monolayer, monolayer and bulk, according to the corresponding (saturation) coverages observed in TDS. Hence, the corresponding films have been prepared with nominal film thicknesses determined in the TD experiments, i.e. the 1/2 monolayer is 0.15 nm for 4P and 0.2 nm for 6P. The full monolayer film is 0.3 nm for 4P and 0.4 nm for 6P, respectively. The bulk films have been prepared with thicknesses > several nm.

The first important aspect concerns the orientation of the nP molecules within the **first semilayer** on Au(111), respectively. There has been an ongoing discussion whether or not the nP molecules adopt a planar flat lying conformation upon adsorption on the Au(111) surface or some intramolecular twisting or tilting is still present comparable to the inter-ring twisting observed in the gas phase. For adsorbed flat lying nP molecules that exhibit a truly coplanar conformation a vanishing π^* resonance in the 90° curve should be expected. However, this assumption is not fully corroborated by the experiment, because the corresponding π^* peaks are strongly decreased, but not fully suppressed, as shown in the following. Figure 4.26(a)-(b) presents the NEXAFS spectra of 4P and 6P semilayer and monolayer grown on Au(111) around 300 K. Compared to the monolayer spectra, the semilayer spectra exhibit a π^* absorption in the 90° scan that is significantly suppressed with respect to the 30° curves. This indicates that the nP molecules are rather adsorbed in a flat manner, i.e. the aromatic plane being roughly parallel to the substrate surface, instead of being aligned almost perpendicular to it. This aspect of the proposed structural model of the first nP semilayer presented in Section 4.2 is corroborated. However, the non-vanishing π^* resonance in the 90° scans indicates that there exists still a small component of the π^* transition dipole momentum, which is parallel to the surface plane. A possible explanation is that the adsorbed nP molecules still exhibit a small **interring twisting**. On the other hand, there exists also an alternative explanation for the non-vanishing π^* resonance at 90°, which does not rely on an interring twisting. Due to surface defects (steps, vacancies, adatoms) or microfacets the surface of the Au(111) single crystal is not ideally planar. Hence, a small fraction of nP molecules may adsorb in a not truly coplanar conformation with respect to the macroscopic surface plane.

A careful orientation analysis of the NEXAFS data, which is based on the calculation of the π^* intensity values for different incident angles θ, however, shows a rather poor agreement between experiment and calculation [101]. This can be seen in Figure 4.27, where the experimental intensity values, which are represented as open triangles ($\triangle$), are

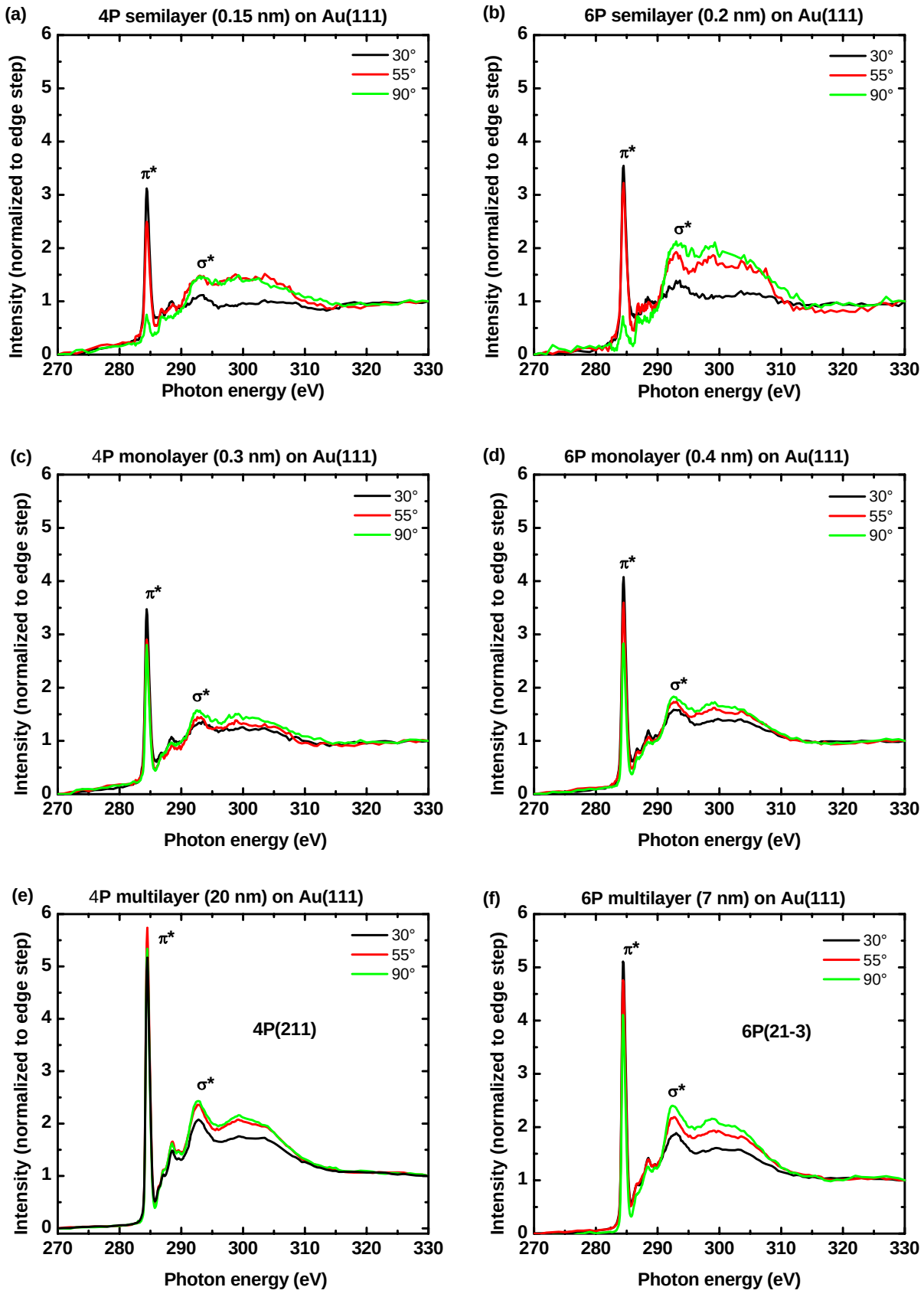

Figure 4.26: NEXAFS spectra of 4P and 6P on Au(111) at 300 K. (a)-(b) semilayer, (c)-(d) monolayer and (e)-(f) multilayer regime.

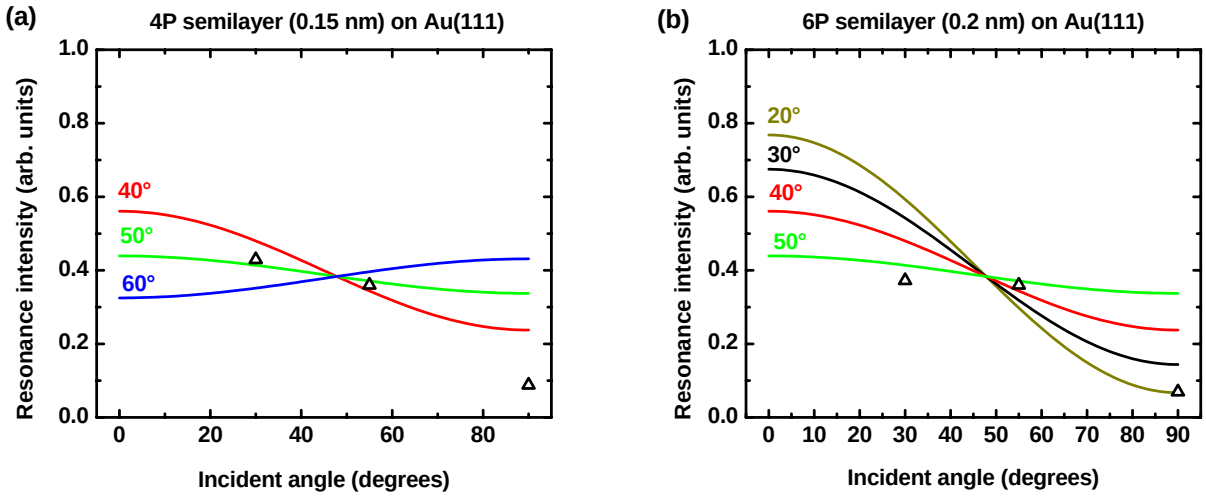

Figure 4.27: NEXAFS orientation plots for (a) 4P and (b) 6P semilayer films on Au(111). The open triangles (△) represent the experimental π^* intensities and the solid curves are the theoretically calculated ones.

compared to the calculated curves (solid lines). Obviously, the experimental data deviate considerably from the theoretical values, which may be partially explained by an interring-twisting, which has not been considered in the theoretical calculations, at all. Hence, it is impossible to determine the values of the mean molecular tilt angle with a high accuracy. However, considering the results of recent STM experiments conducted on 6P grown on Ag(111) surfaces [122] as described earlier, it seems plausible to suggest a maximum tilt angle of about $\alpha = 10 \pm 10°$ for the nP molecules within the first semilayer.

Increasing the coverage up to a fully **saturated nP monolayer** yields the NEXAFS spectra presented in Figure 4.26(c)-(d). Different from the situation in the first semilayer, the π^* resonance of the 90° scan is strongly developed in this case. An orientation analysis like the one described before has been conducted based on the theoretical framework described in [101]. However, in this case two separate types of differently oriented nP molecules with tilt angles α_1 and α_2 have to be considered in the theoretical calculation of the orientation curves because of the proposed edge-face packing structure of the nP monolayer described in Section 4.2. The π^* resonance intensity is given by:

$$I = C \cdot [P \cdot I^{\parallel} + (1 - P) I^{\perp}] \tag{4.8}$$

where C is an instrument specific constant, P is the degree of polarization of the incident x-rays[6] and $I^{\parallel}$ and $I^{\perp}$ are intensity components parallel and normal to the sample surface. The latter are given by [101]:

$$I^{\parallel} = \frac{A}{3}[1 + \frac{1}{2}(3 \cdot cos^2\theta - 1)(3 \cdot cos^2\alpha - 1)] \tag{4.9}$$

[6]For the BESSY II synchrotron facility, a value of P=0.85 is reported, while the ideal value would be P=1.

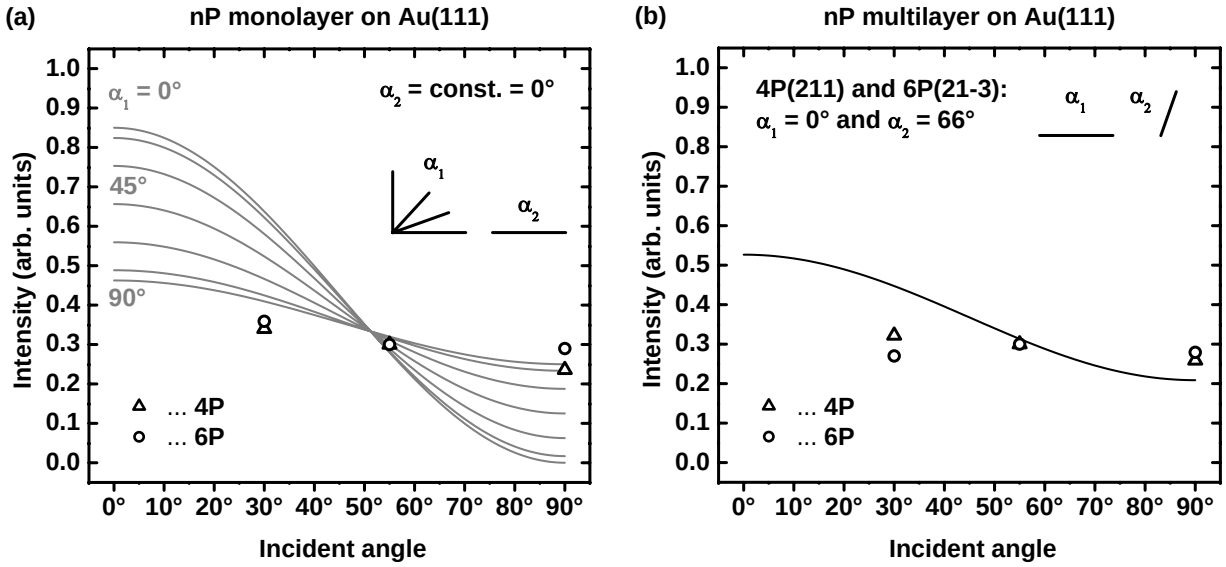

Figure 4.28: NEXAFS orientation plots (a) for the 4P and 6P monolayer films on Au(111). The open symbols represent the experimental π^* intensities and the solid curves are the theoretically calculated ones considering two differently oriented molecules. The tilt angles are labelled α_1 and α_2, respectively.

$$I^{\perp} = \frac{1}{2} A \cdot sin^2\alpha \tag{4.10}$$

for a single type of planar aromatic species on a three-fold symmetric substrate. In order to consider two coexisting species of differently oriented molecules with tilt angles α_1 and α_2 the intensities $I^{\parallel}$ and $I^{\perp}$ can be re-written as the sums over two independent intensities that correspond to the two different types of molecules:

$$I^{\parallel} = \frac{1}{2} \cdot I_1^{\parallel}(\theta, \alpha_1) + \frac{1}{2} \cdot I_2^{\parallel}(\theta, \alpha_2) \tag{4.11}$$

$$I^{\perp} = \frac{1}{2} \cdot I_1^{\perp}(\theta, \alpha_1) + \frac{1}{2} \cdot I_2^{\perp}(\theta, \alpha_2) \tag{4.12}$$

This has been the basis for the simulations presented in the following. Figure 4.28(a) shows the comparison of the calculation (grey lines) with the experimental data (symbols) for both 4P (△) and 6P (◯) monolayer NEXAFS data. The simulated curves are shown for different combinations of one variably side tilted molecule ($\alpha_1 = 0° \ldots 90°$ in steps of 15°) and one fixed flat lying molecule ($\alpha_2 = 0$), respectively. Obviously, the agreement between calculation and experiment is quite poor again and no exact determination of the side tilt angle is possible. Comparing the experimental data of the nP semilayer with those of the nP monolayer clearly shows a significant difference: The 90° intensity values are considerably higher for the monolayer spectra. Assuming for the saturated monolayer structure that the molecular conformation (interring-tilt angle) of the molecules in the first semilayer is maintained similar to that of the plain semilayer this clearly indicates

that the molecules in the second semilayer exhibit a net side tilt angle $> 0°$ compared to the first semilayer, which is in good agreement to the proposed edge-face packing scenario comprising flat and side-tilted molecules.

The NEXAFS spectra of the **nP multilayer** presented in Figure 4.26(e)-(f) are qualitatively very similar to that of the saturated monolayer shown in (c)-(d). For the nP multilayer, however, the molecular orientation has been accurately determined with XRD and an edge-face packing structure could be affirmed hereby. For both 4P(211) and 6P($21\bar{3}$) crystal orientations a side tilt angle of 66° can be found [123]. The simulated orientation curve for the well-known 4P(211) and 6P($21\bar{3}$) crystal planes, i.e. $\alpha_1 = 0$ and $\alpha_2 = 66$, is shown in Figure 4.28(b) (solid curve). Although the agreement between calculation and experiment is again quite poor, the experimental data corroborate the above interpretations, i.e. the experimental NEXAFS results agree well with the proposed structural models for the nP semilayer and monolayer on Au(111) as presented in Section 4.2 and 4.3. In particular, they corroborate the proposed edge-face packing structure of flat (first semilayer) and side-tilted molecules (second semilayer). Compared to the structural representations shown in Figure 4.10, however, one important amendment has to be considered additionally: Both types of molecules of the edge-face packing structure that have been labelled "flat lying" and "side-tilted", respectively, may exhibit an intermolecular interring twisting and the molecular conformation is not necessarily truly coplanar.

4.7 From monolayer to bulk structure

It has been shown in the last sections that the system nP/Au(111) exhibits different molecular packing structures for the semilayer, monolayer and multilayer or bulk, respectively. This can be easily seen by comparing the corresponding surface unit cells. A compilation of these data for 4P and 6P is given in Table A.2. Such behaviour has been reported in the literature for many different organic semiconducting oligomers grown on regular solid substrates and it can be concluded that a **structural transition** takes place between the initial semi- or monolayer packing structure and the bulk crystal structure, respectively.

As shown in Section 4.5, both 4P and 6P exhibit certain bulk crystal orientations with respect to the Au(111) surface in several ten nm thick multilayer films, where the original bulk crystal structure already predominates. Comparing the regular 2D structures within those bulk crystal planes parallel to the substrate surface to the 2D monolayer structures, as listed in Table A.2, demonstrates that particularly for the transition from the semilayer to the saturated monolayer an **enhanced packing density** is obtained for both 4P and 6P. The driving force for this structural compression is most probably the build-up of a herringbone-like edge-face packing structure that is enabled by the presence of the side-tilted molecules of the second semilayer β_2 that decrease the repulsion between the flat lying molecules of the first semilayer β_1. This demonstrates the interplay between adsorbate-substrate and adsorbate-adsorbate interactions, which determine the molecular packing within the interfacing first monolayer as pointed out in Section 1.3.

In the following we will focus on the interstitial coverage regime, i.e. the range between

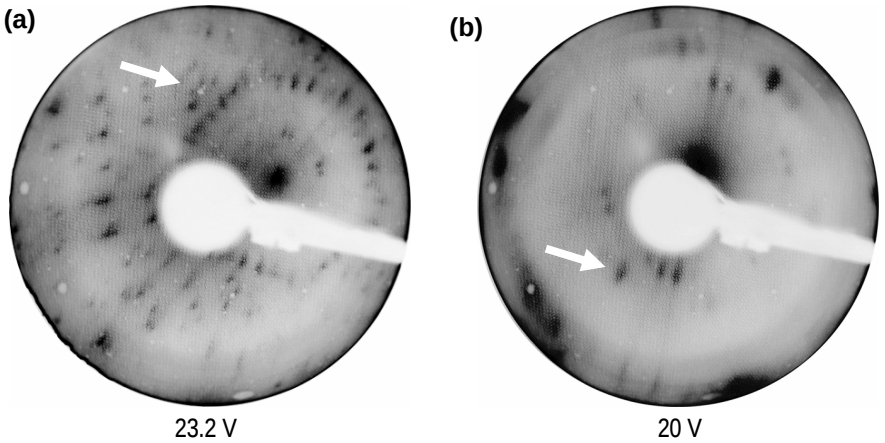

Figure 4.29: LEED images of (a) 2 ML thick and (b) 7 ML thick 6P films grown on Au(111) at 300 K. The arrows mark extra reflections that do not comply with the LEED pattern of the first monolayer.

the saturated monolayer at 0.3-0.4 nm and the beginning bulk phase around several nm. Unfortunately, in the case of nP, this coverage regime is considerably difficult to investigate experimentally, because of the tendency of island growth for coverages > 1 ML (Stranski-Krastanov). Hence, the following results describe only some specific aspects of the nP coverage regime at the transition from the monolayer to the bulk phase that could be investigated experimentally. Two key questions are important in this context, concerning 1) the coverage dependence of the film structure and 2) the thickness of the transition regime.

In the case of 6P on Au(111), TDS has clearly shown the existence of a distinct second monomolecular layer labelled β_3. However, the existence of β_3 does not necessarily imply that it exhibits a different packing structure compared to the first 6P monolayer. Hence, detailed LEED investigations have been conducted. For a nominally 2 ML 6P film on Au(111) similar LEED patterns have been observed as for a 1 ML film. All recorded LEED images clearly exhibit the well-known diffraction pattern that corresponds to the first 6P monolayer, which has been described in full detail in Section 4.2. However, some additional LEED reflections are observed, too, which do not comply with that pattern of the first layer. Obviously, a superposition of at least two diffraction patterns is observed, which indicates that the second 6P monolayer grows in a different regular structure. Figure 4.29(a) shows a representative LEED image of a 2 ML 6P film grown on Au(111) at 300 K. The arrow marks the position of some extra reflections that correspond to the superposed pattern that is caused by the second 6P layer. Unfortunately, the number of observable diffraction spots from the second layer is too small for a comprehensive analysis of the corresponding LEED pattern. Upon growing thicker films, however, more and more reflections appear that can be attributed to the superposed LEED pattern. This is demonstrated in Figure 4.29(b), where some representative LEED images are shown for different 6P coverages between 2 ML and 7 ML. This behaviour can be explained by the island like type of growth of the second

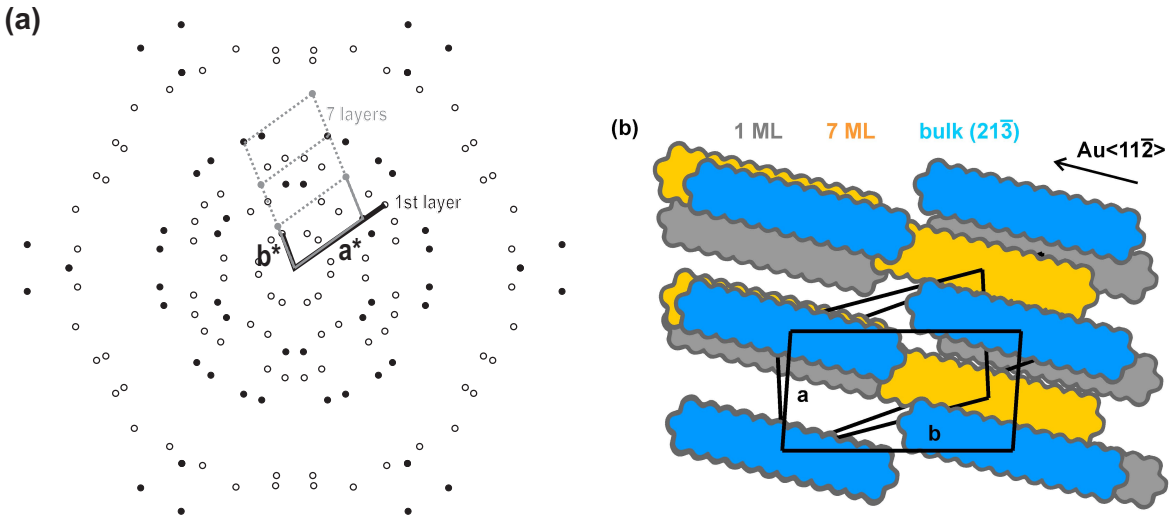

Figure 4.30: (a) LEED pattern representation of a 7 ML thick 6P film on Au(111). Two diffraction patterns are superposed, i.e. the 1st layer pattern (open circles) and an additional pattern corresponding to the average regular structure of a nominally 7 ML thick film (black dots). (b) Comparison of the 2D surface unit cells observed for a 1 ML (grey) and 7 ML (yellow) thick 6P film with the 2D unit cell of the 6P(21$\bar{3}$) bulk crystal orientation (blue).

layer that has been observed in the previous TD experiments. The number of observable LEED reflections of the superposed pattern steadily increases with film thickness and at about 7 ML it is sufficiently high for a LEED pattern analysis. The result of the latter are presented in Figure 4.30(a). The deformation free representation of the LEED pattern has been gained from additional reflections under the assumption that they all belong to a single superposed diffraction pattern. Hence, while the first monolayer is still visible in LEED (open circles) also a single second regular pattern is observed (black dots). To a first approximation, the latter can be attributed to the superposition of the regular structures within of the second and subsequent monolayers that exist in the nominally 7 ML thick 6P film. Due to the pronounced island formation (Stranski-Krastanoc), one has to be particularly careful to avoid an over-interpretation of the observed LEED pattern and attribute it exclusively to the second layer.

The analysis of the superposed LEED pattern of the 7 ML thick film yields the following unit cell parameters: $a = 1.5\ nm$, $b = 2.5\ nm$, $\gamma = 78°$, and $\phi = 18°$, respectively. As can be seen already in Figure 4.30(a), the azimuthal orientation of the short cell vector $\vec{a}$ is almost the same as for a 1 ML thick film alone. These two surface unit cells can be compared to that of the experimentally determined bulk 6P(21$\bar{3}$) orientation, which corresponds to the 6P crystal orientation at higher coverages, as discussed in the previous section. The latter has geometric parameters of $a = 1.377\ nm$, $b = 2.692\ nm$ and $\gamma = 85.87°$, respectively (cf. Figure 1.3). A rather continuous structural transition between these three structures can be observed, as shown in Figure 4.30(b). The molecules are aligned along the Au$\langle 11\bar{2}\rangle$ direction, corresponding to the experimentally determined inter-azimuthal orientation. For

a better visibility, only the flat lying molecules are shown in the figure.

The previous results indicate, that for the system 6P/Au(111) the actual bulk structure is established not until a considerably high 6P coverage, who's thickness can be estimated to several tens of monolayers. This is an important result that shows the dominant influence of the substrate structure for the nP systems.

Chapter 5

Effect of Substrate Geometry

This chapter investigates oligo-phenylene thin films grown on different vicinal (stepped) Au surfaces. These exhibit a high degree of geometric anisotropy, which effects the film growth. A properly prepared poly-crystalline substrate enables the investigation of the thin film growth simultaneously on a variety of different stepped Au surfaces.

The term "substrate geometry" denotes in this context the crystalline structure of the surface on a nanoscopic length scale, e.g. the surface crystal orientations, step widths and directions. Besides the highly symmetric Au(111) surface investigated in Chapter 4, also polycrystalline or vicinal single crystalline Au surfaces have been used as substrates for the growth of nP films. The vicinal surfaces exhibit periodic monoatomic steps that separate low-index terraces. In some cases, like on the Au(433) surface, a step bunching is observed (cf. Section 1.5), which induces a second periodicity on the surface. In some cases the super-periodicity can be up to several ten nm. The existence of periodic steps causes a structural anisotropy of the surface compared to the Au(111) surface. If the adsorbate-substrate interaction is strong enough to influence the structure of the organic thin film, it should be expected that the anisotropy of the stepped surface also causes an anisotropy of the nP crystal growth. In particular, two different Au substrates have been used for the following experiments, i.e. a re-crystallized Au(433) single crystal and a poly-crystalline Au foil. The latter exhibited a microcrystalline Au surface with grain diameters between 50 and 200 μm, as described in detail in Section 3.3.

5.1 Desorption kinetics

The adsorption and desorption kinetics of nP molecules on vicinal Au surfaces is qualitatively similar compared to that on Au(111). Figure 5.1 presents the monolayer regime TD spectra of 4P and 6P grown on a polycrystalline Au surface at 93 K and 300 K. Two distinct monolayer desorption peaks, labelled β_1 and β_2 can be clearly seen in both TD series. The **nP monolayer** is saturated at a nominal film thickness of roughly 0.25 nm for

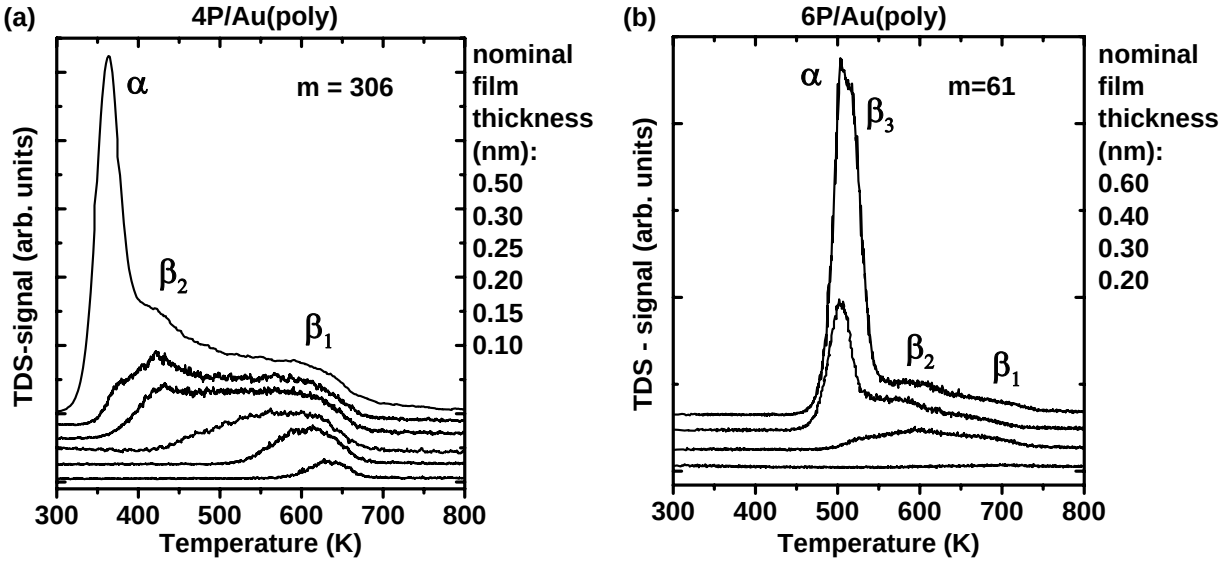

Figure 5.1: Monolayer regime of the TDS series of (a) 4P and (b) 6P grown on Au(poly) at 93 K and 300 K, respectively.

4P and 0.4 nm for 6P. These values are similar to those of nP grown on Au(111) and indicate that also on the polycrystalline Au surface a monomolecular wetting layer exists that comprises **lying molecules**. Please note, that for 6P still no significant desorption can be observed even for a coverage as high as 0.2 nm, which equals roughly half a monolayer. This is significantly different from the 4P spectra and can be explained by the strongly increased tendency of 6P to dehydrogenate already on the surface instead of desorbing as an intact molecule (cf. Chapter 6). The β_1 peak maximum lies at about 610 K for 4P and 670 K for 6P, which is roughly 90 K (40 K) higher compared to the Au(111) surface. Also the width of the monolayer desorption double-peak appears extended up to higher temperatures for both 4P and 6P spectra. This can be attributed to an increased number of energetic adsorption/desorption states on the polycrystalline surface compared to the single-crystal Au(111) surface, which is caused by the larger surface density of defect sites on the polycrystalline surface (vacancies, steps, kinks). After the saturation of the first monolayer a sharp desorption peak starts to emerge. In the case of 4P, this peak is not saturated and therefore assigned to the zero-order desorption from the multilayer. Different from that, the spectra of 6P indicate, that a distinct **second layer desorption peak**, β_3, exists that saturates at a nominal thickness of roughly two monolayers (0.8 nm). The β_3 peak lies already very close to the multilayer desorption peak α, as can be seen in Figure 5.1(b).

Comparing the threshold temperature for the multilayer desorption α, in the case of 4P it is similar compared to the Au(111) surface, whereas for 6P it appears roughly 30 K higher (compare to Figures 4.1 and 4.2). The latter result is surprising insofar, as the multilayer desorption is not expected to be influenced that much by the sample surface properties. A

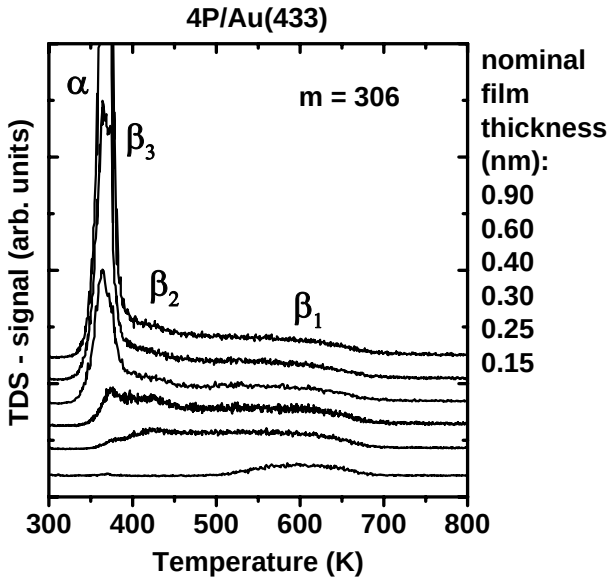

Figure 5.2: Monolayer TDS regime of 4P grown on Au(433) at 300 K.

possible explanation could be as follows: due to the significant fraction of dehydrogenated 6P (roughly 0.2 nm) the multilayer desorption is still not fully developed in the nominal 0.6 nm spectrum shown in (b) and therefore appears to lie at higher temperatures. As will be shown below, however, the threshold temperature for multilayer desorption, as observed for nP bulk films of several nm film thickness, can be regarded independent of the substrate and monolayer properties to a first approximation.

Unfortunately, the quantitative comparison of the TD data of nP films grown on Au(poly) and Au(111) surfaces that has been made so far allows no derivation of a simple systematic scheme that can explain all the particular differences between 4P and 6P observed in the experimental TD data, e.g. concerning the width and peak maximum temperatures. This may indicate that rather complicated kinetic processes govern the monolayer desorption of nP molecules on different Au surfaces, and in particular on the polycrystalline Au surface. Nevertheless, a rather qualitative first conclusion can be drawn: The pronounced existence of surface defects and steps on the polycrystalline Au surface leads to a stronger bonding of the nP monolayer to the Au(poly) surface compared to Au(111), which causes the monolayer desorption peaks β_1 and β_2 to shift to higher temperatures.

A similar situation has been observed for 4P grown on a vicinal Au(433) surface, which exhibits a periodic step structure (for details see Section 1.5). The corresponding monolayer TD spectra are shown in Figure 5.2. The monolayer desorption peaks, β_1 and β_2, are very similar to those found for 4P on Au(poly) and, in particular, the peak maximum temperatures of about 420 K and 600 K. However, the width of β_1 is significantly increased compared to the Au(poly) surface. This may indicate that the 4P molecules are even

Table 5.1: Comparison of the multilayer desorption energies of 4P and 6P grown on different clean Au surfaces around 300 K as determined from TD data.

	substrate	E_{des} (eV/molecule)
4P	Au(111)	1.56
	Au(poly)	1.53
	Au(433)	1.43
6P	Au(111)	2.40
	Au(poly)	2.54

stronger adsorbed on the Au(433) surface than on Au(poly). At higher coverages, a new peak labelled β_3 is observed that saturates at a coverage, which corresponds to nominally two monomolecular 4P layers, i.e. roughly 0.5-0.6 nm. Hence, the β_3 peak is assigned to the desorption from the second 4P layer. Finally, at coverages > 2 ML a multilayer peak, labelled α, is observed. Interestingly, neither for 4P grown on Au(111) nor on Au(poly) such a distinct second layer desorption has been observed, different from 6P on Au(111), where it has been found, indeed.

The reason for this remarkable finding is not fully understood, yet. However, a plausible explanation would be that the absolute magnitude of the interaction energy between the adsorbed nP molecules of the first monolayer and the Au surface is the determining factor. In case, that the adsorbate-substrate interaction energy is sufficiently high, also the molecules in the second layer may be influences by the substrate to a significant extent and a distinct second layer desorption peak is observed in TDS. The multilayer desorption regime starts not before the nP coverage reaches nominally the third layer in these systems. This interpretation is corroborated by the following experimental finding: A distinct second layer desorption has been observed for the systems 4P/Au(433), 6P/Au(111) and 6P/Au(poly). [1] These systems also exhibit a very pronounced de-hydrogenation behaviour, as described in Chapter 6, which is a clear indication that the adsorbate-substrate interactions are rather strong compared to the more weakly interacting system 4P/Au(111).

Concerning the desorption kinetics of the nP multilayer, the question is posed, if the nP **multilayer desorption energy**, E_{des}, is influenced by the structure of the substrate surface, or not. A comparison of the multilayer TD data of 4P and 6P on different Au surfaces is given in Table 5.1. First of all, the experimental values of E_{des} can be divided into two separate groups that correspond to 4P and 6P, respectively, where each group comprises roughly similar values. Hence, it can be concluded, that the length of the nP molecule, i.e. the number of phenyl rings, is the dominant factor that determines the multilayer desorption energy. Interestingly, however, it is not the only factor as can be seen by a closer analysis: The E_{des} values for a single type of nP molecule recorded for films grown on different substrate geometries lie all within a range of a few tenths of eV per

[1] In the case of 4P/Au(poly), which behaves similar to 4P/Au(433), the existence of a distinct second layer desorption peak has not been investigated in great detail. However, the existing data suggest no second layer peak (cf. Figure 5.1(a)).

molecule. [2] This indicates that some additional influence exists which effects the multilayer desorption.

It may be presumed that in addition to the molecular size also the geometry of the substrate surface can effect the nP multilayer desorption kinetics. This seems puzzling at a first glance, because the interaction range between the adsorbate molecules and the Au substrate is too small as to that the molecules within a several nm thick bulk film could be directly influenced. However, a possible explanation can be given as follows: It is discussed in Chapter 4 that the crystal orientation of the nP multilayer is strongly influenced by the properties of the first nP monolayer (wetting layer). The latter being determined by the properties of the substrate surface via adsorbate-substrate interactions. The monolayer can be regarded as a structural pre-stage for the bulk crystal growth. In case that a certain change of the substrate geometry induces a significant change of the nP monolayer structure, i.e. the molecular packing and orientation, this will also affect the bulk structure of the nP film. For instance, it is shown in Chapter 7 that the bulk crystal orientation of nP films on partially C-covered Au surfaces is strongly determined by the monolayer structure and can be easily tailored by changing the latter. Therefore, it seems plausible to attribute the small variations of the multilayer desorption energy of <0.3 eV/molecule (for 6P), which are described above, to the fact that different bulk crystal orientations are adopted depending on the geometry of the Au surface. The largest differences should be expected between orientations that comprise only lying or upright standing molecules. In the case of standing molecules this is the (001) orientation and in the case of flat lying molecules it is the 4P(211) and 6P($21\bar{3}$) orientation, respectively. Estimating a maximum difference in the desorption energy between the upright and flat lying orientation of about < 0.3 eV per 6P molecule, this yields roughly 8 meV per carbon atom. From the fact that such small energy changes are involved, it seems possible that the crystal orientation is responsible for the observed slight variations of the multilayer desorption energy. Unfortunately, no experimental or calculated values of the surface energy of different nP cleavage planes are available to the best of our knowledge.

5.2 Film structure and morphology

As will be shown in the following, a big advantage of using the recrystallized Au(poly) substrate is the possibility to investigate a large variety of different vicinal Au surfaces simultaneously. Furthermore, it is guaranteed that all the nP films on the different vicinal Au surfaces have been prepared exactly under the same conditions, which is a non-trivial task using several different Au single crystallites as samples. In addition to that, 4P films grown on a vicinal Au(433) single crystal sample have been investigated.

The morphologies of 30 nm thick 4P and 6P films evaporated on a recrystallized gold sample at 300 K have been investigated in detail. Optical micrographs of these samples are shown in Figure 5.3, which already contain important features of the film morphology. In many cases the individual grains of the Au substrate surface can be clearly distinguished

[2] The measurement error has been estimated to about ± 0.05 eV.

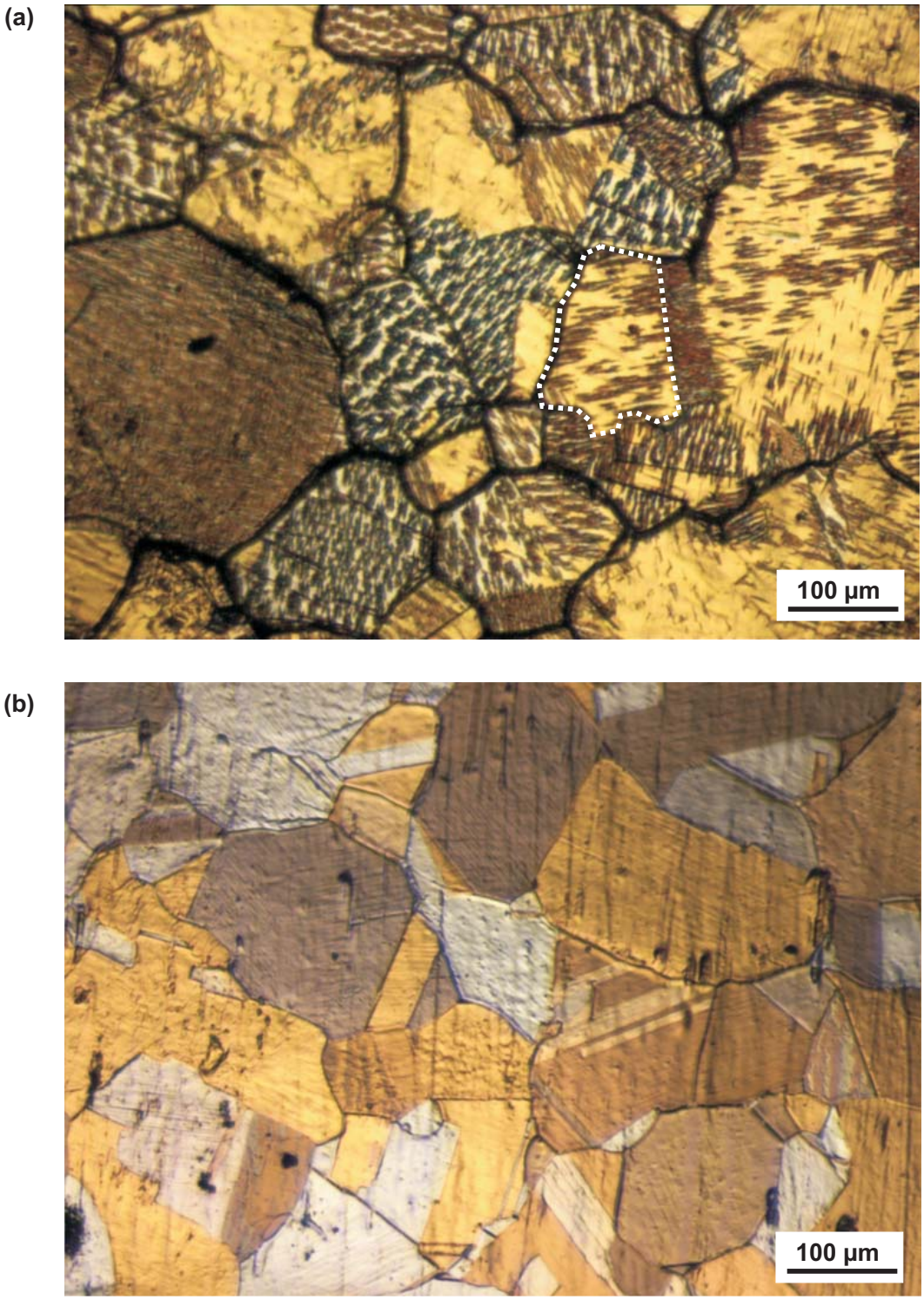

Figure 5.3: Optical micrograph of a 30 nm film of (a) 4P and (b) 6P grown on a recrystallized polycrystalline Au surface at 300 K. The dotted line marks the visible grain boundary of an arbitrary Au grain.

because they appear separated by grain boundaries. This is indicated for an arbitrary Au grain by a dotted line in Figure 5.3(a). In particular, the 4P sample has been subject to a thorough structural analysis, because already in the OM image as presented in (a) various different film morphologies with 4P crystallites of different size, shape and orientation can be seen. The deposition of 4P on a polycrystalline gold surface clearly reveals the influence of the substrate geometry on the film morphology. The dark areas in the OM image represent 4P crystallites that have at least microscopic dimensions > several hundred nm. This can be concluded from their visibility in OM. On the other hand, the areas that appear bright in the OM image are presumably either denuded or the 4P film has grown in a homogeneous, layer-like manner. It could be shown, that the latter is true: SEM and AFM results suggest a homogeneous coverage with terrace like crystal grains (layer growth), which appear transparent in OM. Additionally, temperature dependent XPS measurements (cf. Chapter 8) show that the whole sample is covered by nP molecules, i.e. no de-wetting of such large areas (several μm^2) occurs. Different from 4P, the 6P sample presented in (b) exhibits only homogeneously covered Au grains, where each Au grain appears in a different colour. This suggests a very homogeneous layer-like film growth of 6P on all kinds of different stepped Au surfaces, at least for an adsorption temperature of 300 K. However, the results presented in Section 8.2 indicate that at higher temperatures the 6P film will also exhibit an island like growth on certain Au grains similar to the 4P sample.

In the following, we will focus on the 4P sample presented in Figure 5.3(a). Apparently, the 4P thin film growth proceeds in quite different ways on the individual Au grains. Only in a few cases the 4P film seems to cover smoothly the Au surface. In the case of elongated 4P island formation a strong azimuthal alignment can be seen. Those areas on individual Au grains that appear bright in OM all show the same brightness. For comparison with an OM image of a clean Au(poly) surface please refer to Figure 3.3 on page 60. This demonstrates that the terminating surface planes of all the Au grains are oriented nearly parallel to the macroscopic sample surface. This fact is very important for the structural analysis presented in the following, because it guarantees that the topmost surface planes of the Au grains are nearly parallel to the (hkl) planes of the Au crystal orientations that are determined with EBSD.

Figure 5.4 shows representative SEM images of selected sections of the same film at higher magnification. In the area labelled A in Figure 5.4(a) several micrometer long needle-like 4P crystallites are visible. Their azimuthal alignment is not pronounced, although several preferential orientations seem to exist. This can also be seen in (b) at double magnification of a neighbouring sample area. The crystallites are not uniformly distributed over the surface. Instead, bunches of several tens of 4P crystallites exist. These bunches are separated by rather wide denuded areas (several micrometers), which are not covered by crystallites. Only about 40% of the type A grain surface is covered with 4P crystallites. In Figure 5.4(a)+(b) also the grain boundaries of neighbouring Au grains can be clearly seen. In area B a highly anisotropic island growth is observed, where the individual crystallite needles are well aligned along a single preferential direction. Compared to the former case, no pronounced bunching of the crystallites is observed. Roughly 60% of the type B grain surface is covered by 4P. In contrast to that, in area C more than 90% of the

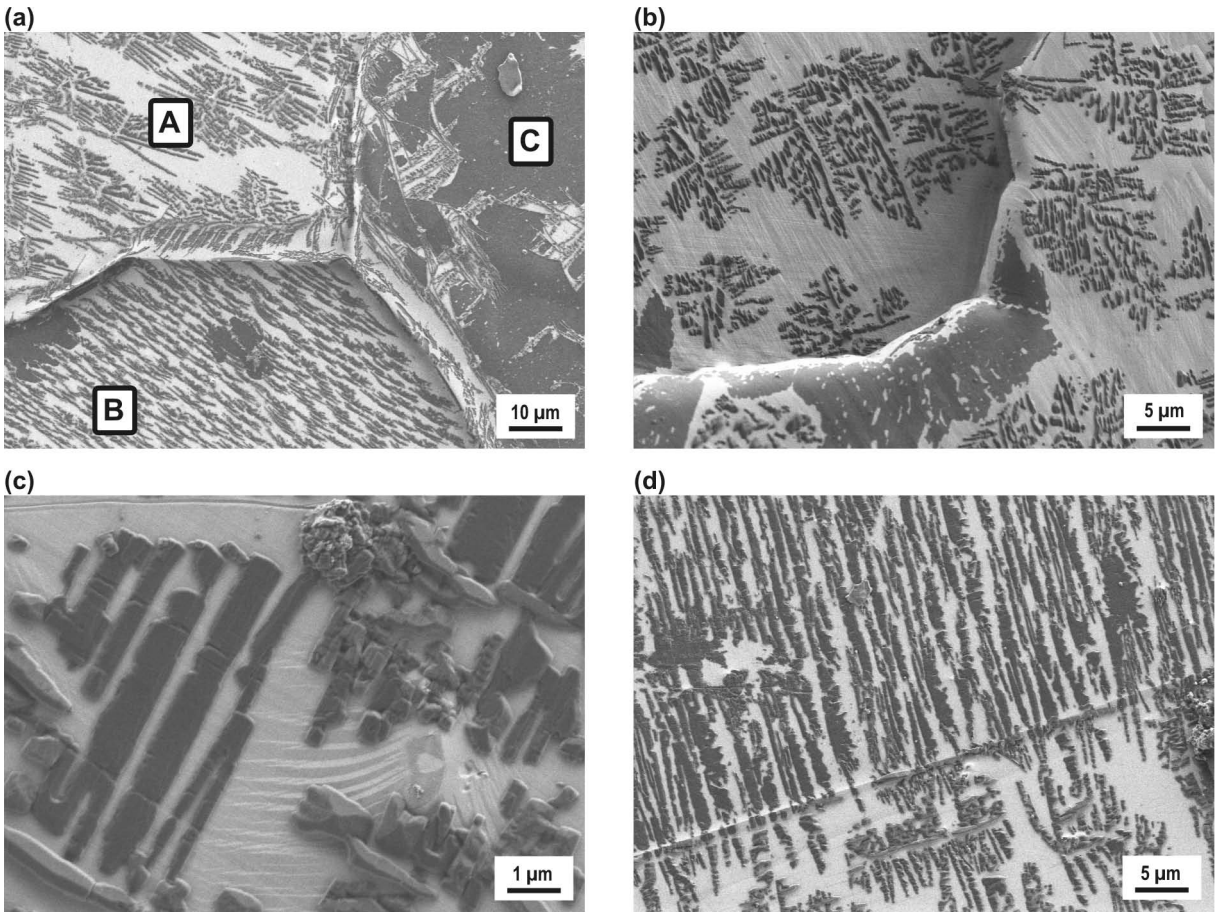

Figure 5.4: SEM micrographs of a 30 nm 4P film grown on Au(poly) at 300 K. In (a) three different film morphologies can be observed on the three grain surfaces labelled A, B and C. (b)-(d) show different areas on the same sample exhibiting different combinations of the morphology types A-C.

surface is covered by a continuous 4P film. The growth of discrete crystallite needles seems to be suppressed on this Au grain surface. In most cases, the grain boundaries between adjacent Au grains are also structural phase boundaries for the growth of the 4P films. This is clearly visible in Figures 5.3(a) and 5.4(a)+(b). Although in a few cases the growth of single 4P crystallites across a grain boundary has been found, no explicit preference for a cross-talk between adjacent crystal planes can be observed. Different from that, it has been frequently observed that the 4P crystallites grow apparently undisturbed across microscopic scratches on the surface of a gold grain, as shown in Figure 5.4(d).

In order to gain a more detailed understanding of the shapes of the 4P crystallites formed on individual Au grains, high resolution SEM images were recorded. In Figures 5.5(a)+(b), two SEM images with different magnifications are depicted, which correspond to area A in Figure 5.4(a). It turns out that the needle-like islands actually consist of individual 4P crystallites, which are connected and aligned along a preferential direction. Hence, the needles should be rather denoted as "chains" consisting of separate, linearly

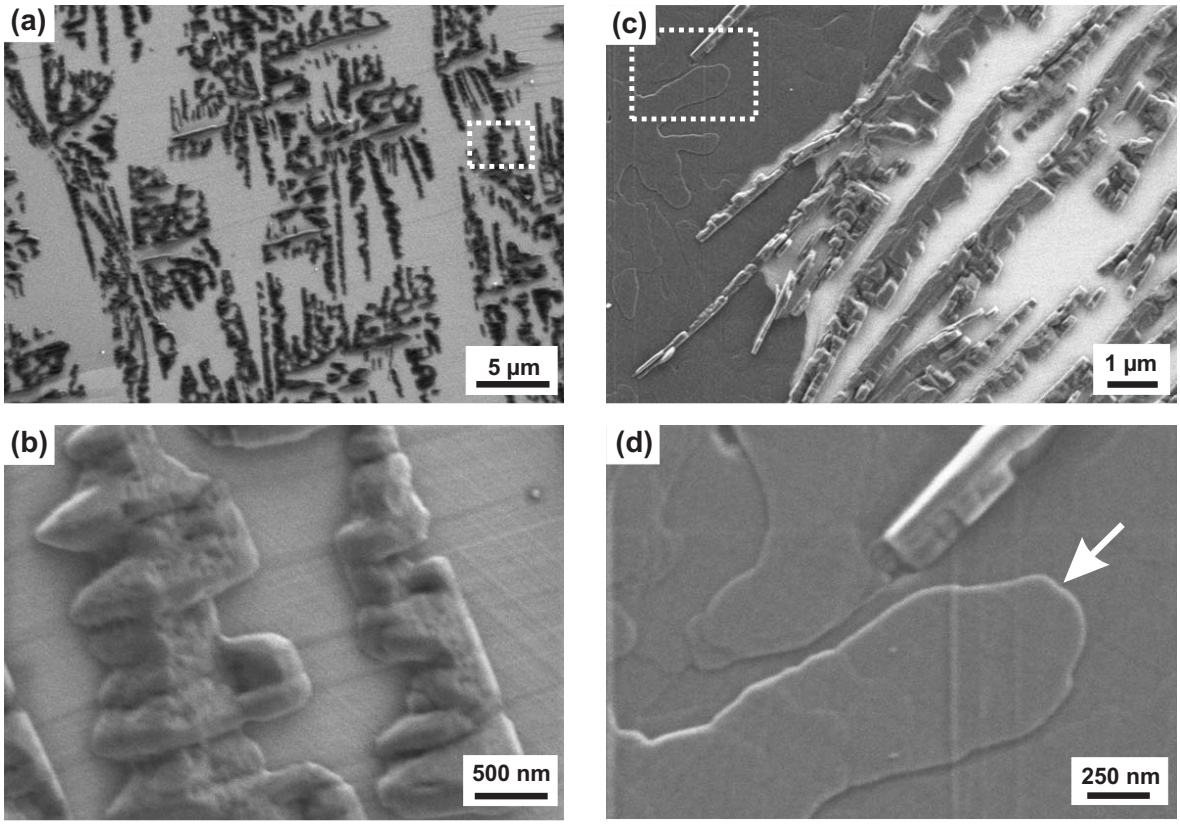

Figure 5.5: High resolution SEM images showing detail scans of selected areas of the 30 nm 4P film on Au(poly) presented in Figure 5.4. (a)-(b) type *A* and (c)-(d) type *C* morphology. The dotted rectangles define the sample areas for the higher resolution images (b) and (d).

aligned 4P crystallites. The regular shape and strict azimuthal alignment of those individual 4P crystallites indicates a highly regular orientation of the 4P molecules within the 4P crystallites. Furthermore, the individual needles have roughly the same width of $0.5-1$ μm and are of similar height, as observed in AFM investigations described below. A closer inspection of Figure 5.5(a) reveals that several predominant needle orientations exist, which differ roughly by integer multiples of 15°. This strongly indicates that the single crystal surface of the gold grain acts as a template for the 4P crystal growth. The strong azimuthal dependence of the 4P crystallites indicates that those needlelike 4P crystallites consist of regularly arranged 4P molecules aligned with their long axes parallel to the substrate surface. Indeed, LEED and XRD investigations performed on 4P thin films grown on Au(111) have shown that the 4P molecules in the needle-like crystallites are oriented with their long axes parallel to the substrate surface, as discussed in Section 4.5. Furthermore, it has been shown that the molecules can either arrange parallel to the Au$\langle 1\bar{1}0\rangle$ or Au$\langle 11\bar{2}\rangle$ direction, respectively.

The quite different behaviour of film growth in area *C* of Figure 5.4(b) (continuous

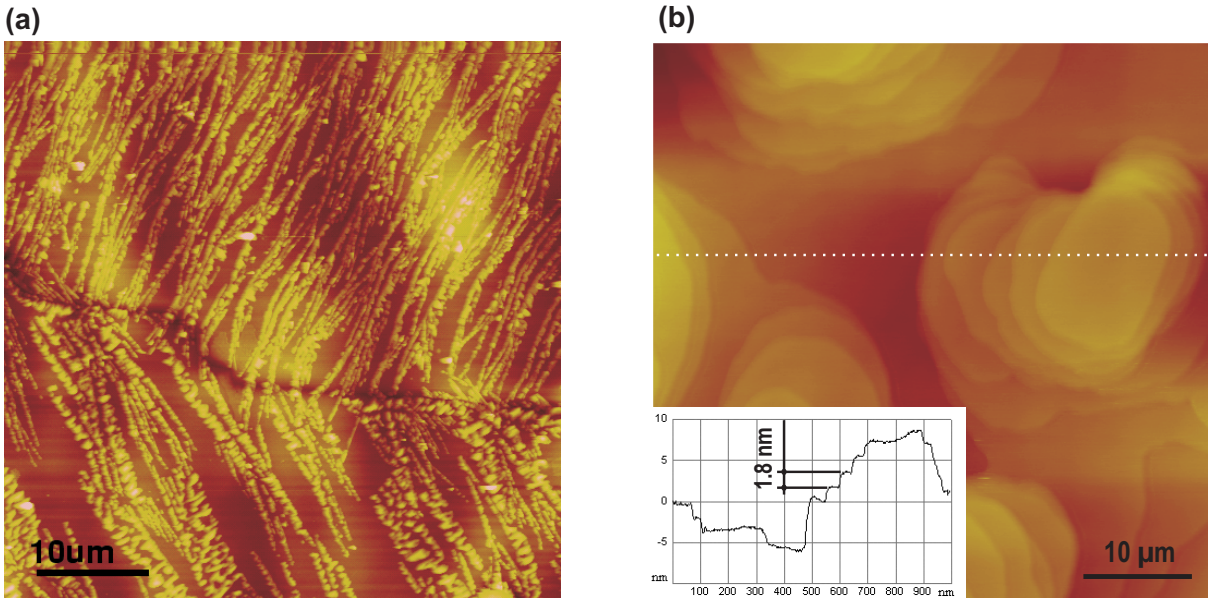

Figure 5.6: High resolution AFM micrographs of a 30 nm 4P film on polycrystalline Au grown at 300 K. (a) 4P growth on two neighbouring gold grains and across the grain boundary (z-scale 600 nm). (b) Terrace like 4P crystallites. The line scan across the horizontal line is shown in the inset.

film) is more clearly represented in the high resolution SEM images of Figure 5.5 (c)+(d). In this case a small amount of needle shaped 4P islands coexists with large areas covered by continuous layers resembling 4P terraces. This can be clearly seen in the high resolution image presented in Figure 5.5(c). These terraces are of arbitrary shape and seem to be very flat. A close-up picture shown in Figure 5.5(d) reveals the characteristic terrace steps, as indicated by the arrow.

In order to determine the size of the 4P crystallites high resolution AFM measurements were performed for the 30 nm 4P film on Au(poly). The results are presented in Figure 5.6. In particular, image (a) shows the type A film morphology on two neighbouring gold grains. Chains of individual 4P islands have different orientations suggesting that the chain orientation is controlled by the surface geometry. It is remarkable that sometimes the orientation of a chain can be retained for a short distance when growing across a boundary into the next grain with a different surface orientation. This can be explained by the fact that in the small strip around a grain where the chains grow in the wrong direction, the grain surface may be distorted due to the influence of the grain boundary. The grain boundary leads to a change in crystallography and to a deformation of the grain surface. The area between the chains is at least partly covered by a type C terrace like 4P film morphology as presented in Figure 5.6(b). A linear scan across the horizontal line is presented in the inset of the figure revealing a step height of approximately 1.8 nm.

This is in good agreement to the long side of the 4P crystal structure unit cell, $c = 1.79$ nm), cf. Table 1.2, indicating that the terraces consist of stacked layer of nearly upright standing 4P molecules. It seems plausible to attribute a certain crystal orientation to that

terrace like morphology, i.e. the 4P(001) plane being parallel to the substrate surface. This shows that crystallites that are assumed to comprise of lying molecules and layers of upright standing molecules can exist simultaneously in close proximity. The coexistence of such two growth modes has been shown recently also for 4P grown on mica [58].

Similar results have been obtained also for 4P films grown on carbon covered Au(111), as described in Chapter 7. This demonstrates that not only the surface crystal structure but also the chemical composition of the surface is of considerable importance for the layer growth. Therefore, the continuous 4P terraces observed on some sample areas could be caused by some amount of segregated carbon at the substrate surface, which could not be totally removed by the cleaning procedure. In contrast to that, the needle-like 4P crystallites presented in Figure 5.5(a) and (b) are mainly composed of flat lying molecules, as described above. In Figure 5.3(a) it can be seen that surface areas larger than about 0.1 mm^2 seem uncovered in optical microscopy, apart from the clearly visible needle/crystallite covered areas. However, a complete de-wetting of such large areas is not plausible. The optical visibility of a 4P film in the present case (image contrast) is determined by absorption and scattering effects. In particular, the latter is suppressed in case of a very smooth film morphology. This can be clearly seen in Figure 5.3(b) for a 30 nm 6P film grown on Au(poly). Obviously, not a single Au grain exhibits a needlelike 6P film similar to that found for 4P. Instead, 6P adopts a terrace-like morphology comprising nearly upright standing molecules. This leads to an optically homogeneous film that can be discerned from a clean Au grain only by the colour impression that is caused by absorption effects in the 6P film. This enables an important conclusion also for the 4P film: Those areas that appear uncovered in OM might exhibit a smooth terrace-like 4P film morphology comprising upright standing molecules, similar to that shown in Figure 5.5(d).

5.2.1 Orientation Mapping

The most important challenge in this context is to find out the relationship between the substrate crystallography and the correlated 4P film growth modes. Identifying the orientation of the individual gold grains and comparing the results with the roughness and morphology data obtained by AFM, should give the possibility to find the best substrate orientation for given growth parameters. For this purpose we have carried out laterally resolved electron backscatter diffraction (EBSD) measurements on the same film. The results for a small section of the sample surface are depicted in Figure 5.7(a) and (b). In Figure 5.7(a) again the SEM image shows individual gold grains, which are covered with characteristically shaped 4P islands/terraces. Figure 5.7(b) represents an orientation map (inverse pole figure map, [001]) of the individual substrate grains of the same surface area with respect to the macroscopic sample surface. Firstly, each individual Au grain (numbered from 1 through 13) appears as one homogeneous single-crystalline entity of uniform crystal orientation. Sharp grain boundaries can be observed between the Au grains. Secondly, a distinct correlation between the individual Au grains with their specific grain orientation (orientation map) and the corresponding 4P film morphology (SEM image) can be clearly observed. For the determination of the absolute Au grain orientation a reference

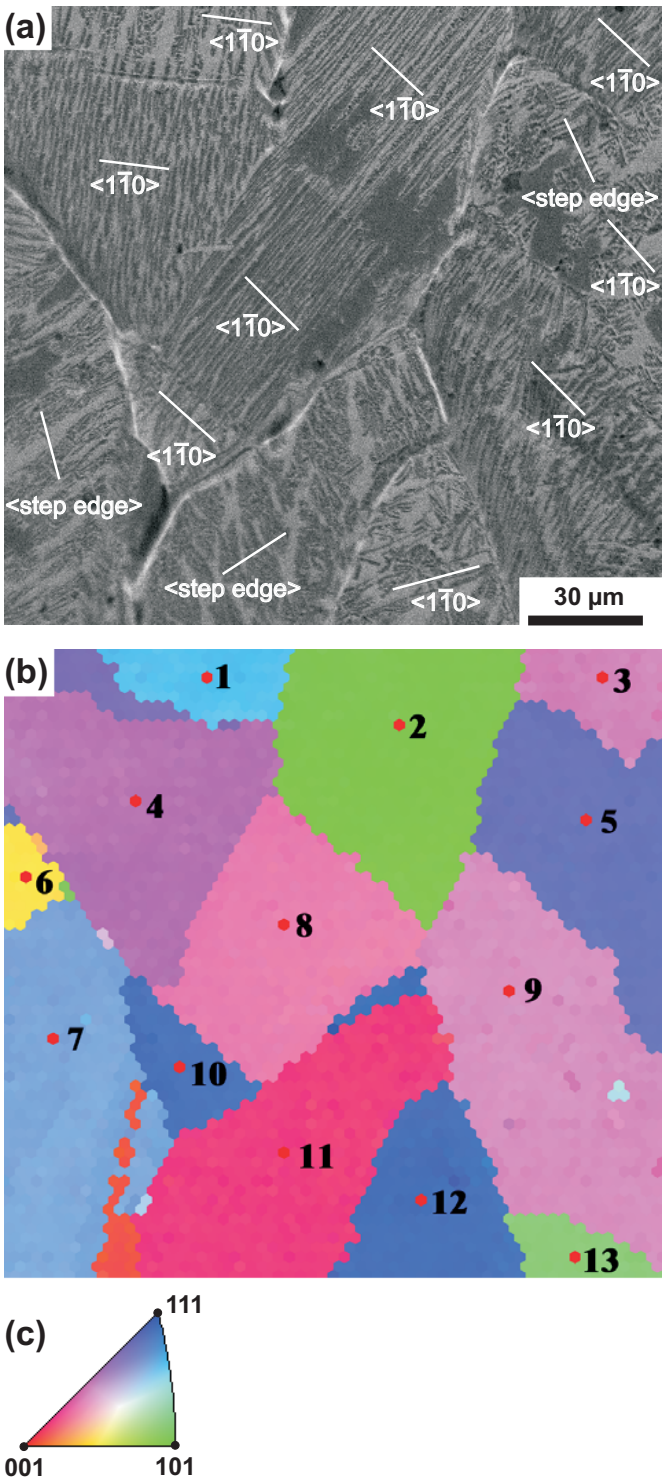

Figure 5.7: (a) SEM image of a 30 nm thick 4P film on the recrystallized Au surface. (b) Corresponding inverse pole figure map ([001]) as obtained by EBSD, with the Au grain orientations according to the colour code of the colour triangle shown in (c). The Au grains are labelled by 1 through 13. The white bars in (a) indicate either the Au$\langle 1\bar{1}0\rangle$ directions or the directions of the step edges of the Au grains as obtained from the EBSD measurements. The growth of needle like 4P islands normal to the Au$\langle 1\bar{1}0\rangle$ directions can clearly be seen on most grains.

Table 5.2: Euler angles (ϕ_1, Φ, ϕ_2), Miller indices (hkl) and azimuthal directions $[uvw]$ for the measured orientations of the individual gold grains ♯1 through ♯13 of Figure 5.7(b).

	Euler angles			(hkl)			$[uvw]$		
Grain ♯	ϕ_1	Φ	ϕ_2	h	k	l	u	v	w
1	80.3	67.7	44.6	5	5	3	-1	-2	5
2	137.9	47.1	359.4	0	10	9	-10	-6	7
3	42.2	25.8	50.2	4	3	10	0	-10	3
4	81.9	29.5	43.4	2	2	5	-7	-10	7
5	101.0	57.9	326.2	-7	10	8	1	-3	5
6	151.4	22.3	273.0	-2	0	5	2	-5	1
7	57.7	43.8	33.2	5	8	10	1	-10	7
8	215.7	20.8	235.6	-3	-2	10	0	-10	-2
9	39.5	25.2	53.2	4	3	10	0	-10	3
10	49.1	50.5	41.0	8	9	10	2	-10	7
11	291.1	11.7	130.3	2	-1	10	5	-10	-2
12	47.0	58.7	43.3	9	10	8	3	-10	8
13	130.9	42.5	8.1	1	9	10	-10	-6	7

frame was chosen by calibration with a Si single crystal reference specimen. Accordingly, the fcc(100) plane is parallel to the macroscopic sample surface and the [100] direction is parallel to the vertical axis of Figure 5.7(a). From EBSD one directly obtains the orientations of the individual Au grains relative to the reference frame, which are represented by their Euler angles [124]. For a given set of Euler angles, the corresponding Miller indices (hkl) of the characteristic set of crystal planes of the Au grain, which are oriented parallel to the sample surface, can be calculated [124]. Those are either in close vicinity to or even identical to the actual terminating surface planes of the Au grains. In Table 5.2 the Euler angles, ϕ_1, Φ, ϕ_2, the corresponding Miller indices, (hkl), of the crystal planes parallel to the surface and the azimuthal directions, $[uvw]$, parallel to the [100] direction of the reference frame are compiled for the individual Au grains 1 through 13. The colouring of the grains in Figure 5.7(b) shows the orientation of the respective grains according to the associated colour triangle in Figure 5.7(c). In Figure 5.7(a) white bars indicate the azimuthal orientations of the dense packed $\langle 1\bar{1}0\rangle$ directions for each individual Au grain.

We will start the discussion of the relationship between the orientation of the individual Au grains and the corresponding 4P morphologies with the grains ♯2 and ♯8. The corresponding Miller indices of these two grain surfaces parallel to the macroscopic sample surface are quite different, i.e. (0 10 9) for grain ♯2 and ($\bar{3}$ $\bar{2}$ 10) for grain ♯8, respectively. However, the 4P film morphology on both grains is very similar, as shown in Figure 5.7(a). Both grains exhibit a growth of long needle-like 4P islands aligned along a single direction. The common feature of these grain surfaces is that the Au$\langle 1\bar{1}0\rangle$ direction is oriented in nearly the same way. On both grains the orientation of the 4P islands is preferentially perpendicular to the $\langle 1\bar{1}0\rangle$ direction. Figure 5.8(a) and (c) shows sphere models of these two surface orientations. The (0 10 9) plane consists of 2.4 nm wide (011) terraces where the step edge orientation is normal to the $\langle 1\bar{1}0\rangle$ direction. Apparently, this configuration is an ideal template for the oriented growth of 4P molecules. The Van der Waals dimen-

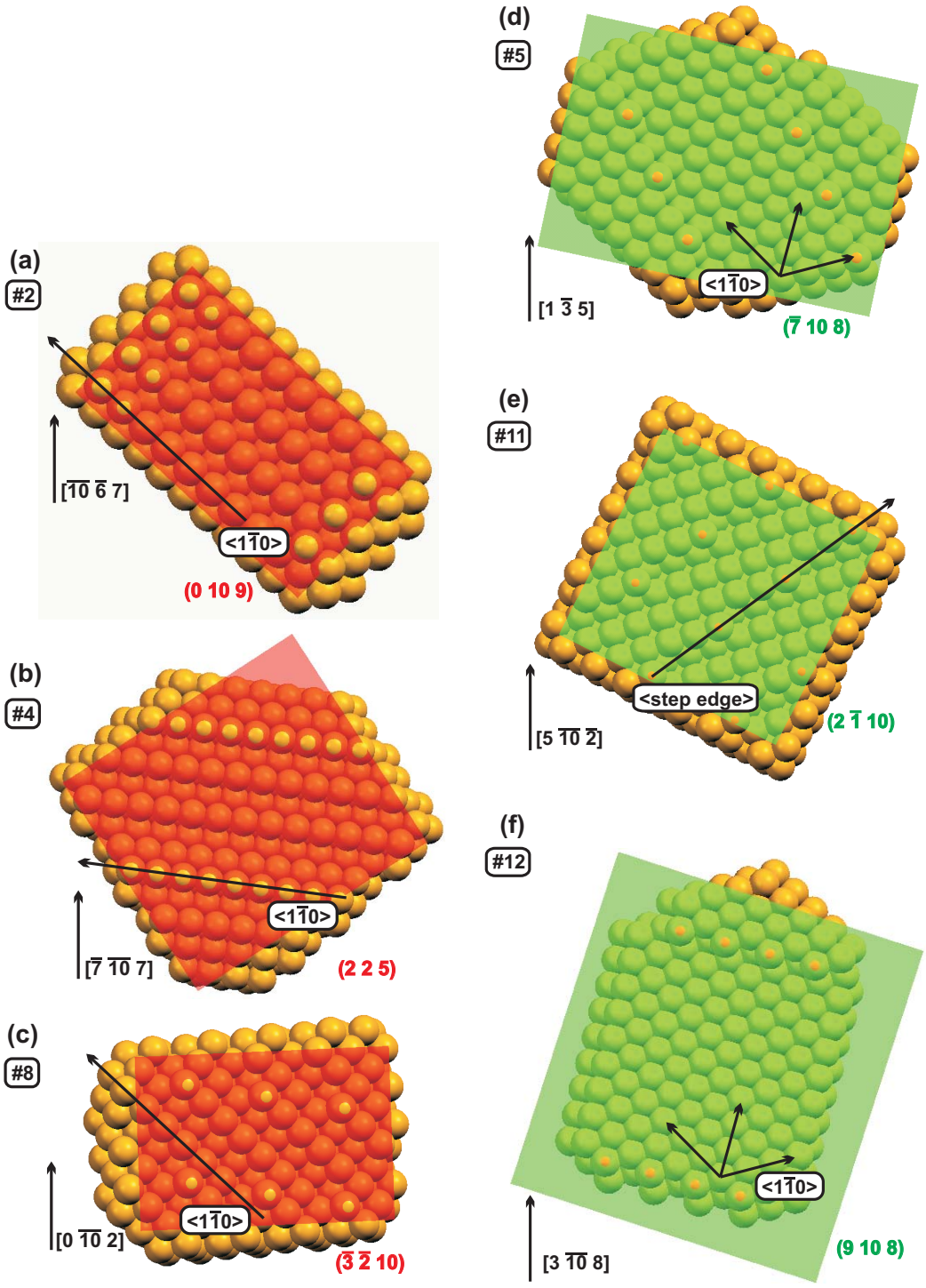

Figure 5.8: Sphere models of selected Au grain orientations. The area coloured in red or green indicates the (001) reference plane. The vertical [100] reference direction and the Au$\langle 1\bar{1}0\rangle$ direction is indicated in each image.

sions of a 4P molecule are $2.04 \times 0.67 \times 0.35$ nm^3. Therefore, the 4P molecules can easily accommodate on a terrace when oriented with their long axis along the dense packed $\langle 1\bar{1}0 \rangle$ direction. It has been demonstrated for the system 4P/Au(111) that the orientation of the first monolayer determines the arrangement of the molecules in the multilayer and hence the morphology of the multilayer, as described in Chapter 4. The sphere model of the surface plane of grain ♯8, which exhibits a similar 4P morphology as grain ♯2, is depicted in Figure 5.8(c). The ($\bar{3}$ $\bar{2}$ 10) plane dominating this structure does not exhibit a clear step-terrace structure, but again the dense packed Au$\langle 1\bar{1}0 \rangle$ rows act as a template for the monolayer growth of 4P. Grain ♯4, with a surface orientation (2 2 5), also shows a pronounced anisotropic 4P growth. Again, the 4P needle directions are normal to the Au$\langle 1\bar{1}0 \rangle$ direction (compare Figure 5.7(a) and 5.8(b)). In this particular case the Au$\langle 1\bar{1}0 \rangle$ direction is identical to the step direction of this vicinal plane. The terrace width is only 0.5 nm (cf. Figure 5.8(b)), which is quite small to accommodate the short axis of a flat lying 4P molecule. This might lead to a larger strain within the 4P film resulting in shorter needles compared to the former case.

A quite different behaviour of the 4P film morphology is observed for the grains ♯5, ♯11 and ♯12. The surfaces of these crystallites are mainly composed of (111) or (100) terraces. The sphere models corresponding to grain ♯5 (($\bar{7}$ 10 8) orientation), ♯11 ((2 $\bar{1}$ 10) orientation) and ♯12 ((9 10 8) orientation) are compiled in Figure 5.8(d)-(f), respectively. In the case of the exposed (111) planes (♯5, ♯12), where three equivalent $\langle 1\bar{1}0 \rangle$ directions exist and the widths of the (111) terraces are comparable to the Van der Waals length of the 4P molecule, no single preferential orientation for the macroscopic alignment of the 4P needles can be seen. Instead, at least six different but equal orientations exist, reflecting the high symmetry of these grain surfaces. Apparently, the potential energy surface of these planes is not corrugated enough to act as a template for highly anisotropic, oriented layer growth. In addition to the needlelike structures patches of continuous 4P film exist within this layer. There is evidence that in this case the 4P molecules are standing upright relative to the surface (AFM results). The grain ♯11 exposes terraces of (100) orientation with a terrace width of about 0.9 nm. In the corresponding 4P film only a weak preference for elongated island growth can be observed. The 4P needle orientation on this grain is roughly perpendicular to the step edge direction, indicating that the 4P molecules are aligned parallel to the step edges. Different from all the other grains analyzed above, the $\langle 1\bar{1}0 \rangle$ direction is not characteristic for this particular surface and the 4P molecules align along the step edges, instead.

In addition to the SEM/EBSD measurements, combined STM/SEM experiments have been performed. With the help of a combined STM/SEM instrument, the position of the STM tip relative to the substrate surface could be monitored in-situ with SEM. This is shown in Figure 5.9(a), where the position of the STM tip is visible together with the surface of the plain Au substrate. The two Au grains involved are labelled A and B, accordingly. In particular, STM measurements of the plain Au substrate prior to the film deposition clearly reveal the stepped surfaces of the Au grains. Figure 5.9(b) presents a 30×30 nm^2 STM image of the plain Au surface, which has been recorded at the same position as shown in Figure 5.9(a), i.e. on grain A left of the grain boundary. Almost

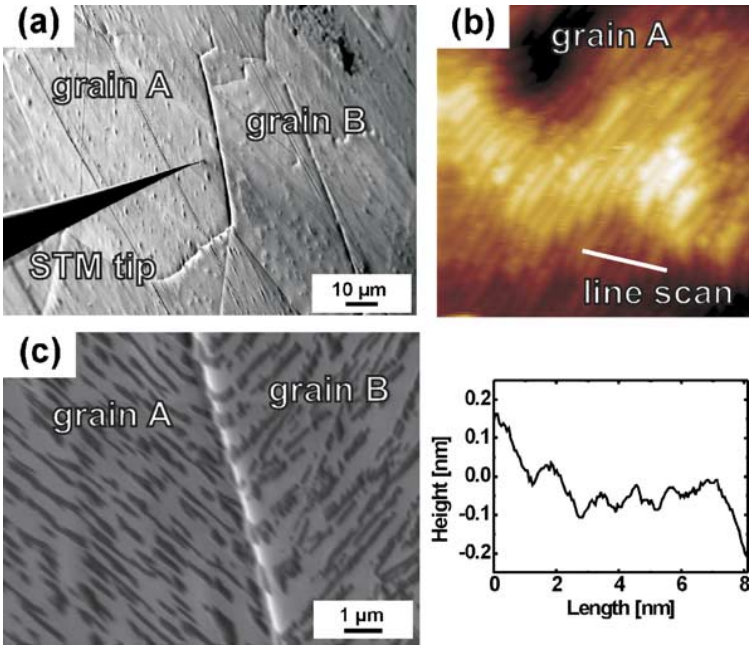

Figure 5.9: (a) SEM image showing the position of the STM tip relative to the Au surface for the combined STM/SEM measurements. Two neighbouring grains are labelled A and B, respectively. (b) 30 nm × 30 nm STM image ($U_{Sample} = 2.0$ V, $I = 2.0$ nA) taken on grain A at the tip position shown in (a). The height profile (line scan) shown below is taken across the straight line as indicated. (c) SEM image at higher resolution after deposition of a 20 nm 4P film taken at a position next to the STM tip shown in (a).

parallel rows of bunched steps are visible, with an inter-row distance of 11.5 nm. This can be seen from the height profile (line scan) presented below, which has been taken along the straight line indicated in Figure 5.9(b). After deposition of the 4P film, SEM measurements with higher resolution have been made at the same sample position as shown in Figure 5.9(a). This is presented in Figure 5.9(c), where elongated 4P aggregates can be observed. On the grain labelled A the 4P aggregates are aligned along a single preferential direction, which is perpendicular to the direction of the corresponding step bunch rows of the Au surface underneath. Obviously, the width of the step bunched terraces (about 1 nm) is small enough to hinder an isotropic distribution of the crystallite orientations. Instead, a highly anisotropic growth of 4P is observed. This corroborates the results of the EBSD experiments.

In addition to the polycrystalline gold surface also a vicinal Au(433) single crystal has been used as substrate for the growth of multilayer 4P films. In particular, the influence of carbon pre-coverages has been investigated. The results are presented in Chapter 7. For small amounts of surface carbon similar film morphologies have been found compared to 4P grown on Au(poly). This demonstrates the influence of a stepped surface geometry on the 4P film growth: On stepped Au surfaces like Au(poly) or Au(433) a similar tendency is found as on the Au(111) surface.

1. The 4P molecules prefer to align along high symmetry directions, in particular along the Au$\langle 1\bar{1}0\rangle$ direction. However, such a molecular alignment is preferred only in case that the step separation (terrace width s) is large enough to prevent the molecules from lying across terrace steps. The limiting factor s depends, of course, on the terminating crystal plane of the Au surface. If s is larger than the Van der Waals length L of the organic molecule, then the molecular orientation is similar to that on Au(111), i.e. the molecules align parallel to the Au$\langle 1\bar{1}0\rangle$ direction. In these cases, the existence of step edges does not influence the molecular packing, even, if the step edges are not parallel to the Au$\langle 1\bar{1}0\rangle$. Accordingly, anisotropic islands grow along several preferential directions. On very large and flat areas dendritic structures are observed.

2. If, however, the steps are sufficiently narrow, i.e. $s < L$, then the molecules prefer to align along the step edges instead. Consequently, needle-like crystallites grow highly anisotropic (oriented) with the needle direction perpendicular to the step edges.

Chapter 6

Dehydrogenation

This chapter describes the experimental finding that a significant fraction of oligo-phenylene molecules adsorbed on different Au surfaces are dehydrogenated and finally dissociated at elevated substrate temperatures. Depending on the length of the phenylene molecules and surface properties, large differences in the dehydrogenation/dissociation behaviour have been observed.

Adsorption of oligo-phenyls on clean Au surfaces and subsequent thermal treatment can lead to a considerable amount of dehydrogenation of the nP molecules at temperatures above 600 K. A further increase of the substrate temperature to about 1000 K results in a complete dehydrogenation of the molecular species and consequently to a contamination of the surface with carbon. This carbon uptake is very fast but levels off at a specific C coverage. The dehydrogenation process causes a considerable amount of molecular hydrogen that desorbs from the sample surface at these high temperatures. This H_2 desorption could be directly observed in the experiment. The high desorption temperature of 600 to 1000 K clearly discerns the experimentally observed H_2 desorption from a possible H_2 desorption which is caused by atomic hydrogen adsorbed from the residual gas phase of the UHV chamber. The latter proceeds at very low temperatures around 170 K [125].

During the thermal desorption of different thick nP films grown on various Au substrates multiple H_2 desorption peaks have been observed at temperatures between 600 K and 1000 K. The H_2 peaks were recorded by monitoring the time dependence of the H_2 partial pressure of the UHV chamber during the sample heating. As a first example Figure 6.1(a) depicts the increase of the H_2 partial pressure which is caused by the dehydrogenation of a 0.4 nm 4P film grown on a Au(433) surface at room temperature. The recorded spectra exhibit two distinct H_2 peaks labelled A and B around 650 K and 850 K, respectively. The H_2 signal was recorded off-line, i.e. the sample was positioned far away from the QMS entrance slit. This is necessary in order to exclude any unwanted influences, such as, for instance, some additional H_2 signal that is caused by C_xH_y cracking processes within the QMS ionization chamber due to some nP molecules that can reach the QMS upon desorption. It was carefully checked that the recorded H_2 signal is indeed caused by an H_2 desorption from the sample surface. The lower part of Figure 6.1(a) shows the

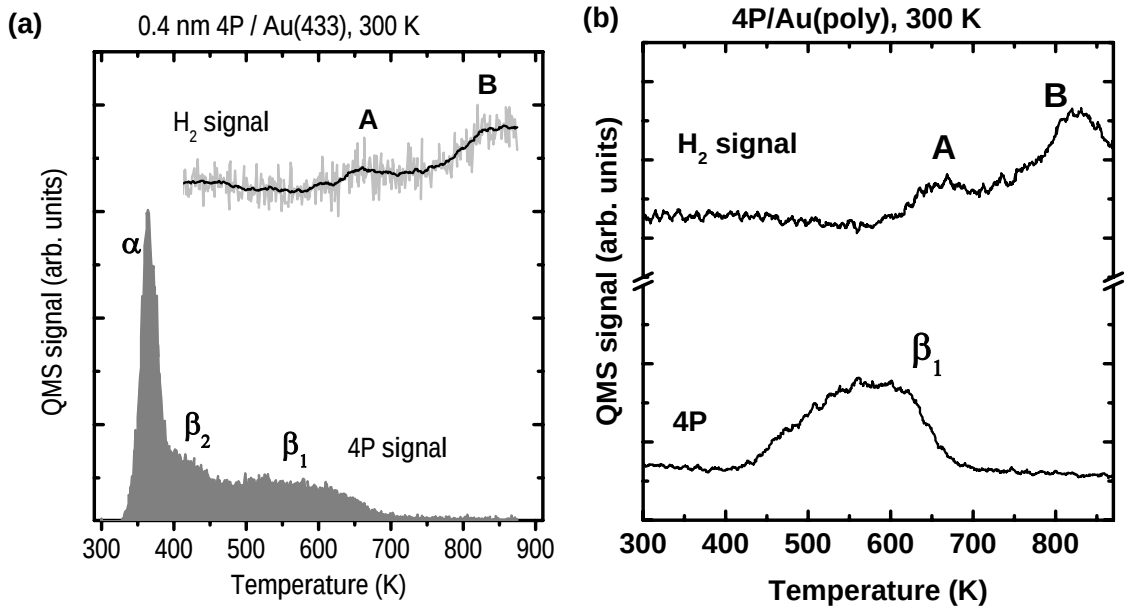

Figure 6.1: (a) Upper curve: TD signal (2 amu) of the H_2 desorption caused by the dehydrogenation of a 0.4 nm 4P film on Au(433). Lower curve: The corresponding TD signal of the 0.4 nm 4P film (304 amu). (b) The same as (a) for 0.2 nm 4P adsorbed on poly-crystalline Au.

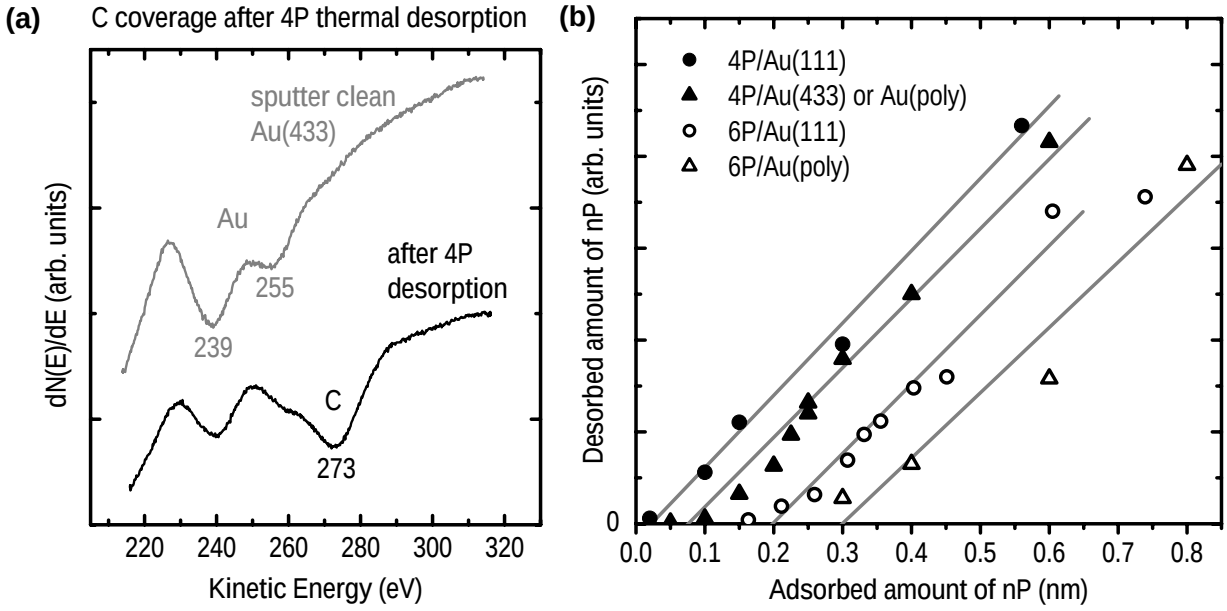

Figure 6.2: (a) Auger spectra showing the surface carbon uptake caused by a series of repetitive adsorption/desorption cycles of 0.4 nm 4P films on Au(433). (b) Compilation of TD data showing the adsorbed vs. desorbed amount of nP during the thermal desorption from different Au surfaces. The grey lines represent the linear fits to the individual data sets.

corresponding TD spectrum of a similar 4P film on Au(433). Comparing the two spectra shows that the H_2 desorption sets in at the high temperature end of the 4P monolayer desorption. Nearly all of the nP molecules that desorb intact from the surface do this before the H_2 desorption sets in. A quantification of the TD data with the microbalance reveals that a considerable fraction of about 0.1 nm of the 4P has not desorbed intact from the surface. Instead, it is dehydrogenated and the two experimentally observed H_2 peaks are caused by the thermal desorption of that hydrogen from the sample surface. It has been carefully checked that no additional molecular species desorbs from the sample surface upon the 4P dehydrogenation process. The only desorbing species observed was H_2 , which corroborates what was said so far. A similar behaviour has been observed for 4P grown on poly-crystalline Au, as shown in Figure 6.1(b). The residual carbon atoms are not desorbed, but stay on the Au surface. This is illustrated in Figure 6.2(a), where a distinct carbon peak emerges around 273 eV (lower curve) in the Auger spectrum of the Au(433) surface after several consecutive adsorption/desorption cycles of 0.4 nm 4P films compared to the sputter clean surface (upper curve).

For 4P grown on different Au surfaces like single crystalline Au(111) or poly-crystalline Au as well as for 6P grown on these surfaces a qualitatively similar dehydrogenation scenario has been observed. However, significant quantitative differences have been found, depending on the combination of nP molecule and substrate surface involved. Accordingly, the total amount of dehydrogenated nP molecules can vary by two orders of magnitude for the investigated combinations of nP molecules and different Au surfaces. The **quantification** of the total amount of dissociated nP molecules has been performed by two independent methods. The first one is based on the TD data of nP films with different thickness. In this case, an integration of each TD curve yields a measure of the absolute amount of nP molecules that have been desorbed intact from the Au surface upon sample heating. This can be compared to the corresponding total amount of molecules that have been initially adsorbed during the film preparation. Figure 6.2(b) shows a compilation of TD data for various combinations of nP molecules and Au surfaces and different film thicknesses. The intersection points of the linear fits, which are indicated by grey lines, with the abscissa yield approximately the total amount of nP molecules that are dissociated during a single adsorption/desorption cycle. It follows that the amount of dissociated nP varies roughly between 0.07 and 0.3 nm, depending on the nP-substrate combination. The corresponding values are summarized in Table 6.1 on page 142.

The second quantitative method was based on a direct quantification of the observed H_2 peaks which yields the total number of desorbed H_2 molecules. The quantification procedure has been done by calculating the integral peak areas of the H_2 spectra and comparing them with a well-known H_2 reference spectrum that has been recorded under the same experimental conditions. The latter has been obtained with the help of a calibrated tungsten filament that exhibits a total hydrogen saturation coverage of $1.48 \cdot 10^{15}$ H atoms. A flash desorption of the H saturated tungsten filament enables to record reproducible H_2 desorption spectra that can be used for the calibration of the 4P dehydrogenation spectra. Figure 6.3(b) presents such an H_2 reference spectrum. The corresponding integral peak area is 2.9854×10^{-8} mAs. Details on the calibration procedure can be found in [126].

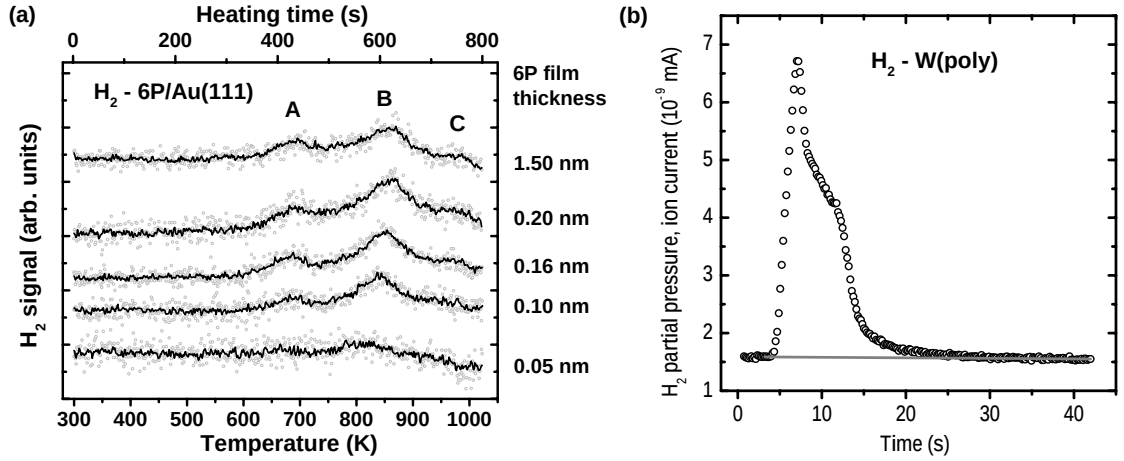

Figure 6.3: (a) Comparison of the H_2 desorption signals for different thick 6P films on Au(111) upon heating from 300 K up to 1023 K at a rate of 1 K/s. The experimental data (grey circles) are smoothed (black line). The characteristic H_2 peaks are labelled by A-C. (b) H_2 reference spectrum obtained for the calibrated tungsten filament. The peak area corresponds to a total amount of 1.48×10^{15} H atoms that desorb from the filament surface.

In the case of 6P films, again, all the H_2 spectra were recorded off-line under fixed experimental conditions. Due to the higher desorption temperatures observed for 6P compared to 4P the temperature range for the H_2 desorption experiments has been extended up to 1023 K. This has revealed a third high-temperature H_2 desorption peak around 950 K that has been labelled *C*. The latter can be clearly seen in Figure 6.3(a), where the H_2 desorption spectra of different thick 6P films adsorbed on atomically clean Au(111) at room temperature are shown. The film thickness ranges from 0.05 nm to 1.5 nm. At a very low initial 6P coverage of about 1/8 ML (0.05 nm) only one fairly broad H_2 desorption peak is observed that splits into three distinct peaks upon an increase of the film thickness. At a coverage of about 1/2 ML (0.2 nm) the three H_2 peaks $A - C$ are fully developed. A peak integration yields that the peaks *A* and *B* have approximately a ratio of 2 : 3, whereas the feature *C* is significantly smaller. In contrast to the peaks *A* and *B*, that are perfectly reproducible, in some experiments the peak *C* has not been observed, at all. An increase of the 6P coverage up to about 4 ML causes no further change of the H_2 features any more. Such a behaviour indicates that the dehydrogenation process of the 6P molecules is exclusively related to the molecules within the first semilayer. Otherwise, an increase of the H_2 peaks should be observed at higher 6P coverages. The first 6P semilayer consists of strongly adsorbed, flat lying molecules as described in full detail in Chapter 4.2.

The remarkable dependence of the H_2 desorption peaks $A - C$ on the 6P film thickness, which is demonstrated in Figure 6.3(a), together with the splitting of the H_2 desorption feature into three separated peaks can be interpreted by a proposed **multi-step dehydrogenation process** of the 6P molecules. Also in the case of 4P similar H_2 desorption features have been observed. This indicates that a similar dehydrogenation process exists for different nP molecules on various Au surfaces. The dehydrogenation is proposed to

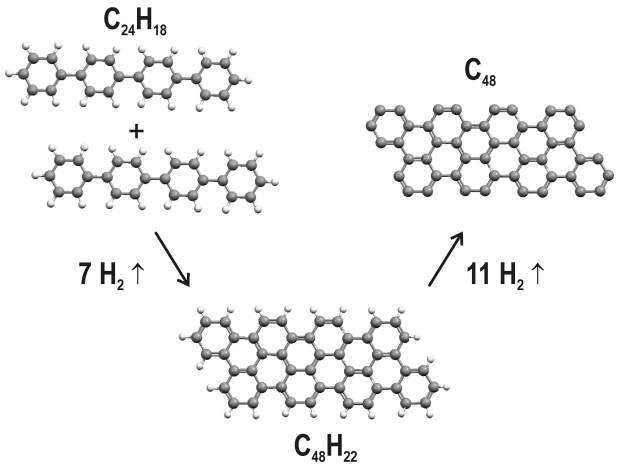

Figure 6.4: Schematics of the proposed two-step dehydrogenation process (cyclo-dimerisation) of nP molecules adsorbed on Au surfaces upon thermal treatment for the case of 4P. In a first step two 4P molecules undergo a condensation reaction to form a new polycyclic molecular species. The latter is fully dehydrogenated in a second step.

proceed as follows: 1st step: Around 650-700 K the nP molecules undergo a pairwise **condensation reaction** (cyclo-dimerisation) to form supermolecular "double-nP" polycyclic aromatic compounds. This process requires a partial dehydrogenation of the original nP molecules as illustrated in Figure 6.4. In the case of 4P, the intermediate molecular species formed is proposed to be hexabenzo-pyranthrene (HBP). This first reaction step causes the H_2 desorption that is observed as peak A. Similar surface reactions, i.e. thermally activated cyclo-dehydrogenations, have been reported in the literature for the system hexaphenylbenzene (HPB) on Cu(110) [127]. The new polycyclic molecular species are even stronger bound to the Au surface due to the enlarged π electron system compared to a single nP molecule. Consequently, they are prone to stay adsorbed on the surface up to higher temperatures. 2nd step: Between 800-900 K they fully dehydrogenate, releasing the residual H atoms. Again, H_2 desorbs from the surface causing peak B. The ratio of H_2 desorption $A : B$ is $14 : 22 \approx 1 : 1.6$ for 4P and $22 : 30 \approx 1 : 1.4$ for 6P, respectively. This is in good agreement with the experiment and hence corroborates the interpretation. 3rd step: The third peak C is very small compared to A and B. This may indicate that a minor fraction of the nP species can undergo a condensation reaction that involves three instead of two nP molecules. Consequently, "triple-nP" polycyclic species are formed, which are even stronger adsorbed on the Au surface compared to the former ones and they decompose not until around 950 K (peak C).

At the end of the dehydrogenation reactions the carbon molecular backbones stay on the surface resulting in a carbon overlayer on the Au surface. Although the existence of the carbon layer can be clearly identified by Auger spectroscopy, is has been impossible to observe a regular carbon structure in the LEED experiments. Obviously, the carbon atoms adsorbed on the Au surface do not form a regular superstructure, and in particular, not

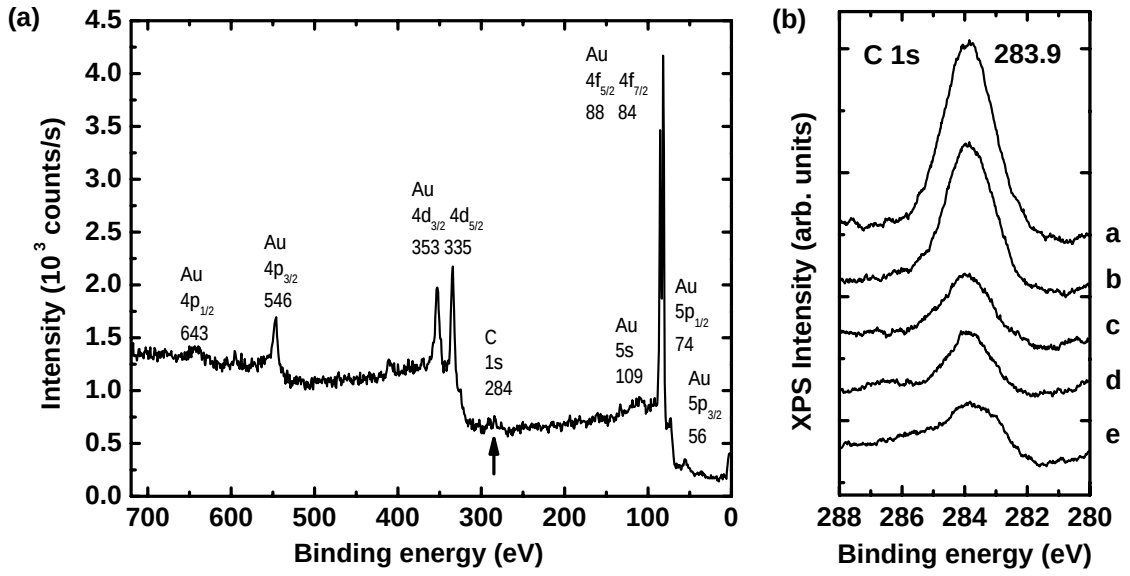

Figure 6.5: (a) Overview XPS spectrum of a 2 ML C coverage on Au(111) taken in the $\Delta E = const.$ mode with MgK_α radiation. The C 1s peak is marked by the arrow. (b) Detail scan of the C 1s energy regime for different overlayers of nP or carbon on Au(111). Curves a-c: 2 ML (0.8 nm), 1 ML (0.4 nm) and 1/2 ML (0.2 nm) 6P films, curves d-e: 1/2 ML 6P annealed at 750 K and 1000 K, respectively.

even on a single crystalline Au(111) surface. Unfortunately, to our best knowledge, in the literature information has been reported neither on the regularity nor on the chemistry of (sub)monolayer carbon coverages on a Au(111) surface. The latter has been investigated in XPS experiments in the present work. It has been observed, that a carbon overlayer prepared by thermal dissociation of nP on Au as described above, exhibits a C 1s peak with a binding energy around 284 eV. As an example is shown in Figure 6.5(a) the XPS spectrum of an approximately 2 ML thick carbon overlayer on Au(111). Figure 6.5(b) shows a detail scan of the C 1s energy regime for different overlayers of nP or carbon on Au(111). In the literature it has been reported that carbon bound to itself and/or hydrogen only, no matter what hybridization, gives a C 1s binding energy around 285.0 eV [87]. This can be used as an additional binding energy reference for the above discussion.

This particular carbon layer has been prepared by 6P dissociation. However, also C coverages that stem from dissociated 4P molecules exhibit similar C 1s binding energies. These results suggest a graphitic like conformation of the C overlayer on the Au surface, since a carbidic like carbon conformation would imply a significantly lower C 1s binding energy of about 280 to 283 eV [128]. The C 1s of pure graphite lies around 284 eV and aromatically bound carbon exhibits a C 1s binding energy around 285 eV.

Annealing an nP film slightly above the peak temperature of the first H_2 desorption peak (peak A) should result in a film that is composed exclusively of the "double nP" molecules. In the case of 6P, a series of LEED experiments has been performed in order to investigate the structural properties of such films. Two alternative preparation methods

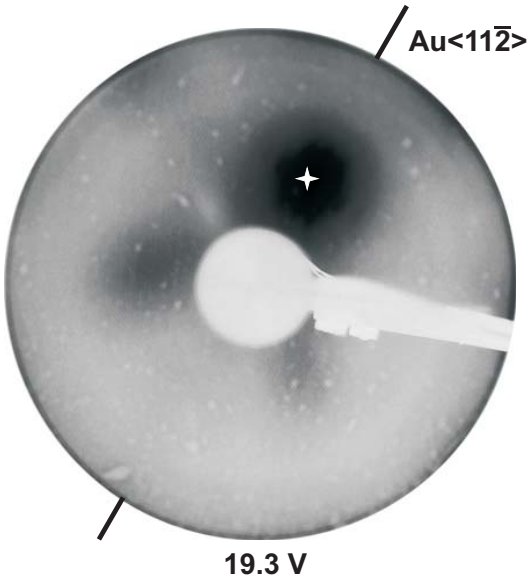

Figure 6.6: LEED image recorded for an overlayer of "double-nP" poly-cyclic aromatic species after deposition of 2 ML 6P on Au(111) at 690 K. The white star indicates the 00 reflection.

have been applied: 1) post-growth heat treatment of the 6P film and 2) deposition of 6P at high temperature slightly above the maximum of the H_2 peak *A*. The latter method resulted in the better results, i.e. the LEED pattern exhibited additional diffraction spots that could be attributed to an ordered overlayer of "double 6P" molecules. Clearly, a six-fold symmetric pattern is superposed over the original Au(111) pattern, which is a direct proof of an ordered overlayer of the polycyclic hydrocarbon species. Unfortunately, the observable LEED reflections of the organic overlayer have been very diffuse, as can be seen in Figure 6.6. The corresponding film has been prepared by deposition of 2 ML 6P onto the clean Au(111) surface kept at 690 K. The analysis of the inmost visible diffraction spots yields an inter-row distance of about $d = 0.78\ nm$.

Another important finding concerning the dehydrogenation of nPs on Au surfaces has been the fact that several different processes can occur simultaneously during the thermal treatment of an nP film.

1. **Pinning** of single molecules to surface defects. This effect is very pronounced on poly-crystalline or stepped vicinal Au surfaces that exhibit a high density of kinks and steps. The pinned nP molecules are prone to the dehydrogenation reactions described above, because they stay on the surface up to higher temperatures. In the case of the $(22 \times \sqrt{3})$ reconstructed Au(111) surface an estimate of the surface density of "elbow" defect sites can be made: According to the literature (cf. Section 1.4) an elbow unit cell is at least 12×6.3 nm^2, containing two elbow sites. Thus about 2.6×10^{12} elbow sites per cm^2 exist on the reconstructed Au(111) surface. Assuming that each elbow site acts as a pinning center for the adsorbed nP molecules that are consequently dehydrogenated upon thermal treatment, yields an approximate carbon

coverage of about $6-9\times10^{13}$ C atoms/cm^2 or in other words 4-6% of the Au surface density. Hence, the elbow sites could be principally responsible for a considerable fraction of the total amount of dehydrogenated nP molecules.

2. A relatively strong covalent-like bonding of the nP molecules to the Au surface via the π electron system. This effect is enhanced for the longer nP molecules like 6P.

3. Carbon atoms can passivate Au surface defects, which leads to a reduced dehydrogenation activity of partially C covered Au surfaces compared to atomically clean Au surfaces and also to an enhanced surface mobility of the adsorbed nP molecules.

4. A fourth, yet hypothetic effect can be the planarization of nP molecules upon adsorption on the solid surface. This effect is supposed to loosen the intra-molecular binding and thus de-stabilizes the planarized molecules compared to nP molecules in the gas phase, which exhibit a twisted conformation. Hence, the adsorbed nP molecules become prone to dehydrogenation due to the planarization. This is supposed to be pronounced with increasing length of the nP molecules.

The C coverage of the Au surface that is caused by a single nP adsorption/desorption cycle can be significantly increased by applying additional cycles without interstitial sputter cleaning of the surface. Such a behaviour is observed independent of the nP film thickness adsorbed during each cycle. The **C saturation coverage** is reached typically after < 10 repeated cycles. At this point, no more nP molecules are dissociated upon substrate heating and all of the adsorbed nP molecules are intactly desorbed. Consequently, no H_2 desorption is observed, too. However, during the build-up of the C coverage upon the application of several consecutive adsorption/desorption cycles, a H_2 desorption can be clearly observed. Between two consecutive cycles the H_2 desorption peaks decrease until they completely vanish once the C saturation is reached. Such a behaviour is demonstrated in Figure 6.7(a) for the system 6P/Au(111) at 300 K. Five consecutive adsorption/desorption cycles each of 0.2 nm 6P have been recorded. The substrate has not been cleaned between the cycles, which enables a cumulation of the surface C coverage. It can be seen that after five cycles the H_2 desorption has dropped nearly below the detection limit. Simultaneous to the decrease of the H_2 desorption, the amount of 6P molecules increases which are desorbed intact from the Au surface upon sample heating. This can be seen in Figure 6.7(b), where the TD spectra of seven consecutive adsorption/desorption cycles each of 0.2 nm 6P are shown. Two effects are important: Parallel to the increase of the C coverage the integral peak area increases. This shows the decrease of the dissociated amount of 6P during each single cycle. Secondly, the shape of the TD spectra changes from one cycle to the other, according to the increasing C coverage. During the 1st cycle, which is done on the originally clean Au(111) cycle, only about 0.04 nm 6P are desorbed intact. Hence the shape of the 6P TD spectrum is identical to that of a 0.2 nm thick 6P film grown on clean Au(111) as described in Chapter 4 (see page 70). On the other hand, the last recorded cycle represents a TD spectrum of a 0.2 nm 6P film grown on the already C saturated Au(111) surface.

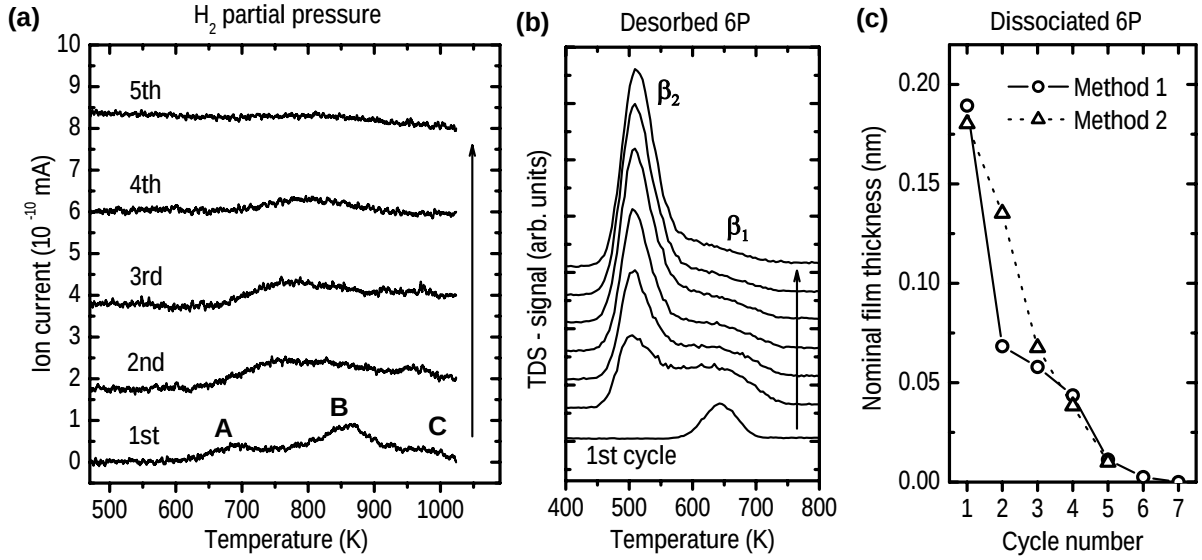

Figure 6.7: Carbon saturation of the Au surface is reached by a cumulative series of adsorption/desorption cycles each with 0.2 nm 6P on originally clean Au(111) at 300 K. The substrate is not cleaned between the cycles. (a) The H_2 desorption decreases to zero when the C saturation coverage is reached. The integral peak areas of the cycles 1 to 5 are 1.6, 1.2, 0.6, 0.3 and $0.1 \cdot 10^{-8}$ mAs, respectively. (b) The amount of intactly desorbed 6P increases as long as the carbon saturation of the surface is not reached. (c) Simultaneously, the amount of dissociated 6P per cycle decreases. The quantification has been done by two independent methods, that are based on the TD spectra of 6P (method 1) or H_2 (method 2).

Hence, the high-temperature desorption peak β_1 is reduced, an effect which is described in full detail in Chapter 7.

The amount of 6P molecules that are dissociated during one cycle has been obtained from either one of three independent quantification methods: 1) Quantification of the 6P TD spectra with the quartz microbalance. 2) Quantification of the H_2 desorption spectra with the help of a calibrated H_2 reference spectrum. A comparison of the results from these two methods for the system 6P/Au(111) is shown in Figure 6.7(c). It can be clearly seen that a good agreement has been obtained between these two quantification methods. 3) Quantitative photoelectron spectroscopy has been successfully applied in some cases. The details of this method are described in Appendix E.

A summation of the partial carbon coverages from several consecutive adsorption/desorption cycles yields the C saturation coverage of the Au surface. Equally, the overall total amount of dissociated 6P (in nm) can be obtained. Such an analysis has been performed for all of the investigated nP/Au systems. The corresponding data are summarized in Table 6.1 for the different combinations of nP films and Au surfaces. It has been clearly shown that 6P adsorbed on Au surfaces is significantly more "reactive" upon thermal treatment than 4P. The different types of surface geometry (steps, etc.) has a great influence on the dehydrogenation behaviour of the adsorbed nP molecules. And thirdly, the difference in the total amount of dissociated nP between a single cycle and the C saturation coverage

Table 6.1: Total amount of thermally dissociated nPs on different Au surfaces (mean film thickness equivalents). The saturation is reached after several consecutive adsorption/desorption cycles. The carbon coverage equivalents are also given.

	1st cycle (nm 6P)	C saturation (nm 6P)	C saturation (ML)
4P/Au(111)	$\ll$	0.01	0.03
4P/Au(poly)	0.05	0.07	0.3
4P/Au(433)	0.07	0.1	0.4
6P/Au(111)	0.2	0.37-0.42	1.5-1.8
6P/Au(poly)	0.24	0.48	1.9

can be seen, which is caused by the accumulation of carbon during several consecutive adsorption/desorption cycles.

The latter method has been frequently applied in the experiments in order to prepare C saturated Au surfaces (see Chapter 7). Additionally, an alternative routine for preparing C saturation coverages has been used, which utilizes the deposition of nP molecules directly onto the heated Au substrate. Of course, the substrate temperature has to be larger than the temperature which is necessary for thermal dissociation of nP on Au, i.e. about 1000 K. This way, the dissociation takes place already upon the adsorption of the nP molecules on the Au surface. Empirically determined preparation parameters, that yield good results for the saturated carbon coverage, are: substrate temperature 1023 K, deposition rate 0.3 nm/min, overall exposition time 5 to 10 min.

Chapter 7

Effect of Substrate Chemistry

This chapter investigates oligo-phenyl thin films grown on different carbon pre-covered gold surfaces. The surface carbon changes the chemistry of the substrate surface compared to the clean Au surface. It is demonstrated that the structure and morphology of oligo-phenyl films can be significantly changed already by low carbon pre-coverages (< 1 ML), which enables a tailoring of the organic films.

In Chapter 6 the carbon contamination of different Au surfaces during the heat treatment of nP films grown on atomically clean Au has been discussed in detail. In a next step, the dehydrogenation process of the nP molecules, that is responsible for the build-up of the surface carbon contamination, has been utilized experimentally in order to prepare well-defined carbon pre-coverages on different Au surfaces. These partially C-covered Au surfaces were used as new substrates for the growth of nP films. Various different combinations of Au substrates and carbon pre-coverages have been investigated. Table 7.1 gives an overview of the sample combinations used in this work.

7.1 Surface mobility of nP molecules

The growth of (sub)monolayer 4P and 6P films on atomically clean Au(111) surfaces results in disordered films at substrate temperatures < 200 K. The build-up of regular 4P film structures, however, could be observed in LEED experiments, when the organic films were either grown or annealed at higher temperatures, as described in Section 4.2. Obviously, a re-crystallisation of the annealed nP films occurs above a certain threshold temperature. In both cases, the existence of a regular nP film structure requires a sufficiently high surface mobility of the adsorbed nP molecules on the substrate surface. The above findings suggest that at low substrate temperatures the surface mobility of the nP molecules is reduced, which hinders a regular film growth.

It has been observed, though, that very small carbon pre-coverages on the Au(111) surface in the order of only a few percent of a monolayer, that have been applied prior to the nP deposition, can enable a regular nP film growth already at low temperatures. This is attributed to an increased surface mobility of the nP molecules, which is caused by

Table 7.1: The different combinations of nP film, C pre-coverage and Au substrate investigated in this work. The bold symbols indicate the corresponding C coverage representing the saturation coverage reachable via thermal de-hydrogenation of nP. In some cases also X-rays have been used for preparing the C-covered samples.

C pre-coverage (ML)	Au(111)	Au(poly)	Au(433)
0.03	**4P**	-	-
0.15	4P	-	-
0.3	-	**4P**	-
0.4	-	-	**4P**
0.5	4P	-	-
0.6	-	4P	-
0.7	-	-	4P
1.5-2	**6P**	**6P**	-

the C pre-coverages. On Au(111), for instance, a pre-coverage as small as 0.03 ML carbon is sufficient to enable a highly ordered 4P film growth already at a temperature of 93 K. Figure 7.1 shows two examples of LEED images obtained for (a) 0.5 ML and (b) 1 ML 4P grown on a 0.03 ML C/Au(111) surface at 93 K. The obtained structures of the regular 4P semilayer and full monolayer are identical to those found for 4P grown on the clean Au(111) surface at 300 K, as described in Section 4.2 and 4.3, respectively. Although the threshold temperature for a regular film growth is significantly reduced by the 0.03 ML surface carbon, it does not influence the molecular packing within the first semilayer or monolayer.

A possible explanation for this finding is as follows: On the atomically clean Au(111) surface some 4P molecules are pinned to defect sites and cannot diffuse over the surface below a certain threshold temperature. These pinned molecules hinder the residual "free" (or unpinned) molecules to form a regular film structure. Above the threshold temperature enough thermal energy is available for the pinned molecules to overcome their increased activation barrier for surface diffusion and a regular film growth is possible. On the slightly C-covered surface, however, the carbon atoms passivate the Au surface defects, which can no longer act as pinning centers for adsorbed 4P molecules, independent of the substrate temperature. Hence, a regular film growth is possible at low temperatures, too.

This explanation includes several important conclusions: 1) The actual surface mobility of 4P molecules on a clean and perfect Au(111) surface is quite high and enables the growth of regular structures already at 93 K. An estimation of the corresponding activation barrier for the surface diffusion, E_{diff}, can be made on the basis of the value of kT at 93 K and yields roughly $E_{diff} \leq 8$ meV. Comparing this value to the experimentally determined activation barrier for desorption, E_{des}, for 4P and 6P (cf. Appendix A), shows that E_{diff} is approximately two orders of magnitude lower than the E_{des}. 2) In the real experimental situation the Au(111) surface exhibits defect sites. These defects can either be vacancies, adatoms, kinks, steps or reconstruction elbows of the reconstructed Au(111) surface, which act as pinning centers for the adsorbed nP molecules. Hence, the

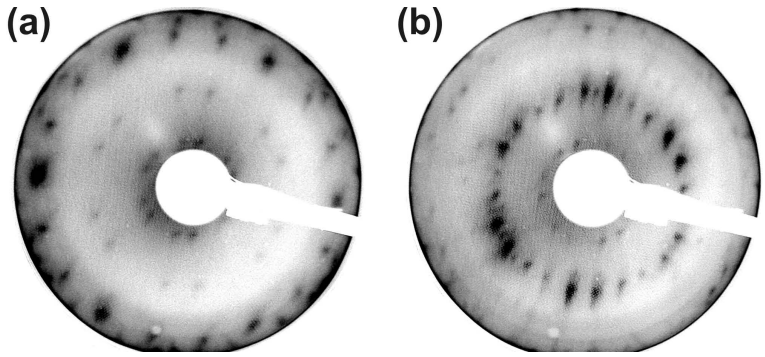

Figure 7.1: LEED images recorded for (a) semilayer and (b) monolayer 4P grown on a 0.03 ML C/Au(111) surface at 93 K. The corresponding beam voltages are 19.2 and 18.7 V, respectively.

C-passivated 0.03 ML C/Au(111) surface can be considered as similar to an ideal Au(111) surface. 3) The density of Au surface defects can be estimated from the value of the C coverage on the passivated surface, i.e. 0.03 ML or 3%, respectively.

7.2 Monolayer

As far as the structure of the 4P monolayer is concerned, it has been shown that a carbon pre-coverage of 0.03 ML has no significant influence on the monolayer packing compared to the growth on atomically clean Au(111). Also the TD data of 4P grown on the 0.03 ML C/Au(111) surface is similar to that on clean Au(111). The corresponding TD spectra are presented in Figure 7.2(a).

To begin with the low coverage regime (curves $a-d$), the first desorption peak, labelled β_1, appears above 550 K. With increasing coverage the peak maximum shifts to lower temperatures until β_1 is saturated at a mean film thickness of about 0.15 nm. At even higher coverages a second peak, labelled β_2, appears around 380 K which saturates at about 0.3 nm (curve d). Both peaks β_1 and β_2 comprise roughly the same total amount of 4P molecules. They have been attributed to first-order desorption from the 4P monolayer. The shift of the peak maxima of both peaks to the low temperature side with increasing coverage indicates repulsive forces acting between neighbouring molecules within the monolayer. The saturation coverage of the first monolayer is about $0.25-0.3$ nm. At higher coverages, a sharp desorption peak, labelled α, is observed that steadily increases with increasing coverage. This is shown in the insert of Figure 7.2(a). The peak α is attributed to zero-order desorption from the multilayer.

In the following it will be shown that increasing the surface carbon pre-coverage to values higher than approximately 0.1 ML changes the structure of the saturated nP monolayer. This could be concluded from the experimental TD and LEED data. In particular, 4P grown on a 0.15 ML C and 0.5 ML C pre-covered Au(111) surface has been investigated.

On the 0.15 ML C/Au(111) surface the desorption kinetics of 4P in the monolayer

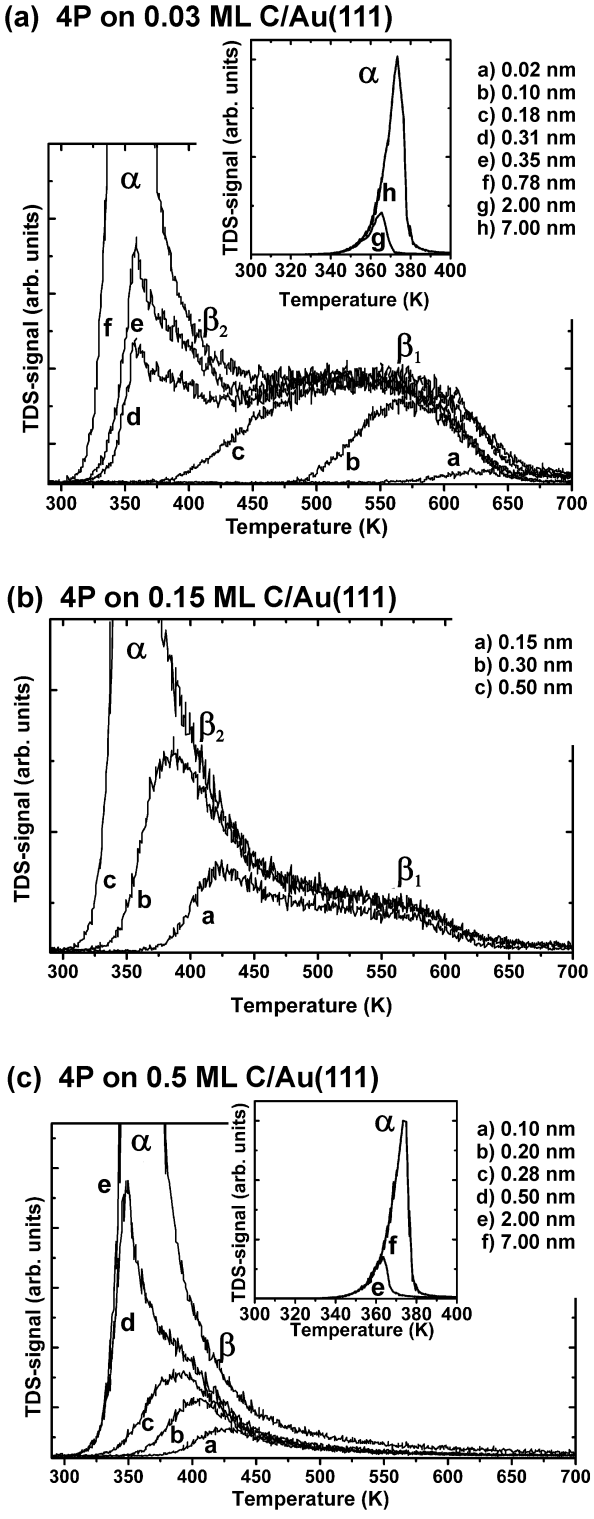

Figure 7.2: Series of TD spectra of 4P grown on variably C covered Au(111) surfaces at 93 K. The multi- and monolayer desorption peaks are denoted by α and β, respectively. The total amount of deposited 4P for each single TD spectrum is given as the mean film thickness in nm. (a) TDS-series on 0.03 ML C/Au(111). Insert: large scale view at higher coverages. On this scale, the monolayer desorption peaks are hardly visible. (b) TDS series on 0.15 ML C/Au(111). (c) TDS series on 0.5 ML C/Au(111). Insert: large scale view at high coverages.

regime is significantly different from that on the clean surface. The corresponding TD data is shown in Figure 7.2(b). Again, the 4P films were grown at 93 K. Similar to the previous case, two monolayer desorption peaks, labelled β_1 and β_2, have been observed and a similar interpretation for the origin of the peaks can be given. Although the positions of the two desorption peaks are similar to those on the 0.03 ML C/Au surface, however, the saturation coverages are significantly different. The high temperature monolayer peak, β_1, is significantly decreased in favour of an enhanced β_2 peak. The ratio of the integral peak areas, $\beta_2 : \beta_1$, is roughly 3 : 1. The saturation coverage of the full 4P monolayer, $\beta_1 + \beta_2$, however, is nearly unchanged with respect to the previous case: Again, the full 4P monolayer saturates at about 0.3 nm of mean film thickness, which equals 8×10^{13} 4P molecules/cm^2. The changed ratio of the two monolayer desorption peaks already suggests that the molecular packing of the 4P monolayer is changed due to the 0.15 ML carbon coverage compared to the clean surface.

The TDS monolayer spectrum in Figure 7.2(b) can be interpreted in terms of a **superposition** of two different types of 4P monolayer packing domains, denoted "type A" and "type B". The type A domains exhibit both flat and edge-on adsorbed 4P molecules (edge-face packing) similar to the monolayer structure found on the C-free Au(111) surface shown in Figure 4.10(a) and they contribute in equal shares to the β_1 and β_2 peak, respectively. Hence, the β_2 peak in Figure 7.2(b), which corresponds to edge-on adsorbed molecules, is attributed to a superposition of two peaks, i.e. $\beta_2 = \beta_{2,A} + \beta_{2,B}$. The $\beta_{2,B}$ peak corresponds to the second type of packing domains (type B), which comprise solely edge-on oriented 4P molecules. Apparently, this type B domains are by far the dominating ones.

This finding has been corroborated by LEED experiments. Growing a saturated monolayer (0.3 nm) of 4P on a 0.15 ML C/Au(111) surface leads to a significant change of the observed LEED images with respect to 4P on clean Au(111). Figure 7.3 presents some LEED images recorded for 1 ML 4P grown at 300 K[1]. The LEED pattern is significantly different from that of the type A domains presented in Figure 4.7(a) that was found for 4P on the clean Au(111) surface. All the observed diffraction spots of the new LEED pattern can be unambiguously attributed to one single structural domain, i.e. the type B domain. An analysis of the LEED data has yielded the parameters of the regular 4P surface unit cell: $a = 10.5$ nm, $b = 2.21$ nm, $\gamma = 71°$ and $\phi = 11°$, where a and b denote the length of the real space unit cell vectors, γ is the cell angle and ϕ is the azimuthal rotation angle of the cell relative to the Au$\langle 1\bar{1}0\rangle$ direction. The matrix representation of this structure is

$$M = \begin{pmatrix} 4.09 & 0.83 \\ 5.61 & 9.03 \end{pmatrix} \approx \begin{pmatrix} 4 & 1 \\ 5.5 & 9 \end{pmatrix} \tag{7.1}$$

This indicates a point-on-line coincidence type of epitaxy for the type B domains. Also a simulation of the evaluated overlayer structure has been made. The results show a good agreement between the experimental data (black) and the simulated LEED pattern (grey)

[1]Similar LEED images have been obtained for films grown at 93 K, too, but with inferior quality, which can be attributed to the beneficial influence of annealing on the crystallinity of the organic film.

for the type B structural domain, as shown in Figure 7.4. Compared to the type A domains of 4P grown on clean Au(111), the unit cell dimensions of the type B saturated monolayer are only slightly changed. In particular, the lengths of the cell vectors, a and b and the cell angle, γ, are nearly unchanged, whereas the azimuthal angle, ϕ, is significantly different.

Although from the LEED experiments no proper information on the molecular packing within the 4P monolayer surface unit cell can be derived, a further insight can be gained as follows: Similar to the argumentation given in Section 4.2, the results from additional XRD investigations performed on several nm thick 4P films help to propose a structural model for the type B domains found for the 4P monolayer on 0.15 ML C/Au(111). The 4P bulk films used for the XRD measurements have been prepared under the same conditions as the monolayer films used for LEED. Although the XRD data will be discussed in full detail not before Section 7.5, one important result is already given here: The 4P bulk crystallites exhibit the (201) orientation, which comprises lying, side tilted molecules, as illustrated in Figure 1.3. No edge-face packing exists for the (201) orientation. Instead, all molecules exhibit the same relative tilt angle with respect to the (201)-plane. In analogy to Section 4.2, a molecular packing for the type B domains is presumed, which is similar to that observed for the bulk orientation. The molecules adopt similar adsorption geometries relative to the Au(111) surface, instead of an edge-face packing with flat and side-tilted molecules. This indicates a weakening of the adsorbate-substrate interactions due to the surface carbon.

Based on the particular molecular packing motif of the 4P(201) plane, a structural model for the 4P monolayer has been proposed, which is illustrated in Figure 7.5. The 4P molecules exhibit a lying conformation where the aromatic plane is side-tilted with respect to the Au(111) plane by an angle δ, as shown in Figure 7.5(a). In agreement to the quantitative TD data the presented structure comprises two molecules per unit cell. For spatial reasons the tilt angle δ is supposed to be > 0. This is also in agreement to the interpretation of the TD data shown in Figure 7.2(b), where the β peak of the type B domain is attributed to edge-on oriented molecules. Unfortunately, no NEXAFS measurements have been performed for the system 4P/0.15 ML C/Au(111) and therefore no experimental value has been obtained for the tilt angle δ. In Figure 7.5 the angle δ has been chosen as one thinks best. Additionally, an alignment of the 4P molecules along the Au$\langle 11\bar{2}\rangle$ direction similar to the findings on a C-free Au(111) surface has been proposed, as it seems most probable.

The decrease of the β_1 peak with increasing C pre-coverage of the Au(111) surface is even more pronounced on the 0.5 ML C/Au(111) surface. The corresponding TDS series is presented in Figure 7.2(c). At low coverages only a single desorption peak, β, arises in the temperature range between 350 and 450 K, similar to the β_2 peak found for the less C covered surfaces. It is attributed to monolayer desorption. No second, high temperature desorption peak exists on the 0.5 ML C/Au surface. Interestingly, the total coverage of the saturated β peak still corresponds to a mean 4P film thickness of 0.3 nm. This suggests that the 4P monolayer again consists of lying molecules, i.e. the long molecular axes are almost parallel to the Au(111) plane. The basic TD data are listed in Table A.3. From the obvious similarity of the shape and position of the β_2 peak on the C-free surface and

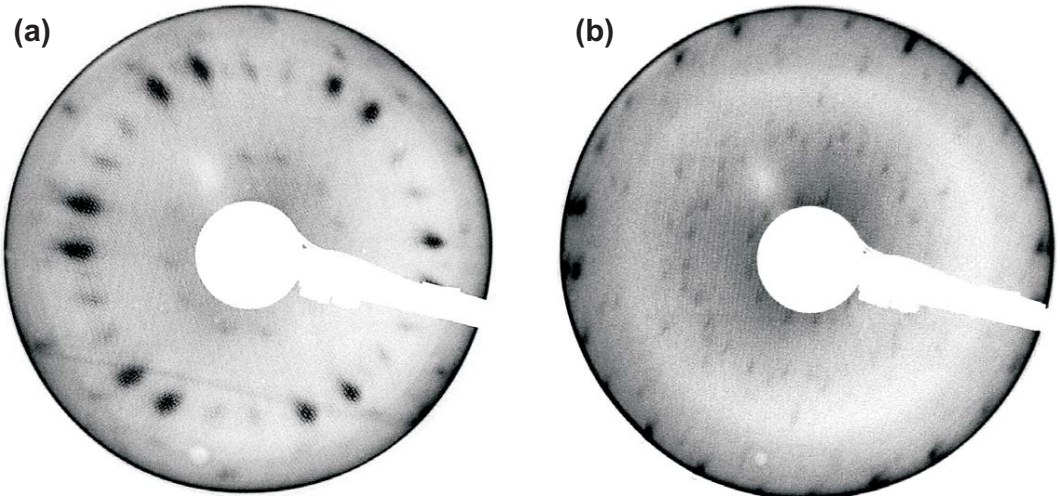

Figure 7.3: LEED images of 1 ML 4P on 0.15 ML C/Au(111) at 300 K, recorded at (a) 12.1 V and (b) 24.3 V.

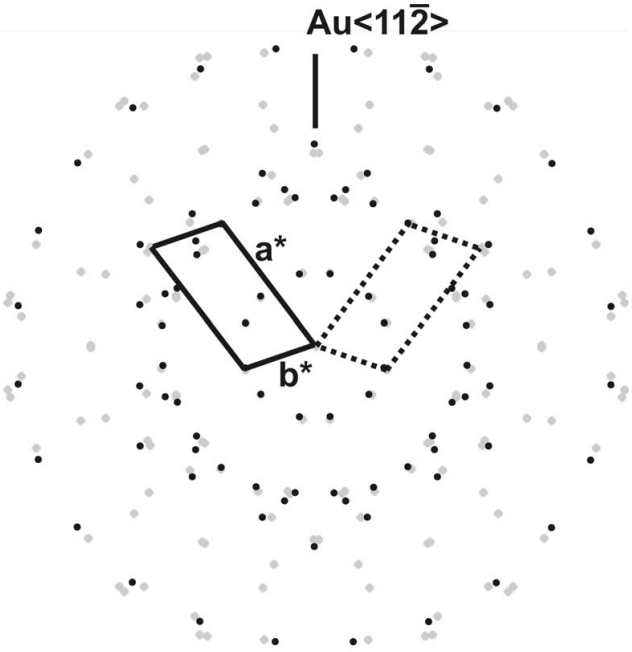

Figure 7.4: 4P monolayer on 0.15 ML C/Au(111): Comparison of the experimental LEED data (black) with simulation (grey) for a common beam voltage of 20V. The reciprocal unit cell is indicated (solid) together with a mirror equivalent unit cell (dotted).

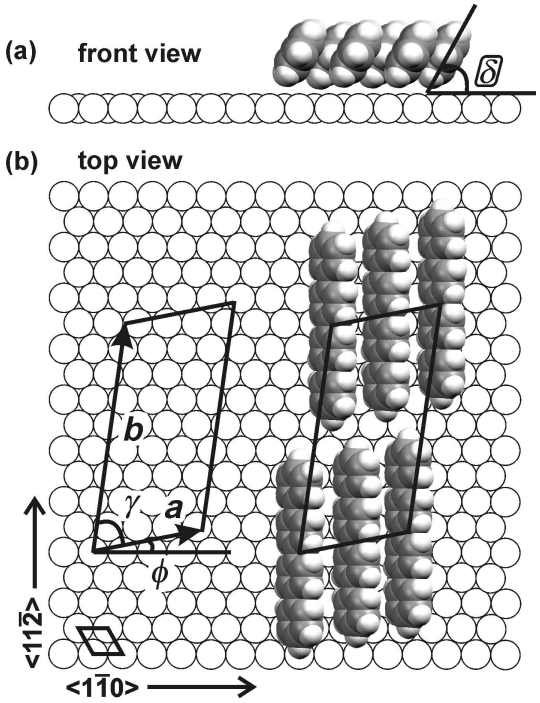

Figure 7.5: Proposed real space van der Waals representation of the 4P monolayer structure on a 0.15 ML C/Au(111) surface. The surface unit cell is characterised by the lengths of the unit cell vectors, a and b, the cell angle, γ, and the azimuthal angle, ϕ. The aromatic planes of the 4P molecules are side-tilted with respect to the Au(111) plane by an angle δ.

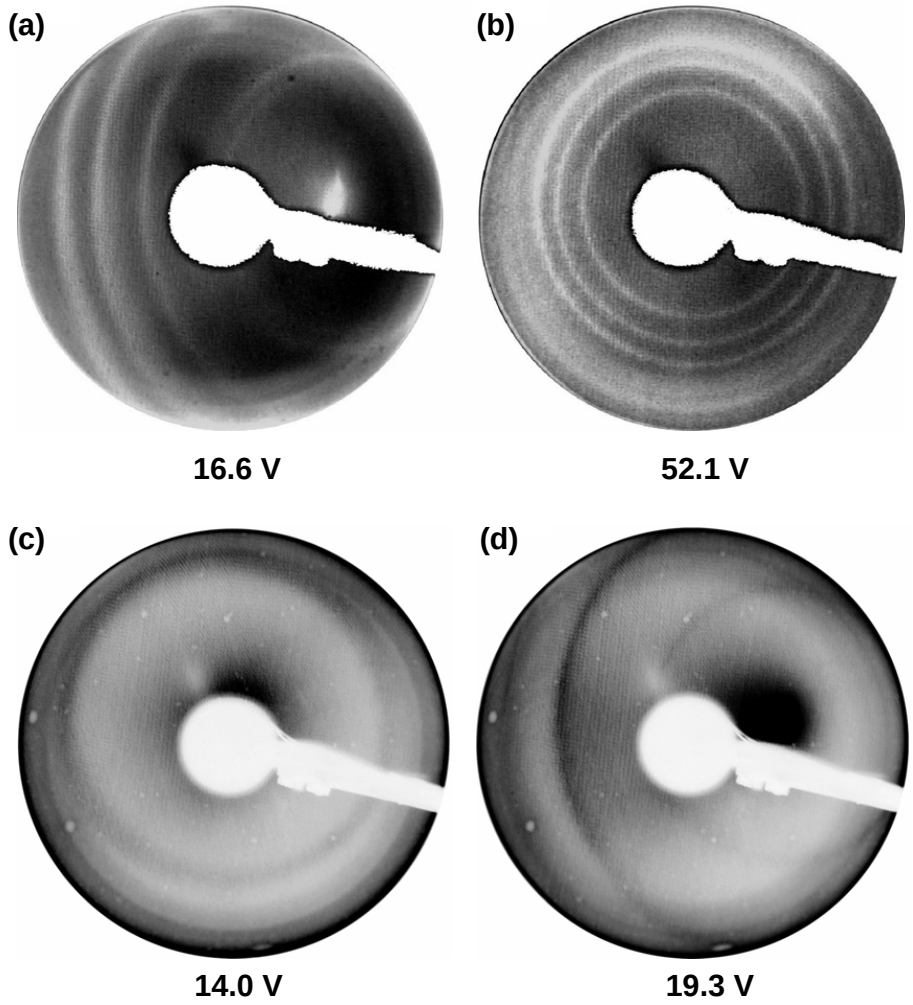

Figure 7.6: LEED images (a)-(b) of a 3 nm 4P film grown on 0.5 ML C/Au(111) at 300 K. (c)-(d) 2.4 nm 6P grown on 2 ML C/Au(111) at 300 K.

the β peak on the 0.5 ML C/Au surface, it seems plausible to attribute the β peak to an edge-on adsorption geometry, similar to the former case. The total suppression of a high temperature β_1 peak suggests that the 4P monolayer comprises only edge-on adsorbed molecules.

However, no regular LEED patterns could be observed for the 4P monolayer (0.3 nm) grown on the 0.5 ML C/Au(111) surface at room temperature. This suggests that the 4P monolayer predominantly grows in a **disordered** manner. Apparently, the 0.5 ML surface carbon induces a high degree of disorder on the Au surface, which destroys a defined epitaxial relationship between the adsorbed 4P molecules and the Au surface. Such an explanation is in good agreement with the experimental finding, that the surface carbon coverage alone produces no distinct LEED pattern, i.e. it is adsorbed in an amorphous manner.

If the 4P coverage is further increased above the saturated 4P monolayer of lying molecules, however, it could be observed with LEED that regular 4P domains start to grow. However, these regular 4P domains no longer show any preferential azimuthal orientation relative to the C/Au(111) surface. Accordingly, **ring-like LEED patterns** have been observed, as shown in Figure 7.6(a)-(b) for a 3 nm thick 4P film grown on 0.5 ML C/Au(111) at room temperature and (c)-(d) for a 2.4 nm 6P film grown on 2 ML C/Au(111), respectively. Although in this case no complete determination of the corresponding real space surface unit cell is possible, an analysis of the inmost ring observable with LEED at a minimum beam voltage allows a further insight: This particular ring radius corresponds to the length, b, of the largest possible real space surface unit cell vector of a regular 4P overlayer structure. Assuming, for a first approximation, a rectangular surface unit cell, a length of $b = 1.1$ nm is obtained in the case of 4P. This is significantly smaller than the van der Waals length of a 4P molecule (roughly 2 nm). Therefore, the regular 4P domains responsible for the ring-like LEED structures cannot comprise any lying 4P molecules, as found for the less C-covered surfaces. Instead, the 4P molecules are supposed to be nearly **standing upright** with respect to the C/Au surface, i.e. the long molecular axes are oriented roughly normal to the Au(111) plane. These findings are corroborated by the results of XRD experiments performed on a 30 nm thick 4P film grown on 0.5 ML C/Au(111), where also an upright molecular orientation was found for the 4P crystallites in the bulk phase (see Section 7.5). Also for 6P a similar interpretation can be given. Assuming for a first approximation that the upright standing molecules adopt the 4P(001) orientation, allows to compare the above value of 1.1 nm with the geometric parameters of the corresponding 4P(001) plane unit cell (cf. Figure 1.3). Unfortunately, the geometric parameter derived from the ring-like LEED patterns presented in Figure 7.6(a)-(b) do not agree well with the experimentally observed (001) orientation in a 30 nm thick 4P film. This discrepancy may be due to the fact that in the 3 nm thick 4P film investigated with LEED, which comprises upright standing molecules, still the 4P bulk structure is not fully established. Instead, similar to the case of flat lying molecules, the packing structure undergoes a change upon the transition from standing monolayer to bulk structure.

In this context, the question arises, if these nP films (about 2-3 nm thick) still exhibit an underlying monomolecular wetting layer comprised of flat lying molecules. Alternatively, a different scenario is possible, where the initially lying molecules in the amorphous 0.3-0.4 nm thick wetting layer are forced into an upright standing orientation upon increasing nP coverage. This would imply that for thicker nP films no distinct wetting layer exists underneath the bulk crystallites. Instead, the film grows already in a standing crystal orientation for coverages around 2-3 nm. A continuous layer of upright standing nP molecules would exhibit a nominal film thickness similar to the Van der Waals length of the nP molecules. Although no direct experimental evidence was found to distinguish between these two scenarios, the second one seemed more plausible, because it agrees with the experimental finding that already a 0.5 ML carbon pre-coverage (for 4P) significantly weakens the adsorbate-substrate interactions compared to the clean Au surface. This can be deduced from the fact that no preferential azimuthal orientation of the 4P crystallites relative to the Au(111) surface was observed for bulk crystalline films. Hence, the

molecule-molecule interactions within the nP film are supposed to be responsible for the upright standing conformation. This would also effect the initially lying molecules and change their orientation above some critical nP coverage.

7.3 Desorption kinetics

A similar decrease or even complete suppression of the β_1 peak due to a carbon coverage has been observed in different TD experiments for the systems 4P/0.5 ML C/Au(poly) shown in Figure 7.7, 6P/2 ML C/Au(poly) shown in Figure 7.8 and 6P/2 ML C/Au(111) shown in Figure 7.9, respectively. For all of these systems a similar interpretation of the observed TD spectra holds true as already described in the previous section: with increasing C coverage the high-temperature monolayer peak β_1 is decreased in favour of an increased low-temperature monolayer peak β_2. A continuous change of the TD spectrum upon an accumulation of surface carbon similar to the previous cases is also demonstrated in Figure 6.7(b) for 6P on partially C-covered Au(111). Similar to the previous cases, the β_1 peak vanishes in favour of an enhanced β_2 peak with increasing carbon coverage. All these TD results of nP grown on different C-covered Au surfaces reflect the general effect of a weakening of the adsorbate-substrate interactions caused by the surface carbon.

The desorption peaks appearing in the multilayer coverage regime exhibit clearly zero-order desorption characteristics: A common leading edge, peak maxima shifting to higher temperature with increasing coverage, and a sharp cut-off at high temperature.[2] The calculation of the **multilayer desorption energy** for nP on heavily carbon-covered Au(111) surfaces based on the TD spectra of 7 nm thick films has yielded the values

$$\begin{aligned} 4P/0.5\ ML\ C/Au(111): \quad E_{des} &= 1.6\ eV/molecule \\ 6P/2\ ML\ C/Au(111): \quad E_{des} &= 2.2\ eV/molecule \end{aligned}$$

A compilations of the basic TD data of nP on different Au based surfaces can be found in Table A.3.

Comparing the values for different Au surfaces shows slight variations of E_{des} for a single type of molecule, which lie in the range of about 0.1-0.2 eV/molecule. This can be explained by the fact that nP grows preferential crystal orientations on certain substrates. Hence, the values of E_{des} for one type of nP molecule may vary depending on the crystal orientation of the deposited nP film. This aspect has already been discussed in Section 5.1 for the case that different bulk crystal orientations are adopted depending on the different substrate geometries. Interestingly, in both cases (substrate geometry or chemistry) similar

[2] A closer inspection of the multilayer desorption spectra reveals slight deviations of the trailing edge of the α peak at high temperature that depend on the QMS mass signal used for recording the spectra. In particular, it has been found that in the case of 4P(6P) the mass 128(61) signal, which proceeds almost simultaneous to the original 4P(6P) mass of 306(458), gives the best signal-to-noise ratio. However, the high rate for detecting this signal leads to a slower signal drop at the trailing edge compared to the original molecular mass. To overcome this instrument specific effect, it is better to use the TD spectra of the original 4P or 6P molecular mass for determining the desorption energies.

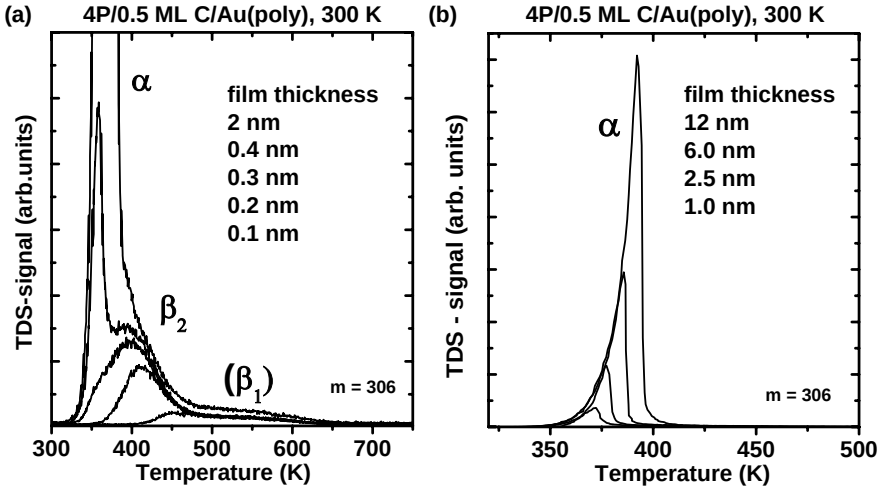

Figure 7.7: TDS series of 4P/0.5 ML C/Au(poly) grown at 300 K for (a) the monolayer and (b) multilayer coverage regime.

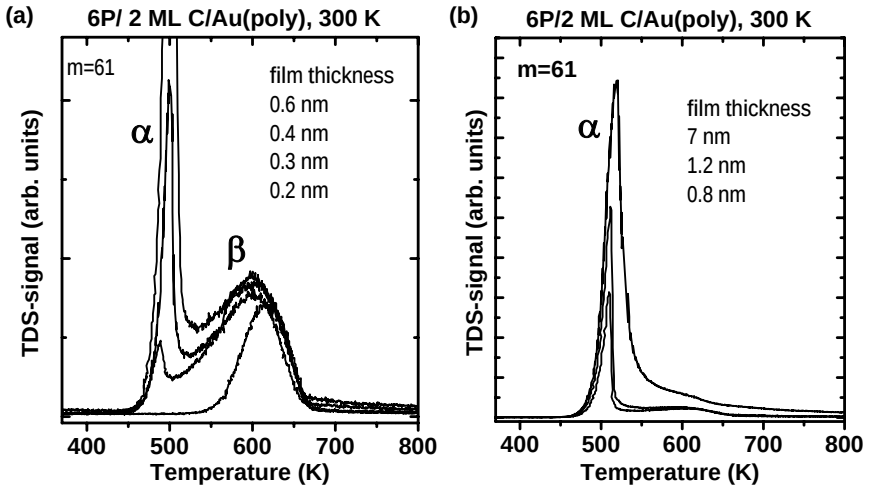

Figure 7.8: TDS series of 6P/2 ML C/Au(poly) grown at 300 K for the (a) monolayer and (b) multilayer coverage regime.

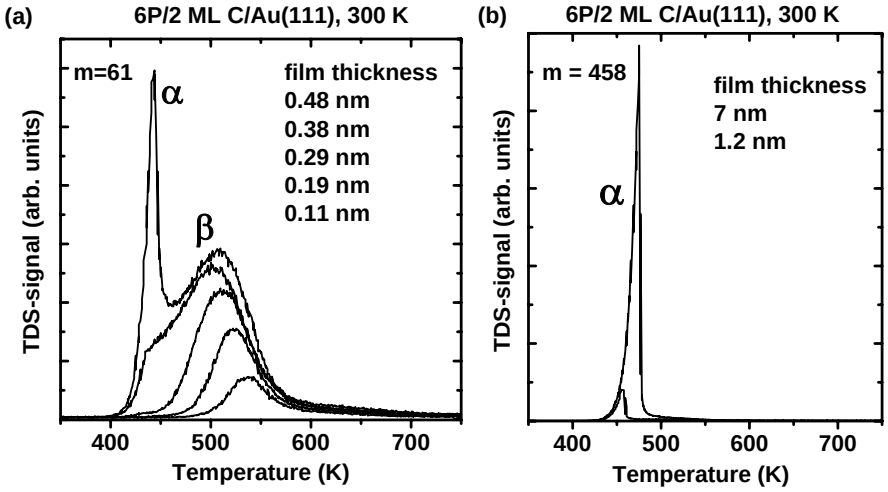

Figure 7.9: TDS series of 6P/2 ML C/Au(111) grown at 300 K. in the (a) monolayer and (b) multilayer coverage regime.

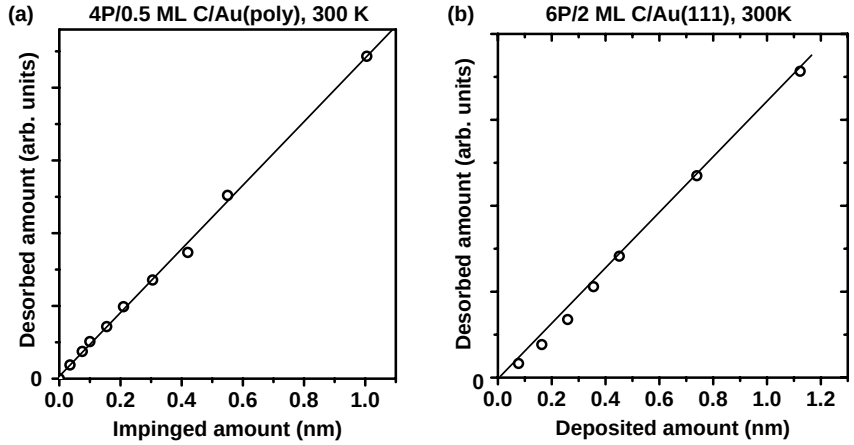

Figure 7.10: Integrated desorption spectra versus the amount of impinged nP molecules on the carbon-covered gold surface, as determined in situ by the quartz microbalance. (a) 4P on 0.5 ML C/Au(poly) and (b) 6P on 2 ML C/Au(111) grown at 300 K. The straight line indicates a linear fit.

qualitative effects could be observed: 1) The (001) orientation that is observed on heavily C-covered Au surfaces lowers the values of E_{des} independent of the type of nP molecules used. Larger values of E_{des} are found for orientations comprising flat lying molecules. 2) On the other hand, comparing the E_{des} values for films with the same crystal orientation (as determined with XRD) yields very similar values, independent of whether this particular orientation is due to the geometry or the chemistry or the temperature of the substrate.

In particular, on the clean polycrystalline Au surfaces the highest values of E_{des} are observed. Here, the nP films exhibit a high degree of polymorphism (co-existence of different crystal orientations) with dominantly lying molecules.

7.4 Sticking coefficient

From thermal desorption data, also the sticking coefficient has been determined for 4P and 6P adsorption at room temperature and at 93 K, as a function of coverage in the mono- and multilayer regime on different Au surfaces. In Figure 7.10 two examples are presented for 4P and 6P, respectively. The adsorbed amount, as measured by thermal desorption spectroscopy, is plotted versus the impinged amount, as measured during evaporation by the calibrated quartz microbalance held at room temperature. Similar results have been obtained for a sample temperature of 93 K. In particular, these experiments have been performed on the C pre-covered gold surfaces where no de-hydrogenation of the nP takes place. For both adsorption temperatures a close to linear relationship between the offered and the adsorbed amount of nP has been observed over a broad coverage range. The observation that the sticking coefficient is independent of coverage and temperature suggests that it is unity in all cases. This result has been extrapolated also to the case of nPs adsorbed on clean Au surfaces.

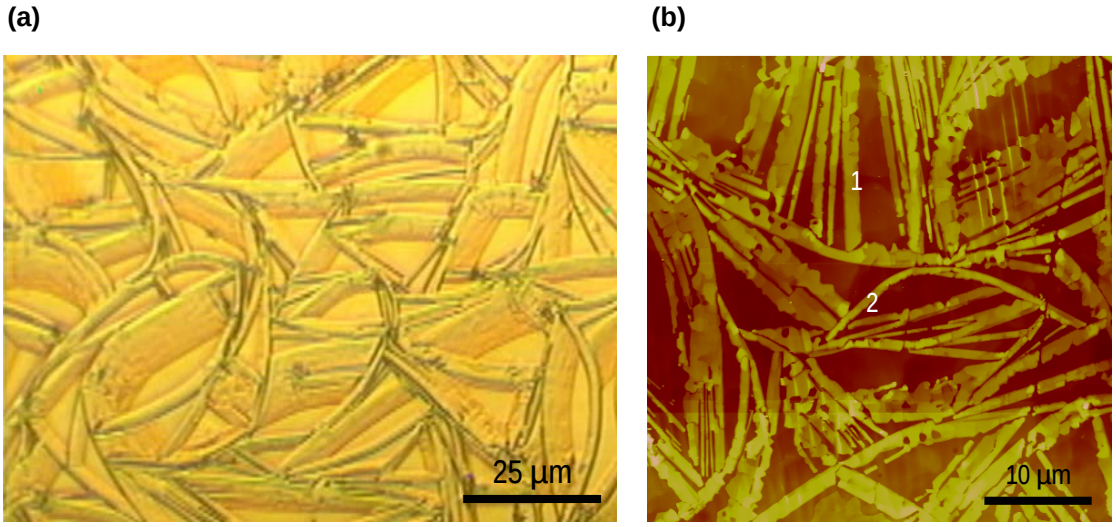

Figure 7.11: (a) Optical micrograph of a 30 nm 4P film on 0.15 ML C/Au(111) at room temperature. The arrow indicates a scratch applied to the organic film after deposition. Here, the underlying gold substrate becomes visible. (b) Atomic-force micrograph (50×50 μm, z-scale 400 nm) revealing a coexistence of straight (1) and bent (2) needle-like crystallites.

7.5 Bulk crystal orientation and film morphology

The method of surface carbon contamination prior to the nP film growth is a powerful tool, which enables a **tailoring** of the nP thin films. Depending on the amount of surface carbon applied, it is possible to intentionally "set" the molecular packing within the first interfacing monolayer. Several different packing structures with either lying or standing molecules have been demonstrated. The new molecular packing structures of the nP monolayers on different C-covered Au(111) described in the previous section then act as structural pre-stages for the growth of thicker nP films. This behaviour is similar to the growth on atomically clean Au surfaces, where the monolayer structure also determines the crystal orientation of the bulk. Consequently, one can expect new thin film morphologies for several nm thick nP films on different partially C-covered Au surfaces. The tailoring of the nP crystal orientation and film morphology by the application of very small amounts of surface carbon may be of great interest for the development and/or the optimization of organic based (opto-)electronic devices.

As a first example, the system 4P/C/Au(111) will be discussed. In particular, three different C pre-coverages have been applied, i.e. 0.03 ML, 0.15 ML and 0.5 ML and the thickness of the 4P films was constantly 30 nm. The lowest C pre-coverage (0.03 ML) exhibited no significant influence on the film morphology. However, a slight increase of the surface carbon up to 0.15 ML leads to a dramatic change of the film morphology, as can be seen in Figure 7.11(a). Similar to the growth on clean Au, a needle-like morphology is observed in OM, but the needles are up to 10 μm wide instead of 1-2 μm on the

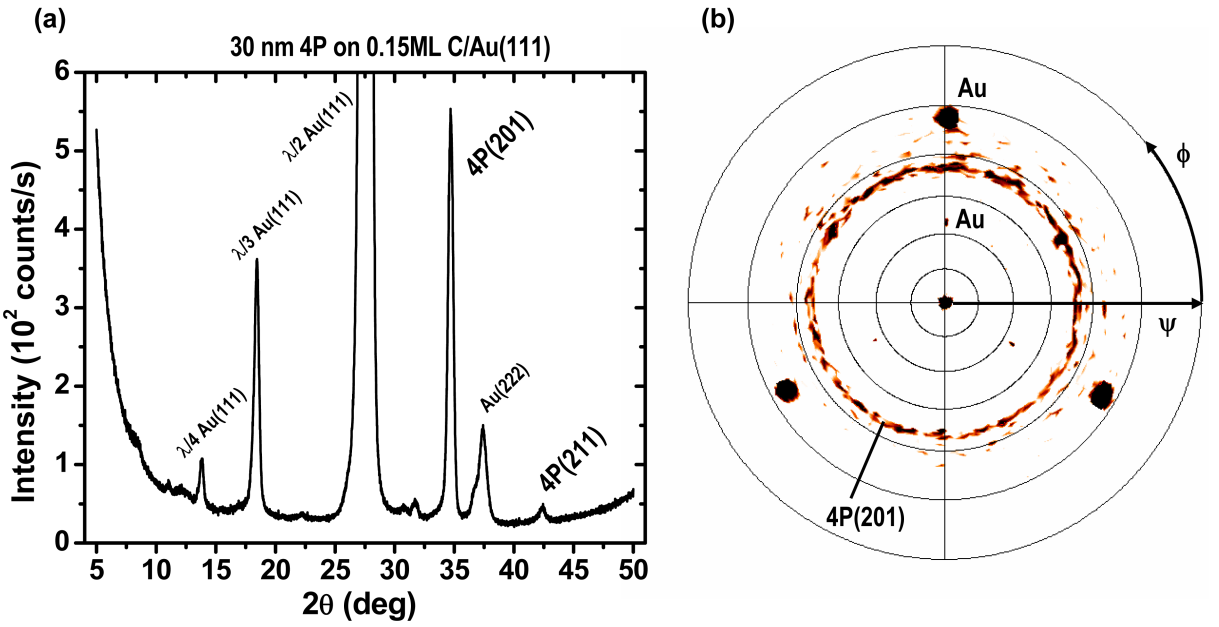

Figure 7.12: (a) XRD $\Theta/2\Theta$ scan of a 30 nm 4P film on 0.15 ML C/Au(111) surface. (b) XRD pole figure of 4P(110) at $\Theta = 28.7°$. The scans were recorded for $CrK_{\alpha 1,2}$ radiation.

clean Au surface. The mean length of the needle-like crystallites has not significantly changed, though. A high resolution AFM analysis reveals, indeed, needle like 4P crystallites rather that crystallite chains, as shown in Figure 7.11(b). The height distribution of the crystallites is nonuniform in this film, with dominant heights appearing at 60, 90 and 120 nm, respectively [15]. The rms roughness of the film is about 50 nm. Interestingly, besides straight needles (1) also curved needles (2) can be found. This may indicate a weakening of the azimuthal alignment of the 4P molecules along the high symmetry directions of the Au(111) surface. As will be seen below, the azimuthal locking of individual 4P crystallites is lost. An explanation for the increased needle width can be given in terms of the nP surface diffusion, which has been found significantly higher on C-covered Au surfaces compared to the clean ones. Obviously, the surface carbon increases the nP surface mobility preferentially in the directions perpendicular to the high-symmetry directions on the Au(111) surface. Hence, the probability for diffusion "jumps" of nP molecules, that are locked to e.g. the Au$\langle 11\bar{2} \rangle$ direction, between neighbouring atom rows is increased. This, of course, favours an agglomeration of molecules that sit on the same atom row, facing each other in an end-to-end configuration. Accordingly, the width of the crystallite needles increases relative to their length.

XRD specular scan measurements have revealed a high crystallinity of the 30 nm 4P film on 0.15 ML C/Au(111). Interestingly, a co-existence of two different crystal orientations has been found. This fact is in good agreement to the interpretation of the corresponding TD data, where two structural domains (type A and type B) have been proposed. The

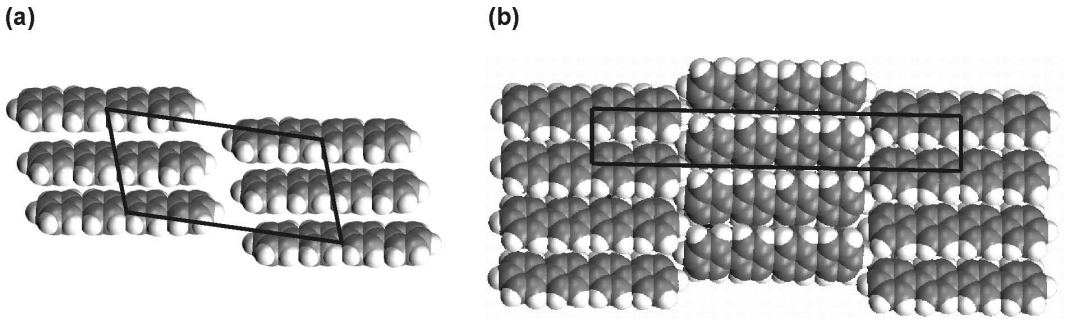

Figure 7.13: Comparison of the molecular packing structures (top view) within the (a) monolayer and (b) (201) bulk crystal plane of 4P grown on 0.15 ML C/Au(111).

crystal orientations can be seen in the $\Theta/2\Theta$ scan presented in Figure 7.12(a). The by far dominating one is the 4P(201) orientation, which amounts for roughly 95% of the crystallites[3]. The residual 5% of the crystallites adopt the (211) orientation, which is the dominating orientation for 4P grown on the clean Au(111) surface. The molecular packing motif within the $4P(201)$ plane is depicted on page 35 and has also been discussed in the previous section. The molecules adopt a lying conformation with respect to the (201) plane, i.e. the long molecular axes lie within this plane. They are aligned in rows of parallel oriented molecules, where the aromatic planes are side tilted out of the (201) plane. Within one row the side tilt is in the same direction, however, the neighbouring rows exhibit the inverse side tilt.

The XRD pole figure of the 30 nm 4P film shown in Figure 7.12(b) clearly shows a ring-like structure instead of distinct spots of enhanced pole density for the 4P(201) orientation, which is typical of a so-called fibre texture. It indicates that there is no preferential azimuthal alignment of the 4P crystallites with respect to the Au(111) surface. Although this finding helps to explain the existence of curved crystallite needles, still, the AFM results would suggest at least some degree of azimuthal ordering. A considerable fraction of the crystallites seems to be aligned along some preferential directions on the Au(111) surface, as can be seen in the AFM image in Figure 7.11(b). Similar to the case of 4P on clean Au, no LEED pattern from the 4P bulk structure could be observed.

The 2D unit cell of the (201) plane can be defined by the following parameters: a = 0.56 nm, b = 3.75 nm and γ= 90°. The basis consists of two molecules at the positions $(0, 0)$ and $(1/2, 1/2)$. The two molecules are side tilted relative to the (201) plane and the tilt direction is complementary with respect to each other. Comparing the 2D unit cell of the 4P(201) plane with the surface unit cell of the regular 4P monolayer on the 0.15 ML C/Au(111) surface (Figure 7.5) enables an insight into the structural transition between the monolayer and bulk structure. This is illustrated in Figure 7.13. The rows of parallel oriented neighboring molecules found in the 4P(201) plane exist already in the monolayer. The only major structural adaption between the monolayer and bulk

[3]The reflectivity of the net plane has been considered in terms of the structure factor $F(hkl)$. Relative to $F(211)$, $F(201)$ is 1.38 (see also Table 4.4)

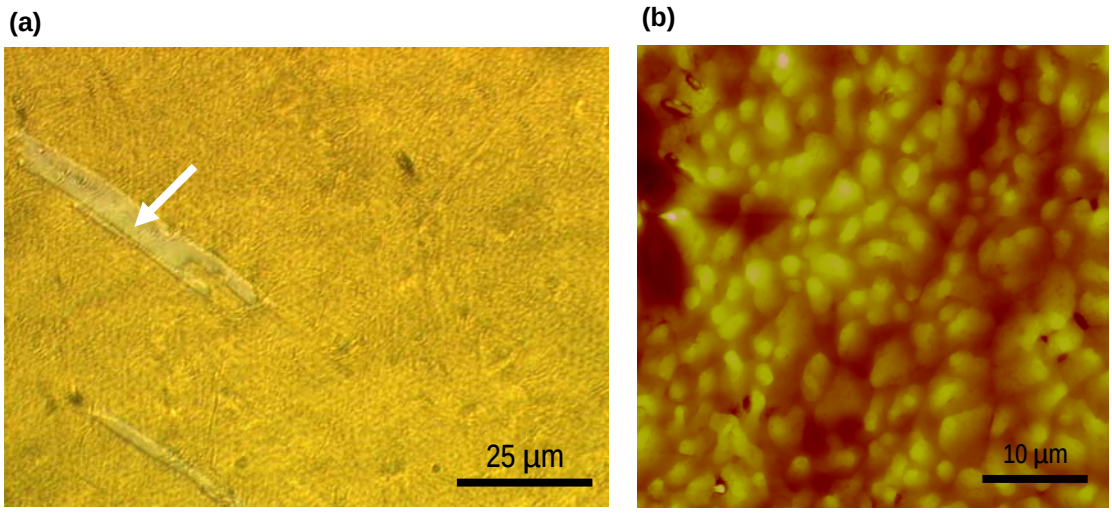

Figure 7.14: (a) Optical micrograph of a 30 nm 4P film on 0.5 ML C/Au(111) at room temperature. (b) Atomic-force micrograph (50×50 μm, z-scale 50 nm).

structure is a lateral relaxation in the direction parallel to the molecules by about 15% and a compression in the direction perpendicular to the molecules by about 7%, respectively. It should be emphasized again, that the side tilt of the molecules in the monolayer structure shown in Figure 7.13(a) has not been measured experimentally, but proposed instead. Therefore, this degree of freedom must still be regarded as variable for the monolayer structure.

With respect to the previous 4P film, a completely different film morphology is observed for a 30 nm 4P film grown on a 0.5 ML C/Au(111) surface, as shown in Figure 7.14(a). The film appears very homogeneous in optical microscopy. In order to get a sufficient image contrast relative to the underlying Au substrate, the film has been scratched (indicated by the arrow). The high resolution AFM image in Figure 7.14(b) exhibits a granular morphology. No needle-like crystallites or azimuthally ordered structures can be found. The rms roughness is further reduced to about 8 nm. The crystallites have a nearly circular base and typical lateral dimensions of these columnar grains are about 0.7 μm in diameter. The measured height from the visible background (dark) up to the highest features (bright) of 15 nm indicates a continuous film. The absolute height with respect to the clean Au surface could not be unambiguously determined with AFM in this case.

The XRD $\Theta/2\Theta$ scan for this film again reveals a high crystallinity of the organic film. As shown in Figure 7.15, only one crystallographic orientation, the $4P(001)$ orientation, has been found. This result is very interesting insofar, as the (001) is a cleavage plane of the bulk crystal structure where the 4P molecules adopt a nearly **upright standing** "end-on" orientation, as illustrated on page 35. This completely different crystal orientation compared to the previously discussed films helps to explain the layer-like growth mode observed in AFM instead of the needle-like growth mode found on less C-covered Au(111)

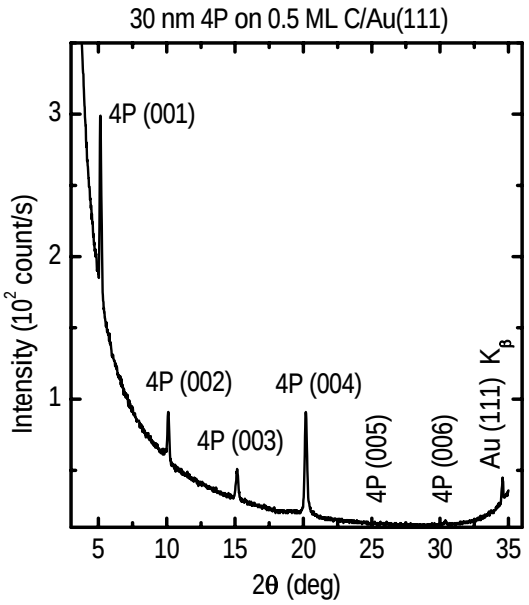

Figure 7.15: XRD $\Theta/2\Theta$ scan of a 30 nm 4P film grown on a 0.5 ML C/Au(111) surface at 300 K. The scans were recorded for $CuK_{\alpha 1,2}$ radiation.

surfaces. The herringbone layers of the 4P bulk crystal structure as shown in Figure 1.2 grow coplanar to the substrate surface plane in two dimensions. This results in a relatively smooth film morphology compared to the needle-like films described before with a typical step height of about one molecular length. As described in the previous section, the upright conformation is also preserved, when the film thickness is reduced to a value of about 2-3 nm, which corresponds to a single close packed monomolecular layer of upright standing 4P molecules. Investigated with LEED, such films exhibit rings instead of distinct spots, as shown in Figure 7.6 for a 3 nm thick 4P film grown on a 0.5 ML C/Au(111) surface. The origin of these rings is attributed to the existence of highly ordered 4P domains with an arbitrary azimuthal orientation. The lateral size of these domains can be up to 700 nm, as observed in AFM.

The film morphology observed in AFM, which is a considerably local method, is corroborated by the results of XPS, which is an integral technique and thus well-suited to complement the AFM results. The Au4$f_{7/2}$ signal of the substrate has been measured for a nominally 7 nm thick nP film grown at 93 K and 300 K, respectively. The details of these measurements are described in Section 8.2. The important point here, however, is that the film thickness of 7 nm has been properly chosen: it is the minimum thickness for which the Au4$f_{7/2}$ signal is zero for a film grown at 93 K. In particular, this enables to monitor the changes of the film morphology (recrystallisation) upon film growth at different temperatures or annealing of the films. The higher the Au4$f_{7/2}$ signal, the more substrate area is (partially) uncovered with nP due to recrystallisation, i.e. the nP crystallites grow preferentially in the direction of the surface normal instead of a continuous layer growth.

Table 7.2: Relative intensity of the Au4$f_{7/2}$ photoelectron signal of different partially C-covered Au(111) substrates covered with a nominally 7 nm thick nP film. The nP films were either grown at 300 K or at 93 K and subsequently annealed to 300 K, respectively. The intensity values have been normalized with respect to the pure Au substrate with no nP coverage.

Sample	grown at 300 K	annealed to 300 K
6P/Au(111)	42%	10%
4P/Au(111)	70%	22%
4P/0.03 ML C/Au(111)	70%	22%
4P/0.5 ML C/Au(111)	50%	30%

The results are summarized in Table 7.2. The results for the films grown at 300 K clearly show the tendency for a better wetting of the substrate by the nP film with increasing C pre-coverage. The same trend has been observed in OM and AFM on a microscopic length scale.

Surprisingly, however, a slightly different situation is observed for nP films that have been grown at 93 K and subsequently annealed at 300 K. These films exhibit a more pronounced layer growth (better wetting) compared to the films that were originally grown at 300 K. Hence, during the film re-crystallisation the growth of 3D crystallites in the direction perpendicular to the surface is hindered compared to the original growth at 300 K. This may be caused by the fact that the re-crystallisation of the films involves significantly less material transport (nP diffusion) in order to achieve thermodynamically stable nP crystallites. Note, that 6P exhibits a lower diffusion than 4P due to the increased interaction energies (intermolecular and adsorbate-substrate) compared to 4P. Also it has to be considered that the different nP crystal orientations may influence the surface diffusion energy of the nP molecules. However, the best layer growth (smallest Au4$f_{7/2}$) signal has been achieved for an annealed film at no (very low) C pre-coverage. This still remains a puzzling result and shows that in the presented case the particular processes that determine the combined crystal orientation and film morphology are not fully understood at the moment.

The existence of surface carbon prior to the growth of nP films can also de-activate surface steps on the substrate. This is shown for a 30 nm 4P film grown on a partially C-covered vicinal Au(433) surface in Figure 7.16. The C coverage, however, is not homogeneous over the whole sample, instead, it was possible to discern between areas of low and high surface carbon. Unfortunately, the amount of surface carbon could not be quantified. Nevertheless, a qualitative trend can be clearly seen. On the low surface carbon areas tetragonal crystallites are found with lateral dimensions of about 100 - 500 nm (a)-(c). The crystallites are azimuthally aligned, suggesting that a structural influence of the surface steps of the Au(433) surface exists. On the other hand, in the high surface carbon areas the 3D crystallites do not show any azimuthal alignment. Obviously, the surface steps have been de-activated by the surface carbon, which results in a loss of azimuthal ordering. A significant fraction of the film in the high C-covered areas exhibits a layer-by-layer morphology (d) with roughly 1 μm large terraces (e). The typical step height of 1.7 nm

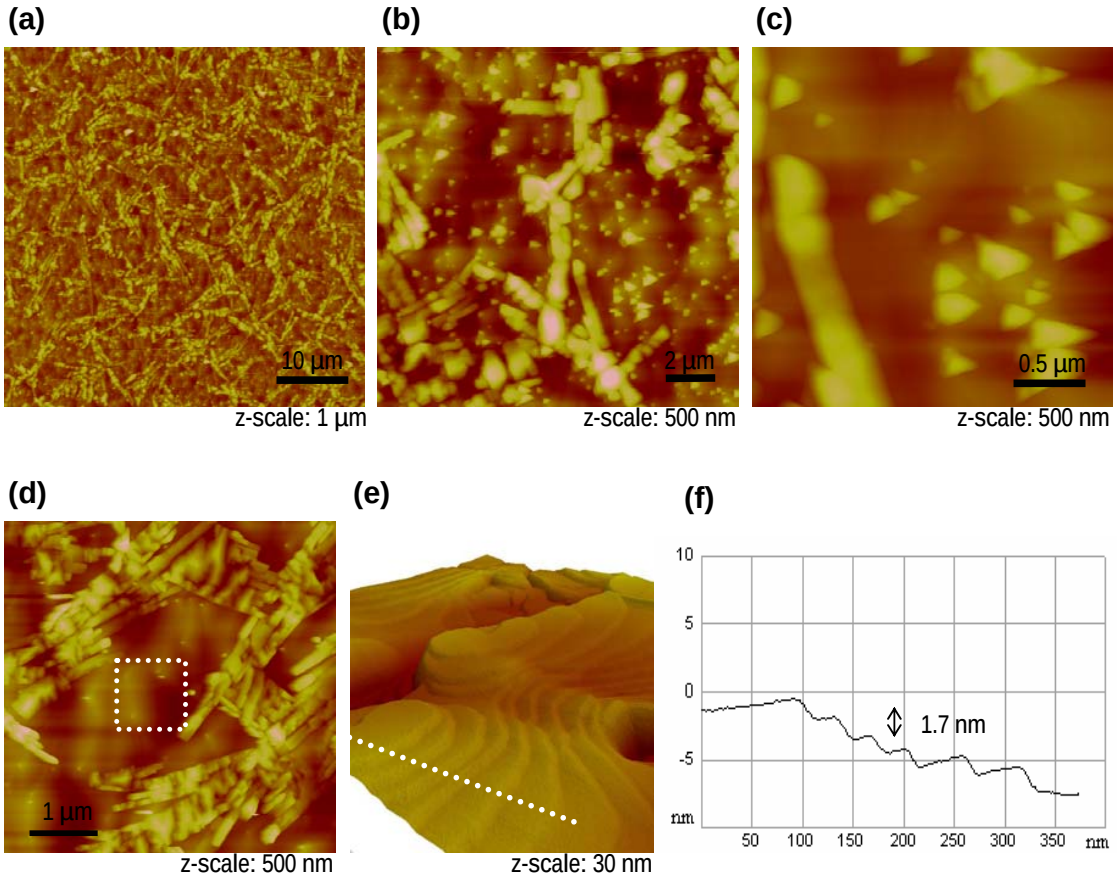

Figure 7.16: High resolution AFM micrographs of a 30 nm 4P film on partially C-covered Au(433) at room temperature. (a)-(c) Area of low C coverage, the resolution is increased between the images. (d) Area of high C coverage. (e) Detail scan (1×1 μm) in 3D representation of the area indicated by the dotted square in (d). (f) Line scan height profile across the dotted line in (e).

indicates that these terraces consist of monomolecular layers of nearly upright standing, close packed 4P molecules, presumably in a (001) crystal orientation (f).

Chapter 8

The Influence of Temperature

Several experimental findings are reported in this chapter concerning the effect of the substrate temperature on the growth and/or recrystallisation of nP films on clean and partially C-covered Au surfaces.

8.1 Surface mobility

As already described in Section 4.2, for films grown below 270 K no regular monolayer structure can be observed in LEED. Presumably, also the bulk film is disordered at low temperature, although no direct experimental proof has been gained in the case of thicker films. For temperatures > roughly 270 K, the adsorption temperature has no significant effect on the nP monolayer structure over a wide temperature range as already pointed out in Section 4.2. In particular, annealing of a film closely below the onset of nP monolayer thermal desorption does not change the packing structure of the monolayer film. However, from an improved sharpness of the observed LEED reflections it can be concluded that the annealed films exhibit larger regular domains compared to films grown at lower temperature. This indicates an **improved surface mobility** of the nP molecules on the surface at elevated temperatures. An increased surface mobility of the nP molecules has also been made responsible for the experimental finding that the azimuthal alignment of the molecules in a 30 nm 6P film on Au(111) at 300 K deviates from that of a film grown at 330 K. The details are described in Section 4.5.

8.2 Film morphology and structure

LEED investigations conducted on bulk films of 6P grown at 300 K on Au(111) show that a regular LEED pattern is visible, which comprises a superposition of the 6P monolayer pattern and additional reflections that can be attributed to the bulk phase. As described in Section 4.7, the bulk LEED pattern diminishes with increasing film thickness, whereas the monolayer pattern is still visible up to film thicknesses of several nm. Figure 8.1(a) shows a representative LEED image recorded for a 7 nm thick 6P film on Au(111) at 300 K.

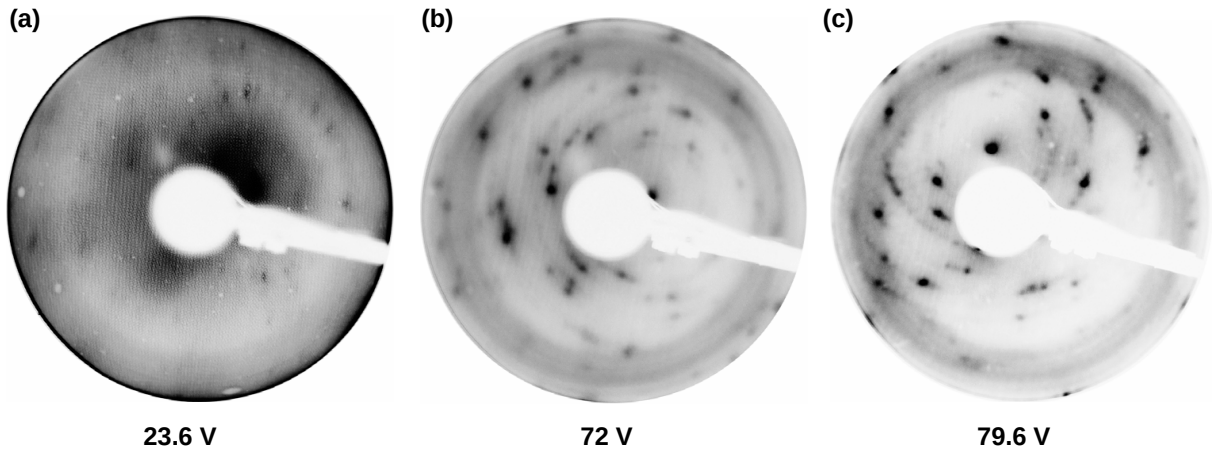

Figure 8.1: Representative LEED images of 6P bulk films grown on Au(111) at different temperatures. (a) 7 nm film grown at 300 K, (b) 10.4 nm film grown at 380 K and (c) 7 nm film grown at 420 K. The beam voltage is indicated below each image.

For a comparison with a 6P monolayer LEED pattern confer to Figure 4.6. Additionally, proper LEED reflections of the film grown at 300 K can only be observed for low beam voltages approximately lower than 25 V, whereas for higher voltages the LEED reflections vanish and no higher order reflections are visible. However, for films grown at 380 K and 420 K, also for beam voltages as high as 70-80 V proper LEED reflections can be seen, as shown in Figure 8.1(b) and (c), i.e. higher order reflection can be additionally observed. A similar effect has been observed also for films that have been originally grown at 300 K and then have been annealed to 380 K. This behaviour is remarkable insofar, as it has been shown in XRD experiments that the 6P bulk films exhibits a high crystallinity already at 300 K, which suggests that the bulk phase should also be clearly visible in LEED. The reason why this is not the case around room temperature can be attributed most probably to the **morphology** of the 6P bulk film, which is **temperature dependent**.

It has been already mentioned in Section 4.5 that the substrate temperature greatly effects the processes that determine the energetics and kinetics of the 6P film growth, which, in turn, determines the film morphology of 6P bulk films. The same holds true for 4P. However, the system 6P/Au(111) is better suited for investigating the effect of the substrate temperature on the film morphology, because the temperature regime from the beginning of an ordered crystal growth around 270 K until the onset of multilayer desorption above 430 K is much larger compared to 4P, where the multilayer desorption starts already around 330 K. A comparison of three 30 nm thick 6P films grown at different adsorption temperatures between 300 K and 430 K on Au(111) presented in Figure 4.14(d)-(f) shows the effect of the adsorption temperature on the morphology. As depicted in (d), at 300 K an **island-like film morphology** is predominant. The granular, island-like morphology can also be observed in AFM as shown in Figure 4.16. It has been observed in XRD experiments conducted for both 4P and 6P that the nP crystallites in a bulk film with an island-like morphology typically exhibit crystal orientations where the molecules

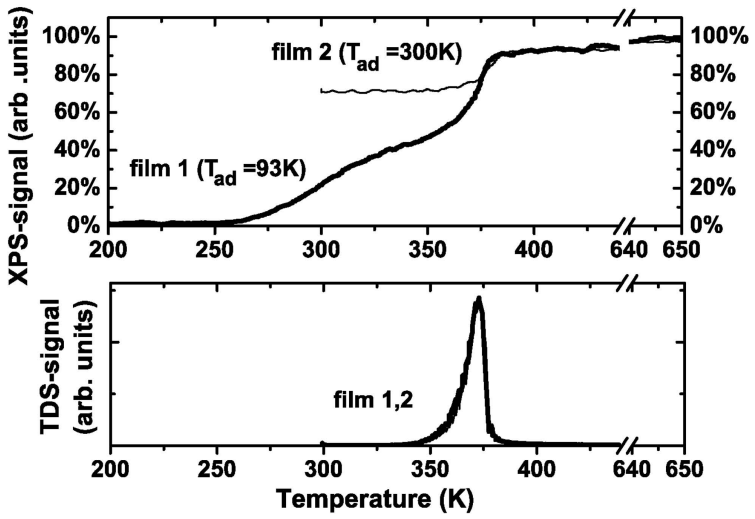

Figure 8.2: Combined XPS and TDS measurement of 7 nm thick 4P films grown on Au(111) at different adsorption temperatures, T_{ads}, of 93 K and 300 K, respectively. The upper part shows the temperature dependence of the Au $4f_{7/2}$ signal, which is roughly proportional to the fraction of uncovered Au(111) surface area. The lower part shows the TD spectra of equivalently deposited 4P films on the same substrate.

are oriented with their long axes almost parallel to the substrate surface plane, i.e. flat lying molecules. At 430 K, however, the 6P film presented in Figure 4.14(f) exhibits a predominantly **layer-like morphology** with a small fraction of coexisting needle-like crystallites. As shown previously, a layer-like morphology is typical of upright standing molecules and therefore it can be concluded already from the optical micrographs shown in Figure 4.14(d)-(f) that a structural phase transition of the 6P film occurs within the investigated temperature range. This aspect will be discussed in more detail below.

The temperature dependence of the morphology of 4P and 6P bulk films grown on different Au surfaces has been investigated in combined XPS and TDS experiments. The temperature dependence of the Au $4f_{7/2}$ signal of the underlying Au substrate is monitored for 7 nm thick nP films. In particular, it has been shown that independent of the substrate for films grown at low temperatures (93 K) a thickness of 7 nm is sufficiently high for the Au $4f_{7/2}$ signal to be zero, whereas for thinner films it is not. This fact can be utilized for an analysis of the film morphology as follows. As long as no desorption takes place, which reduces the nominal film thickness, a temperature-induced change (increase) of the Au $4f_{7/2}$ signal can be attributed to a **recrystallisation** of the nP bulk film, i.e. a temperature-induced phase transition, that reduces the width of the nP crystallites in favour of an increased height. Additionally, it has been verified that the peak position of the Au $4f_{7/2}$ signal does not change with nP coverage, which could result in a misinterpretation of the spectra.

Figure 8.2 shows temperature dependent XPS (upper part) and TDS (lower part) data of two 7 nm thick 4P films, deposited at different adsorption temperatures. To begin with

film 1 grown at 93 K, the Au $4f_{7/2}$ signal is close to zero in a temperature range from 93 K to 270 K. This is attributed to the existence of a continuous 4P film of unknown structure covering the whole Au(111) surface. In the temperature range from 270 K to 310 K the XPS signal increases and runs into a flat plateau at about 350 K. In this range still no significant desorption occurs, as can be seen from the TDS underneath. Obviously, a recrystallisation of the 4P film takes place, where the formerly continuous film changes to a morphology of separated 4P islands. A further temperature increase leads to 4P multilayer desorption between 325 K and 375 K, where the Au $4f_{7/2}$ signal also shows a sharp increase and then stagnates at about 90% of the signal of the clean Au(111) surface. At this point, only the 4P monolayer is still present on the surface. Finally, for temperatures around 375 K the monolayer starts to desorb and correspondingly the Au $4f_{7/2}$ signal shows a slight increase until it reaches 100% at about 650 K. In contrast to that, film 2 adsorbed at 300 K exhibits a significantly higher initial Au $4f_{7/2}$ signal of about 70%, which corresponds to an island-like 4P film morphology. Apparently, the mean island height can be determined to about 23 nm (3.3 times higher than the mean film thickness at 93 K). The signal remains nearly constant until significant multilayer desorption sets in at about 350 K. A closer inspection shows that even at the beginning of the multilayer desorption no significant change in the Au $4f_{7/2}$ signal is observed. This happens most probably because at the beginning of the multilayer desorption mainly the height but not the lateral width of the 4P islands is reduced. Only when the mean island height has become sufficiently small, i.e. during the desorption of the last fraction of the multilayer around 375 K, a sharp increase of the Au $4f_{7/2}$ signal can be observed. Obviously, at this point the island height has fallen below the mean free path of the Au $4f_{7/2}$ photoelectrons (with energy 1170 eV) in the 4P material. The latter has been determined separately, as described on page 93 to $\lambda = 2.4 \pm 0.3$ nm. These findings suggest that 4P exhibits a layer-like growth at low temperatures and a Stranski-Krastanov type of growth at $\geq$270 K.

A second important aspect of Figure 8.2 concerns the different morphologies between film 1 and film 2 at 300 K. The experiment shows that film 2 exhibits a significantly more pronounced island morphology compared to film 1. A similar scenario can also be found for other systems as shown in Figures 8.2, 8.3 and 8.5 of different nP films grown on clean Au surfaces. A general interpretation of this behaviour can be given as follows. Growing organic films on a solid substrate is usually done by depositing the desired amount of material with a finite deposition rate at some fixed substrate temperature T_0. A comparison of the annealed film with the film originally grown at $T_1 > T_0$ yields the following differences: The final morphology of the annealed film upon recrystallisation is similar to that of a hypothetic film that has been grown already at T_1 but with a very large (infinite) deposition rate. According to classical theory of crystal growth, however, an increased deposition rate causes an increased nucleation rate which reduces the size of the critical nuclei, but increases their absolute number. Therefore, the annealed film 1 in our example will exhibit a more granular-like structure with smaller crystallites that cover more substrate surface area compared to film 2.

A qualitatively similar behaviour as described above for the system 4P/Au(111) has been observed for the systems 4P/Au(poly) shown in Figure 8.3, 6P/Au(poly) shown in

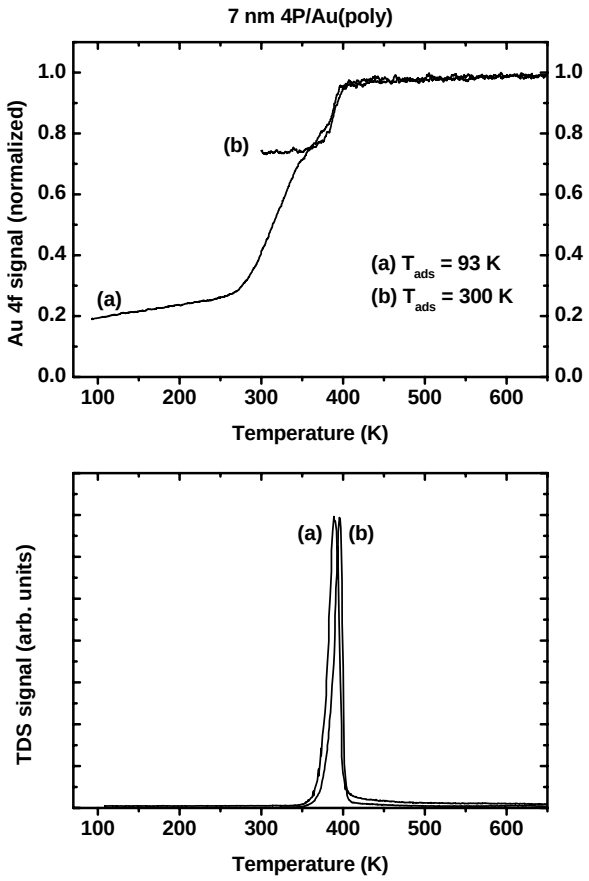

Figure 8.3: Temperature dependence of the substrate Au $4f_{7/2}$ signal for 7 nm thick 4P films grown on Au(poly).

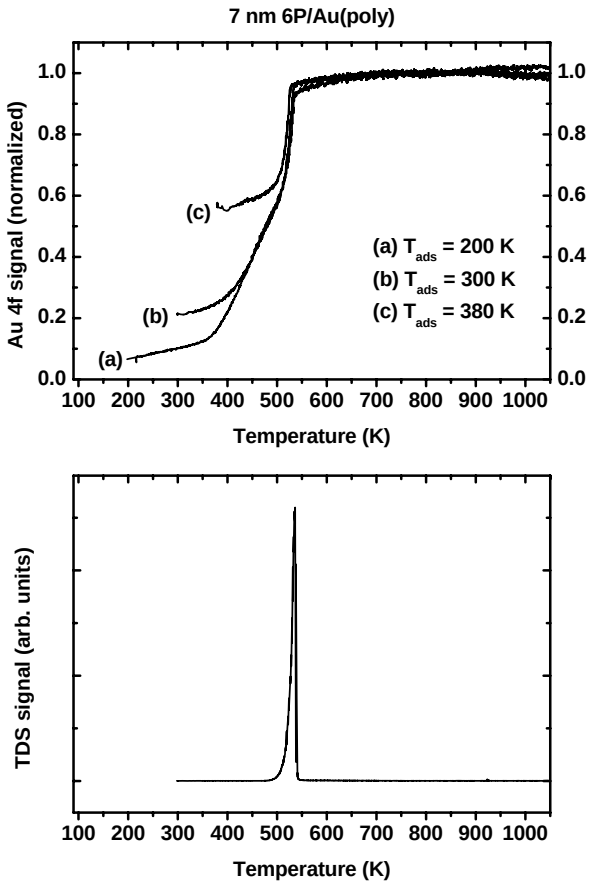

Figure 8.4: Temperature dependence of the substrate Au $4f_{7/2}$ signal for 7 nm thick 6P films grown on Au(poly).

Figure 8.4 and 6P/Au(111) shown in Figure 8.5(a) (compare curves a and c). In the case of 6P grown on Au(111), however, the transition of a disordered continuous film at 93 K into a crystalline island-like film at 300 K is not as pronounced as it is for 4P. The Au $4f_{7/2}$ signal of the 6P film grown at 300 K (curve c) is only at about 40% of the clean surface signal. Accordingly, the mean height of the 6P crystallites can be estimated to about 12 nm (1.7 times the initial height of the continuous film). This can be explained by the stronger intermolecular interactions of the 6P molecules compared to 4P, which causes a higher activation temperature for the recrystallisation processes. Apparently, for 6P a temperature of 330 K is necessary to form an island morphology with a Au $4f_{7/2}$ signal of about 70% (curve d).

Interestingly, a further increase of the adsorption temperature up to 410 K causes the Au $4f_{7/2}$ signal to decrease (curves e-g). This means that the 6P film recrystallizes into a more layer-like morphology again, i.e. a better wetting, because at these temperatures the 6P desorption has not started yet. This behaviour can be explained in terms of a change

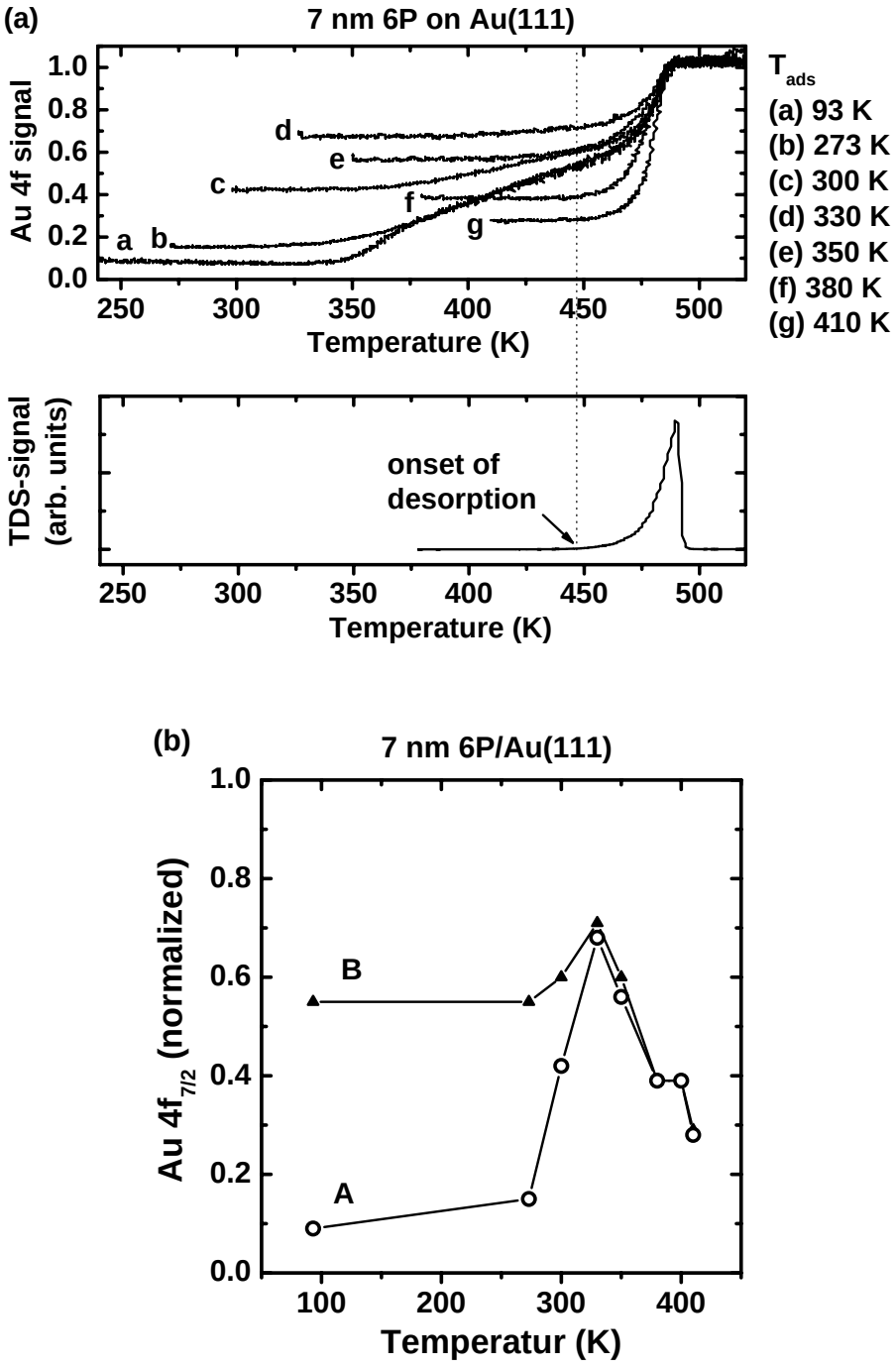

Figure 8.5: (a) Temperature dependence of the substrate Au $4f_{7/2}$ signal for a 7 nm thick 6P film grown on Au(111) at different adsorption temperatures between 93 K and 410 K. (b) Comparison of two selected situations taken from graph (a). Curve A (open circles) represents the Au $4f_{7/2}$ signals of the films a-g at the initial growth temperatures. Curve B represents the (increased) signals of the same films after annealing to a temperature just below the onset of thermal desorption at about 450 K.

of the bulk crystal orientation **from lying molecules to upright standing molecules**. For the latter crystal orientation, a layer-like morphology has previously been observed also on carbon pre-covered surfaces (cf. section7.5). This remarkable finding is corroborated by XRD measurements conducted on a 30 nm 6P film grown on Au(111) at 410 K. The $\Theta/2\Theta$-scan presented in Figure 8.6 clearly shows the existence of highly regular 6P crystallites in the (001) orientation. In addition, however, also the 6P($21\bar{3}$) orientation is observed, indicating a coexistence of two crystal orientations with both lying and upright standing molecules. Obviously, for adsorption temperatures between 350 K and 430 K a considerable fraction of the 6P molecules re-orients into a 6P(001) crystal orientation.

An approximate quantitative determination of the total amount of molecules adopting either the (001) or the ($21\bar{3}$) orientation can be made based on the relative peak intensities of the (006) and ($21\bar{3}$) peaks appearing at 20.48° and 28.15°, respectively. A rough estimate can be made considering the different reflectivities I_{rel} of the (006) and ($21\bar{3}$) crystal planes that can be determined with the PowderCell software for the case of a crystalline powder sample. The calculated relative peak intensity[1] for the (006) peak is 15% and for the ($21\bar{3}$) peak 63%, respectively. This yields as a rough approximation that the (001) and ($21\bar{3}$) crystal orientations in the investigated sample occur with a ratio of about 1 : 1. As discussed earlier, also the OM image in Figure 4.14(f) has already indicated the coexistence of at least two different morphologies that can be clearly distinguished, i.e. 1) layer-like terraces of upright standing molecules that appear as a very homogeneous film in OM and 2) needle-like islands comprising flat lying molecules that appear as elongated needle-like crystallites.

The (001) oriented nP crystallites can be expected to loose their well-defined azimuthal alignment relative to the Au surface in favour of a fibre-texture, similar to the case of nP grown on carbon covered gold surfaces described in Section 7.5. Apparently, the 6P bulk LEED images for high adsorption temperatures shown in Figure 8.1(b)-(c), however, do not corroborate this assumption. At first glance, sharp spot-like LEED reflections are visible instead of rings that would indicate the complete absence of azimuthal alignment, as shown, for instance, in Figure 7.6 for a 3 nm 4P film on carbon covered Au(111). A closer inspection, however, shows a beginning evolution of diffraction rings rather than sharp spots, in particular for the images (b) and (c). This is an indication for a loss of azimuthal alignment of the (001) oriented 6P bulk crystallites relative to the Au(111) surface.

Concerning the application of the findings presented so far in the context of device fabrication, the following comment may be of importance. The observed difference in the resulting film morphology between 1) a film A initially grown at low T and subsequently annealed at high T and 2) a film B grow originally at high T can be utilized to optimize the film growth conditions. Given that the crystal orientation is the same in both films (this is the case if the annealing temperature is properly chosen), the film B exhibits more pronounced islands. Therefore it may be desirable for the application, where a

[1]The calculation also considers the different multiplicities of the net planes, which are 2 for (006) and 4 for ($21\bar{3}$), respectively. However, an exact analysis requires also to consider the peak profiles and the size distributions of the 6P crystallites.

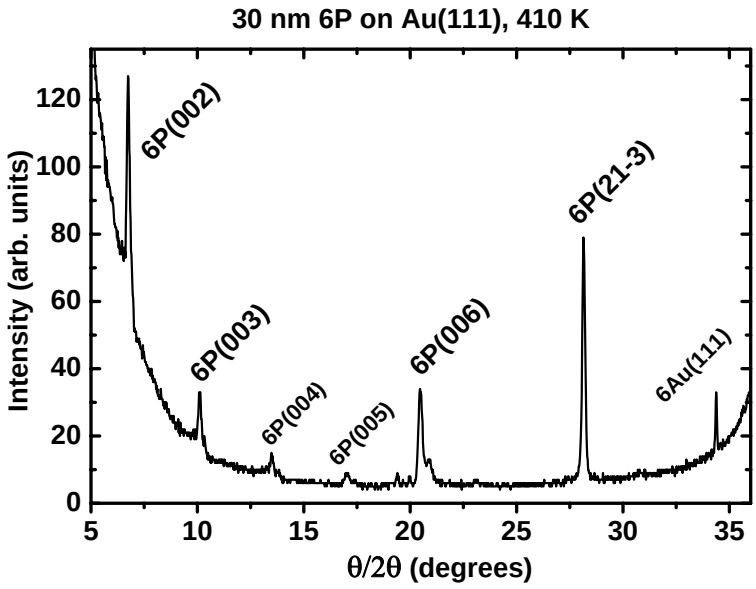

Figure 8.6: $\Theta/2\Theta$ scan of a 30 nm 6P film grown on Au(111) at 410 K. The curve was recorded for $CuK_{\alpha 1,2}$ radiation.

homogeneous film is needed, to grow at low T and subsequently anneal, in order to get a smoother film with less pronounced islands.

The growth kinetics of 4P films grown on differently carbon covered Au(111) surfaces at different substrate temperatures has also been investigated with temperature dependent XPS measurements. Figure 8.7 shows the temperature dependence of the Au $4f_{7/2}$ signal for four independently prepared 7 nm thick 4P films grown on 0.03 ML C/Au(111) and 0.5 ML C/Au(111) surfaces, respectively. The adsorption temperatures were 93 K for the curves (a) and (c) and 300 K for the curves b and d, respectively. In addition, TD spectra were recorded for equivalently prepared 4P films in order to distinguish between a possible recrystallisation and 4P desorption. As the 4P multilayer TD spectra did not change significantly upon a variation of substrate chemistry or temperature, only one representative spectrum is shown (curve (e)). The investigated temperature range can be divided into four regimes according to the degree of structural and/or coverage change of the 4P films. First, the case of adsorption at 93 K is described (curves (a) and (c)). Regime I below 260 K shows neither a structural change, as indicated by the constant Au $4f_{7/2}$ signal, nor a coverage change, as indicated by the zero TDS signal. In regime II between 260 K and 325 K the films (a) and (c) show a large change in the Au $4f_{7/2}$ signal. This is attributed to a structural change (recrystallisation) within the 4P films, since no 4P desorption occurs in this temperature regime. The increasing Au $4f_{7/2}$ signal indicates the formation of 4P islands, which are becoming higher and at the same time laterally smaller with increasing temperature, hence uncovering larger areas of the Au substrate. Within the temperature regime III between 325 K and 380 K the 4P multilayer desorbs, which results in a further increase of the Au signal to about 90%. Finally, the regime IV above

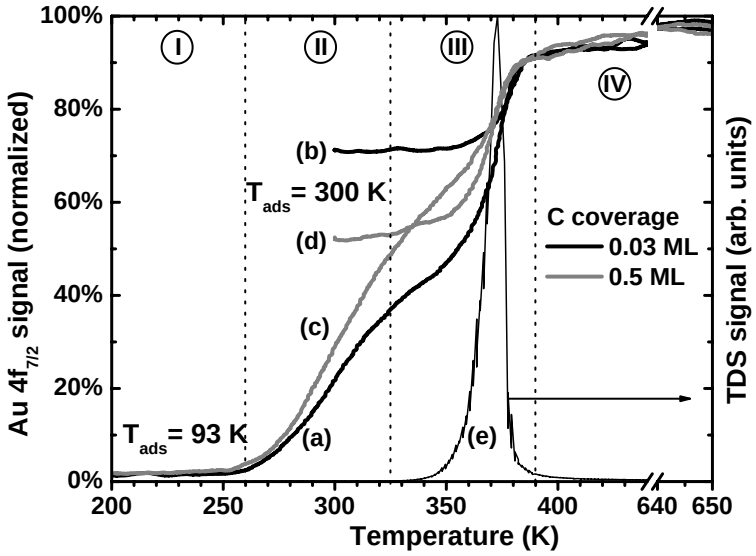

Figure 8.7: (ad) Temperature dependent XPS Au $4f_{7/2}$ measurement and (e) TDS measurement of 7 nm thick 4P films grown on variably C covered Au(111) surfaces at 93 and 300K, respectively. The adsorption temperature and C pre-coverage of the Au(111) substrate during the 4P film deposition are (a) 93 K, 0.03 ML C, (b) 300 K, 0.03 ML C, (c) 93 K, 0.5 ML C and (d) 300 K, 0.5 ML C. The temperature range is divided into four regimes, labelled IIV (see text).

380 K covers the 4P monolayer desorption, where a slight and nearly linear increase of the XPS signal can be seen until it reaches 100% of the clean Au surface at about 650 K. In the case of adsorption at 300 K, both curves (b) and (d) exhibit a significantly higher Au $4f_{7/2}$ signal than in the previous case, after heating to the same temperature. Moreover, they show nearly no change of the Au $4f_{7/2}$ signal in regime II, whereas the qualitative trend within the regimes III and IV is similar to the former case.

In Section 7.2 it has been shown that the existence of a carbon pre-coverage influences the structure of the first 4P monolayer. Additionally, the particular monolayer structure influences also the mesoscopic film morphology of several nm thick 4P films, as inferred from the combined XPS/TDS measurements shown in Figure 8.7. Here, the influence of the adsorption temperature and/or the carbon pre-coverage on the 4P film morphology can be separately analyzed by comparing the corresponding curves: (1) Adsorption temperature: Both films grown at room temperature, (b) and (d), exhibit a significantly large Au signal at 300 K. The signals remain nearly unchanged upon a further heat treatment until desorption sets in. Hence, independent of the amount of carbon pre-coverage, a thermodynamically stable 4P island morphology is achieved already at 300 K. This is due to a high surface mobility of the 4P molecules in the multilayer. The 4P islands are highly crystalline, as determined by XRD (cf. Section 7.5). In contrast to that, the surface diffusion is hindered at 93 K, resulting in continuous 4P films, (a) and (c), as indicated by the close to zero Au signal. During the recrystallisation both films (a) and (c) aspire a thermodynamically stable island morphology. However, the corresponding Au signals at 300K are still

significantly lower than for the films initially grown at 300 K, (b) and (d). This indicates a higher degree of wetting. Apparently, both kinetic and thermodynamic effects influence the 4P film morphology. (2) The influence of a C pre-coverage on the film morphology seems to be strongly dependent on the growth temperature. At 93 K the morphology of 4P films grown at 93 K is independent of a C pre-coverage. However, upon heat treatment (regime II) an improved de-wetting is observed in the case of a high C pre-coverage. This is indicated by curve (c) being higher than curve (a) within regime II. Different from that, films grown at 300 K exhibit an opposite trend. Here, a carbon pre-coverage causes an improved wetting, as indicated by a smaller Au signal of (d) compared to (b) at 300 K. This behaviour is most probably due to an interplay between kinetic and thermodynamic effects influencing the film morphology.

Chapter 9

Summary and Conclusions

The experimental findings contained in this work are summarized and some important conclusions that follow from these results are recapitulated.

The results presented in this thesis cover a wide range of different aspects concerning the adsorption and growth of oligo-phenyl molecules on solid surfaces and, in particular, on clean and carbon covered Au surfaces. Important conclusions that have been obtained in the course of the work are listed in the following:

- The crystallographic structural properties of 4P and 6P thin films grown on Au(111) have been solved applying LEED, TDS and XRD. This has been done for films covering a thickness range from the sub-monolayer regime below 1 ML to the multilayer regime (bulk phase) up to 100 nm. In particular, three separate phases are distinguished, i.e. the 1/2 monolayer (semilayer), the saturated monolayer and the multilayer phase.

- We have demonstrated the existence of **quasi-epitaxial growth** of both 4P and 6P monolayers and multilayers on Au(111) (coincident overlayers). The monolayer structure is governed by adsorbate-substrate interactions, leading to a regular structure with the molecules lying parallel to the surface plane. A highly anisotropic azimuthal alignment of the nP molecules with their long molecular axes parallel to the Au$\langle 1\bar{1}0\rangle$ or Au$\langle 11\bar{2}\rangle$ direction has been identified. This monolayer, which exhibits a characteristic edge-face packing of flat and side-tilted molecules, serves as a structural pre-stage for the further film growth. For both 4P and 6P bulk films one crystal orientation is predominant, i.e. the 4P(211) and 6P(21$\bar{3}$) orientation, respectively. The molecules in the bulk exhibit the same azimuthal alignment as that found in the monolayer.

- The **film morphology** of several nm thick nP films has been investigated in detail with OM, AFM and XPS. It is demonstrated that the morphology not only reflects the kinetic conditions during film growth, but also the crystal orientation of the nP bulk crystallites in the film. In particular, for two complementary orientations

of either lying or upright standing nP molecules two clearly distinguishable film morphologies have been observed, i.e. island-like growth for lying molecules and a layer-by-layer growth for upright standing molecules. The needle-like morphology is a consequence of anisotropic surface diffusion sticking of the adsorbed nP molecules to already existing 4P crystallites. In the case of layer-like growth, anisotropic sticking happens at the edges of the terraces, which results in a quasi-two-dimensional growth.

- We have investigated the energetics and kinetics of nP **adsorption and desorption** on several different Au surfaces (Au(111), Au(433) and poly-crystalline Au) as well as on different partially carbon covered Au surfaces. The activation energies for 4P and 6P desorption from the multilayer, E_{des}, could be determined. A listing of these data is given in Appendix A. In addition, the pre-exponential factor ν (frequency factor) for zero-order multilayer desorption could be determined according to the Polanyi-Wigner formalism. In particular, for nP grown on Au(111) also the desorption energies for the monolayer have been determined. To the best of our knowledge no such data has been determined previously.

- We have demonstrated that the the structure and morphology of nP thin films grown on various Au surfaces can be dramatically changed already by the application of very small **carbon pre-coverages** in the sub-monolayer regime (a few % C). This shows the importance of well-controlled fabrication conditions and, in particular, a proper substrate cleaning for the preparation of organic thin films. In the case of 4P, with increasing carbon coverage a structural change of the 4P monolayer was observed, revealing different molecular packing modes compared to 4P grown on C-free Au(111). Simultaneously, a significant change of the 4P desorption kinetics was observed, reflecting the different adsorption situations of 4P molecules on variably C-covered Au(111) surfaces. A carbon pre-coverage as small as 3% passivates surface defects on the Au(111) surface, which significantly increases the **surface mobility** of 4P molecules in the monolayer. The 4P monolayer structure, however, is identical to that found on a carbon-free Au(111) surface. Evaporation on a 15% carbon covered Au(111) surface changes the orientation of the bulk crystallites. A coexistence of at least two different 4P monolayer structures has been identified, with a dominating 4P(201) orientation, which exhibits a different molecular packing compared to previously found structures, i.e. exclusively edge-on adsorbed molecules. The typical morphology of the 4P films at these low carbon coverages is needle-like. In contrast to that, evaporation on a 50% carbon covered Au(111) surface leads to a (001) crystal orientation featuring upright standing molecules. The corresponding film morphology is terrace-like (layer-by-layer).

- Combined XPS and TDS measurements revealed a strong **temperature dependence of the morphology** of several nm thick nP films grown on various clean and carbon covered gold surfaces.

- Oligo-phenylene molecules adsorbed on different gold surfaces in the sub-mono and monolayer regime tend to partially **dehydrogenate** upon heat treatment at elevated temperatures roughly between 650 K and 850 K. The fraction of dehydrogenated nP material strongly depends on the substrate surface geometry and the length of the molecule, possibly due to the stronger bonding of the molecules to the surface. In general, long molecules on stepped surfaces (poly, 433) result in the largest degree of dehydrogenation. This is most probably due to the higher reactivity at defects on the surface, where dehydrogenation may start. The dehydrogenation proceeds at least in a two-step process, where in the first step the dehydrogenating molecules only loose part of their H-atoms and form polycyclic aromatic hydrocarbon (PAH) intermediates ("double-np" molecules), while molecular hydrogen desorbs exclusively from the surface and no other hydrocarbon species release is observed. This represents a convenient surface reaction routine for the surface-mediated synthesis of this molecular species. Even for these large PAHs it has been shown that a regular (sub)monolayer phase exists on the Au(111) surface. A further heating leads to the complete dehydrogenation of the PAHs (second step) leaving behind a graphitic-like carbon adlayer on the Au surface. The latter is presumably disordered.

- Detailed investigations of the **initial nP film growth** on Au(111) in a coverage regime between the first monolayer and a few monolayers have shown that the film growth proceeds as follows: 1) The regular monolayer structure is determined by the balance between intermolecular forces between neighbouring nP molecules and adsorbate-substrate interactions. Hence, it is influenced by the substrate and reflects certain substrate properties, in particular, an anisotropic azimuthal orientation. 2) The next layers adopt a similar packing structure like the monolayer. However, in the case of lying molecules, their packing slightly changes to enable a structural transition to the packing structure of the bulk phase. The latter is identical to the well-known nP crystallographic bulk phase, however, depending on the properties of the monolayer structure, different crystal orientations are adopted in such a way that the contact plane of the bulk crystal is most similar to the monolayer structure.

- Due to the several possibilities of influencing the nP thin film properties described in this work, we propose some "fabrication routines" for a well-defined nP thin film growth, which enable a dedicated **tailoring** of the nP films. For instance, an island-like nP film growth can be efficiently hindered by growing the film at low temperature and afterwards anneal it in order to get a high degree of ordering and the right crystal orientation. Alternatively, the application of defined carbon pre-coverages on the Au substrate prior to the deposition of the organic film opens several possibilities of tailoring the nP thin films. With the combination of surfactant and substrate orientation a wide variety of film morphologies can be grown. On the other hand, surfactants can be used to grow a continuous film with reduced vertical roughness.

- TDS has proven to be a very suitable technique for investigating the existence of an organic wetting layer. The latter is an important aspect for all organic thin films grown on solid surfaces, yet, finding an answer is still a permanent challenge throughout the community, in particular on electrically isolating substrates, where methods like STM are not applicable. Thus, the technique recommends itself to be applied for similar systems, too.

- A recrystallized **polycrystalline gold foil** was successfully applied to study the growth modes of 4P thin films on a large number of single crystal gold surfaces with different orientations at the same time. Needle-like islands with a more or less anisotropic alignment, strongly wetting continuous films and surface areas with very little wetting ability could be observed simultaneously as function of the substrate surface structure. Those crystallite surfaces which consist mainly of (110) terraces tend to favour needle-like 4P growth with the needle orientation perpendicular to the $\langle 1\bar{1}0 \rangle$ direction. Furthermore, steps on vicinal planes with narrow terraces also act as templates for 4P layer growth to induce elongated layer growth normal to the step direction. In all these cases the 4P molecules are oriented with their long axes parallel to the surface. In contrast, an isotropic distribution of needle orientations is observed on the highly symmetric (111) and (100) crystal planes of the gold surface. In general, the application of the poly-crystalline Au substrate provides a new routine for simultaneously investigating organic thin film growth on a large variety of different crystalline surfaces under identical growth conditions like substrate temperature and deposition rate. This way, the application of poly-crystalline foils enables to find the best substrate surface orientation, which is a promising approach for device fabriaction.

The thesis is embedded in a project cluster called "Highly ordered epilayers", which is financed by the Austrian Science Fund FWF. Therefore, a lot of co-operative work has been done by the cross-linked research groups on similar systems. The present work has been carried out within the project number P15625, entitled "Adsorption von organischen Molekülen auf Einkristallen".

Part III

Supplements

Appendix A

Data compilation

Table A.1: Some useful numbers for converting coverage values.

film thickness	nP molecules/cm^2	H-atoms/cm^2	C-atoms/cm^2	ML Carbon
0.1 nm 4P	$2.47 \cdot 10^{13}$	$4.5 \cdot 10^{14}$	$6 \cdot 10^{14}$	0.4
0.1 nm 6P	$1.69 \cdot 10^{13}$	$4.4 \cdot 10^{14}$	$6 \cdot 10^{14}$	0.4

Table A.2: Compilation of regular surface unit cells of different 4P and 6P film structures.

	phase	unit cell dimensions ($nm \times nm,\ °$)	cell area (nm^2)
4P	1/2 ML	$1.4 \times 2.4,\ 63°$	3.0
	1 ML	$1.1 \times 2.2,\ 74°$	2.3
	bulk (211)	$1.4 \times 1.9,\ 79°$	2.6
6P	1/2 ML	$1.4 \times 3.2,\ 74°$	4.3
	1 ML	$1.2 \times 3.3,\ 73°$	3.8
	2 ML	$1.5 \times 2.5,\ 78°$	3.6
	bulk ($21\bar{3}$)	$1.4 \times 2.7,\ 86°$	3.7

Table A.3: Compilation of TDS data. Θ_{sat} denotes the monolayer saturation coverage, T_{ads} the adsorption temperature, $T(\beta_i)$ the peak maximum temperature of the monolayer desorption peak β_i, α the multilayer desorption peak and E_{des} the desorption energy. The symbol † indicates the carbon saturation coverage for thermal desorption of nP molecules. Values of non-existing peaks are marked with "n.e." and values that have not been measured by "-".

	T_{ads}	Θ_{sat}	$T(\beta 1)$	$T(\beta_2)$	$T(\beta_3)$	$E_{des}(\alpha)$
	K	nm	K	K	K	±0.05 eV
6P/Au(111)						
clean	300	0.35	640	520	465	2.40
clean	380	0.3-0.4	640	520	475	2.21
2 ML C †	300	0.4	n.e.	508	n.e.	2.22
2 ML C †	380	0.3	n.e.	538	n.e.	1.94
6P/Au(poly)						
clean	300	(0.4)	(600)	(500-550)	515	2.54
2 ML C	300	0.29	n.e.	600	n.e.	2.22
4P/Au(111)						
clean	93	0.27	520	400	n.e.	1.52
clean	306	0.25-0.3	520	400	n.e.	1.56
0.03 ML C	93	0.25-0.3	550	370-420	n.e.	-
0.15 ML C	93	0.3	550 (≪)	380	n.e.	-
0.5 ML C	93	0.28-0.3	n.e.	390	n.e.	1.60
4P/Au(433)						
clean	300	0.25	550 n.e. 600	425	n.e.	1.43
0.4 ML C †	300	0.3	550	400	n.e.	1.62
0.7 ML C	300	0.3	n.e.	400	n.e.	1.68
4P/Au(poly)						
clean	93	0.25	600	430	n.e.	1.61
clean	310	0.25	600	430	n.e.	1.53
0.5 ML C †	93	0.3	(550)	400	n.e.	1.72
0.5 ML C †	310	0.27-0.3	(550)	416	n.e.	1.64

Appendix B

Quantitative TDS analysis

B.1 TDS for molecular beams

The signal, which is actually measured during the TDS experiments is the ion current from the QMS, which is proportional to the density n (particles/cm^3) within the instruments ionization source volume. The QMS is often referred to as "density detector". In case of measuring n for an **isotropic gas** it is well-known that n is directly proportional to the partial pressure p of the corresponding atomic or molecular species. For instance, $p \propto n$ holds true for an ideal gas.

The situation, however, becomes different when the QMS probes an atomic or **molecular beam** (particle flux). In this case, the density n depends on the retention period τ of the gaseous species within the ionization volume, which is simply connected to the velocity v of the gas molecules (or atoms). The faster molecules will cross the ionization volume in a shorter time period compared to slower ones and, hence, will produce an under-weighted QMS signal. Therefore, in the case of molecular beams the TD spectra have to be corrected. The gas kinetic theory provides the simple relation $v \propto \sqrt{T}$ [129] [1]. Accordingly, the density n, which is actually measured with the QMS instrument, can be re-written as

$$n \propto \frac{1}{v} \propto \frac{1}{\sqrt{T}} \tag{B.1}$$

This means that the QMS signal has to be multiplied by $\sqrt{T}$ in the TD spectra in order to obtain the correct representation, i.e. the QMS signal being proportional to the desorption rate.

[1] This is valid for the average velocity, the root-mean-square velocity as well as the most probable velocity.

B.2 Absolute rate measurement

An absolute determination of the desorption rate is very useful, for instance, for a proper analysis of the TD spectra. It can be done with the help of combined TD and quartz microbalance measurements, respectively.

The measured QMS signal (usually given in arbitrary units or Ampere of ion current) is proportional to the desorption rate R_{des}, in molecules/(cm^{2}s), after correction for $\sqrt{T}$, as described in the previous section. In the following, it will be shown how to determine a proportionality factor for an absolute quantification of R_{des}.

If the (corrected) QMS signal $I(t)$ is plotted against the measuring time t then the integral area underneath the $I(t)$ curve is proportional to the total number of desorbed molecules N_0: [2]

$$N_0 = C_1 \cdot \int I(t)dt \tag{B.2}$$

The proportionality factor C_1 is simply the ratio of N_0 over the integral peak area. The latter can be easily determined by a numerical integration of the QMS spectrum with a properly set base line. The number of desorbed molecules N_0, however, equals also the total amount of initially deposited molecules [3], which can be absolutely quantified with the quartz micro-balance. Therefore, the proportionality factor C_1 is fixed.

In order to determine the desorption rate R_{des}, one has to consider also the area of the sample surface A_{sample}. In the case of the cylindrical Au single crystals purchased from MaTecK Inc. (1 cm diameter), it is 0.785 cm^2. Finally, R_{des} is given by:

$$R_{des}[\frac{molecules}{cm^2 s}] = \frac{I(t) \cdot C_1}{A_{sample}} \tag{B.3}$$

[2] Note, that t is related to the temperature T over the heating rate β as: $T(t) = T_0 + \beta t$.

[3] This is only valid, of course, if no dissociation occurs.

Appendix C

Remarks on the 2D reciprocal lattice

A two-dimensional periodic structure in real space, e.g. a crystalline metal surface, can be comfortably described by two linearly independent lattice vectors $\vec{a_1}$ and $\vec{a_2}$ that generate the 2D surface unit cell [51, 90]. To the set of $\vec{a_i}$ $(i = 1, 2)$ there corresponds in the vector calculus a set of reciprocal lattice vectors $\vec{a_i^*}$, which are defined by the well-known relation [1]

$$\vec{a_i} \cdot \vec{a_j^*} = \delta_{ij} \tag{C.1}$$

Distinguishing the two cases $i \neq j$ and $i = j$ it follows that the $\vec{a_i^*}$ can be constructed from the $\vec{a_i}$ according to the following relations [130]:

$$\vec{a_1^*} \perp \vec{a_2}, \qquad \vec{a_2^*} \perp \vec{a_1} \tag{C.2}$$

$$\mid \vec{a_1^*} \mid = \frac{1}{\mid a_1 \mid \cdot sin(\gamma)}, \qquad \mid \vec{a_2^*} \mid = \frac{1}{\mid a_2 \mid \cdot sin(\gamma)}, \qquad \gamma^* = 180 - \gamma \tag{C.3}$$

where γ (given in degrees) is the real space unit cell angle, i.e. the angle enclosed by $\vec{a_1}$ and $\vec{a_2}$, and γ^* is the reciprocal unit cell angle between $\vec{a_1^*}$ and $\vec{a_2^*}$. By analogy with the well-known Miller indices (hkl) that are attributed to lattice planes within a three-dimensional lattice, the lattice points of a two-dimensional lattice can be arranged in **rows** that are classified by "two-dimensional Miller indices" (**hk**). A simple example showing the (10) and (01) atomic rows is given in Figure 2.3. The inter-row distance corresponding to a set of parallel rows (hk) is labelled d_{hk}. By analogy with the three-dimensional case, the intensity maxima or reflections that appear in a two-dimensional diffraction pattern are attributed to scattering at rows (hk). The reciprocal lattice points are labelled accordingly.

[1] Per definition the Kronecker symbol δ_{ij} equals 0 if $i \neq j$ and 1 for $i = j$.

Overlayer Structures

The cell vectors of a regular two-dimensional overlayer structure $\vec{b_i}$ $(i = 1, 2)$ can be expressed in terms of the substrate vectors

$$\begin{aligned} \vec{b_1} &= m_{11} \cdot \vec{a_1} + m_{12} \cdot \vec{a_2} \\ \vec{b_2} &= m_{21} \cdot \vec{a_1} + m_{22} \cdot \vec{a_2} \end{aligned} \tag{C.4}$$

where the coefficients m_{ij} can be arranged in terms of the so-called **transformation matrix** or epitaxy matrix M

$$M = \begin{pmatrix} m_{11} & m_{12} \\ m_{21} & m_{22} \end{pmatrix} \tag{C.5}$$

Representing the unit cell vectors $\vec{a_i} = (a_{i1}, a_{i2})$ and $\vec{b_i} = (b_{i1}, b_{i2})$ as row vectors they can be rewritten in a matrix representation, too. Consequently, the epitaxial relationship between an overlayer structure $\vec{b_i}$ and a substrate structure $\vec{a_i}$ can be expressed using the transformation matrix

$$\begin{pmatrix} \vec{b_1} \\ \vec{b_2} \end{pmatrix} = M \cdot \begin{pmatrix} \vec{a_1} \\ \vec{a_2} \end{pmatrix} \tag{C.6}$$

The same type of representation can be applied for the reciprocal vectors $\vec{b_i^*}$ and the corresponding coefficients m_{ij}^* define a second matrix M^*.

A frequently encountered problem in LEED pattern analysis is to determine the real space vectors $\vec{b_i}$ corresponding to a certain regular overlayer structure. One way of doing so is to calculate the epitaxy matrix $M = (m_{ij})$ using the reciprocal matrix $M^* = (m_{ij}^*)$. The latter is the inverse transposed of M so that $M^* = \tilde{M}^{-1}$ and $M = \tilde{M^*}^{-1}$, respectively [90]. Hence, the coefficients m_{ij} can be calculated as

$$\begin{aligned} m_{11} &= +\frac{1}{det\ M^*} \cdot m_{22}^* \\ m_{12} &= -\frac{1}{det\ M^*} \cdot m_{21}^* \\ m_{21} &= -\frac{1}{det\ M^*} \cdot m_{12}^* \\ m_{22} &= +\frac{1}{det\ M^*} \cdot m_{11}^* \end{aligned} \tag{C.7}$$

Appendix D

Practical analysis of the LEED pattern

For electrons scattered elastically at a set of parallel rows (hk), the **scattering vector** $\Delta\vec{k}_{(hk)}$ is defined as the vector difference between the wave vector $\vec{k}_{(hk)}$ of the scattered electrons and the incident wave vector $\vec{k}_0$

$$\Delta\vec{k}_{(hk)} = \vec{k}_{(hk)} - \vec{k}_0 \tag{D.1}$$

The quantity which is actually measured with the LEED instrument, is the radial distance of a diffraction spot with respect to the 00 reflection denoted as $k_{||out}$. The labelling of this characteristic length, for instance in mm, already indicates that it is closely related to the component of the scattered wave vector parallel to the surface plane $\vec{k}_{||}$. However, the **diffraction condition** according to the kinematic scattering theory states that the parallel component of the scattering vector, $\Delta\vec{k}_{||}$, is the determining quantity, i.e. it is equal to a reciprocal space vector $\vec{g}_{(hk)}$

$$\Delta\vec{k}_{||} = \vec{g}_{(hk)} \tag{D.2}$$

In general, these two quantities ($\vec{k}_{||}$ and $\Delta\vec{k}_{||}$) are NOT identical. However, in the special case of **normal incidence** they are, as illustrated in Figure D.1. Thus, only under normal incidence, the measurement of the radial distance $k_{||out}$ enables a correct analysis of the LEED pattern with the presented formalism. The scattering angle Θ can then be expressed in terms of the measured distance $k_{||out}$ and the radius, R, of the hemispheric grid.

$$sin(\Theta) = \frac{k_{||out}}{1.2 \cdot R} \tag{D.3}$$

The factor 1.2 is provided by the instrument manufacturer and results from the fringe field correction (cf. Figure D.2). In the present work an Omicron series 855 MCP-LEED instrument has been used. The geometric parameters of this instrument are listed in Table D.1. Inserting them into the equations 2.9 and 2.10 yields an instrument-specific

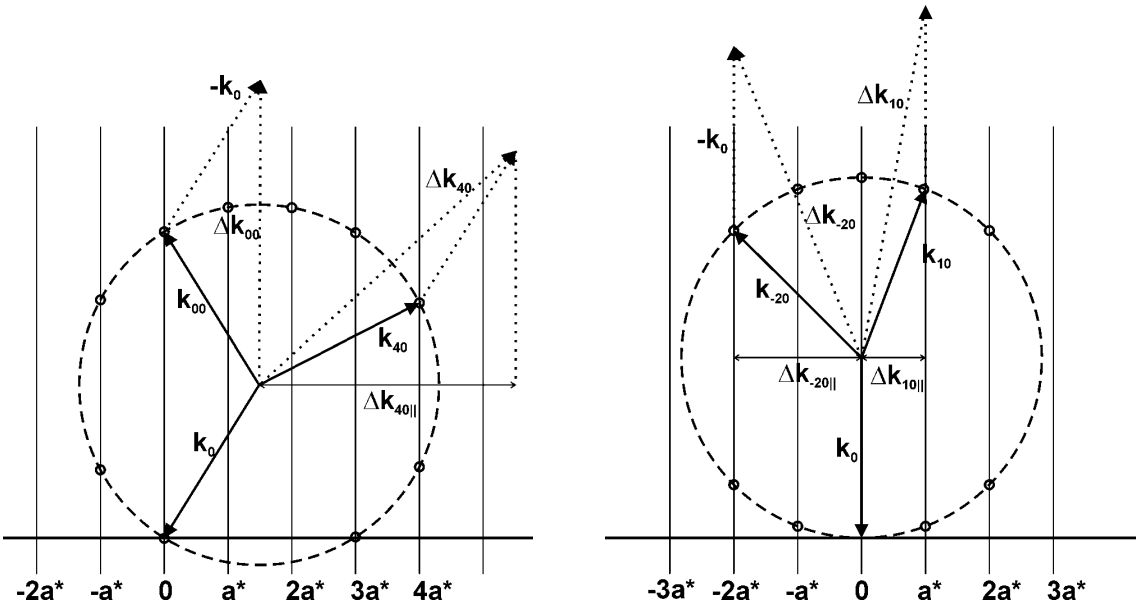

Figure D.1: Ewald construction for angular incidence (left) and normal incidence (right).

Table D.1: Geometric parameters of the Omicron 855 LEED instrument. R is the radius of the grid hemishpere, L_{0out} is the radius of the fluorescent screen and Θ_0 is the maximum detectable scattering angle.

R	51.7 mm
L_{0out}	37.5 mm
Θ_0	37.2°

numerical equation for kinematic LEED analysis.

$$d_{hk}[nm] = \frac{76.03}{k_{||out}[mm] \cdot \sqrt{U[V]}} \tag{D.4}$$

It is important to note, that this numerical equation is only valid if the value of $k_{||out}$ is properly scaled. The maximum $k_{||out}$ must be equal to the radius of the fluorescent screen, L_{0out}, which restricts the maximum detectable scattering angle Θ_0. This is illustrated in Figure D.2.

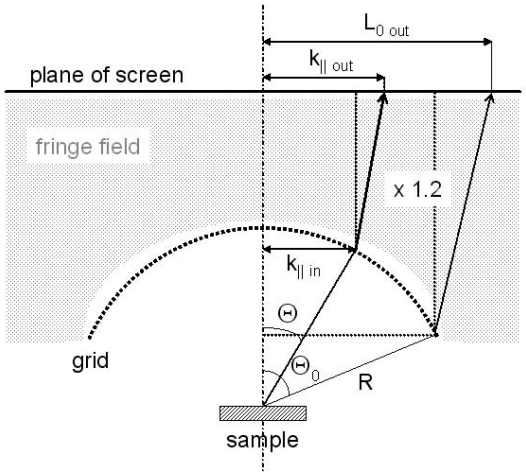

Figure D.2: Microchannel plate LEED geometry schematic. (The symbols are described in the text.)

Correction of the main equation

The "ideal" equation D.4 has to be corrected because of two practical reasons: Firstly, it is very difficult and time consuming to exactly adjust the sample position, which causes a systematic error in the value of R [1] (cf. Figure D.2). Secondly, the fringe field correction may deviate from the factory specifications. Thus, equation D.4 has to be corrected by the use of a reference sample, e.g. the Au(111) surface. Given the inter-row distance of Au(111), $d_{111} = 0.249$ nm [2], equation D.4 can be re-written according to $k_{||out}$. Additionally, a power law correction factor $f(U) = \alpha \cdot U^{\beta}$ is introduced:

$$k_{||out}[mm] = 305.3577 \cdot n \cdot \frac{f(U)}{\sqrt{U}} \tag{D.5}$$

A numerical fit of the experimentally determined values of $k_{||out}$ for a certain Au(111) diffraction spot yields the parameters α and β. Such a correction procedure has been carried out each time the crystal mounting position has been changed by transferring it in and out of the vacuum chamber. The corrected kinematic LEED equations that have been used in this work for the different samples are listed below:

$$4P/Au(111) : d_{hk}[nm] = \frac{108.7}{k_{||out}[mm] \cdot U^{0.540}[V]} \tag{D.6}$$

$$6P/Au(111) : d_{hk}[nm] = \frac{109.1}{k_{||out}[mm] \cdot U^{0.553}[V]} \tag{D.7}$$

The correction curve diagram for equation D.6 is presented in Figure D.3.

[1] A significant misalignment of the sample can also cause image deformation because the hemispheric geometry is lost.

[2] The mean atomic nearest-neighbour distance of the Au(111) surface is $a_{111} = 0.288$ nm. The inter-row distance is $d_{hk} = \frac{\sqrt{3}}{2} \cdot a_{111} = 2.49$ nm.

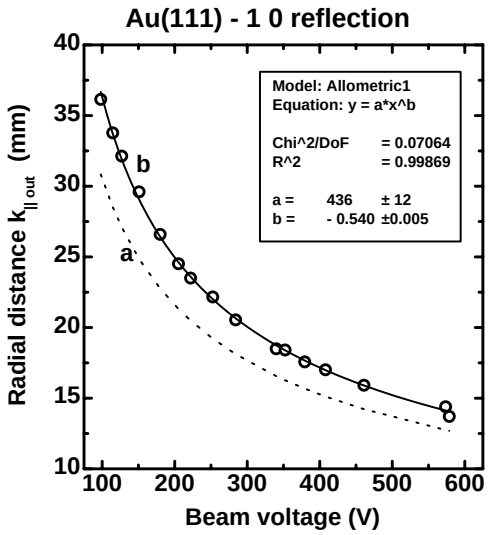

Figure D.3: Experimental determination of the parameters for the correction of the LEED analysis. The dotted curve (a) shows the calculated values ($\propto \sqrt{U}$ dependency). The experimental data, indicated by the open circles, have been fitted by a power law indicated by the solid curve (b) ($\propto U^{-0.540}$ dependency, cf. equation D.6).

LEED Pattern analysis

For practical reasons it is necessary to record a series of LEED images of a certain overlayer structure at various voltages. This way it is possible to overcome the limitations imposed by the LEED optics (limited detection angle) and interference effects (suppression of certain diffraction spots). This way a number of different LEED reflections can be recorded, which is sufficiently large for a proper pattern analysis. In a second step, the positions of the low-index reflections are measured in each of the recorded images. In particular, one has to carefully look for the 01 and 10 reflections, which are in some cases difficult to detect because of the low beam voltages necessary. In a third step, the inter-row distances d_{hk} corresponding to the reflections in each experimental LEED image have to be calculated. In the present work this has been done with the help of the corrected numerical LEED equations D.6 and D.7. Additionally, the azimuthal angles ϕ_{hk} at which the spots appear relative to some preferential direction, e.g. the Au$\langle 11\bar{2}\rangle$ direction, have to be measured. In a forth and final step, the reflection data is transformed to a uniform pre-set voltage, e.g. 20 V, and graphically illustrated. This way it is possible to draw a single LEED pattern diagram for a single fixed voltage, which includes all the experimentally observed reflections taken from different LEED images at different voltages. Finally, such a representation of the LEED pattern is free of image deformations and can be used for pattern analysis.

The latter can be simplified to a great extent by considering the particular symmetry properties of the substrate surface. In the case of Au(111) the $(22 \times \sqrt{3})$ herringbone surface reconstruction has to be considered, too. However, for several reasons described in Section 4.4, it is sufficient for the LEED pattern analysis to consider the Au(111)

surface as an "ideal" fcc (111) surface with $p3m1$ symmetry (2D spacegroup number 14). Accordingly, there exists a 3-fold rotational symmetry and three mirror planes along the Au$\langle 11\bar{2} \rangle$ directions. In most cases the overlayer structure of nPs exhibits an oblique surface unit cell, which is azimuthally rotated with respect to the substrate lattice. Therefore, mirror domains occur in both reciprocal and real space.

Simulation

The supplemental software packages "LEEDpat" (version 2.0)[3] and "LEEDSim" (demo version 1.3.6)[4] have been used for simulating the experimentally observed LEED patterns. For a description of these programs the reader is referred to the program manuals available over the WWW (see footnotes).

The starting point for the simulation is the unit cell parameters, a, b, γ, Φ, of both the substrate surface and the organic overlayer. For the Au(111) surface the parameters are well-known: $a = b = 0.288$ nm, $\gamma = 120°$ and $\Phi = 0°$, respectively. The symmetry group is $p3m1$. The $22 \times \sqrt{3}$ surface reconstruction of the Au(111) surface cannot be considered by the simulation programs.

For the organic overlayer the experimentally determined unit cell parameters from the above analysis procedure are used as initial values. The simulated LEED pattern, which is based on these data, is then compared to the experimental LEED pattern. At this stage it has been frequently encountered that the match between both patterns was still not good enough, i.e. some (high order) reflections exhibit an unacceptably large deviation from the simulated pattern. The reason for such a mismatch lies in small measuring errors for the angle and/or distance measurements of the reflections described above. In particular, the positions of the higher order reflections react very sensitive to small deviations of the cell parameters. Hence, a recursive refinement procedure of adapting the values of the cell parameters and simulating the LEED pattern can be made until the match between simulation and experiment is sufficiently good. At the end of this procedure, when the simulated pattern finally matches the experimental one, the "right" cell parameters that describe the organic overlayer are gained.

[3]Created by K. Hermann and M. A. Van Hove. http://electron.lbl.gov/software/intsoftware.html
[4]Created by S. Mannsfeld. http://www.creaphys.de/webseiten/software/leedsim.html

Appendix E

Quantitative XPS analysis

For the sake of simplicity, the quantitative XPS analysis performed in this work has been made, disregarding any corrections of the photoelectron intensity due to "second order" effects, like self-absorption processes.

Due to the ionization of atom core levels nl by x-ray quanta of energy $h\nu$ photoelectrons are emitted. In case of a pure solid substrate S, the photoelectron intensity I_S corresponding to a certain core level is given by [88, 89, 131]:

$$I_S = \frac{I_0}{\cos(\gamma)} \cdot K_S \cdot \sigma_S \cdot L_S \cdot n_S \cdot \lambda_S \cdot \cos(\delta) \tag{E.1}$$

The subscript S indicates that the quantities correspond to the substrate. I_0 is the x-ray characteristic line flux intensity of the primary beam incident under the angle γ with respect to the sample surface normal as shown in Figure E.1, $K_S(E)$ is the spectrometer detection efficiency for a photo-electron with kinetic energy E. It also includes the spectrometer transmission function. In case of measuring in the constant ΔE mode it depends inversely on the photo-electron kinetic energy E [87]:

$$I(E) \propto E^{-1} \tag{E.2}$$

$\sigma_S(nl, h\nu)$ is the photoionisation cross-section of the core-level nl by a photon with energy $h\nu$, $L_S(\gamma + \delta, \beta_S)$ is the angular asymmetry factor of the photo-electron intensity distribution. It depends on the angle $\gamma + \delta$ between the photon and the photo-electron direction, where δ is the collection angle with respect to the surface normal (see Figure E.1), and also on $\beta_S(nl, h\nu)$, which is the asymmetry parameter for emission of a photoelectron from a certain core-level nl by a photon of energy $h\nu$. n_S is the number of atoms per unit volume and $\lambda_S(E)$ is the inelastic mean free path of photoelectrons with kinetic energy E.

If the sample surface is covered by an adlayer A, whose thickness is ≤ 1 monolayer, the above formula is not suitable for calculating the corresponding photoelectron intensity I_A. Instead, a linear dependency of I_A on the adsorbate coverage Θ_A is given [132]:

$$I_A = \frac{I_0}{\cos(\gamma)} \cdot K_A \cdot \sigma_A \cdot L_A \cdot \Theta_A \tag{E.3}$$

Table E.1: Photoelectron properties of selected core-level states. E_{kin} is the photoelectron kinetic energy, β the asymmetry parameter for photoelectron emission, L the angular asymmetry factor, σ the differential photoelectric cross-section (after Scofield), λ the photoelectron inelastic mean free path and n the mean number of atoms per unit volume (atoms/cm^3). The literature references are also given.

	E_{kin} (eV) †	β	L§	σ ‡	λ (nm)	n ($10^{23} atoms/cm^3$)
Au 4f	1169	1.00	1.063	3.96	1.46	0.588
C 1s	969	2.00	1.125	0.225		
ref.	[133]	[134]		[135, 136]	[137]	

† for excitation with MgK$_\alpha$ radiation (1253.6 eV).
§ calculated from equation E.6
‡ relative to F 1s.

The subscript A indicates that the quantities correspond to the adsorbate. The combination of the equations E.1 and E.3 enables the quantitative determination of the adsorbate coverage $\Theta_A(atoms/cm^2)$ on the substrate. This can be done by measuring the two intensities I_A and I_S, respectively, under constant experimental conditions. The intensity values are experimentally gained from an integration over the corresponding photoelecton peaks (peak area determination). The adsorbate coverage then results as

$$\Theta_A = \frac{I_A}{I_S} \cdot C_0 \tag{E.4}$$

$$C_0 = const. = \frac{K_S}{K_A} \cdot \frac{\sigma_S}{\sigma_A} \cdot \frac{L_S}{L_A} \cdot n_S \cdot \lambda_S \cdot \cos(\delta) \tag{E.5}$$

The constant factor C_0 only depends on the instrumental setup (geometry, beam energy) and some material specific parameters of the adsorbate and substrate. Table E.1 lists the relevant parameters for the materials used in this thesis, i.e. gold and carbon.

For the Leybold XPS instrument used in this work the measuring geometry is determined by the angle $\gamma = 60°$ of the incident photon beam and the detection angle $\delta = 0°$. The angular asymmetry factor L can be written as [87]

$$L(\gamma - \delta, \beta) = 1 - \frac{\beta}{4}(3\cos^2(\gamma - \delta) - 1) \tag{E.6}$$

For the angles given above this yields the L values listed in Table E.1. The factor $cos(\delta)$ is equal to 1 in the present work ($\delta = 0°$). Including the spectrometer transmission function according to equation E.2 the constant factor C_0 from equation E.5 for the combination of C (adsorbate) on Au (substrate) becomes

$$C_0 = \frac{969}{1169} \cdot \frac{3.96}{0.225} \cdot \frac{1.063}{1.125} \cdot\ 0.588 \cdot 10^{23} \cdot 1.46 \cdot 10^{-7} \cdot 1 \approx 1.18 \cdot 10^{17} atoms/cm^2 \tag{E.7}$$

The determination of the intensity values, I_A and I_S, is not straight-forward, since the photoelectron intensity is attributed to the integral area underneath the corresponding peak

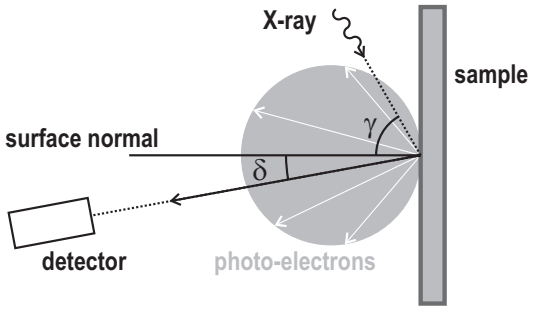

Figure E.1: Measuring geometry for the XPS experiments. The symbols are explained in the text.

in the measured photoelectron spectrum, which is superposed by the inelastic background. The latter has to be subtracted before the peak area can be evaluated properly. Several different methods of peak integration are described in the literature that are based on analytical expressions for fitting the peak-shapes and the inelastic background, separately. The most frequently used methods for fitting the photoelectron peaks are Gaussian or Doniach-Sunjic line profiles. For the inelastic background the Shirley or Tougaard method are commonly used [87, 138], however, for a first-order approximation, even a straight baseline can be used for the background subtratction. The latter has been applied in this work. The peak area determination was done by numerical integration of the experimental data. For the recording of the XPS spectra the hemispherical electron energy analyzer was driven in the constant ΔE mode.

Appendix F

Quantitative Auger analysis

Quantification of recorded Auger spectra using first principles is theoretically possible but rarely done due to significant complications in properly describing the ionization process as well as the attenuation of the electron beam current in the sample [87]. In many cases this method is too complicated for practical use. Instead, a more practical way of analyzing is to use relative sensitivity factors S_X [139]. Those can be conveniently derived from reference spectra described in the literature, for instance, they can be found in reference [140]. The sensitivity factors are usually derived for pure elements and referenced to some other material, for instance silver ($S_{Ag} := 1.00$). The relative sensitivity factor of element X, S_X, can be simply calculated as

$$S_X = \frac{I_X}{I_{Ag}} \tag{F.1}$$

where I_X and I_{Ag} are the Auger peak-to-peak heights of element X and silver taken from the derivated Auger reference spectra ($\frac{dN(E)}{dE}$) of the pure substances, respectively. Accordingly, the atomic concentration C_X of the homogeneously distributed element X can be calculated by

$$C_X = \frac{I_X/S_X}{\Sigma_i I_i/S_i} \tag{F.2}$$

In the case of **samples with a thin overlayer** A residing on top of a bulk B a similar approach can be made. The fractional monolayer coverage Θ_A of the adlayer, which lies in the range between $0 \leq \Theta_A \leq 1$, is approximately given by the relation [87]

$$\Theta_A = Q_{AB} \frac{I_A/S_A}{I_B/S_B} \tag{F.3}$$

where S_A, S_B are the corresponding sensitivity factors of the adlayer and substrate material, respectively. The so-called monolayer matrix factor Q_{AB} can be calculated from first principles according to [87, 139].

Appendix G

Appropriate Software Packages

For some specific aspects of data processing, data evaluation and visualization that have been encountered in the course of this work a selection of helpful software packages have been used. These will be briefly described in the following.

Crystal structure representation: Both *Mercury*[1] and *PowderCell*[2] provide convenient functions for the visualization of the bulk crystal structures of atomic or molecular crystals. In order to use these programs one has to provide the proper crystal structure data files that contain the complete crystallographic information of the investigated material. These structure files are normally plain text files containing the structural information, which is represented in a specific data format. Depending on the data format in the text files, the file extensions are named accordingly. For instance, the standard data format for *Mercury* is *.mry and for *PowderCell* it is *.cel, respectively. The structure files can either be downloaded from online databases[3] or they can be created manually. Although there exists a large variety of well over 30 different file formats, which is due to the large number of available structure representation programs, only a few selected file formats can be imported/exported by *Mercury* and *PowderCell*, respectively. Therefore, it is quite useful to have at hand a file format interconversion program like *BabelWin*[4]. Unfortunately, the *.cel file format is one of the few formats that can be neither read by *BabelWin* nor by *Mercury*.

One of the most remarkable feature of *Mercury* is the possibility of displaying user-defined crystal planes (*hkl*) along which the crystal structure can be sliced. This enables a convenient illustration of the molecular packing within a specific crystal plane as well as the representation of a stepped vicinal surface. On the other hand, PowderCell offers the possibility of calculating x-ray powder diffraction patterns and the structure factors corresponding to specific net planes can be easily extracted.

[1] Version 1.4, `http://www.ccdc.cam.ac.uk/mercury/`

[2] Version 2.4, `http://www.ccp14.ac.uk/`

[3] Inorganic Crystal Structure Database (ICSD) `http://icsdweb.fiz-karlsruhe.de/index.php`

[4] Version 1.03b, `http://www.ccp14.ac.uk/`

Both programs allow measurements of distances and angles between arbitrary atoms of the presented structure.

LEED pattern simulation: In particular the *LEEDSim*[5] program is designed for simulating the LEED patterns of (organic) adlayers on solid substrates. Different from *LEEDpat*[6], one can superpose several adlayers simultaneously. Additionally, *LeedSim* can perform not only simple geometric LEED pattern calculations but also kinetic calculations considering a basis of one or more organic molecules within the surface unit cell. For this purpose it is necessary to import the proper structure file of the material, which contains at least the atomic positions of the corresponding molecule. The desired file format is the "Alchemy mol file format (*.mol)" that can be interconverted with the help of *BabelWin*.

[5] Demo version 1.3.6, `www.creaphys.de`

[6] Version 2.0, `http://w3.rz-berlin.mpg.de/~hermann/LEEDpat/`

Appendix H

List of publications and conference contributions

H.1 Publications in international scientific journals

1. *Initial Growth of Hexaphenyl on Au(111)*, S. Müllegger and A. Winkler, Surf. Sci. (submitted).

2. *Dehydrogenation of oligo-phenylenes on gold surfaces*, S. Müllegger and A. Winkler, Surf. Sci. (in press).

3. *Structure and morphology of quaterphenyl thin films on Au(111) - The influence of surface contamination by carbon*, R. Resel, M. Oehzelt, T. Haber, G. Hlawacek, C. Teichert, S. Müllegger and A. Winkler, J. Cryst. Growth 283 (2005) 397.

4. *Substrate structure dependence of the growth modes of p-quaterphenyl thin films on gold*, S. Müllegger, S. Mitsche, P. Pölt, K. Hänel, A. Birkner, C. Wöll and A. Winkler, Thin Solid Films 484 (2005) 408.

5. *The influence of carbon on the adsorption/desorption kinetics and monolayer formation of para-quaterphenyl on Au(111)*, S. Müllegger and A. Winkler, Surf. Sci. 574 (2005) 322.

6. *X-ray diffraction line broadening in thin film layers of p-quaterphenyl on C-covered gold (111)*, M. Oehzelt, S. Müllegger, A. Winkler, G. Hlawacek, C. Teichert, R. Resel, Mat. Structures 11 (2004) 155.

7. *Pattern formation in para-quaterphenyl film growth on gold substrates*, G. Hlawacek, C. Teichert, S. Müllegger, R. Resel and A. Winkler, Synth. Met. 146 (2004) 383.

8. *Growth kinetics, structure, and morphology of para-quaterphenyl thin films on gold(111)*, S. Müllegger, I. Salzmann, R. Resel, G. Hlawacek, Ch. Teichert, and A. Winkler, J. Chem. Phys., 121, 2272 (2004).

9. *Adsorption, initial growth and desorption kinetics of p-quaterphenyl on polycrystalline gold surfaces*, S. Müllegger, O. Stranik, E. Zojer, and A. Winkler, Appl. Surf. Sci., 221 (2004) 184.

10. *Epitaxial growth of quaterphenyl thin films on gold(111)*, S. Müllegger, I. Salzmann, R. Resel, and A. Winkler, Appl. Phys. Lett., 83 (2003) 4536.

H.2 Invited Talks

1. *Surface science studies of ultra-thin oligo-phenyl thin films*, S. Müllegger, 30. June 2005, University of Leoben, Austria.

2. *Control of the structure and growth of organic nanofibers: A surface science approach*, S. Müllegger and A. Winkler, NANOFIBER Workshop, 2.-3. September 2004, Syddansk University Odense, Denmark.

H.3 Conference contributions

1. *Chain-length dependence of oligo-phenyl thin film formation on Au(111)*, S. Müllegger, T. Haber, R. Resel, G. Hlawacek, C.Teichert and A. Winkler, 55. ÖPG Jahrestagung, 27-30th September 2005, Vienna, Austria. (Talk Müllegger)
`http://gerda.univie.ac.at/oepg2005/main.php`

2. *Controlling the thin film growth of oligo-phenylenes on gold by surface structure and surface modifications*, A. Winkler, S. Müllegger, S. Mitsche and P. Pölt, ECASIA, 25th - 30th September 2005, Vienna, Austria. (Talk Winkler)

3. A. Winkler and S. Müllegger, Dehydrogenation of oligo-phenylenes on gold surface, ECOSS 23, 4-9th September 2005, Berlin, Germany. (Poster Winkler)

4. *Monolayer and thin film formation of sexiphenyl on Au(111) surfaces*, S. Müllegger and A. Winkler, Cluster Workshop, June 2005, Linz, Austria. (Talk Müllegger)

5. *Effect of substrate structure on organic thin film morphology: Oligo-phenylenes on gold*, S. Müllegger, S. Mitsche, P. Pölt, K. Hänel, A. Birkner, C. Wöll and A. Winkler, DPG spring meeting, 4th - 9th March 2005, Berlin, Germany. (Talk Müllegger)
`http://www.dpg-einstein.de/index.html.en` or
`http://www.dpg-tagungen.de/prog/`

6. *Ultra-thin hexaphenylene films grown on Au(111) and Au(433)*, S. Müllegger, A. Stupnik, M. Leisch and A. Winkler, DPG spring meeting, 4th - 9th March 2005, Berlin, Germany. (Poster Müllegger)

7. *Surface Science investigations of Ultra-thin Hexaphenyl layers on Au(111)*, S. Müllegger and A. Winkler, Cluster Workshop, December 2004, Linz, Austria. (Talk Müllegger)

8. *The influence of carbon on the quaterphenyl thin film growth on a Au(111) surface*, S. Müllegger, T. Haber, R. Resel, G. Hlawacek, C. Teichert and A. Winkler, 54. ÖPG Jahrestagung, 28-30th September 2004, Linz, Austria. (Talk Müllegger) `http://www.somap.jku.at/oepg_2004/`

9. *Multilayer growth of upright standing oligo-phenyl molecules*, G. Hlawacek, C. Teichert, S. Müllegger, A. Winkler, O. Lengyel, R. Resel, S. Berkebile, G. Koller and M. Ramsey, 54. ÖPG Jahrestagung, 28-30th September 2004, Linz, Austria. (Talk Müllegger) `http://www.somap.jku.at/oepg_2004\`

10. *The influence of carbon on the quaterphenyl thin film growth on a gold (111) surface*, S. Müllegger, T. Haber, R. Resel, G. Hlawacek, C. Teichert and A. Winkler, JVC-10, Sept 2004, Portoroz, Slovenjia. (Talk Winkler)

11. *Fashioning of Quaterphenyl Thin Films on Au*, S. Müllegger, T. Haber, M. Oehzelt, R. Resel, G. Hlawacek, Ch. Teichert and A. Winkler, ICSS-12, 28th June - 2nd July 2004, Venice, Italy. (Poster Müllegger) `http://www.ivc16.org/`

12. *Tailoring of 4P thin films on Au*, S. Müllegger and A. Winkler, JRP Cluster Workshop, June 2004, St. Gallen (Stmk), Austria.(Talk Müllegger)

13. *Formation and structure of oligo-phenyl thin films for organic optoelectronics*, R. Resel, O. Lengyel, T. Haber, M. Oehzelt, S. Müllegger, A. Winkler, B. Winter, G. Koller, M. Ramsey, G. Hlawacek, C. Teichert, A. Andreev and H. Sitter, 28th Workshop on compound Semiconductor Devices and Integrated Circuits, May 2004, Wosdice, Slovakia. (Talk Resel)

14. *Pattern formation in para-quaterphenyl film growth on gold substrates*, G. Hlawacek, C. Teichert, S. Müllegger, R. Resel, A. Winkler, E-MRS Spring Meeting, 24-28th May 2004, Strasbourg, France. (Poster Hlawacek)

15. *The influence of Carbon on the mono- and multilayer growth of p-quaterphenyl on Au(111)*, A. Winkler, S. Müllegger, T. Haber, R. Resel, DPG, 8-12th March 2004, Regensburg, Germany. (Poster Müllegger)
`http://www.physik.uni-regensburg.de/akf2004/`

16. *AFM investigations of oligo-phenyl thin films on crystallite substrates*, G. Hlawacek, C. Teichert, S. Müllegger, A. Winkler, R. Resel, S. Berkebile, M. Ramsey, DPG, 8-12th March 2004, Regensburg, Germany. (Poster Hlawacek)
`http://www.physik.uni-regensburg.de/akf2004/`

17. *The manipulation of thin film layer growth of quaterphenyl on Au(111)*, A. Winkler, S. Muellegger, I. Salzmann, R. Resel, G. Hlawacek, C. Teichert, 3S04, 29th February - 6th March 2004, St. Christof am Arlberg, Austria. (Talk Winkler) `http://www.iap.tuwien.ac.at/www/3s04/`

18. *Tailoring of 4P Thin Films on Au(111)*, S. Müllegger, T. Haber, R. Resel, G. Hlawacek, C. Teichert and A. Winkler, EUROFET Winterschool, 6th-12th March 2004, Planneralm, Austria. (Poster Müllegger)

19. *Monolayers of quaterphenyl on gold surfaces*, S. Müllegger and A. Winkler, Cluster Workshop, Dec. 2003, Graz, Austria. (Talk Müllegger)

20. *Growth kinetics and structure of p-quaterphenyl thin films on gold surfaces*, S. Müllegger, I. Salzmann, R. Resel, G. Hlawacek, C. Teichert, E. Zojer, A. Winkler, MRS Fall Meeting, 1-5th December 2003, Boston, USA. (Poster Müllegger) `http://www.mrs.org/meetings/fall2003/`

21. *Self-alignment of oligomer nanocrystals*, C. Teichert, G. Hlawacek, A. Andreev, H. Sitter, G. Matt, N.S. Sariciftci, S. Müllegger, A. Winkler, EURESCO, 4-9th October, 2003, Kerkrade, The Netherlands. (Talk Teichert)

22. *Initial growth of p-quaterphenyl on gold surfaces*, S. Müllegger, I. Salzmann, R. Resel, G. Hlawacek, C. Teichert, A. Winkler, 53. ÖPG Jahrestagung, 1-2nd October 2003, Salzburg, Austria. (Poster Müllegger) `http://www.sbg.ac.at/bio/oepg_2003/`

23. *High resolution AFM investigations of p-quaterphenyl island growth on gold substrates*, G. Hlawacek, C. Teichert, S. Müllegger, I. Salzmann, R. Resel, A. Winkler, 53. ÖPG Jahrestagung, 1-2nd October 2003, Salzburg, Austria. (Poster Hlawacek) `http://www.sbg.ac.at/bio/oepg_2003/`

24. *High-resolution AFM investigations of para-quaterphenyl island growth on gold surfaces*, G. Hlawacek, C. Teichert, S. Müllegger, I. Salzmann, R. Resel, A. Winkler, SPM Workshop, 24-26th September 2003, Mainz, Germany. (Talk Hlawacek)

25. I. Salzmann, R. Resel, S. Müllegger, A. Winkler, G. Hlawacek, C. Teichert, Autumn Meeting RTN Network EUROFET, Sept 2003, Varenna, Italy. (Talk Salzmann)

26. *Adsorption and growth of p-quaterphenyl on gold surfaces*, S. Müllegger, I. Salzmann, R. Resel, G. Hlawacek, C. Teichert, S. Mitsche, P. Pölt, A. Winkler, ECOSS 22, 7-12th September 2003, Prague, Czech Republic. (Poster Müllegger) `http://www.fzu.cz/~ecoss22/`

27. *Adsorption and initial growth of p-quaterphenyl on gold surfaces*, Cluster Workshop, June 2003, Admont, Austria. (Talk Müllegger)

28. *Epitaxial growth of oligo-phenylenes on Al(111) and Au(111) surfaces*, R. Resel, I. Salzmann, T. Haber, S. Müllegger, A. Winkler, C. Teichert, G. Hlawacek, B. Winter, J. Ivanco, M. Ramsey, EMRS Meeting, June 2003, Strasbourg, France. (Talk Resel)

29. *Adsorption, growth kinetics and structure of thin quaterphenyl films on gold surfaces*, O. Stranik, S. Müllegger, E. Zojer, I. Salzmann, R. Resel and A. Winkler, 3S03, April2003, La Plagne, France. (Talk Winkler)

30. *Growth of ultrathin p-quaterphenyl films on gold surfaces*, S. Müllegger and A. Winkler, DPG Frühjahrstagung, 24-28th March 2003, Dresden, Germany. (Poster Müllegger)
`http://www.ifw-dresden.de/imw/akf2003/`

Bibliography

[1] D. J. Gundlach, Y. Y. Lin, and T. N. Jackson, *Appl. Phys. Lett.*, 1997, **71**, 3853.

[2] H. E. Katz and Z. Bao, *J. Phys. Chem. B*, 2000, **104**, 671.

[3] C. D. Dimitrakopousol and D. J. Mascaro, *IBM J. Res. Dev.*, 45, **11**, 2001.

[4] M. Era, T. Tsutsui, and S. Saito, *Appl. Phys. Lett.*, 1995, **67**, 2436.

[5] J. Kalinowski, *J. Phys. D: Appl. Phys.*, 1999, **32**, R179.

[6] S. R. Forrest, *Chem. Rev.*, 1997, **97**, 1793.

[7] A. Andreev, G. Matt, C. J. Brabec, H. Sitter, D. Badt, H. Seyringer, and N. Sariciftci, *Adv. Mat.*, 2000, **12**, 629.

[8] J. Fraxedas, *Adv. Mat.*, 2002, **14**, 1603.

[9] G. Witte and C. Wöll, *Phase Transitions*, 2003, **76**, 291.

[10] G. Horowitz and E. Hajlaoui, *Adv. Mat.*, 2000, **12**, 1046.

[11] G. Witte and C. Wöll, *J. Mater. Res.*, 2004, **19**, 1889.

[12] S. Müllegger, I. Salzmann, R. Resel, and A. Winkler, *Appl. Phys. Lett.*, 2003, **83**(22), 4536.

[13] S. Müllegger, O. Stranik, E. Zojer, and A. Winkler, *Appl. Surf. Sci.*, 2004, **221**, 184.

[14] S. Müllegger, I. Salzmann, R. Resel, G. Hlawacek, C. Teichert, and A. Winkler, *J. Chem. Phys.*, 2004, **121**(5), 2272.

[15] G. Hlawacek, C. Teichert, S. Müllegger, R. Resel, and A. Winkler, *Synth. Met.*, 2004, **146**, 383.

[16] M. Oehzelt, S. Müllegger, A. Winkler, G. Hlawacek, C. Teichert, and R. Resel, *Mat. Struct.*, 2004, **11**, 155.

[17] S. Müllegger and A. Winkler, *Surf. Sci.*, 2004, **574**, 322.

[18] S. Müllegger, S. Mitsche, P. Pölt, K. Hänel, A. Birkner, and C. Wöll, *Thin Solid Films*, 2005, **484**, 408.

[19] S. Müllegger and A. Winkler, *Surf. Sci.*, 2005, p. in press.

[20] S. Müllegger and A. Winkler, *Surf. Sci.*, in preparation.

[21] R. Resel, M. Oehzelt, T. Haber, G. Hlawacek, C. Teichert, S. Müllegger, and A. Winkler, *J. Cryst. Growth*, 2005, **283**, 397.

[22] ed. H. Ehrenreich and F. Spaepen, *Solid State Physics*, Vol. 49, Academic Press Inc., San Diego California, 1995.

[23] P. W. Atkins, *Physical Chemisty*, Oxford University Press, Oxford, 1998.

[24] W. R. Salaneck, R. H. Friend, and J. L. Bredas, *Phys. Rep.*, 1999, **319**, 231.

[25] F. Schreiber, *Prog. Surf. Sci.*, 2000, **65**, 151.

[26] N. Karl, *Synth. Met.*, 2003, **133-134**, 649.

[27] E. A. Silinsh, *Organic Molecular Crystals*, Springer, Berlin, 1980.

[28] C. Weißmantel, *Grundlagen der Festkörperphysik*, Johann Ambrosius Barth, Heidelberg, 1995.

[29] ed. T. A. Skotheim, R. L. Elsenbaumer, and J. R. Reynolds, *Handbook of Conducting Polymers*, Marcel Dekker, New York, 1998.

[30] J. L. Bredas, *Adv. Mat.*, 1996, **8**, 447.

[31] A. Niko, F. Meghdadi, C. Ambrosch-Draxl, P. Vogl, and G. Leising, *Synth. Met.*, 1996, **76**, 177.

[32] C. Ambrosch-Draxl, P. Puschnig, R. Resel, and G. Leising, *Synth. Met.*, 1999, **101**, 673.

[33] P. G. Schroeder, M. W. Nelson, B. A. Parkinson, and R. Schlaf, *Surf. Sci.*, 2000, **459**, 349.

[34] P. Puschnig and C. Ambrosch-Draxl, *Phys. Rev. B*, 1999, **60**, 7891.

[35] H. Yanagi, S. Okamoto, and T. Mikami, *Synth. Met.*, 1997, **91**, 91.

[36] E. Zojer, N. Koch, and P. P. et al., *Phys. Rev. B*, 2000, **61**, 16 538.

[37] T. Mikami and H. Yanagi, *App. Phys. Lett.*, 1998, **73**, 563.

[38] H. Yanagi and T. Morikawa, *Appl. Phys. Lett.*, 1999, **75**, 187.

[39] F. Balzer, V. G. Bordo, A. C. Simonsen, and H.-G. Rubahn, *Phys. Rev. B*, 2003, **67**, 115408.

[40] F. Quochi, F. Cordella, R. Orru, J. E. Communal, P. Verzeroli, A. Mura, G. Bongiovanni, A. Andreev, H. Sitter, and N. S. Sariciftci, *Appl. Phys. Lett.*, 2004, **84**, 4454.

[41] E. Zojer, J. Cornil, G. Leising, and J. L. Bredas, *Phys. Rev. B*, 1999, **59**, 7957.

[42] N. Koch, G. Heimel, J. Wu, E. Zojer, R. Johnson, J.-L. Bredas, K. Müllen, and P. Rabe, *Chem. Phys. Lett.*, 2005, **413**, 390.

[43] K. N. Baker, A. V. Fratini, T. Resch, H. C. Knachel, W. W. Adams, E. P. Socci, and B. L. Farmer, *Polymer*, 1993, **34**, 1571.

[44] G. Koller, A. Surnev, M. G. Ramsey, and F. P. Netzer, *Surf. Sci.*, 2004, **559**, L187.

[45] D. E. Williams and Y. Xiao, *Acta Cryst. A*, 1993, **49**, 1.

[46] Standard reference database. NIST; http://webbook.nist.gov/chemistry/, 2004.

[47] Y. Delugeard, J. Desuche, and J. L. Badour, *Acta Cryst. B*, 1976, **32**, 702.

[48] J.-L.Baudour, Y.Delugeard, and P.Rivet, *Acta Cryst. B*, 1978, **34**, 625.

[49] L. Athouël, G. Froyer, and M. T. Riou, *Synth. Met.*, 1993, **57**, 4734.

[50] A. Zangwill, *Physics at Surfaces*, Cambridge University Press, Cambridge, 1988.

[51] M. Henzler and W. Göpel, *Oberflächenphysik des Festkörpers*, B. G. Teubner, Stuttgart, 1991.

[52] E. Umbach, M. Sokolowski, and R. Fink, *Appl. Phys. A*, 1996, **63**, 565.

[53] F. Rosei, M. Schunack, Y. Naitoh, P. Jiang, A. Gourdon, E. Laegsgaard, I. Stensgaard, C. Joachim, and F. Besenbacher, *Prog. Surf. Sci.*, 2003, **71**, 95.

[54] D. E. Hooks, T. Fritz, and M. D. Ward, *Adv. Mat.*, 2001, **13**, 227.

[55] E. Umbach, K. Glöckler, and M. Sokolowski, *Surf. Sci.*, 1998, **402-404**, 20.

[56] A. C. Hillier and M. D. Ward, *Phys. Rev. B*, 1996, **54**, 14 037.

[57] E. J. Kintzel, D. M. Smilgies, J. G. Skofronick, S. A. Safron, D. H. V. Winkle, T. W. Trelenberg, E. A. Akhadov, and F. A. Flaherty, *J. Vac. Sci. Technol. A*, 2001, **19**, 1270.

[58] F. Balzer and H.-G. Rubahn, *Surf. Sci.*, 2004, **548**, 170.

[59] Y. Yoshida, H. Takiguchi, T. Hanada, N. Tanigaki, E. M. Han, and K. Yase, *J. Cryst. Growth*, 1999, **198/199**, 923.

[60] L. Athouël, G. Froyer, M. T. Riou, and M. Schott, *Thin Solid Films*, 1996, **274**, 35.

[61] F. Balzer and H. G. Rubahn, *Appl. Phys. Lett.*, 2001, **79**, 3860.

[62] H. Plank, R. Resel, S. Purger, J. Keckes, A. Thierry, B. Lotz, A. Andreev, N. S. Sariciftci, and H. Sitter, *Phys. Rev. B*, 2001, **64**, 235423.

[63] H. Plank, R. Resel, A. Andreev, N. Sariciftci, and H. Sitter, *J. Cryst. Growth*, 2002, **237-239**, 2076.

[64] B. Winter, J. Ivanco, F. P. Netzer, and M. G. Ramsey, *Langmuir*, 2004, **20**, 7512.

[65] R. Resel, I. Salzmann, G. Hlawacek, C. Teichert, B. Koppelhuber, B. Winter, J. Krenn, J. Ivanco, and M. Ramsey, *Organic Electronics*, 2004, **5**, 45.

[66] C. B. France and B. A. Parkinson, *Appl. Phys. Lett.*, 2003, **82**, 1194.

[67] C. Wöll, S. Chiang, R. J. Wilson, and P. H. Lippel, *Phys. Rev. B*, 1989, **39**, 7988.

[68] J. V. Barth, H. Brune, G. Ertl, and R. J. Behm, *Phys. Rev. B*, 1990, **42**, 9307.

[69] P. Zeppenfeld, *Appl. Surf. Sci.*, 1998, **130-132**, 484.

[70] S. Narasimhan and D. Vanderbilt, *Phys. Rev. Lett.*, 1992, **69**, 1564.

[71] C. B. Carter and R. Q. Hwang, *Phys. Rev. B*, 1995, **51**, 4730.

[72] A. R. Sandy, S. G. J. Mochrie, D. M. Zehner, K. G. Huang, and D. Gibbs, *Phys. Rev. B*, 1991, **43**, 4667.

[73] H. Bulou and C. Goyhenex, *Phys. Rev. B*, 2002, **65**, 045407.

[74] M. A. V. Hove, R. J. Koestner, P. C. Stair, J. P. Bibrian, L. L. Kesmodel, I. Bartos, and G. A. Somorjai, *Surf. Sci.*, 1981, **103**, 189.

[75] F. Pourmir, S. Rousset, S. Gauthier, M. Sotto, J. Klein, J. Lecoeur, and J. Bellier, *Surf. Sci.*, 1995, **324**, L337.

[76] S. Rousset, F. Pourmir, J. Berroir, J. Klein, J. Lecoeur, P. Hecquet, and B. Salanon, *Surf. Sci.*, 1999, **422**, 33.

[77] A. Stupnik, , Master's Thesis, Institute of Solid State Physics, Graz University of Technology, in preparation.

[78] H. C. Jeong and E. D. Williams, *Surf. Sci. Rep.*, 1999, **34**, 171.

[79] S. Rousset, V. Repain, G. Baudot, Y. Garreau, and J. Lecoeur, *J. Phys.: Condens. Matter*, 2003, **15**, S3363.

[80] P. A. Redhead, *Vacuum*, 1962, **12**, 203.

[81] R. I. Masel, *Principles of adsorption and reaction on solid surfaces*, John Wiley & Sons, New York, Chichester, Brisbane, Toronto, Singapore, 1996.

[82] D. A. King, *Surf. Sci.*, 1975, **47**, 384.

[83] J. W. Nietmantsverdriet and K. Wandelt, *J. Vac. Sci. Technol. A*, 1988, **6**, 757.

[84] D. L. S. Nieskens, A. P. van Bavel, and J. W. Niemantsverdriet, *Surf. Sci.*, 2003, **546**, 159.

[85] K. R. Paserba and A. J. Gellman, *Phys. Rev. Lett.*, 2001, **86**, 4338.

[86] S. Y. Krylov and L. J. F. Hermans, *Phys. Rev. B*, 2002, **65**, 092205–1.

[87] ed. D. Briggs and M. P. Seah, *Practical Surface Analysis by Auger and X-ray Photoelectron Spectroscopy*, John Wiley & Sons, Chichester/New York/Brisbane/Toronto/Singapore, 1983.

[88] ed. K. Oura, V. G. Lifshits, A. A. Saranin, A. V. Zotov, and M. Katayama, *Surface Science*, Springer, Berlin, 2003.

[89] ed. H. Bubert and H. Jenett, *Surface and Thin Film Analysis: Principles, Instrumentation, Applications*, Wiley-VCH, Weinheim, 2002.

[90] G. Ertl and J. Küppers, *Low Energy Electrons and Surface Chemistry*, Vol. 4 of *Monographs in Modern Chemistry*, Verlag Chemie, Weinheim, 1974.

[91] D. P. Woodruff and T. A. Delchar, *Modern Techniques of Surface Science*, Cambridge University Press, Cambridge, 1986.

[92] J. B. Pendry, *Low Energy Electron Diffraction*, number 2 in Techniques of Physics Series, Academic Press, London, New York, 1974.

[93] M. Henzler, *Electron Spectroscopy for Surface Analysis*, Springer-Verlag, Heidelberg, Berlin, New York, 1977.

[94] H. Wagner, *Physical and Chemical Properties of Stepped Surfaces*, Vol. 85 of *Springer Tracts in Modern Physics - Solid Surface Physics*, Springer-Verlag, Berlin, 1 ed., 1979.

[95] L. Alexander and H. Klug, *X-ray Diffraction Procedures*, John Wiley and Sons, Chichester/New York/Brisbane/Toronto/Singapore, 1974.

[96] I. Salzmann, *Structural Order in Epitaxially grown Oligo-phenylene Thin Films on Metallic Surfaces*, Master's Thesis, Graz University of Technology, 2003.

[97] G. Binning, H. Rohrer, C. Gerber, and E. Weibel, *Phys. Rev. Lett.*, 1982, **49**, 57.

[98] G. Binning, C. F. Quate, and C. Gerber, *Phys. Rev. Lett.*, 1986, **56**, 930.

[99] J. Stöhr, *NEXAFS Spectroscopy*, Springer, Berlin, 1992.

[100] G. W. S. Söhnchen, S. Lukas, *J. Chem. Phys.*, 2004, **121**, 525.

[101] J. Stöhr, *Phys. Rev. B*, 1987, **36**, 7891.

[102] J. Stöhr, *Z. Phys. B*, 1985, **61**, 439.

[103] C. Mainka, P. S. Bagus, A. Schertel, T. Strunskus, M. Grunze, and C. Wöll, *Surf. Sci.*, 1995, **341**, L1055.

[104] L. Reimer, *Scanning Electron Microscopy*, Springer, Berlin, 1998.

[105] W. Grogger, *Rasterelektronenmikroskopie*, Lecture notes, Graz University of Technology, 2004.

[106] O. Stranik, *Adsorption und Schichtwachstum von p-Quaterphenyl auf Goldoberflächen*, Master's Thesis, Institute of Solid State Physics, Graz University of Technology, 2002.

[107] I. Inc., *Operating Manual, XTM/2 Deposition Monitor*, Inficon Inc., New York, 1995.

[108] L. Kilian, E. Umbach, and M. Sokolowski, *Surf. Sci.*, 2004, **573**, 359.

[109] C. Seidel, A. Soukopp, R. Li, P. Bäuerle, and E. Umbach, *Surf. Sci.*, 1997, **374**, 17.

[110] G. Koller, R. Blyth, S. Sardar, F. Netzer, and M. Ramsey, *Surf. Sci.*, 2003, **536**, 155.

[111] S. M. Wetterer, D. J. Lavrich, T. Cummings, S. L. Bernasek, and G. Scoles, *J. Phys. Chem. B*, 1998, **102**, 9266.

[112] P. Fenter, F. Schreiber, L. Zhou, P. Eisenberger, and S. R. Forrest, *Phys. Rev. B*, 1997, **56**, 3046.

[113] A. Marchenko, Z. X. Xie, J. Cousty, and L. P. Van, *Surf. Interface Anal.*, 2000, **30**, 167.

[114] C. Seidel, R. Ellerbrake, L. Gross, and H. Fuchs, *Phys. Rev. B*, 2001, **64**, 195418.

[115] C. B. France, P. G. Schroeder, J. C. Forsythe, and B. A. Parkinson, *Langmuir*, 2003, **19**, 1274.

[116] T. Fritz, Private communication, 2005.

[117] M. Böhringer, K. Morgenstern, W.-D. Schneider, R. Berndt, F. Mauri, A. D. Vita, and R. Car, *Phys. Rev. Lett*, 1999, **83**, 324.

[118] T. Yokoyama, S. Yokoyama, T. Kamikado, Y. Okuno, and S. Mashiko, *Nature*, 2001, **413**, 619.

[119] G. Hlawacek, C. Teichert, A. Andreev, H. Sitter, S. Berkebile, G. Koller, M. Ramsey, and R. Resel, *Phys. Stat. Sol. A*, 2005, **in press**, 1.

[120] C. Wöll, *Organic fibres grown by vapour deposition*, Workshop on organic nanofibres Linz, 2005.

[121] S. Tait, Z. Dohnalek, C. T. Campbell, and B. D. Kay, *J. Chem. Phys.*, 2005, **122**, 164708.

[122] K.-F. Braun and S.-W. Hla, *Nano Lett.*, 2005, **5**, 73.

[123] R. Resel, *Thin Solid Films*, 2003, **433**, 1.

[124] ed. U. Shmueli, *International Tables for Crystallography*, Kluwer Academic Publisher, Dordrecht, Boston, London, 1996.

[125] C. Eibl, *Die Wechselwirkung von atomarem Wasserstoff mit Goldoberflächen*, Master's Thesis, Institute of Solid State Physics, Graz University of Technology, 1997.

[126] A. Winkler, *J. Vac. Sci. Tech. A*, 1987, **5**, 2430.

[127] G. Beernink, M. Gunia, F. Dötz, H. Öström, K. Weiss, K. Müllen, and C. Wöll, *ChemPhyschem*, 2001, **5**, 317.

[128] `http://www.lasurface.com/Data_base/Aw_xps_consult_gen.htm`, 2005.

[129] H. Pauly, *Atom, molecule and cluster beams I: basic theory, production and detection of thermal energy beams*, Springer, Berlin Heidelberg, 2000.

[130] ed. T. Hahn, *International Tables for Crystallography*, Vol. A, Kluwer Academic Publisher, Dordrecht, Boston, London, 2002.

[131] T. E. Madey, J. T. Yates, and N. E. Erickson, *Chem. Phys. Lett*, 1973, **19**, 487.

[132] G. Pirug, A. Winkler, and H. P. Bonzel, *Surf. Sci.*, 1985, **163**, 153.

[133] C. D. Wagner, W. M. Riggs, L. E. Davis, J. F. Moulder, and G. E. Muilenberg, *Handbook of X-ray Photoelectron Spectroscopy*, Perkin-Elmer Corporation, Minnesota, USA, 1978.

[134] R. F. Reilman, A. Msezane, and S. T. Manson, *J. Elec. Spec. Rel. Phen.*, 1976, **8**, 389.

[135] J. H. Scofield, *J. Elec. Spec. Rel. Phen.*, 1976, **8**, 129.

[136] S. Evans, R. G. Pritchard, and J. M. Thomas, *J. Elec. Spec. Rel. Phen.*, 1978, **14**, 341.

[137] A. Jablonski and C. J. Powell, *J. Vac. Sci. Technol. A*, 2003, **21**, 274.

[138] D. A. Shirley, *Phys. Rev. B*, 1972, **5**, 4709.

[139] P. Lejcek, *Surf. Sci.*, 1988, **202**, 493.

[140] D. W. Palmberg, G. E. Riach, R. E. Weber, and N. C. MacDonald, *Handbook of Auger electron spectroscopy*, Physical Electronics Industries, Inc., Minnesota, USA, 1972.